Interannual and decadal variability of the primary productivity and oxygen Minimum Zone in the Peruvian Upwelling System

Dante Espinoza Morriberón

Sorbonne Université

l'Ecole Doctorale des Sciences de l'Environnement d'Ile de France (ED129)

Laboratoire d'Océanographie et du Climat: Expérimentation et Approches Numériques

Interannual and decadal variability of the primary productivity and oxygen Minimum Zone in the Peruvian Upwelling System

Par Dante Espinoza Morriberón

Thèse de doctorat de Sciences de la Mer

Dirigée par Dr. Vincent Echevin

Co-directeur de thèse Dr. Francois Colas

Présentée et soutenue publiquement le 12 décembre 2018

Devant un jury composé de:

Prof. Damien Cardinal	Président
Dr. Laurent Mémery	Rapporteur
Prof. Isabelle Dadou	Rapporteur
Dr. Mark Ohman	Examinateur
Dr. Olivier Aumont	Invité

This thesis is dedicated to Martha,
Cris and Rocio. To my family Gina,
Mariacristina and Matias

Acknowledgements

Firstly, I would like to express my sincere gratitude to my advisors Dr. Vincent Echevin and Dr. Francois Colas for the continuous support of my Ph.D study and related research, for their patience, motivation, and immense knowledge. Their guidance helped me all the time of research and writing of this thesis. I could not have imagined having better advisors and mentors for my Ph.D study.

Agradecer a todo el IMARPE, en especial al Dr. Tam y el Dr. Dimitri que me han permitido realizar el PhD sin ningún incoveniente y confiar en mi para hacer investigación. A todos los miembros de mi Laboratorio (LMOECC) en IMARPE: Yvan, Jorge Ramos, Adolfo, Cinthia, Carlos, Jorge Flores, Paul, Maritza, Danny, Fiorela, Hanz, Manon. Ustedes han visto todo el proceso !!!, y gracias a sus enseñanzas pude en cierta forma terminar el doctorado.

A Erich Diaz y Ricardo Oliveros, porque fueron las personas que me impulsaron a hacer ciencia desde que llegué a IMARPE y sin los cuales, quizás no me encontraría en estos momentos terminando esta tesis.

Agradecer a mi familia por todo su apoyo durante estos cuatro largos años, en los cuales nunca dejaron de creer y confiar en mi. Gracias Martha por alentarme e impulsarme a seguir con mis grados académicos, este doctorado es para ti. Gracias Cristina y Rocio, por todo su apoyo, por decir las cosas directas y siempre ayudarme sin dudar en los peores momentos. A mi esposa Gina, por entender mi profesión y ser mi compañera; y a los pequeños en casa: mi Maricris y Matias por esperarme siempre felices luego de mis viajes!!!.

A todos los que han hecho posible este trabajo.

Table of Contents

ABSTRACT

The Peruvian upwelling System, driven by quasi-permanent alongshore winds, is one of the most productive regions of the global ocean. Due to a sluggish subsurface circulation and respiration of a large amount of sinking organic matter, an intense and shallow Oxygen Minimum Zone (OMZ) is present in the subsurface layers. Because of its proximity to the Equatorial Pacific, this system is strongly impacted by El Niño (EN) and La Niña (LN) events at interannual and interdecadal time scales. In the present thesis, we first study how EN and LN events impact on (i) primary productivity and (ii) dissolved oxygen concentrations. Second, we investigate the physical and biogeochemical processes responsible for the productivity and deoxygenation trends observed during the last decades. We make use of a regional physical-biogeochemical coupled model (ROMS-PISCES) and of an in-situ regional data set to study the hydrodynamics and biogeochemical cycles from 1958 to 2008. The model is able to reproduce oceanic conditions associated with EN and LN, and the observed trends in the last decades. During EN periods, surface chlorophyll decreases due to nutrient depletion associated with intense downwelling Coastal Trapped Waves and due to an enhanced light limitation in summer. The surface layer becomes more ventilated as the oxycline deepens in association with the thermocline. The OMZ waters originate from a more ventilated equatorial region. The enhanced eddy kinetic energy also impacts eddy fluxes of nutrient and oxygen during EN. During the last decades, the large-scale remote forcing associated to equatorial variability mainly drives the summer Chl increase and progressive deoxygenation, whereas local winds play a minor role. The nearshore deoxygenation trend could be associated with the decreased mass fluxes of Equatorial Under Current and Tsuchiya jets.

CHAPTER 1:
INTRODUCTION

The Peruvian Upwelling System: A High Productivity Ecosystem with an Intense Oxygen Minimum Zone

1. Generalities

The Peruvian Coastal Upwelling System (PCUS) or Humboldt Current System (HCS) is one of the most productive systems in the ocean [Chavez and Messié, 2009; Lachkar and Gruber, 2012]. It is one of the four Eastern Boundary Upwelling Systems (EBUS; California, Canary and Benguela system) of the global ocean (Fig.1a). As other EBUS, the PCUS presents particular characteristics: cold coastal waters, poor-oxygenated subsurface waters (called Oxygen Minimum Zones, OMZ) [Paulmier and Ruiz-Pino, 2009] and a high surface productivity [Chavez and Messié, 2008; Demarcq, 2009] which supports one of the most abundant fisheries in the word, the anchovy fishery [Pauly and Christensen 1995].

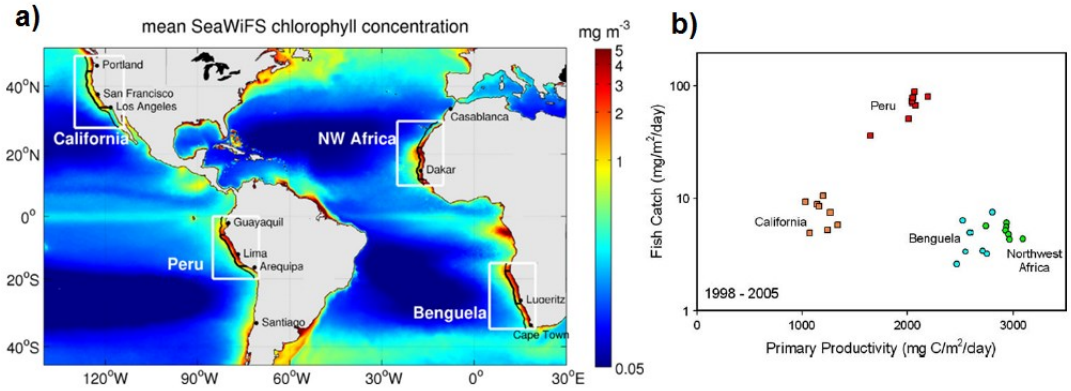

Figure 1. a) The four Eastern Boundary Upwelling Systems: California, Humboldt, Benguela and Canaries. The mean concentration of chlorophyll-a from SeaWIFS averaged over 1997-2008 is shown (colour scale). The figure was modified from Messié and Chavez [2015]. b) Fish catch vs. primary productivity between 1998 and 2005 in the four major EBUS [Chavez et al., 2008].

In the EBUS, subsurface waters are brought to surface by upwelling, which supplies nutrient-rich waters to the surface layer, triggering a phytoplankton bloom near the shores. The different EBUS have different latitudinal range, shelf width, nutrient input concentration, upwelling intensity [Fréon et al., 2009] and primary productivity. For these reasons, understanding the mechanisms which take place in EBUS is one of the hot scientific topics nowadays [Lachkar and Gruber, 2012].

The productivity in the EBUS represents 1% of the ocean productivity, nevertheless 20% of the fish catches on the world are carried out in these systems [Pauly and Christensen, 1995]. From this 20%, half is caught in the PCUS eventhough other EBUS (e.g. the Benguela and Canary Systems) are more productive (Fig. 1b) [Chavez et al., 2008]. Several hypotheses were formulated to explain this particularity: (i) the efficiency of the trophic transfer from zooplankton to small pelagic fish [Bertrand et al., 2014], (ii) the short food chain [Espinoza and Bertrand, 2008], and (iii) the "re-set effect" of the El Niño phenomenon which allows the anchovy to growth without presence of predators and competitors [Bakun and Weeks, 2008].

The formation and maintenance of the Peruvian OMZ result from complex physical and biogeochemical processes. Anoxic conditions have been occasionally evidenced in the coastal region [Paulmier and Ruiz-Pino, 2008]. Besides, the OMZ is one of the shallowest in the world [Fuenzalida et al., 2009]. As it limits the habitat of several species, it has been suggested that the decadal changes in the anchovy and sardine stocks may have been driven by decadal oscillations of the depth of the OMZ upper limit [Diáz and Rosenberg, 2008; Bertrand et al., 2011]. Furthermore, progressive deoxygenation has been evidenced in the open ocean and coastal regions [Breitburg et al., 2018], which could be related with the expansion of the OMZ during the last decades [Stramma et al., 2008].

At interannual time scales, the PCUS is strongly impacted by El Niño Southern Oscillation (ENSO), owing to its proximity to the equatorial Pacific. ENSO originates in the Equatorial Central Pacific region and has an impact on the entire world climate. It presents warm (El Niño, EN) and cold (La Niña, LN) phases. During EN, in the coastal region off Peru, the temperature increases and the productivity decreases [Barber and Chavez, 1983], which triggers a change in distribution of several fish species [Ñiquen and Bouchón, 2004], while during LN opposite impacts are observed.

The PCUS is also impacted at longer time scales by climate change. In the future, under a pessimistic scenario (quadrupling the preindustrial CO_2 atmospheric concentration), Sea Superficial Temperature (SST) and stratification increase [Echevin et al., 2011; Oerder et al., 2015]. More recent results suggest that nearshore primary productivity may slightly decrease [Gévaudan et al., 2017]. Besides, deoxygenation trends are not known in the future, due to the strong oxygen bias in current global earth-system models [Cabré et al., 2015]. Climate change could also influence the distribution of the fish migration (e.g northward, Cheung [2018]) and loss of the biodiversity in the Tropical Ocean.

The above mentioned processes and characteristics of the PCUS make it a crucial and interesting research topic. The dynamical and biogeochemical processes, which occur during EN and LN events, are not well understood, mainly because of the scarcity of sampled data and the lack of data processing. Increasing the knowledge about the mechanisms that produce interannual productivity and oxygenation changes during ENSO is one of the main goals of this thesis. Furthermore, the processes driving the long term evolution of the system are also studied.

In the following, section 1 describes in detail the PCUS mean state and seasonal variations. Section 2 focuses on the impacts of ENSO (EN and LN events) on oceanic conditions in the PCUS, whereas section 3 describes the recent findings about the physical and biogeochemical observed trends off Peru, with a particular emphasis on the primary productivity and OMZ. Section 4 presents a compilation of the modelling biogeochemical studies in the PCUS. Last, section 5 summarizes the objectives of the present thesis.

1.1. Currents in the PCUS

The PCUS presents a particular current system (Fig. 2). Nearshore currents are driven mainly by the surface wind at the surface and impacted by the equatorial circulation at subsurface. The PCUS is composed by two current systems: the Equatorial Current System (ECS) [Tsuchiya 1975; Johnson and Moree, 1997; Ishida et al., 2005; Kessler 2006] and the Peruvian Current System (PCS) [Brockmann et al., 1980; Penven et al., 2005; Montes et al., 2010; Chaigneau et al., 2013; Pietri et al., 2014].

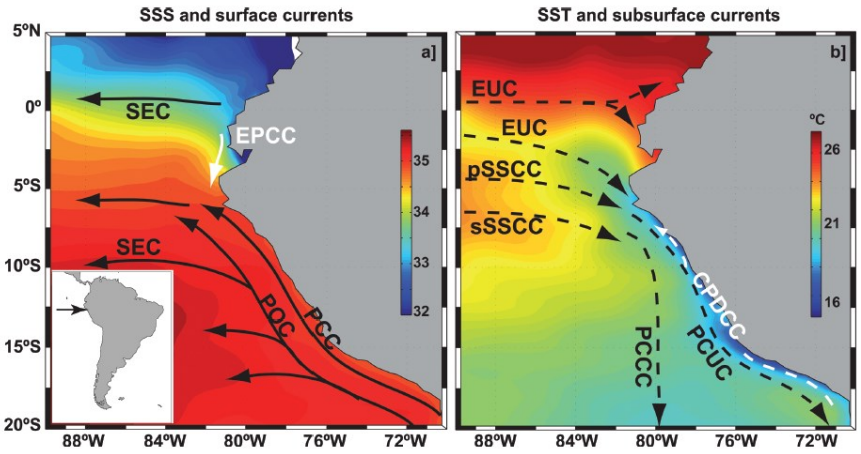

Figure 2. Surface (left panel) and subsurface (right panel) currents in the Peruvian Coastal Upwelling System. The mean surface salinity (in ups, left panel) and temperature (in °C, right panel) are also shown. Figure adapted from Chaigneau et al. [2013].

1.1.1. The Equatorial Current System (ECS)

The ECS is composed by the Surface Equatorial Current (SEC), the subsurface Equatorial Undercurrent (EUC) and the Southern Subsuperficial Countercurrents (SSCC) (Fig. 3). The SEC forms the northern part of the South Pacific Gyre. It flows northeastward across the equator (~ 5°N) and its velocity increases westward [Wyrtki, 1967]. The SEC transports ~ 12 Sv at 95°W above 200 m between 6°S and 6°N, and increases at 140°W (~ 35 Sv) [Kessler, 2006]. SEC splits into two branches when the EUC shoals [Kessler, 2006]. Furthermore, the SEC forms part of the equatorial upwelling system, which is produced by the divergence of the Northern and Southern SEC [Pennington et al., 2006].

At subsurface, the EUC is a permanent current. It flows eastward along the equator [Philander, 1980; Tsuchiya et al., 1989; Ishida et al., 2005] and shoals from west to east [Kessler, 2006]. The EUC splits into two branches at 92°W owing to the presence of the Galapagos Islands [Lukas, 1986]. In average, the EUC is found between 2°N – 2°S and 50 – 300 m depth at 86°W [Kessler, 2006]. Moreover, the EUC intensity presents a marked seasonality. It peaks between January and June and decreases in July-November [Lukas, 1986]. Interannually, the EUC is impacted by ENSO phases. During EN, the EUC vertical extent reduces (70 – 200 m) and its flux is stronger than during neutral and LN periods [Montes et al., 2011]. The EUC is also a source of oxygen in the eastern equatorial Pacific as it transports oxygen-rich waters eastward [Stramma et al., 2010].

Off the equator, the SSCCs (also known as Tsuchiya jets; Tsuchiya [1975]) flow eastward. The northern and southern SSCC are also called primary and secondary jets. The primary and secondary jets (pSSCC/sSSCC) are usually located between 2°S – 6°S and 6°S – 10°S respectively. The pSSCC is stronger than sSSCC, but both are less intense than EUC [Montes et al., 2010]. ENSO phases also impact the SSCCs. During EN, the pSSCC shifts northward and its vertical extent reduces, while during LN its core remains at ~4°S and thickens. In contrast, the sSSCC is closer to the equator, more intense and shallower during EN than during neutral and LN periods [Montes et al., 2011]. The OMZ is highly sensitive to changes in the position and intensity of the SSCCs [Montes et al., 2014].

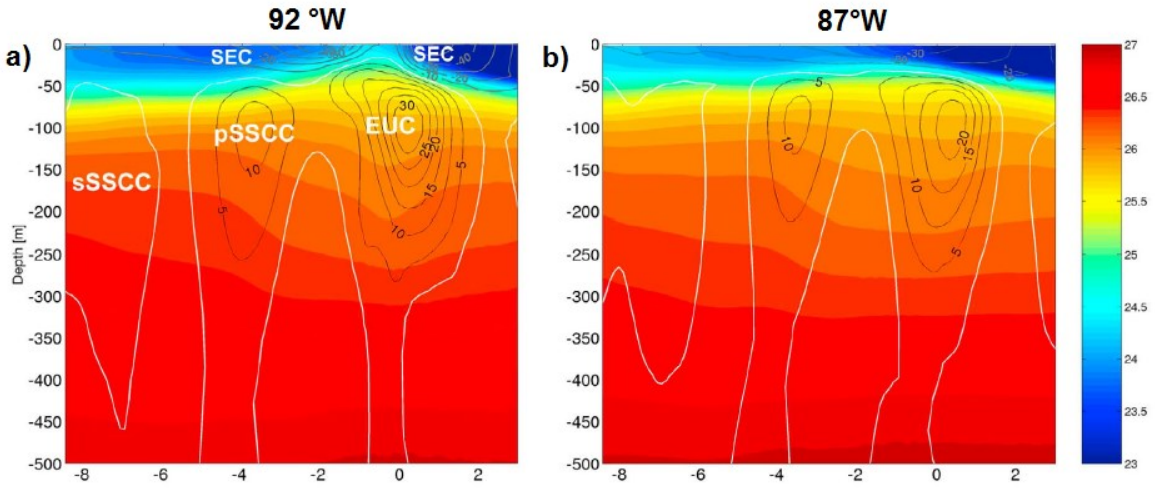

Figure 3. Meridional section of the zonal current (cm s^{-1}, in contours) and density (in colours) between 92°W - 87°W of ROMS outputs from Montes et al. [2011].

1.1.2. The Peruvian Current System (PCS)

At the surface, two equatorward currents dominate the PCS: the Peru Coastal Current (PCC) and the Peru Oceanic Current (POC) (Fig. 2a). The Peru Coastal Current (PCC, also called Humboldt Current) is found within 100 km from the coast and between surface and ~ 50 m [Huyer et al., 1991; Penven et al., 2005; Pietri et al., 2014]. It transports cold and nutrient-rich waters due to coastal upwelling [Huyer et al., 1987]. Its velocity ranges from 5 to 15 $cm.s^{-1}$ and increases equatorward. Moreover, the maximum PCC flow during winter is in phase with the seasonal cycle of the trade winds [Strub et al., 1998]. The offshore POC flows northward (north-eastward between 15°S and 20°S). Using ADCP data in 2008-2012, Chaigneau et al. [2013] observed the POC between 9°S and 12°S, farther than 180 km from the coast and up to 500 m depth.

At subsurface, the Peru-Chile Undercurrent (PCUC) flows poleward [Brockmann et al., 1980] until 48°S [Silva and Neshyba, 1979]. It dominates the subsuperficial circulation on the Peruvian shelf between 100 and 200 m depth [Brink et al., 1983]. The PCUC intensifies from 8°S to 16°S and decreases south of 16°S (Fig. 4) [Chaigneau et al., 2013]. It reaches the surface layer during some periods [Penven et al., 2005; Pietri et al., 2014].

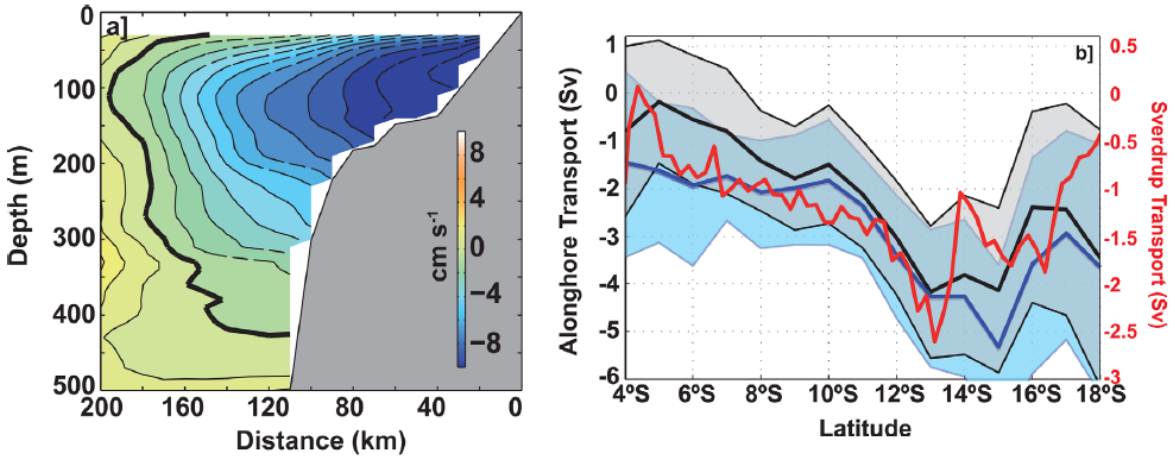

Figure 4. Cross-shore section of alongshore velocity (in cm s^{-1}) (a). Meridional variation of alongshore integrated transports (solid lines) and associated errors (shaded areas) (b). In (b), transports were integrated between 25 m and 500 m depth and from the coast to 200 km offshore. Black solid line marks the total transport, whereas blue solid line corresponds to the transport associated with poleward alongshore velocity components only. Red solid line corresponds to the mean southward Sverdrup transport (2008–2012) integrated from the coast to 200 km offshore and computed from Metop/ASCAT winds. From Chaigneau et al. [2013].

PCUC waters are the main source waters of the coastal upwelling [Huyer et al., 1987]. They have a high salinity and are nutrient-rich and low oxygenated [Tsuchiya and Talley, 1998; Strub et al., 1998]. Seasonally, between 9°S – 12°S, the PCUC intensifies during summer, while is weaker during winter [Chaigneau et al., 2013] (Fig. 5a). Using a hydrodynamic model, Montes et al. [2011] showed that during EN (2002 – 2003) the PCUC shoaled and intensified, whereas during LN (1999 – 2000) it deepened and was slightly more intense than neutral periods. ADCP data from IMARPE also evidenced an intensification of the PCUC during the moderate 2010 El Niño event [Chaigneau et al., 2013] (Fig. 5b). The PCUC is fed (~ 30%) directly by the EUC and SSCCs, the latter being the main contributors [Montes et al., 2010]. Interannually, the PCUC is fed mainly by the sSSCC and pSSCC during EN and LN respectively [Montes et al., 2011].

Last, the poleward Peru-Chile Countercurrent (PCCC) is found further from the coast than the PCUC and spans between 5°S – 35°S [Strub et al., 1998].

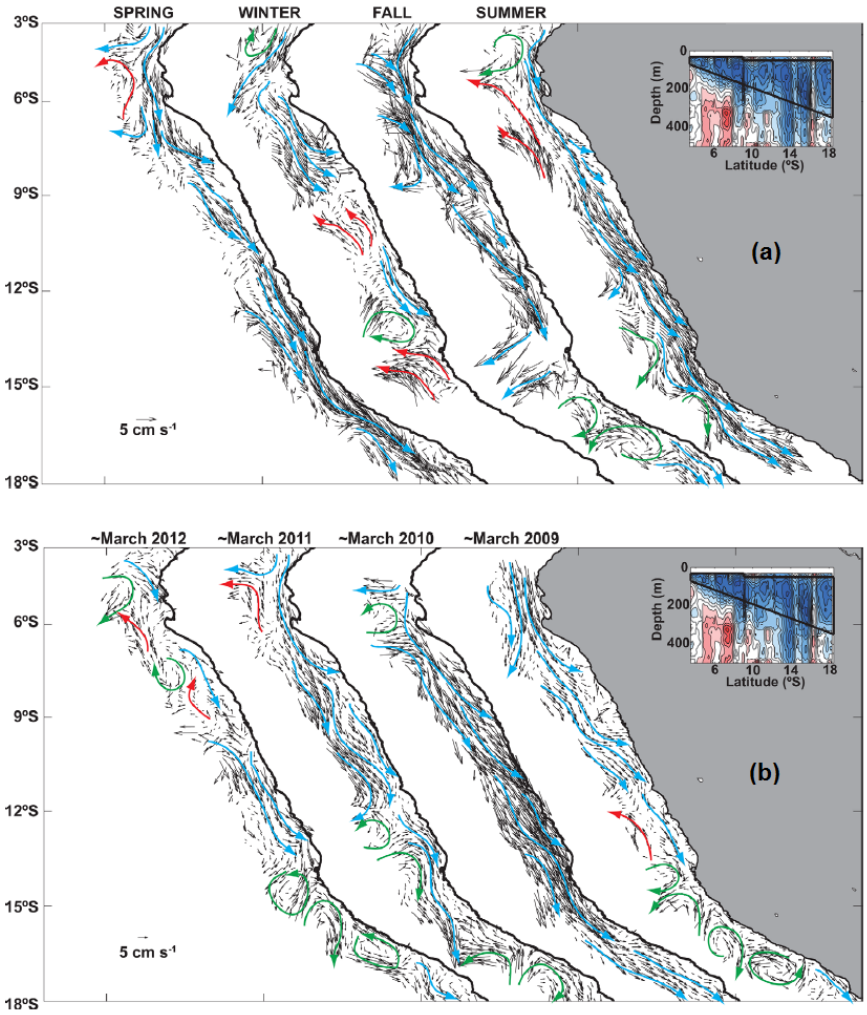

Figure 5. Seasonal cycle of the averaged circulation in the layer corresponding to PCUC core. Red and blue arrows represent schematically the equatorward and poleward flows, respectively, whereas green arrows indicate the presence of mesoscale eddy-like features (a). In (b), same as (a) but for specific surveys realized along the Peruvian coast in March of 2009 – 2012. From Chaigneau et al. [2013].

1.2. Coastal Upwelling

The upwelling is the divergence process by which deep waters are brought to surface layers. This process takes place in the EBUS, but may also occur in other ocean areas (e.g. equatorial upwelling).

As the trade winds blow equatorward along the Peruvian coasts, this produces a motion of surface waters due to friction between the air and the sea surface (Fig. 6a). In the Southern Hemisphere, the movement of surface waters is to the left of the wind direction (with an angle

of 45°), due to the Coriolis Effect. In subsurface layers, this angle increases and the velocity associated to the wind stress decreases (by dissipation of energy) producing the Ekman Spiral (Fig. 6c). Below the Ekman Spiral, the influence of the wind stress is insignificant. The Ekman layer is defined between the surface and the bottom of the Ekman Spiral. The integration of the water velocity over the depth of the Ekman layer is the Ekman transport, perpendicular to the wind direction. The Ekman transport (M) is computed as follows:

$$M = \frac{\tau}{\rho_{sea}|f|}$$

Where τ represents the wind stress, ρ_{sea} the water density (~ 1026 kg.m^{-3}) and |f| the absolute value of the Coriolis parameter.

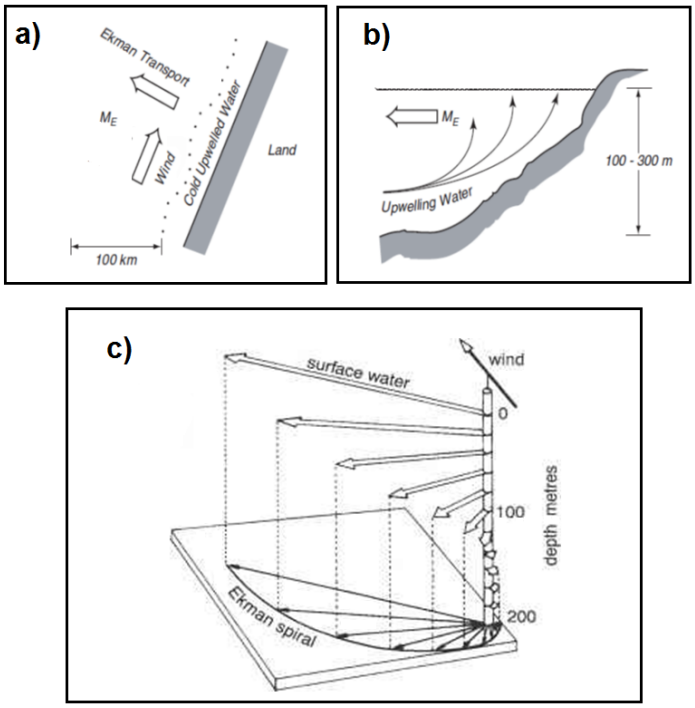

Figure 6. Schematic representation of the Ekman transport at the surface (a) and in a vertical cross-shore section (b). Representation of the Ekman Spiral in the water column (c).

Coastal upwelling is driven mainly by the Ekman transport divergence at the coast. Nevertheless, Ekman transport divergence is not the unique process that produces upwelling. Ekman pumping and "upwelling" Coastal Trapped Wave (CTW) may also trigger coastal upwelling [Kampf and Chapman, 2016]. The role of upwelling CTWs will be detailed in section 2.1.

The Ekman pumping refers to the vertical velocity induced by the divergence of the horizontal Ekman transport associated to wind stress curl. This process takes place offshore and is associated to an upward flux of nutrients. Using a physical-biogeochemical coupled model, Albert et al. [2010] showed that a decrease in Ekman pumping produced a less productive system owing to the deepening of the source nutrient-rich waters transported by the PCUC (Fig. 7). Moreover, using satellite data from ERS (European Remote-sensing Satellite), Halpern [2002] demonstrated that Ekman pumping decreases during EN due to a weakening of wind stress curl.

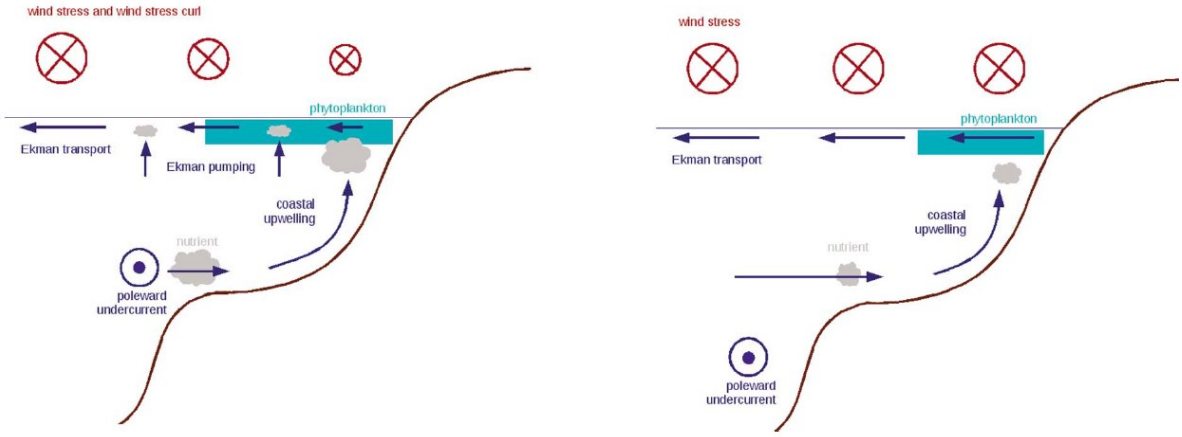

Figure 7. Schematic representation of the mechanisms linking wind stress curl to primary production (left and right panel). The alongshore wind stress (in red) decreases in the dropoff zone (from ~200 km to the coast) leading to negative wind stress curl. Ekman transport (horizontal arrows in blue) is related to wind stress, and Ekman pumping (vertical arrows in blue) is related to wind stress curl. From Albert et al. [2010].

In order to study the upwelling, several upwelling indices (UI) have been developed. They are based mainly on the nearshore wind stress values [e.g. Bakun et al., 1973]. The UI is defined as:

$$UI = M * \cos\alpha$$

M is the Ekman transport and α is the angle of the coastline. For the Peruvian coast, α is ~150° in Trujillo and ~140° in Callao [Mendo et al., 1987].

At seasonal time scales, the UI represents well the variation of the upwelling in the coastal region. The upwelling peaks during winter and decreases during summer [Zuta and

Guillen, 1970]. Figure 8 shows that the seasonal cycles of the upwelling and trade winds are highly correlated [Chamorro et al., 2018].

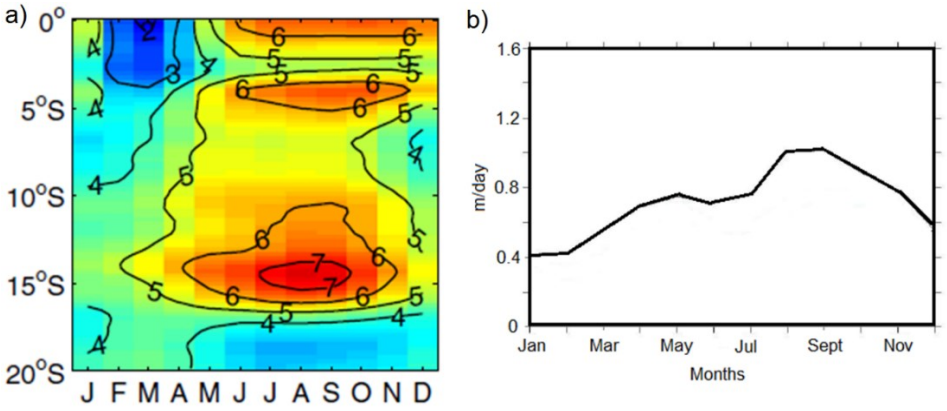

Figure 8. Seasonal cycle of the wind speed alongshore (left panel, in m s^{-1}) from Chamorro et al. [2018] and vertical velocity mean (right panel, m day^{-1}) between 7°S-13°S within 200 km to the coast at 50 m depth from a ROMS simulation [Espinoza-Morriberón, 2012].

At interannual time scales, there is a decoupling between upwelling and wind stress. Indeed, the alongshore winds tend to increase during EN (forced by the strong SST alongshore gradient; Chamorro et al. [2018]), whereas the upwelling decreases. Using in situ data (vertical profiles of temperature) near 10°S, Huyer et al. [1987] evidenced the shutdown of the upwelling during the 1982-83 EN (May 1983) in spite of an enhanced wind stress. Using a numerical model, Colas et al. [2008] evidenced a decrease of the upwelling between 7°S and 13°S during the 1997-1998 EN. Both studies suggest that the decoupling between the wind stress and the upwelling during EN is caused by an onshore geostrophic flow associated to a large scale alongshore sea level anomaly. Thus, the coastal upwelling is driven by the interplay between oceanic (e.g. currents) and atmospheric (e.g. winds) forcing [Colas et al., 2008; Marchessiello and Estrade, 2010].

The alongshore upwelling can be decomposed in localized upwelling cells. Calienes et al. [2014] computed the offshore extension of cold waters and identified six main upwelling centers: Pimentel (~ 7°S), Chimbote (~ 9°S), Huarmey (~ 10°S), Pisco (~ 14°S), San Juan (~ 16°S) and Atico (~ 16.5°S). These areas present cold SST, high nutrient concentration and an intense productivity [Calienes et al., 1985]. The most intense upwelling centers are located between Pisco and San Juan, where SST reaches 17°C in summer and 16°S in winter (Fig. 9; Grados et al. [2018]).

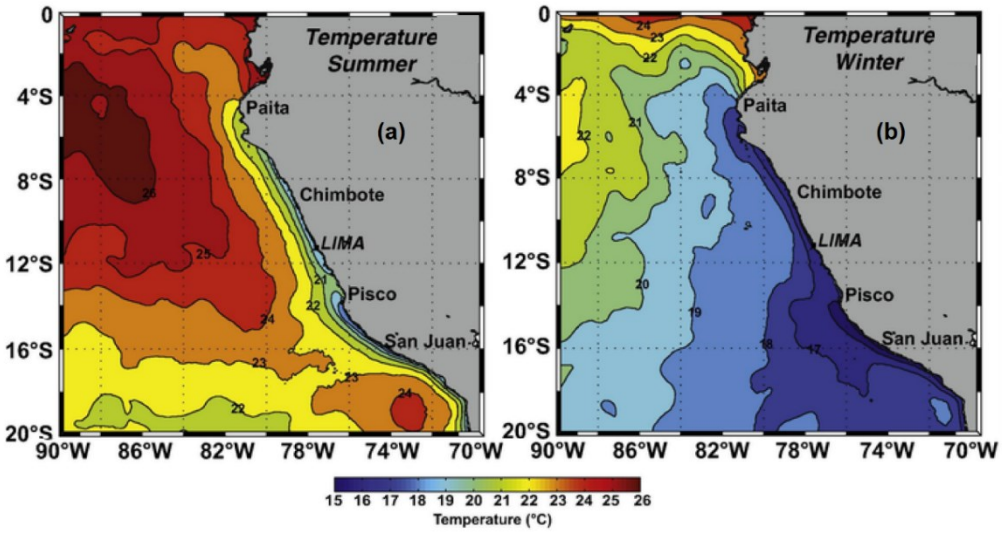

Figure 9. Mean in situ SST during summer and winter (in °C). Figure from Grados et al. [2018].

1.3. Nutrients in the PCUS

The availability of upwelled nutrient-rich waters drives the primary productivity in the EBUS. The main nutrients needed for phytoplankton growth are nitrate (NO3), silicate (SiO2), phosphate (PO4) and iron (Fe). Nutrients increase at greater depths (generally below the picnocline) and decrease in the surface layer due consumption by phytoplankton [Zuta and Guillén, 1970]. Off the Peruvian coasts, the surface nutrients range between 0 to 35 µmol L^{-1} (nitrate), from 0 to 30 µmol L^{-1}(silicate), from 0.2 to 4 µmol L^{-1} (phosphate) [Zuta and Guillén, 1970; Graco et al., 2007; Calienes et al., 2014] and from 0.01 to ~ 12 nmol L^{-1} [iron; Bruland et al., 2005].

Strong nutrients cross-shore (coastal-ocean) gradient are found, with higher concentrations close to the coast. These rich waters are associated to the intense coastal upwelling [Calienes et al., 1985, Zuta and Guillén, 1970] but also to the shelf sediments off central Peru [Dale et al., 2017]. Latitudinally, the higher nutrient concentrations are observed between 6°S and 15°S. During winter, surface nitrate may reach values of 20 µmol L^{-1} between 6°S – 10°S, while lower values (~3 µmol L^{-1}) are found south of 16°S and north of 3°S [Calienes et al., 1985]. This distribution is associated to the presence of contrasted water masses. Cold Coastal Cold Water (CCW) is characterized by high nitrate, silicate and phosphate concentrations, while the offshore Surface Subtropical Waters (SSW) and Surface Equatorial Waters (SEW) are nutrient-poor. The nitrate distribution is also influenced by the chemical

reactions of the nitrogen cycle: nitrification, denitrification and anammox during which nitrogen is lost to the atmosphere in the form of N_2 (Fig. 10).

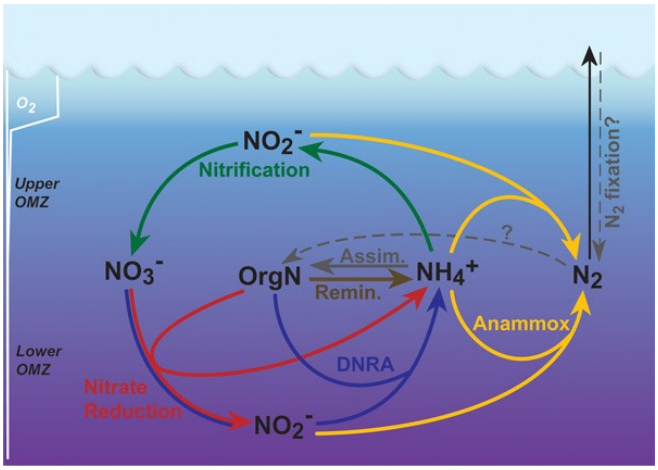

Figure 10. Schematic of the oceanic Nitrogen cycle. From Lam et al. [2009].

Figure 10 describes the nitrogen cycle in the ocean. Nitrification occurs under oxygenated condition and during this process, ammonium is oxidized into nitrite and nitrate. This process is performed by bacteria and produces high concentrations of nitrous oxide (N_2O, a potent greenhouse gas), which are generally observed above 50 meters depth in the PCUS [Kock et al., 2016]. Denitrification is defined as the nitrate reduction to ammonium. In this process, bacteria uses nitrate as the hydrogen accepter under oxygen deficient conditions, (generally less than 6 µmol kg^{-1}) [Dugdale et al., 1977]. In the PCUS, denitrification was observed at 100 – 400 m depths and between 10°S – 25°S. It can remove ~ 2.5 x 10^{13} g N yr^{-1} by N_2O production over a 2 year time period (e.g. 1976-1977, Packard et al. [1983]). Last, anammox (anaerobic ammonium oxidation) transforms nitrite to N_2. Anammox is the predominant pathway for nitrogen loss within the PCUS OMZ [Lam et al., 2009]. These biogeochemical processes are strongly modified by ENSO phases [Mogollón and Calil 2017; Yang et al., 2017] (see chapter 3 and 4).

The seasonal cycles of nutrients and upwelling are highly correlated. During winter, the nutrients reach their maximum values, whereas during summer nutrient-poor waters predominate alongshore. At the surface, the phosphate, silicate and nitrate are low (~ 1 µmol L^{-1}, ~ 5 µmol L^{-1}, ~ 5 µmol L^{-1}, respectively) and increase during winter (~ 2.5 µmol L^{-1}, ~ 25 µmol L^{-1}, ~ 20 µmol L^{-1}, respectively) (Fig. 11) [Calienes et al., 1985; Graco et al., 2007].

ENSO phases also have a strong impact in the nutrients concentration in the column water (see section 2.1).

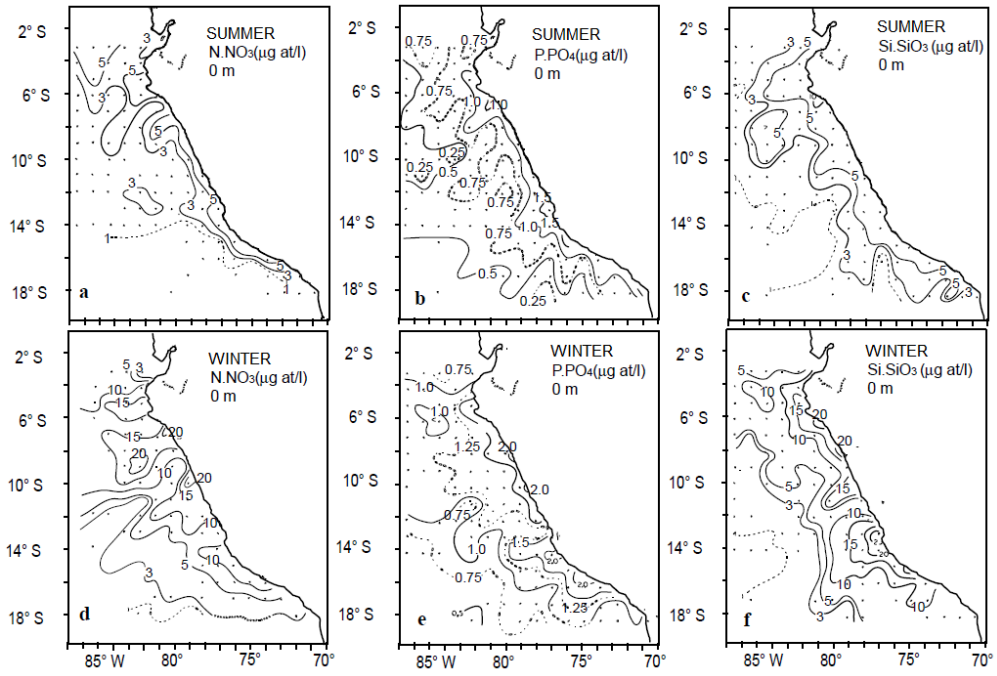

Figure 11. Surface nutrient concentration (nitrate, phosphate and silicate) from IMARPE observations. From Calienes et al. [1985].

In the case of iron, a micro-nutrient, scarce data is available to compute a robust seasonal cycle. However, iron is known to have an important role in the phytoplankton growth. The shelf sediment is considered to be the main source of iron. In the PCUS (as in the open ocean), there are zones known as High-Nitrate and Lower Chlorophyll concentration (HNLC). These low-productive, nitrate-rich waters are due to a deficit of iron, limiting phytoplankton growth [Hutchins et al., 2002]. Bruland et al. [2005] classified the Peruvian waters based on the iron concentration. Offshore "blue waters" are characterized by a low productivity and a low iron concentration, whereas nearshore "brown waters" are highly productive and iron rich. Fertilization experiments in the open ocean demonstrated that productivity in HNLC regions is limited by iron [Boyd et al., 2007].

1.4. Primary Productivity

The PCUS is one of the most productive areas in the world. The permanent upwelling of nutrient-rich waters, along the year, triggers high levels of productivity. Chlorophyll-a (Chl) from both in situ and satellite data (ocean color) is used as a proxy to evaluate the productivity.

Chavez and Messié [2009] showed that the seasonal cycle of productivity and the vertical transport (upwelling) from California, Canary and Benguela systems are in phase (Fig. 12). In contrast, the seasonal cycle of the productivity and the upwelling are out of phase in the PCUS.

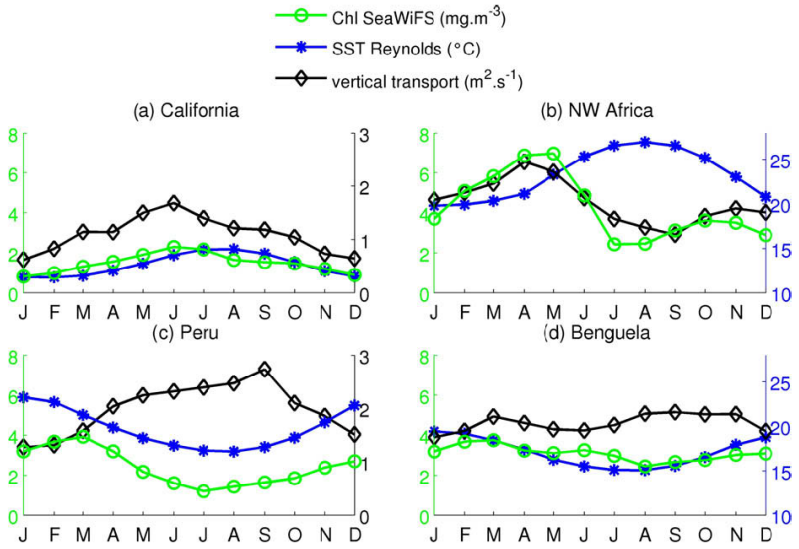

Figure 12. Seasonal cycle of chlorophyll concentration (black), sea surface temperature (blue) and total vertical transport (Ekman transport plus Ekman pumping) in the four EBUS (10°S latitude band up to 150 km offshore). From Chavez and Messié [2009].

Surface Chl patterns in the PCUS are typical of EBUS [Calienes et al., 1985, 2014, Echevin et al., 2008]. Maximum and minimum values are found nearshore and offshore respectively (Fig. 13, SeaWIFS). Using IMARPE in situ data from 1960 to 2000, Calienes et al. [2014] found that Chl ranges from 0.02 to more than 12 mg m^{-3} within 100 km from the coast. The highest values are found between 7°S and 15°S (Fig. 13a). Chl vertical profiles present an U-shaped curve with a peak at ~ 25 m depth, which is related to the euphotic layer and MLD [Calienes et al., 1985, 2014]. Red tides (extreme values of productivity) are often found near the coast, triggered by eutrophic conditions [Kahru et al., 2004].

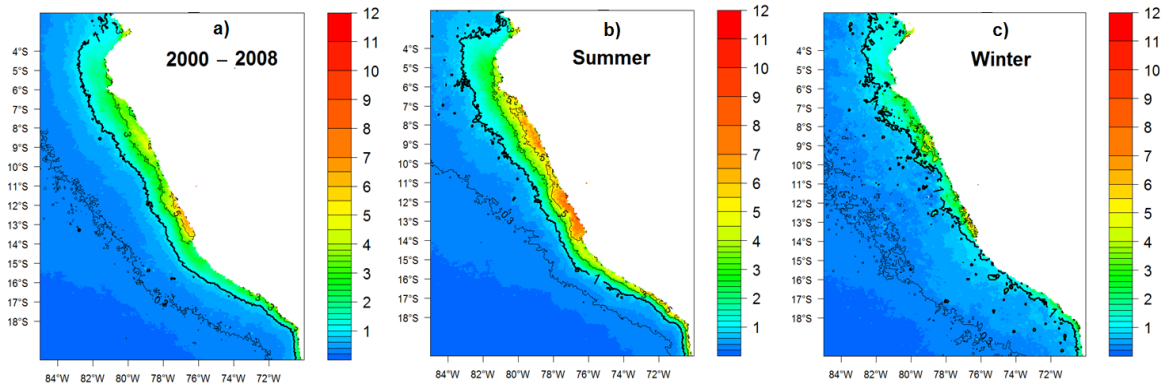

Figure 13. Annual mean surface Chl (a), summer (b) and winter (c) means from satellite SeaWIFS data between 2000 and 2008.

As mentioned previously, the PCUS productivity presents a marked seasonality. The Chl (between 4°S – 15°S and within 200 km to the coast) displays maximum values in late austral summer – early autumn (in situ: ~ 5 mg m^{-3}, SeaWIFS: ~ 2.5 mg m^{-3}), while minimum values during winter are observed (in situ: ~ 0.8 mg m^{-3}, SeaWIFS: ~ 1 mg m^{-3}). The in situ data presents a second peak during spring (~ 3 mg m^{-3}) (Fig. 14a) [Pennington et al., 2006; Echevin et al., 2008]. The amplitude of the seasonal cycle depends of the latitude. It is enhanced in two narrow coastal bands at 8°S – 9.5°S and 11°S – 14°S (Fig. 14b), the latter being the most productive. Both coastal regions present highest values during late summer – early autumn (8°S–9.5°S: ~ 5 mg m^{-3}; 11°S–14°S: ~ 7 mg m^{-3}) and minimum concentrations during winter (~ 2 mg m^{-3}).

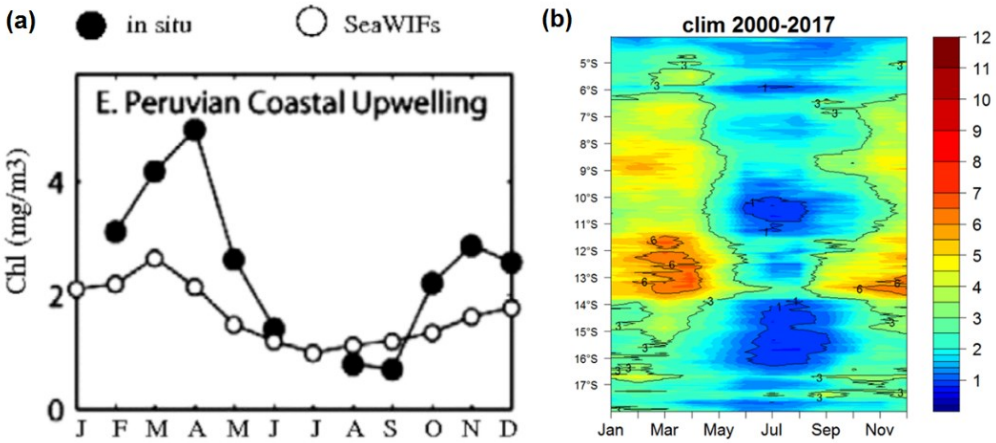

Figure 14. Seasonal cycle from in situ data and SeaWIFS in a coastal band (between 4°S – 15°S and within 200 km to the coast) from Echevin et al. [2008] (a). Alongshore seasonal variation of Chl from SeaWIFS-MODIS (b).

As mentioned previously, the seasonal cycle of Chl and upwelling are out of phase (Fig. 15). Several hypotheses have been proposed to explain this paradox [Calienes et. al., 1985; Echevin et al., 2008; Messié and Chavez et al., 2015]. During summer, Chl is confined a thin surface layer where nutrients are consumed [Messié and Chavez, 2015]. Thus, nutrient limitation is triggered by a stronger stratification and a thinner mixed layer (thus less light limitation) as the wind-forced upwelling is weaker [Gutiérrez et al., 2011a]. In contrast, stronger winds and deeper MLD are encountered in winter [Fig.15; Echevin et al., 2008]. In these conditions, the phytoplankton cells reach depths close to the "critical depth" (zones with low light; Sverdrup [1953]). Thus, productivity decreases due to enhanced light limitation. Echevin et al. [2008], using a physical-biogeochemical model, suppressed the seasonality of the surface insolation, which impacted the amplitude of the Chl signal but not the seasonal variations of Chl. These results are in line with Calienes et al. [1985], who found maximums of Chl under different isolation rates, mentioning that it could be due to changes of MLD.

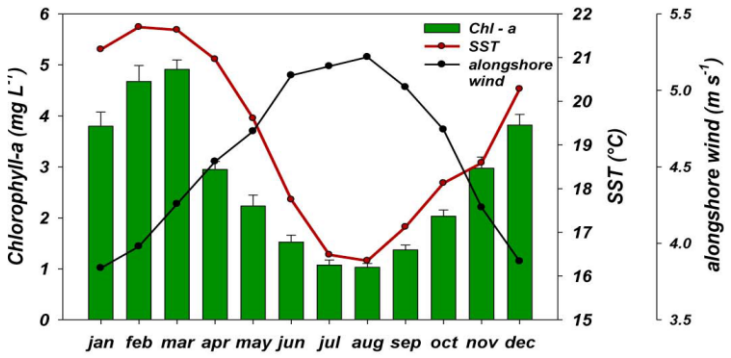

Figure 15. Chl (from SeaWiFS data (1997–2006); green bars), alongshore wind (from ECMWF–ERA40 reanalysis; black line), and SST climatology (red line) at Pisco (15°S). The red line joins the monthly SST-means from Pisco pier SST and GHRSST. From Gutiérrez et al [2011a].

The role of iron in the seasonal cycle of productivity has also been analysed. Messié and Chavez [2015] found that both light limitation and iron limitation impacts the Chl decrease during winter, owing to the larger iron demand under low light conditions [Sunda and Huntsman, 1997]. Echevin et al. [2008] demonstrated in a model sensitivity experiment, that productivity increases mainly between 13°S – 14°S from June to October (~ + 80%) when iron limitation is artificially relaxed.

1.5. The Oxygen Minimum Zone

Oxygen Minimum Zones (OMZ) are large water bodies of the open ocean which present low concentration of dissolved oxygen (DO < 22 µmol.kg-1) at subsurface depths (~ 50 – 900 m) [Karstensen et al., 2008]. The PCUS OMZ is one of the most intense and shallowest OMZ in the open ocean [Paulmier and Ruiz-Pino, 2009]. Complex physical and biogeochemical processes are involved in the PCUS OMZ formation and maintenance:

a) Vertical mixing between the oxygenated surface mixed layer and OMZ waters is reduced due to the relatively weak PCUS winds. Moreover, the permanent strong pycnocline [Fiedler and Talley, 2006] mitigates vertical mixing. Additionally, the PCUS OMZ is located in the unventilated "shadow zone" of the South Eastern Pacific [Luyten et al., 1983].

b) The residence time of OMZ waters is very long. Czeschel et al. [2011] found that the OMZ center is a stagnant area: a deployed float at 8°S in the OMZ core was found at the same location after 15 months.

c) The EUC and Tsuchiya jets ventilate the OMZ, which is sensitive to their changes. Tsuchiya jets transport oxygenated waters eastward which impact directly the PCUS OMZ. Nevertheless, the oxygen content of the EUC and Tsuchiya jests decrease from west to east [Stramma et al., 2010]. Montes et al. [2014], using a physical-biogeochemical coupled model, simulated the change in PCUS OMZ due to different intensities of the equatorial circulation. They evidenced a shrinking of OMZ when the secondary Tsuchiya jets was more intense (Fig. 16).

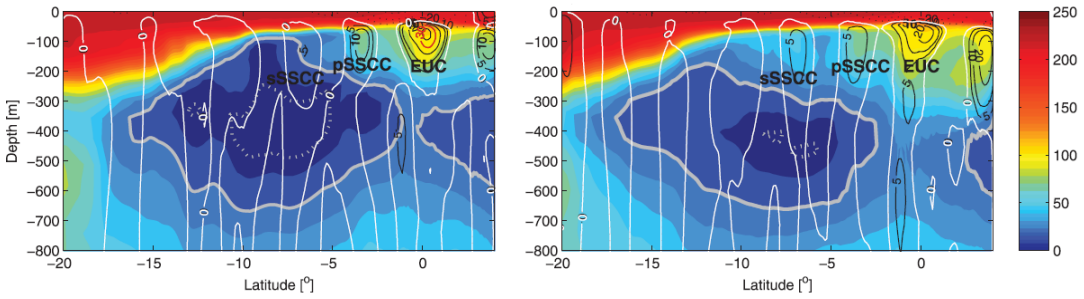

Figure 16. Meridional sections of oxygen annual mean (in µmol kg^{-1}) at 88 °W from two simulations with different equatorial circulation. In contours are shown the zonal currents (in cm s^{-1}). Figure from Montes et al. [2014].

d) The mesoscale circulation plays a role in the shaping the OMZ. Vergara et al. [2016] found that mesoscale structures ventilate the OMZ at its lateral boundaries between 100 – 600 m depth (Fig. 17). Besides, nearshore (sub) mesoescale filaments and fronts ventilate the OMZ across its upper limit (Fig. 18; Thomsen et al. [2016]).

e) The large amount of organic matter (OM), which originates from the high surface productivity, eventually sinks into the OMZ and gets remineralized. In this process, OM is oxidized by the microbial pool that produces a high oxygen consumption [e.g. Cavan et al., 2017].

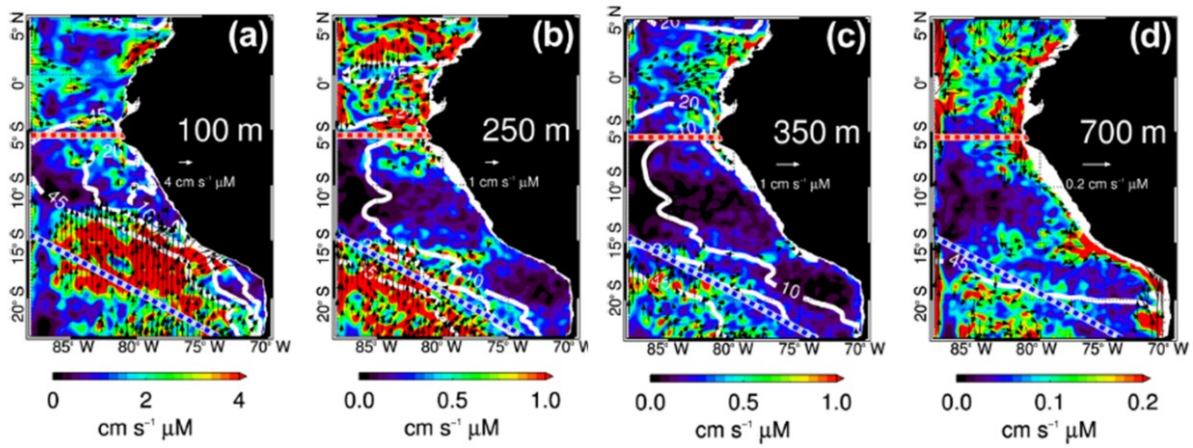

Figure 17. Module (color scale) and direction (black arrows) of the mean DO eddy-flux vector at (a) 100 m, (b) 250 m, (c) 350m and (d) 700m depths. White contours correspond to the 45, 20 and 10 µmol kg^{-1} mean DO values. From Vergara et al. [2016].

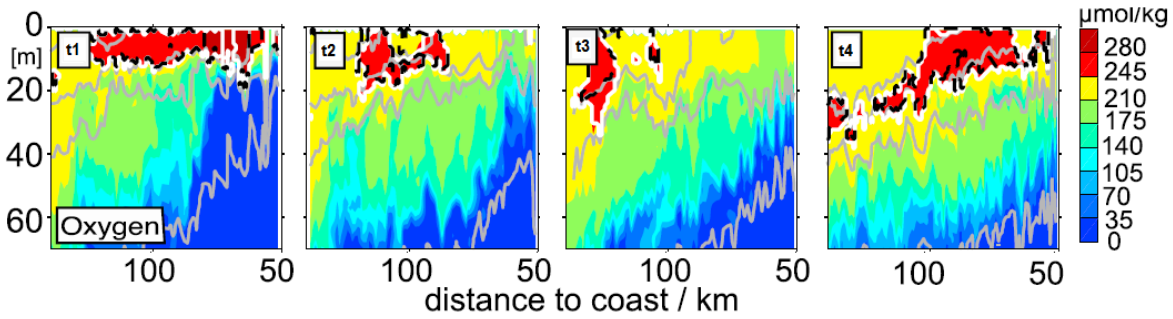

Figure 18. Cross-shore oxygen transect (glider measurements) in a submesoscale cold filament off Peru in January/February 2013. From Thomsen et al. [2016].

The PCUS OMZ is located alongshore and extends westward near 8°S (Fig. 19a). It is thickest between 5°S – 13°S and 500 km offshore. Nearshore, the upper limit of the OMZ (ZO2, proxy of the oxycline in the coastal region) is located at 30 – 50 m depth [Graco et al., 2007].

The nearshore OMZ is shallowest between 12°S – 16°S and deepens north of 8°S (Fig. 19). Extremely shallow depths can be reached, such as ZO2~2.5 m during summer 2006 [Ledesma et al., 2011]. Offshore at 85°S, the lower OMZ limit reaches ~ 600 m depth between 4°S – 15°S. The OMZ core can present values less than 5 µmol kg^{-1} and reaches anoxic conditions (e.g. Czeschel et al. [2015]; Thomsen et al. [2016]). The OMZ core extends vertically between ~ 150 – 500 m depth and at 85°W between 2°S and 18°S [Karstensen et al., 2008].

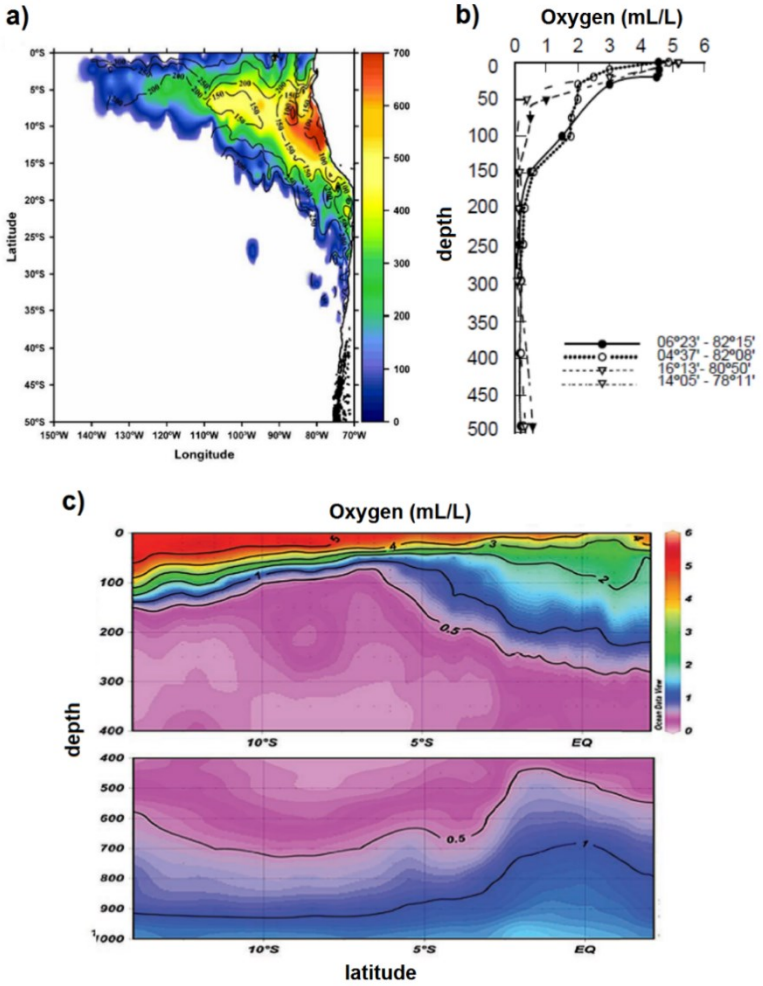

Figure 19. Annual mean depth of the upper OMZ limit (in meters, contour) and OMZ thickness (in meters, colour) from Fuenzalida et al. [2009] (a). Oxygen vertical profiles at different latitudes (IMARPE data) from Graco et al. [2007] (b). Alongshore oxygen concentration [Ledesma et al., 2011] (c). (b) and (c) are in mL L^{-1} and 1 mL L^{-1} is equivalent to 44 µmol L^{-1}.

The PCUS OMZ presents a seasonal cycle related to the wind-driven coastal upwelling, intense remineralization and the mesoscale circulation (eddies and filaments) [Vergara et al. 2016]. During summer, a decrease of DO and a shoaling of the OMZ are observed. DO decrease

is triggered by the decay of enhanced productivity, which induces high remineralization. Additionally, an intense stratification isolates the subsurface waters from oxygenated surface layer. During winter, a deeper OMZ is found. It is mainly due to the well-mixed water column triggered by enhanced wind stress, while the lower productivity does not have a strong impact in the DO. In this season, the offshore OMZ is ventilated by offshore DO eddy fluxes [Vergara et al., 2016]. Zuta and Guillén [1970], using in situ data, also evidenced the oxygen seasonality in the surface layer. They found DO values of ~ 75 μmol kg^{-1} and ~ 90 μmol kg^{-1} during summer and winter respectively, between 0 – 100 m off Callao (12°S).

2. ENSO as driver of the PCUS Interannual Variability

In this section, the main impacts of EN and LN events on the PCUS are described, with emphasis on biogeochemical processes. EN events present different spatial structures. Two types of El Niño have been identified: the so-called "central Pacific" (CP) El Niño (also known as Modoki EN) [Takahashi et al., 2011] and the "Eastern Pacific" (EP) El Niño (also known as Canonical EN) (e.g. 1982-1983, 1997-1998 EN). These EN types have different impacts in the PCUS. For instance, models outputs and satellites data evidenced that the CP EN is related to negative (positive) SST anomalies in the PCUS, while the EP EN presents strong positive (negative) SST anomalies in the Eastern Pacific Ocean [Dewitte et al., 2012; Lee et al., 2014]. These different impacts of the CP and EP EN are associated with the upwelling and downwelling CTW respectively, generated by the equatorial Kelvin waves (see section 2 and 3; Dewitte et al., [2012]). In this section, the impacts of EP EN and LN events off the Peruvian coasts are described.

2.1. Impacts of El Niño events

EN is an ocean-atmospheric coupled phenomenon occuring in the Equatorial Pacific. It occurs every 3 to 5 years and substantially alters the ecosystem functioning associated to coastal upwelling. During EN a weakening of the trade winds in the western equatorial Pacific triggers the eastward displacement of the warm pool [Picaut et al., 1996]. It generates positive SST anomalies in the Central and Eastern Pacific Ocean. The subsurface ocean structure is also impacted. The equatorial thermocline, typically deeper in the Western Equatorial Pacific, deepens in the Eastern Pacific (Fig 20). These changes in ocean conditions are associated to a weakening of the atmospheric pressure in the Eastern Pacific and to a southward displacement of the Intertropical Convergence Zone (ITCZ).

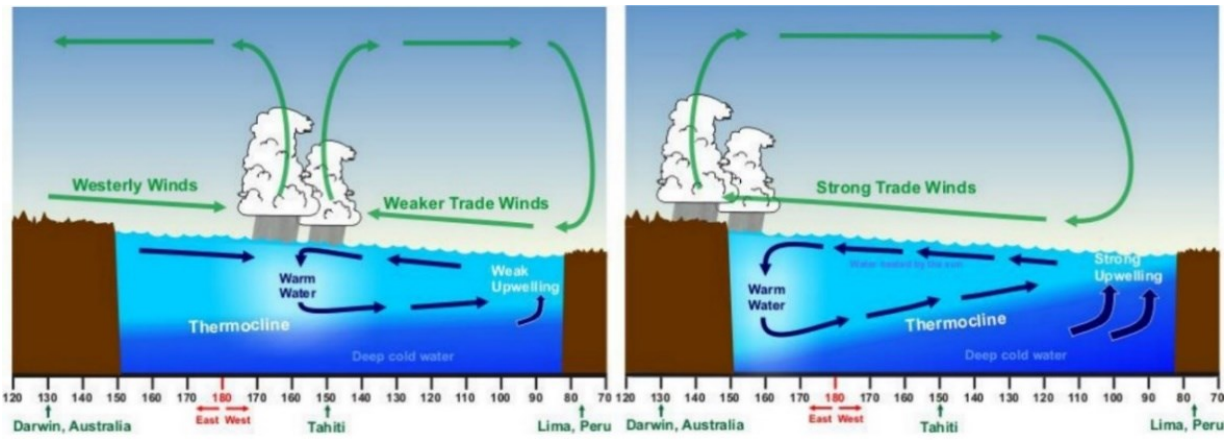

Figure 20. Schematic representation of the modifications of the oceanic and atmospheric zonal circulation during El Niño (left panel) and La Niña (right panel) in the equator. Figure from https://pirca.org.

The westerly winds anomalies generate Equatorial Kelvin Waves (EKW), which propagate eastward across the Equatorial Pacific [Kessler and McPhaden, 1995]. When they reach the coasts of America (Ecuador), EKW trigger Coastal Trapped Waves (CTW), which propagate poleward along the coasts of Peru and Chile. EKW generation occurs every year. However, "warm" (downwelling) and "cold" (upwelling) CTWs are particularly frequent and intense during EN and LN events respectively [McPhaden, 1999; Picaut et al., 2002].

In contrast with LN, EN events strongly impact oceanic conditions in the PCUS. During the propagation of CTW, the Sea Surface Height (SSH) rises. Carr and Broad [2000] using satellite data, showed that two SSH rises (~20 cm anomalies) were found during the 1982-1983 and 1997-1998 EN events (see also Colas et al., [2008]).

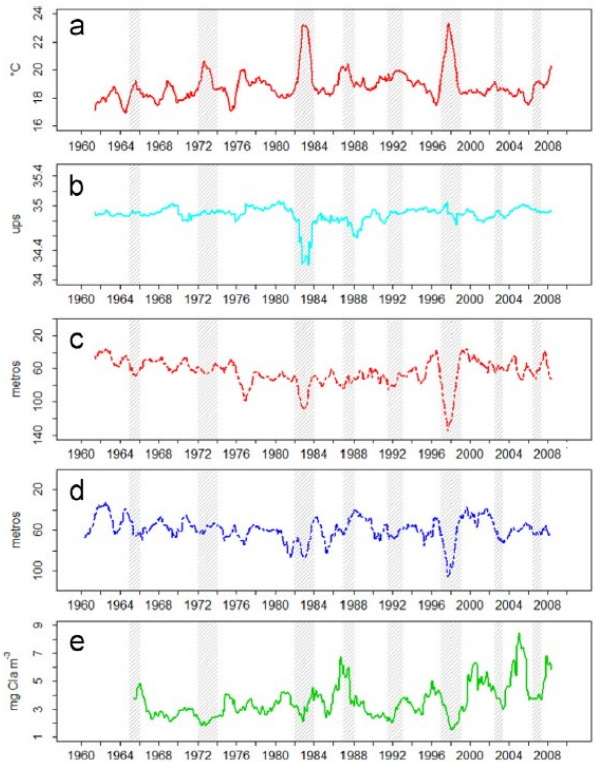

Figure 21. Interannual variability of (a) sea surface temperature (°C), (b) surface salinity (UPS), (c) depth of the 15 °C isotherm (meters), (d) depth of the 1ml L-1 iso-oxygen at the base of the oxycline (meters), (e) surface chloroplyll-a content (mg m^{-3}). The timeseries are monthly averages calculated from IMARPE data (period: 1960–2008; latitude range: 3.5°S–20°S, distance to the coast: 0–100km). Shaded rectangles correspond to El Niño events. From Gutiérrez et al. [2016].

The nearshore temperature and salinity are also strongly impacted (Fig. 21) [Gutiérrez et al., 2016]. Using an extended data set from IMARPE (1960 – 2014), Grados et al. [2018] computed temperature and salinity anomalies composites during EN (Fig. 22) and LN (Fig. 26). During EN, the positive SST anomalies reach maximum values on the Peruvian shelf (~3-4°C) and decrease south of 16°S (~1-1.5°C) (Fig. 22a). The warm waters are observed from the surface to ~ 150 m depth, and the maximum positive anomalies (~ +3°C) are found at 20 m depth between 5°S – 12 °S (Fig. 22b). For example, at Callao station (~12°S), the thermocline (defined as isotherm of 15°C) was found at large depths (~ 100 m depth) during 1997-1998 EN [Barber and Chavez, 1983; Gutiérrez et al., 2008; Graco et al., 2017]. The warming is initiated by the "warm" downwelling CTWs which deepen the thermocline during their propagation, an sustained by the horizontal advection of positive SST anomalies [Chavez et al., 1984] associated with the intrusion of Equatorial Surface Water (ESW) and Tropical Surface

Water (TSW) in the coastal region [Flores et al., 2013]. Furthermore, more saline waters are observed between 7°S – 20°S. Flores et al. [2013] found values up to ~35.5 during 1982-1983 and 1997-1998 EN events. The highest positive salinity anomalies were observed in the center-south region of Peruvian coast (12°S – 20°S) and between surface and 100 m depth (Fig. 22c, d). Thus, the halocline deepens due to an onshore transport of the Subtropical Surface Waters (STSW) [Grados et al., 2018] and the presence of Equatorial Subsurface Water (ESSW) [Llanillo et al., 2013].

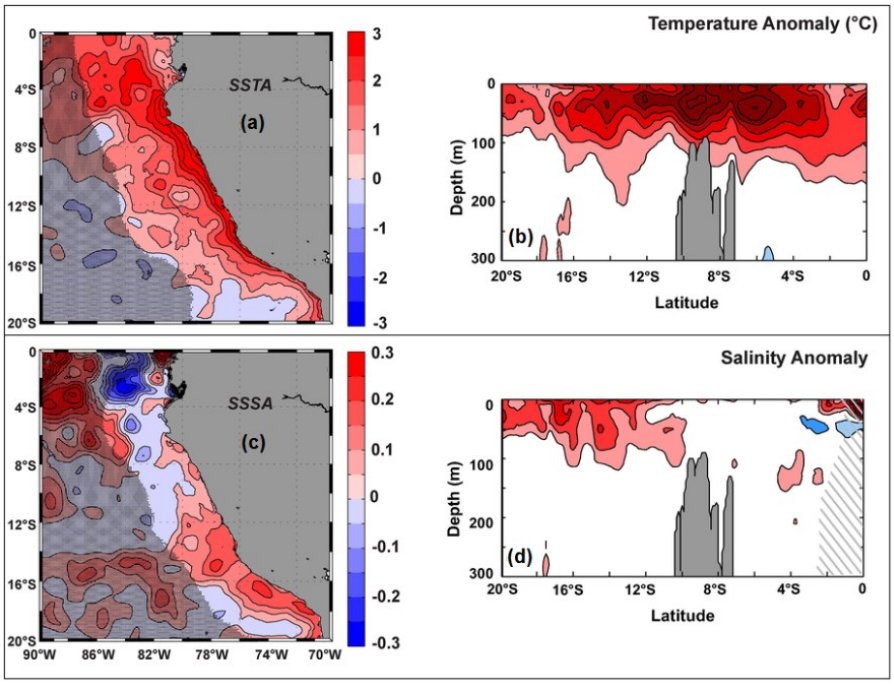

Figure 22. Temperature (in °C, top panel) and salinity (in ups, bottom panel) anomalies during El Niño at surface (left) and within alongshore between 0 and 300m depth (right). From Grados et al. [2018].

The CTWs also impact the biogeochemical conditions. Echevin et al. [2014], using a regional model, demonstrated that the passage of the downwelling (upwelling) CTW triggers the deepening (shoaling) of the thermocline and nutricline. Negative (positive) Chl anomalies also propagate poleward, although with slower propagation speed than the physical signal (Fig. 23).

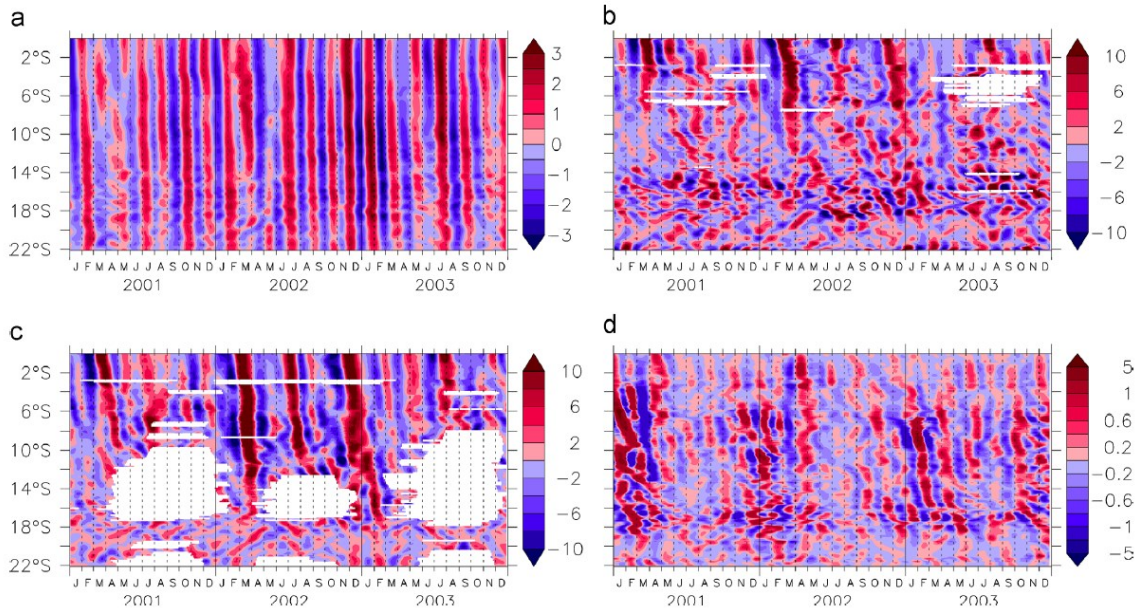

Figure 23. Time-latitude diagram of (a) sea level (in m), (b) depth of the 2 µmol L^{-1} iso-nitrate (in m), (c) depth of the 17°C isotherm (in m), and (d) surface chlorophyll anomalies (in mg m^{-3}) from a ROMS-PISCES simulation. All variables have been averaged in a 100-km-wide coastal band, and band-pass filtered in the [50-80] days band to highlight the intraseasonal signal. From Echevin et al. [2014].

Nutrient-poor waters are also found offshore of the PCUS during EN. Barber and Chavez [1983] evidenced a marked nitrate decrease during 1982–1983 EN: nitrate was lower than 4 µmol L^{-1} (12 µmol L^{-1} in neutral periods) at 85°W between 0°S and 10°S and above 50 m (Fig. 24a). Near the coast at 12°S, Graco et al. [2017] observed a nitrate decrease during the 1997–1998 EN peak. The isolines of 15 µmol L^{-1} for nitrate, 10 µmol L^{-1} for silicate (Fig. 24b) and 1 µmol L^{-1} for phosphate reached greater depths (~ 100 m) than during normal conditions. In addition to CTWs, the onshore displacements of the ESW and TSW might reduce the nutrient concentration close to the coast [Graco et al., 2007].

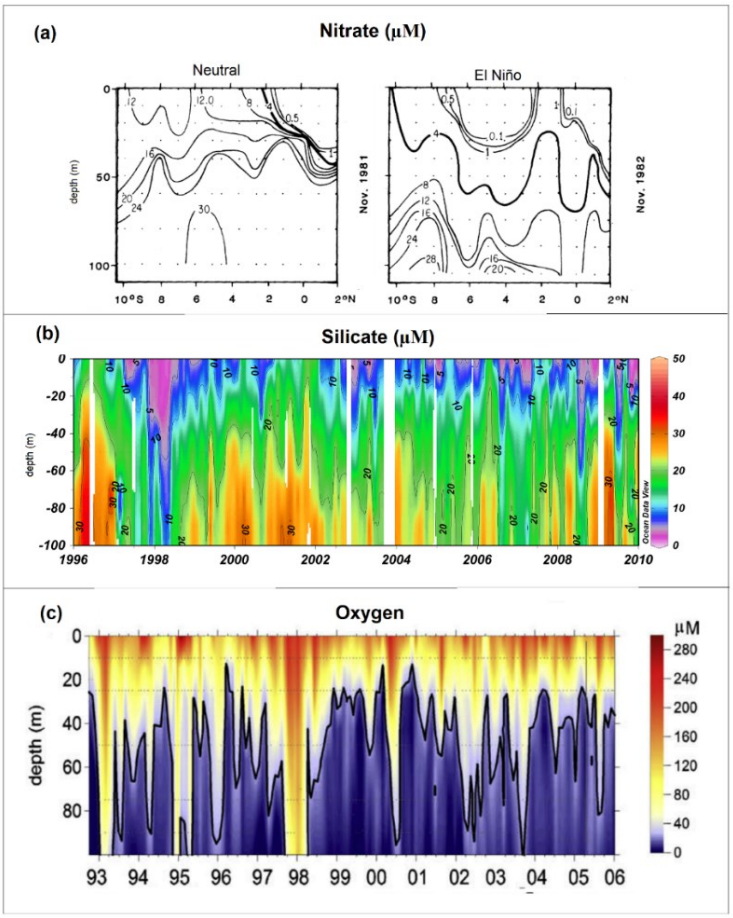

Figure 24. Nitrate concentration off Peru during neutral and El Niño periods from Barber and Chavez [1983] (a). Evolution of the silicate concentration (from 1996 to 2010) from Graco et al. [2017] (b) and oxygen (from 1993 to 2006) from Gutiérrez et al. [2008] (c) at Callao station (12°S).

Expectedly, productivity is strongly impacted during EN (Fig 25). During the last decades, the lowest Chl concentration was observed during 1982-1983 and 1997-1998 EN [Calienes et al., 2014; Gutiérrez et al., 2016]. Strong negative Chl anomalies (< –1 mg m^{-3}) were evidenced using SeaWIFS data during the strong 1997-1998 EN (Fig. 25a, b), mainly between 5°S – 16°S, suggesting that the offshore extension of high Chl coastal band was reduced [Thomas et al, 2001; Carr et al., 2002; Thomas et al., 2009]. A merged SeaWIFS–MODIS product was used to compute EN and LN composites from 1997 to 2017. EN presents negative Chl anomalies alongshore. However, the productivity was less impacted within ~ 20 km to the coast (Fig. 25c). Barber and Chavez [1983] also evidenced a productive narrow coastal band during the 1982-1983 EN, in March 1983. Calienes et al. [2014] hypothesized that

this might be triggered by the nutrient discharge from the Guayas River off Ecuador transported poleward during EN.

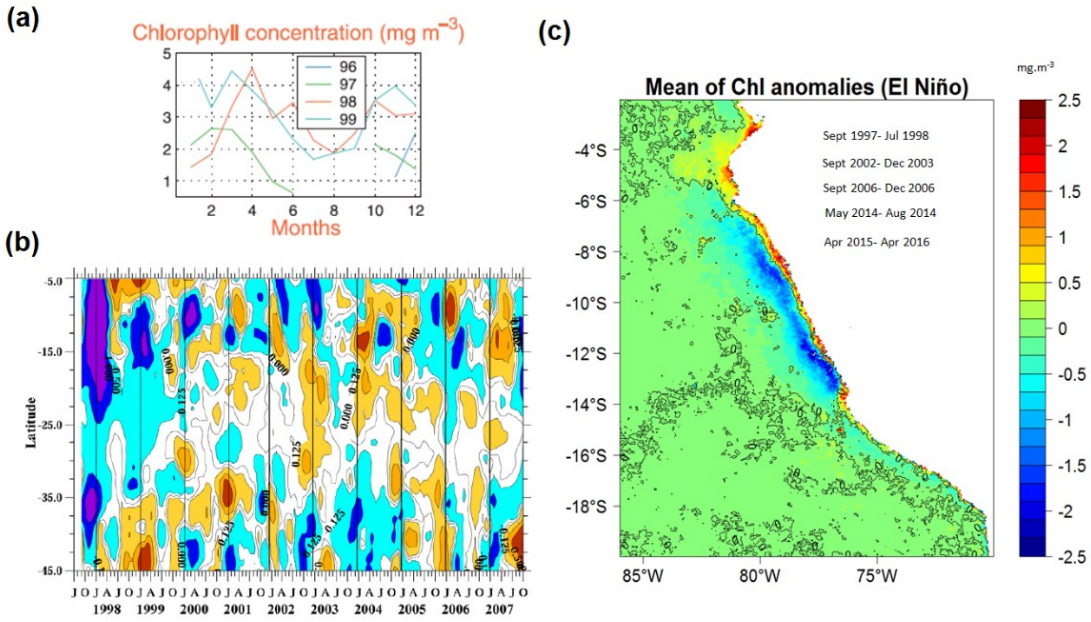

Figure 25. Annual variation of Chl between 1996 and 1999 (a) [Carr et al., 2002]. Chl anomalies alongshore from 1997 to 2008 averaged in a coastal band [Thomas et al., 2009] (b). Mean of Chl anomalies during El Niño (c). (a) and (b) come from SeaWIFS data and (c) from SeaWIFS-MODIS product.

The Chl decrease during EN could be due to various processes: (i) strong downwelling CTWs, which deepen the thermocline/nutricline; (ii) changes in equatorial circulation, which triggers changes in the intensity of nutrient transport fueling the PCUC, and (iii) changes in the mesoscale activity. Gruber et al. [2011] demonstrated that mesoscale eddies and filaments subduct and transports nutrients offshore in the California and West African EBUS. During EN, the frequent passage of intense CTWs may generate enhanced baroclinic instabilities and an EKE increase [Chaigneau et al., 2008]. Mogollon and Calil [2017] found an offshore and downward nitrate eddy fluxes at Pisco (~ 12°S) in a model study of the 1997-1998 EN.

The impact of EN on phytoplankton community has been documented. Diatoms, the most abundant specie in the Peruvian waters [Sánchez, 2000], dominate during cold periods (mainly near 13°S – 16°S), whereas dinoflagellates (smaller phytoplankton cells) dominate in warm periods [Ochoa et al. 2010]. During 1982-1983 EN, Calienes et al. [2014] evidenced abundant presence of the dinoflagellate *Chaetoceros atlanticus*. It could be due to the presence

of offshore waters, which present typically smaller phytoplankton species more tolerant to conditions of stress (e.g. low nutrient levels).

Oxygenated waters are present nearshore during EN [e.g. Llanillo et al., 2013]. Gutiérrez et al [2016] showed a deepening of the oxycline during most EN events (between 1960 and 2008; Fig. 24c). During strong 1997-1998 EN, the oxycline reached ~ 100 m depth at 12°S. Other episodes of less intense oxygenation correspond to moderate EN events (e.g. 2002 – 2003) [Gutiérrez et al., 2008; Graco et al., 2017]. Furthermore, the oxygenation during EN event varies with latitude. Mogollón and Calil [2017]'s regional model simulated a nearshore OMZ vanishing at Chimbote (9°S) during 1997–1998 EN. It was deeper than during normal conditions but persisted further south, off Callao (~ 12°S) and Pisco (~ 15°S). The OMZ core could also be reduced during EN [Llanillo et al., 2013; Yang et al., 2017] and even disappear from the water column [e.g. Gutiérrez et al., 2008; Graco et al., 2017]. Overall, the volume of the PCUS OMZ core could decrease by ~60% with respect to neutral conditions in the PCUS [Yang et al., 2017]. The strong correlation between of the oxycline and thermocline depth variations due to the impact of CTWs [Graco et al., 2017] has been observed for other OMZ regions, as along the west coasts of India. There Vallivattathillam et al. [2017] found a correlation between oxycline and thermocline depths close to 1.0 and 0.9 at seasonal cycle and interannual time scales, respectively. This shows the important role of the remote forcing (e.g. CTWs) in the interannual variability of the OMZ.

Oxygen fluxes into the PCUS associated with the equatorial jets (EUC and Tsushiya jets) contribute to the enhanced ventilation of the OMZ during EN. Stramma et al. [2016] found a strong weakening of the EUC during the onset (October) of 2015 – 2016 EN. However, the SSCCs increase during EN, as shown by Montes et al. [2011] for the moderate 2002-2003 EN. The enhanced eastward SSCC flux of oxygen could thus reduce the offshore OMZ [Montes et al., 2014].

2.2. Impacts of La Niña events

LN is characterized by enhanced easterly trade winds and the predominance of cold waters in the surface and subsurface layer in the Central and Eastern Equatorial Pacific. In the PCUS, upwelling-favorable winds are intensified. Negative SST anomalies (Fig. 26) [Moron et al., 2000; Grados et al., 2018], poorly-oxygenated waters [Graco et al., 2007; Mogollón and

Calil, 2017] and slightly higher phytoplankton biomass (Fig. 27) [Calienes et al., 2014; Gutiérrez et al., 2016] are observed.

The cold (15 – 16 °C) and fresh waters (34.9 – 35) span alongshore and present an offshore extension. The negative SST (from -1°C to -3°C) and salinity (from -0.1 ups to -0.15 ups) anomalies predominate alongshore. However, maximum values are observed offshore (Fig. 26a, b). This could be due to an enhanced Ekman transport triggering a large offshore displacement of near-shore cold waters [Grados et al., 2018].

At subsurface, relatively strong negative SST anomalies are observed north of 12°S and above 50 m (< - 1°C, Fig. 26b). Negative salinity anomalies (< - 0.1) are distributed mainly in three regions above 50 m: 1°S – 4°S, 11°S – 14°S and 17°S – 20°S (Fig. 26d). The shoaling of the thermocline/halocline is related to the passage of upwelling CTWs [Echevin et al., 2014] and enhanced wind forced upwelling.

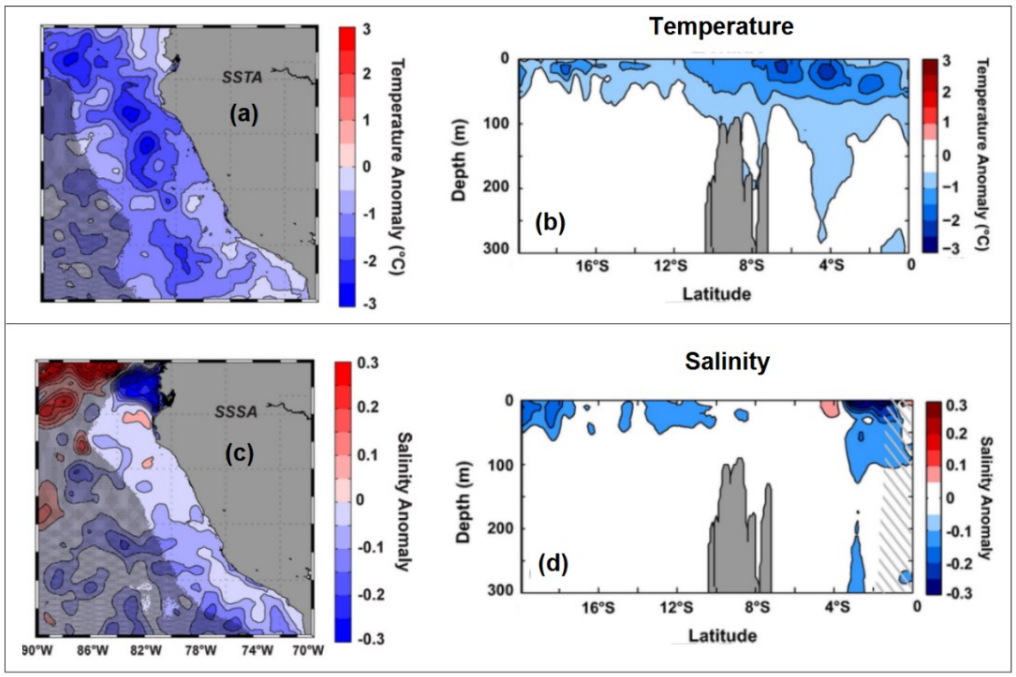

Figure 26. Temperature (in °C, top panel) and salinity (in ups, bottom panel) anomalies at surface (left) and at subsurface alongshore (right) during La Niña. From Grados et al. [2018].

A shoaling of the OMZ and nutricline are also evidenced during LN, partly due to the same processes generating an enhanced upwelling. During the 2009 LN, Llanillo et al. [2013] evidenced an increase of nitrate between 3°S and 10°S offshore at 86°W. During this event, the 25 µmol L^{-1} nitrate isoline reached the surface owing to an upward flux of nutrient-rich ESSW.

Mogollón and Calil [2017] simulation displays an increase of nitrate below 20 m off Chimbote (9°S), Callao (12°S) and Pisco (15°S) during the 1998 – 1999 LN. In contrast, Graco et al. [2017] observed a nitrate decrease off Callao during the same event, which they related to an intensification of the OMZ producing a nitrogen loss. Thus, nitrate loss (by annamox and denitrification) may increase during LN, due to the expansion of the volume of the OMZ core [Yang et al., 2017]. Denitrification and anammox are responsible for 30% and 70% of the nitrogen loss respectively, with high production of N_2O [Graco et al., 2007; Mogollón and Calil, 2017] in LN conditions.

In situ observations do not indicate a higher productivity during LN than during neutral periods from in situ data. Using SeaWIFS data, Thomas et al. [2009] and Carr et al. [2002] evidenced an alternation of positive and negative Chl anomalies alongshore. A LN composite displays positive Chl anomalies (0.5 – 1.5 mg m^{-3}) within the 200 km to the coast. The highest anomalies are found between 12°S – 14°S. In contrast, slightly negative Chl anomalies are observed within the 20 km to the coast and between 6°S – 9°S. They could be produced by the stronger Ekman transport, which displaces further offshore the Chlorophyll-rich waters.

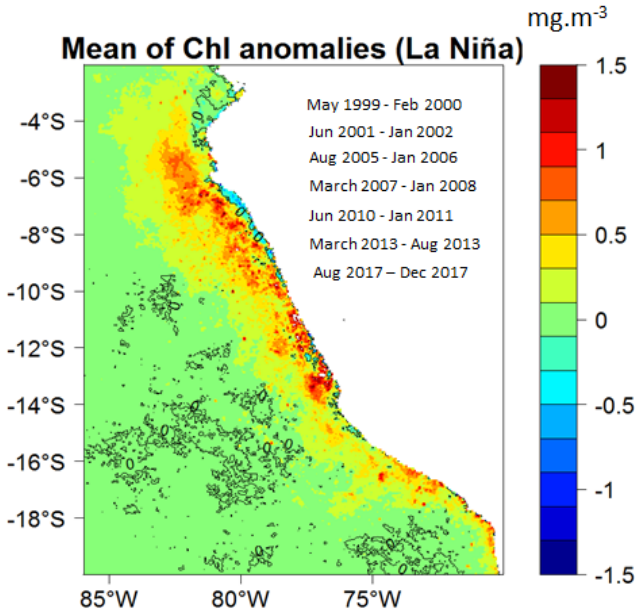

Figure 27. Mean of Chl anomalies (in mg m^{-3}) during La Niña from SeaWIFS-MODIS satellite data (Sept. 1997 to Dec. 2017).

3. Long Term Variability

3.1. SST and wind trends in the PCUS

During the last century an SST increase was evidenced in the global ocean [Smith et al., 2008] associated to the increase of the CO_2 emissions (mainly in the last 50 years). In contrast, the PCUS SST decreased between 1950 and 2010, mainly in the center-south coastal region [Gutiérrez et al., 2011b; Fig. 28]. The SST trend spatial pattern is not homogeneous along the Peruvian coast. IMARPE in situ SST data show a positive trend in the north of Peru at Paita (~ 5°S) (+ 0.26 °C dec-1), whereas no trend is found at Chicama (7°S) and at Chimbote (9°S). Along the southern coast between Callao (~ 12°S) to Ilo (~ 17°S), negative SST trend predominates, with maximum values at Callao and at San Juan (~ - 0.42 °C dec^{-1}) [Gutiérrez et al., 2011b] (Fig. 28a). The Reynolds SST product, which merges data from buoys, ships and satellite [Reynolds et al., 2007], also shows the contrast between positive and negative SST trends alongshore (from 1984 to 2010; Fig. 28b). Dewitte et al. [2012], using the ROMS model, reproduced an SST decrease and a shoaling of the thermocline between 3°S – 18°S from 1958 to 2008.

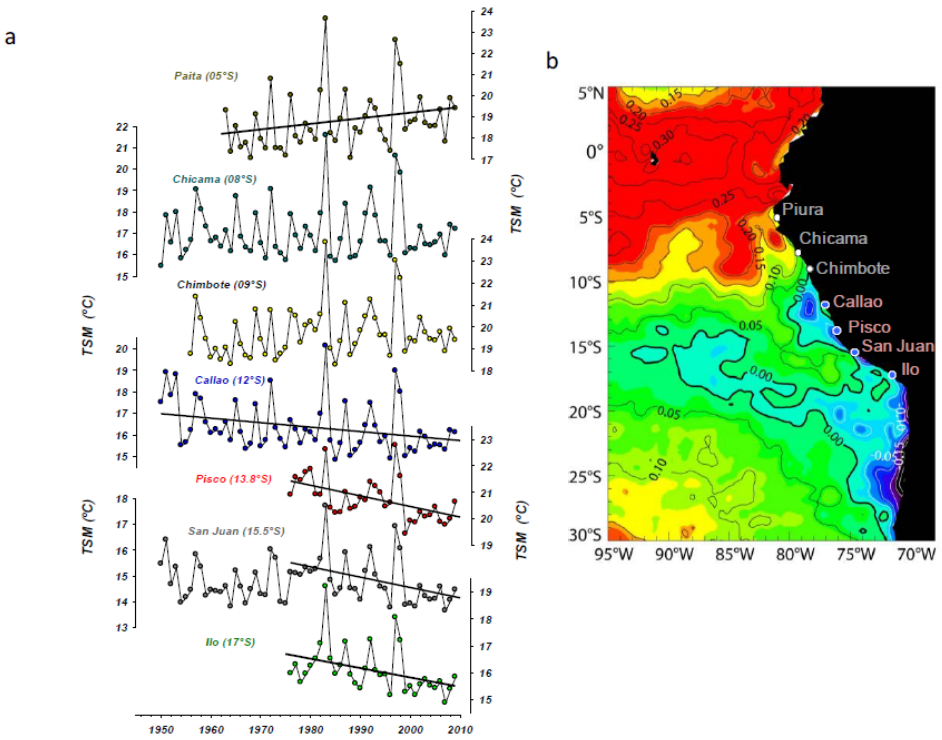

Figure 28. Timeseries of SST from IMARPE coastal stations (in °C) (a) and spatial pattern of the SST trend from Reynold database (in °C dec^{-1}) (b). From Gutiérrez et al. [2011b].

Previous works mentioned that the coastal cooling might be related to the increase of the coastal upwelling during the last years [Gutiérrez et al., 2011a, 2011b; Demarcq, 2009; Narayan et al., 2010]. An increase of alongshore windstress has been reported by Bakun [1990] in the major EBUS and off the Peruvian coasts (from 4.5°S to 14.5°S). Bakun [1990] suggested that enhanced cross–shore atmospheric pressure gradient, which supports the alongshore geostrophic wind, could trigger the wind increase. The increase of the cross–shore pressure gradient is associated to enhanced land-sea thermal gradient [Falvey and Garreaud, 2009]. The increased land-sea thermal gradient could be created by a stronger shortwave downward flux over land associated to a reduction of nearshore cloudiness (e.g. during EN; Enfied, 1981). Besides, Bakun [2010, 2015] suggested that radiative cooling during night time may be suppressed due to the increase in greenhouse gas (e.g. CO_2 or water vapour during EN) concentration, generating a warmer land surface (Fig. 29). Bakun's hypothesis about the increase of the winds in EBUS due to climate change has been supported by some studies (e.g. Sydeman et al. [2014]). However, Chamorro et al. [2018], using an atmospheric model, demonstrated that the increase of the winds during EN events is due to alongshore SST gradients instead of sea-land temperature gradient.

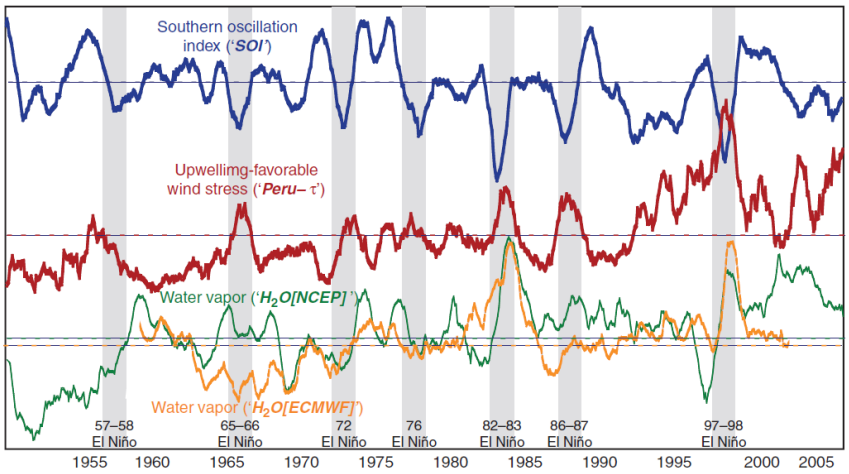

Figure 29. Low-passed (12-month running means) Southern Oscillation Index (SOI), upwelling favorable wind stress off Peru, 'precipitable water' (or 'total water column water vapor') from the National Centre for Environmental Prediction (NCEP) and European Centre for Medium-range Weather Forecasts (ECMWF) reanalysis data sets, at a grid point near the Peru coast (10°S, 80°W). Gray vertical bars identify EN periods. From Bakun et al. [2010]

Jacox et al. [2015] evaluated the influence of the remote (e.g CTW) and local (e.g. winds) forcing in the oceanic trends in the Californian EBUS. They showed that the positive

wind trend increases the upwelling and drives the negative SST trend. In the PCUS, the different wind datasets do not agree on the amplitude of the trends. Gutiérrez et al. [2011a] using the ERA-40 Reanalysis, Bakun at al. [1990, 2008, 2010, 2015] using ICOADS observations and Varela et al. [2015] using the NCEP CFSR reanalysis, found a positive wind trend mainly south of 15°S. In contrast, Goubanova et al. [2010], using a statistical downscaling of NCEP at ~50 km scales (i.e. the wind product used in the model simulations presented in Chapters 3, 4 and 5), found no significant wind trend between 1958 and 2008. Last, Narayan et al. [2010], using NCEP/NCAR reanalysis dataset, showed a negative wind trend between 10°S – 16°S from 1960 to 2006.

3.2. Biogeochemical trends in the PCUS

Biogeochemical trends, such as the increase of coastal productivity and nutrients concentration, an enhanced deoxygenation of the water column, have been evidenced over periods of several decades in the PCUS.

A productivity increase has been observed using in situ [Gutiérrez et al., 2011a; 2016] and satellite data [Demarcq, 2009]. Using SeaWIFS data from Sept. 1998 to Dec. 2007, the latter found a significant positive Chl trend (1.5 – 2 mg m^{-3} dec^{-1}) in most EBUS. In the PCUS, a strong Chl increase was observed mainly between 7°S – 15°S (> 1 mg m^{-3} dec^{-1}) (Fig. 30a). The authors evidenced the strong consistency between the productivity increases and enhanced upwelling-favorable winds (based on QuikSCAT satellite wind data). Gutiérrez et al. [2011a, 2016] evidenced a positive Chl trend (0.7 mg m^{-3} dec^{-1}) at ~ 14°S from in situ data between 1965 to 2005 (Fig. 30b). They also evidenced a significant positive wind trend (from ERA – 40) during spring. Thus, this study hypothesized that the wind increase during warming seasons could influence the positive productivity trend provided the wind mixing depth does not exceed critical levels for phytoplankton growth. Furthermore, the productivity increase could be related to a greater input of nutrients from the offshore equatorial region. Czeschel et al. [2015] found significant positive subsurface (50-300 m) nitrate and phosphate trends in the EUC (2°N – 2°S) and SSCC (5°S – 8°S) latitude ranges, at 84°W – 87°W, whereas silicate does not present a significant trend (Fig. 31).

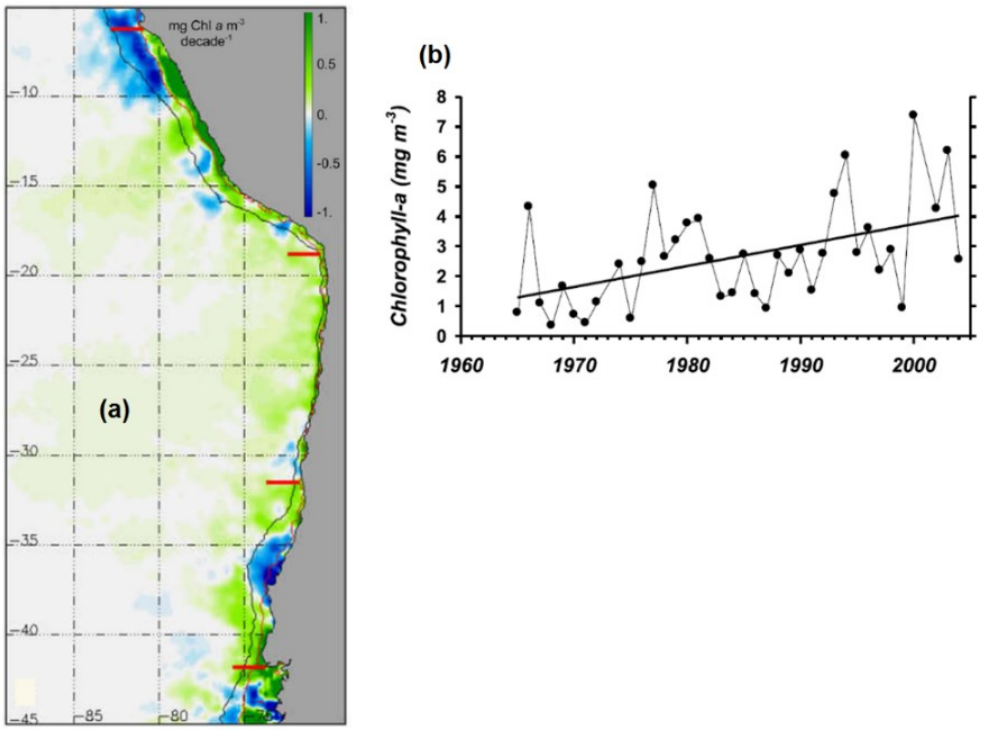

Figure 30. (a) Surface Chl trend from SeaWIFS (1997-2007) [Demarcq et al., 2009] and (b) IMARPE data off Pisco (14°S) (1965 -2005) [Gutiérrez et al., 2011a].

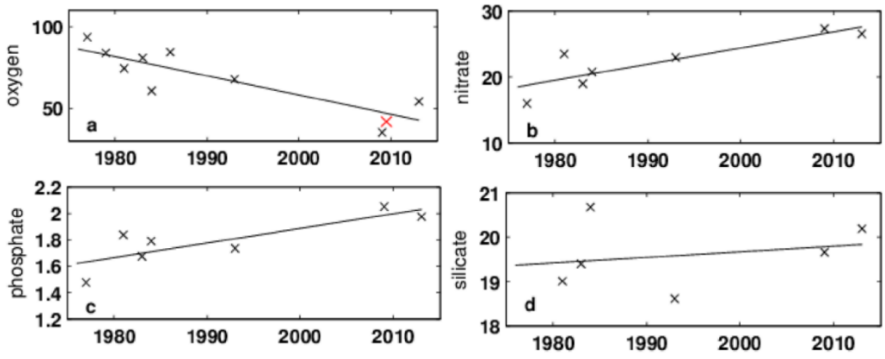

Figure 31. (a) Oxygen, (b) nitrate, (c) phosphate, and (d) silicate trends (in µmol kg^{-1} yr^{-1}) computed between 50–300 m, 2°S–5°S and 84°W–87°W from 1976 to 2010. From Czeschel et al. [2015].

During the last decades, a progressive deoxygenation was observed in the open ocean [Stramma et al., 2008; Breitburg et al., 2018; Duteil et al., 2018]. Stramma et al. [2008] showed that the oxygen decreased at intermediate waters (300 – 700 m) in the eastern Tropical Atlantic and the Equatorial Pacific between 1960 and 2008. They also found an expansion of the OMZ

thickness at 100°W (Fig. 32). Desoxygenation in the eastern equatorial Pacific could be related to the positive phase of Pacific Decadal Oscillation (PDO) [Duteil et al., 2018] in recent decades. Indeed, a positive PDO phase is associated by a decrease of the equatorial trade winds and a slow-down of the eastward equatorial circulation (i.e. EUC).

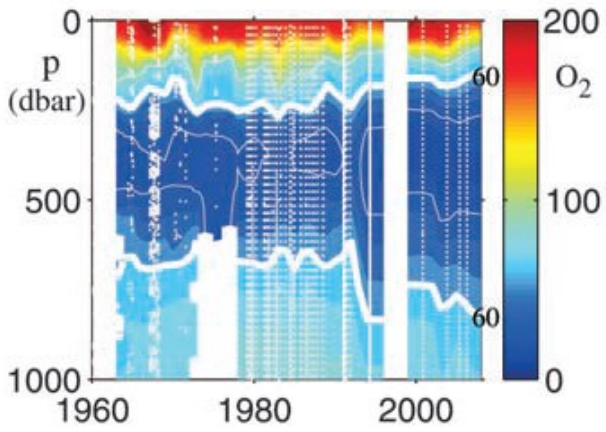

Figure 32. Vertical structure of the oxygen evolution (in µmol kg^{-1}, 5°S – 5°N,105°W - 115°W) between 1960 and 2008. The thick white line represents the isolines of 66 µmol kg^{-1}. Figure from Stramma et al. [2008].

A deoxygenation was also evidenced in the PCUS. The OMZ upper limit shoaled during the last decades. Using shipboard measurements from IMARPE, Bertrand et al. [2011] and Gutiérrez et al. [2016] found a shoaling of the isoline of 22 µmol kg^{-1} (the upper limit of the "biogeochemical OMZ") and 88 µmol kg^{-1} (upper limit of the "biological OMZ") in the coastal region between 6°S – 14°S, from 1980 to 2008. Before the 80's, the PCUS was getting more ventilated. This interdecadal variability of the coastal oxycline depth is associated to the PDO [Bertrand et al., 2011]. Deoxygenation could be driven by different processes: (i) an increase in oxygen consumption caused by an increase in productivity and export of OM, (ii) a decrease of ventilation associated with the equatorial undercurrents (Fig.33a), mainly the EUC and pSSCC [Stramma et al., 2010]. Czechel et al. [2015] evidenced a subsurface oxygen decrease (by ~50 µmol kg^{-1}) between 1993 to 2009 in the equatorial offshore regions where the equatorial undercurrents are located (Fig. 31d).

In contrast, an oxygenation of the nearshore upper water column (0-100m) was observed by in situ data at ~ 12°S during the last decade [Graco et al., 2017]. It seems to be related to more frequent downwelling CTWs, which deepen the coastal oxycline (Fig. 33b).

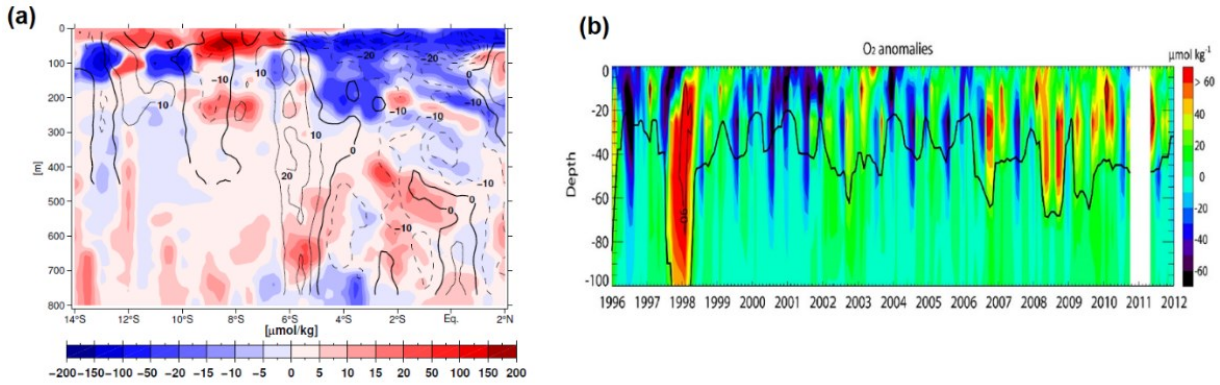

Figure 33. Distribution of oxygen differences (µmol kg^{-1}, in color) between February 2009 and March 1993 at 85°50′W (a). Zonal velocity differences from ADCP measurements are also shown (black contours, in cm s^{-1}) (a). Evolution of oxygen anomalies in the water column at Callao station (12°S, in µmol kg^{-1}) (b). Black line represents the isoline of 44 µmol kg^{-1}. Figures adapted from Czechel et al. [2015] (a) and Graco et al. 2017 (b).

4. Biogeochemical Modelling Studies

Models allow to study processes in the ocean, which are often difficult to observe in situ. The possibility to formulate experiments to test different hypotheses make them very useful tools. Both relatively simple and more complex physical-biogeochemical models have been used to investigate the main physical and biogeochemical processes and their interplay in the PCUS. One of the model most widely used in the PCUS is the Regional Ocean Modelling System (ROMS) [Shcheptekin and Mcwilliams, 2005]. ROMS was first used to simulate the seasonal variability of temperature, salinity and currents in the PCUS [Penven et al., 2005], to investigate the pathways of the PCUC source waters [Montes et al., 2010] and their variability during ENSO phases [Montes et al., 2011]. Dewitte et al. [2012] reproduced the interannual variability and trends of the SST and thermocline during the last 50 years using ROMS forced at open boundaries by the SODA reanalysis. Colas et al. [2008] focused on the dynamics of the 1997 – 1998 EN. Belmadani et al. [2012] studied the propagation of the intraseasonal CTW and their impact on Rossby waves and mesoscale eddies. Colas et al. [2013] focused on the role and impact of the mesoscale variability on the cross-shore transport of heat. ROMS was used to evaluate the response of the PCUS to regional climate change. An enhanced stratification of the water column and increase of coastal SST have been evidenced by Echevin et al. [2011] and Oerder et al. [2015] under pessimistic climate projections (e.g. the idealized 4xCO_2 scenario).

ROMS was also coupled to biogeochemical models of growing complexity. A simple Nitrate Phytoplankton Zooplankton Detritus model (NPZD) simulates the dynamics of the primary and secondary production. It takes into account simple relationships between phytoplankton and zooplankton and assumes that the phytoplankton growth is driven by nitrate availability and zooplankton predation. Nutrient loss is considered to be primarily from phytoplankton uptake and detritus comes from phyto- and zooplankton mortality (e.g. Gruber et al., [2006]). More complex biogeochemical models such as BioEBUS [Gutknecht et al. 2013] and PISCES [Aumont et al., 2015] (see details in the methodology chapter 2) were also coupled to ROMS. The first is a nitrogen–based model, which also simulates the cycle of oxygen, phytoplankton and zooplankton in regional areas. This model includes a parameterization of processes as ammonification/nitrification and nitrification/denitrification/anammox, which occur under oxic and suboxic conditions, respectively.

A few modelling studies have focused on the biogeochemical processes in the PCUS. Findings about the seasonal and interannual variability of the productivity and oxygen are summerized in Table 1.

Table 1. Biogeochemical modelling studies in the PCUS.

Authors	Model	Subject	Main Conclusions
Carr [2003]	NPZD (1D-vertical)	Impacts of 1997-1998 EN and 1999 LN on coastal upwelling and productivity.	During EN the plankton community decrease is driven by the nitrate decrease of the upwelling source water, while during LN the phytoplankton increase is driven by the depth of the upper layer.
Echevin et al. [2008]	ROMS – PISCES	Seasonal cycle of the productivity	Deeper MLD controls the phytoplankton decrease during winter. During spring and fall the productivity increase is due to restratification and destratification of the water column respectively. Fe is a limiting nutrient during winter.
Albert et al. [2010]	ROMS – PISCES	Impact of the wind in the primary productivity.	The absence of nearshore wind drop-off suppresses Ekman pumping and deepens the PCUC. A deeper PCUC impacts on the nutrient content (Iron) of the upwelled water, thus on the productivity.
Echevin et al. [2014]	ROMS – PISCES	Impact of the Intraseasonal CTW in the productivity.	The propagation of intraseasonal downwelling (upwelling) CTW deepens (shoaling) the thermocline/nutricline. A

			deeper (shallower) nutricline triggers a productivity decrease (increase). The propagation of SSH is faster than thermocline/nutricline and surface chlorophyll.
Montes et al. [2014]	ROMS – BioEBUS	Sensitivity of the OMZ to the equatorial subsurface currents.	The mean circulation of the OGCMs (physical OBCs) present small differences; however, the simulated OMZs show significant differences between them. In presence of an intense sSSCC the OMZ is shrinked due to an enhanced eastward transport of oxygenated waters.
Bettencourt et al. [2015]	ROMS – BioEBUS	Impact of the mesoscale activity in the OMZ boundaries	The mesoscale delimits and maintains the OMZ boundaries and injects oxygen within the OMZ.
Vergara et al. [2016]	ROMS – BioEBUS	Seasonality of the OMZ	The seasonality of the coastal OMZ is related to seasonality of winds and productivity. The seasonal cycle of the offshore DO eddy flux and the coastal OMZ are in phase. At the northern OMZ boundary, the DO eddy flux peaks in winter, while at southern boundary it peaks during spring.
Mogollón and Calil [2017]	ROMS – BioEBUS	Impact of 1997-1998 EN and 1999 LN on the oxygen and nitrogen cycles in the main Peruvian upwelling centers.	There is an attenuation and expansion/intensification of the OMZ during EN and LN, respectively.During EN and LN the denitrification/annamox decrease and increase, respectively. The removal nitrogen in the ocean is control by denitrification during EN and by annamox during LN. Enhanced N_2O gas emission is found during LN (+ 36%), while during EN it is reduced (- 32%) respect to neutral period mainly in the northern coastal region.
Yang et al. [2017]	CEMS – BEC*	Impacts of ENSO on denitrification and suboxia.	The denitrification rate during LN (EN) is up to 70% higher (lower) than during neutral periods. The variability of the water colume with DO < 6 μmol kg^{-1} explains 90% of the variability of denitrification.
Yonss et al. [2017]	ROMS – BioEBUS	Nutrients patterns at subsurface within anticyclonic eddies	There is a decoupling between nitrite production and total nitrate change within the eddies.

			The nutrient signature within the eddy is due to the presence of water masses from different origins.
Mogollón and Calil [2018]	ROMS – PISCES	Impact of the wind increase during climate change in the productivity.	An increase of the winds (~ + 40%) leads to a productivity increase of 5%. It is due to the decrease of the nutrient limitation relaxation in ~ 10%, but nutrients are used less efficiently (decrease of ~ 15%) due enhanced eddy-driven offshore transport of nutrients.

*CEMS (Community Earth System Model) [Gent et al., 2011] and BEC (Biological Elemental Cycling) [Moore et al., 2004].

5. Objectives

As shown in the previous sections, a comprehensive study of the impact of El Niño events in the dynamics and biogeochemistry in the PCUS is not available yet. Most studies about El Niño based on observations have focused on particular events such as the extreme 1997-1998 EN and only few studies analysed La Niña events, due to the lack of satellite observations before the 90's and the relative scarcity of *in situ* observations collected by institutes other than IMARPE. On the other hand, few modelling studies described the interannual variability of the productivity and the OMZ. Furthermore, most of the studies are mainly descriptive and few of them focus on the mechanisms driving in the observed variability. Thus, one of the thesis's objectives is understand the mechanisms that trigger the productivity decrease and the oxygenation of the water column during El Niño, with a focus on the different El Niño events present in half a decade (50 years, from 1958 to 2008), using a regional physical-biogeochemical model and taking advantage of a regional data base from IMARPE spanning over more than 50 years. La Niña impacts are also included in the analysis. Processes such as the passage of the Coastal Trapped Waves, changes in the water masses reaching the upwelling regions and variability in the mesoscale activity are thus studied in detail.

Whereas oceanographic trends in the PCUS have been documented in a few studies, the processes that trigger them remain unclear, in particular for the biogeochemical variability. There are no studies that quantify the respective role of different forcings (equatorial oceanic or local atmospheric variability) in the driving of oxygen and productivity trends. Thus, the objective of this thesis is to understand and describe the mechanisms involved in the coastal cooling, the increase of the productivity and the deoxygenation of the water column during the last decades. To this aim, the model is used to simulate some aspects of the observed trends, and to evaluate the role of the remote (e.g. equatorial currents) and local (e.g. winds) forcing in the physical and biogeochemical trends between 1980 and 2008, with emphasis on the productivity and oxygen.

CHAPTER 2:
METHODOLOGY

Models, Observed Data and Statistical Methods

1. Hydrodynamic-Biogeochemical Coupled Model

In order to simulate the hydrodynamics and biogeochemistry of the PCUS, the ROMS-PISCES coupled model was used. This coupled model was previously used in the Humboldt system [Echevin et al., 2008; Albert et al., 2010; Echevin et al., 2014] and in the Canary System [Brochier et al., 2018]. PISCES was coupled to the NEMO hydrodynamics model to simulate the Arabian sea upwelling [e.g. Resplandy et al., 2012; Vallivattathillam et al., 2017]. In this section, we will describe the models and configurations we used.

1.1. The ROMS physical model

The Regional Oceanic Modelling System (ROMS) simulates the ocean circulation and mixing. It is a split-explicit, free-surface oceanic model that resolves the Primitive Equations in an Earth-centered rotating environment, based on the Boussinesq approximation and hydrostatic vertical momentum balance. Several advection schemes are implemented in ROMS, and in our case a third-order, upstream-biased advection scheme was used. It allowed the generation of steep tracer and velocity gradients [Shchepetkin and McWilliams, 1998].

In the horizontal, the primitive equations are discretized in the "staggered" Arakawa C-grid, a grid often used in ocean models. In this type of grid, some of the state variables (temperature, salinity and density) are evaluated at the grid center (“rho point”), while the horizontal velocities are evaluated at the center of the left/right (u) and upper/lower (v) grid faces (Fig. 1).

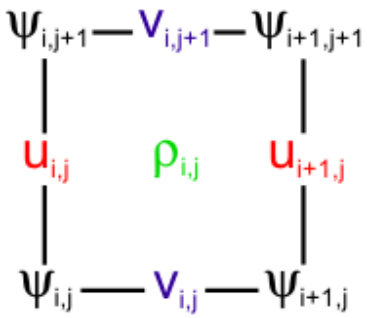

Figure 1. Scheme of the Arakawa C-grid. Ψ indicates the streamfunction value, which is not used in ROMS. Figure from www.myroms.org

In the vertical, sigma coordinates are used. The sigma levels follow the variable bottom topography [Song and Haidvogel, 1994]. This allows an increase of the vertical resolution in shallow areas close to the coast or above seamounts (Fig. 2). For a complete description of the model equations and discretization, the reader is referred to Shchepetkin and McWilliams [2005]. ROMS has been used in the PCUS to describe and understand the processes related to the seasonal and interannual variability of the ocean circulation (see section IV of the introduction).

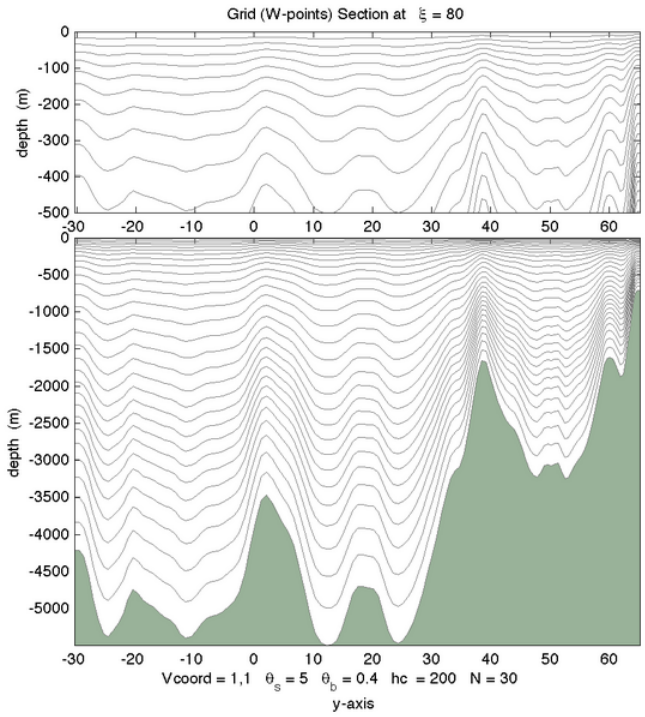

Figure 2. Example of the sigma levels used in ROMS model. Figure from www.myroms.org

1.2. The PISCES biogeochemical model

The 'Pelagic Interaction Scheme for Carbon and Ecosystem Studies' (PISCES) model was used in order to simulate the biogeochemistry of the PCUS. PISCES simulates the marine biological productivity and describes the biogeochemical cycles of carbon and the main nutrients (nitrate, phosphate, silicate and iron; Aumont et al. [2015]) as well as the dissolved oxygen (e.g. Resplandy et al. [2012] ; Fig. 3).

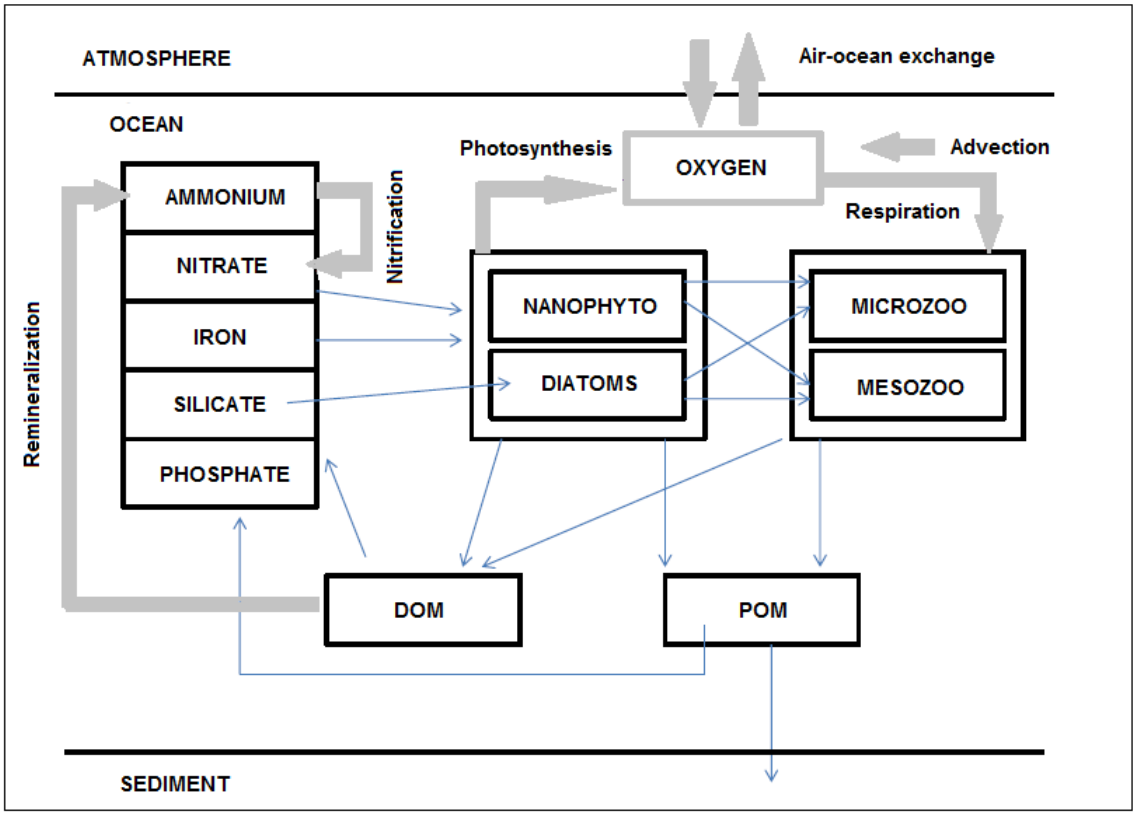

Figure 3. Structure of the PISCES model. Stocks are marked by boxes and fluxes by arrows. From Espinoza-Morriberón et al. [2016]

PISCES assumes a compromise between the Monod and Quota models. As a Monod model, PISCES model assumes that phytoplankton growth depends on external concentration of nutrients and that the main nutrients in the ocean follow the Redfield ratio (C:N:P ~ 106:16:1). However, within phytoplankton cells, the ratios of iron (Fe), silicate (Si) and Chlorophyll (Chl) respect to carbon are computed based in the external concentration of the limiting nutrients like in the Quota models.

PISCES has 24 state variables listed in Table 1. PISCES presents three non-living compartments, which are the semi-labile dissolved organic matter, small sinking particles and large sinking particles. Besides, it has four living compartments represented by two size classes of phytoplankton (nanophytoplankton and diatoms) and two size classes of zooplankton (microzooplankton and mesozooplankton). The growth of phytoplankton is limited by external nutrients concentration and diatoms differ from nanophytoplankton by their need for silicate, higher Fe requirements [Sunda and Huntsman, 1997] and higher half-saturations. This model

also simulates dissolved inorganic carbon, total alkalinity and dissolved oxygen. The bacterial pool is not explicitly modeled in the version of PISCES that we used. The reader is referred to Aumont et al. [2015] for a complete description of the model.

Table 1. State variables from the PISCES model.

PISCES model	
Compartments	**State Variables (abbreviations)**
Dissolved/Nutrients	Dissolved Inorganic Carbon (DIC)
	Alkalinity
	Oxygen (O_2)
	Phosphate (PO_4)
	Silicate (SiO_3)
	Iron (Fe)
	Dissolved Inorganic 13 Carbon ($DI^{13}C$)
	Oxygen 18 ($^{18}O_2$)
Phytoplankton	Nanoplankton (NAN)
	Diatoms (DIA)
	Iron in NAN
	Iron in DIA
	Chlorophyll in NAN
	Chlorophyll in DIA
	Silica in DIA
Zooplankton	Microzooplankton
	Mesozooplankton
Dead Particles/Detritus	Small Particulate Organic Carbon (POCs)
	Large Particulate Organic Carbon (POCl)
	Dissolved Organic Carbon (DOC)
	Carbonate ($CaCO_3$)
	Particulate Silica
	Iron in POCs
	Iron in POCl

2. Simulations

2.1. Parametrization

The parameters of the PISCES model used in our simulations are presented in the Table 2. Most of the parameters values are global estimates from Aumont et al. [2005]. However, for some parameters, in order to reproduce some regional characteristics of the PCUS, we used the same parameter values as in the study of Albert et al. [2010] (e.g. remineralization rate and scavenging rate of iron).

Table 2. Values of the parameters used in our model configuration.

Symbol	Value	Unit	Definition
Phytoplankton			
α	4; 4	$(W\ m^{-2})^{-1}\ d^{-1}$	Initial slope of the PI curve
K_{nh4}	0.1; 0.5	µmol N l^{-1}	Half-saturation constant for ammonium
K_{no3}	2; 10	µmol N l^{-1}	Half-saturation constant for nitrate
K_{Si}^{D}	1.5	µmol Si l^{-1}	Half saturation constant for silicate
K_{Fe}^{min}	0.01; 0.1	nmol Fe l^{-1}	Minimum half-saturation constant for iron
m_P	0.01; 0.01	d^{-1}	phytoplankton mortality rate
w_P	0.001	d^{-1}	Quadratic mortality of phytoplankton
w_P^{max}	0.02	d^{-1} mol C^{-1}	Maximum quadratic mortality of diatoms
K_P	0.1	mol C l^{-1}	Half-saturation constant for mortality
$\theta_{chl;\ max}$	0.033; 0.05	mg Chl mg C^{-1}	Maximum Chl/C ratios of phytoplankton
$\theta_{fe;\ max}$	15; 20	µmol Fe mol C^{-1}	Maximum Fe/C ratios of phytoplankton
K_{Si}^{2}	4	µmol Si l^{-1}	Half saturation constant for Si/C increase
Zooplankton			
ϵ	0.33; 0.33	-	Zooplankton growth efficiency
σ	0.6; 0.6	-	Fecal pellets production
g	4; 0.7	d^{-1}	Maximum grazing rate
K_G	20; 20	µmol C l^{-1}	Half-saturation constant for grazing
p_P^Z, Y_P	0.5; 0.2	-	Preferences for nanophytoplankton
p_D^Z, Y_D	0.5	-	Preferences for diatoms
p_{POC}^Z, Y_{POC}	0; 0.2	-	Preferences for POCs
Y_Z	1	-	Preference for microzooplankton
m^M	0.05	$(\mu mol\ C\ l^{-1})^{-1}\ d^{-1}$	Mesozooplankton mortality
Organic matter			
λ_{DOC}	0.2	d^{-1}	Remineralization rate of DOC
K_{DOC}^{bac}	417	µmol C l^{-1}	Half-saturation constant for DOC remin.
λ_{POC}	0.025	d^{-1}	Degradation rate of POC
w_{min}	3; 50	m d^{-1}	Minimum sinking speed of POC
λ_{Fe}	0.005	d^{-1} μmol^{-1} l	scavenging rate of iron
λ_{BSi}	0.015	d^{-1}	Dissolution rate of BSi
λ_{NH4}	0.05	d^{-1}	Maximum nitrification rate
O_2^{min}	1	µmol O_2 l^{-1}	Half saturation constant for denitrification
Stoichiometric ratios			
R_{CaCO3}	0.4	-	Maximum rain ratio

*Note that in the case of two values: first and second represent the value for nanophytoplankton and diatoms respectively.

2.2. Model configuration

The model domain spans from 15°N to 40°S and from 100°W to 70°W. It is the same model grid as in the studies of Belmadani et al. [2012] and Brochier et al. [2013] used in the PEPS ANR project (Peru Ecosystem Projection Scenarios, 2009-2012). The domain encompasses the Northern and central Chile region, however only the PCUS was studied in this thesis (Fig. 4). The model extends up to 15°N and 100°W westward, in order to simulate correctly the surface and subsurface Equatorial currents, which have an important impact on the currents off Peru [Montes et al., 2010]. The model grid has a horizontal resolution of 1/6° (~18 km) and contains 181x355x32 grid points. The bottom topography comes from ETOPO2 (Smith and Sandwell, 1997). The vertical grid had 32 sigma levels. The model was run from 1958 – 2008 and we save ROMS-PISCES model outputs every 5 days.

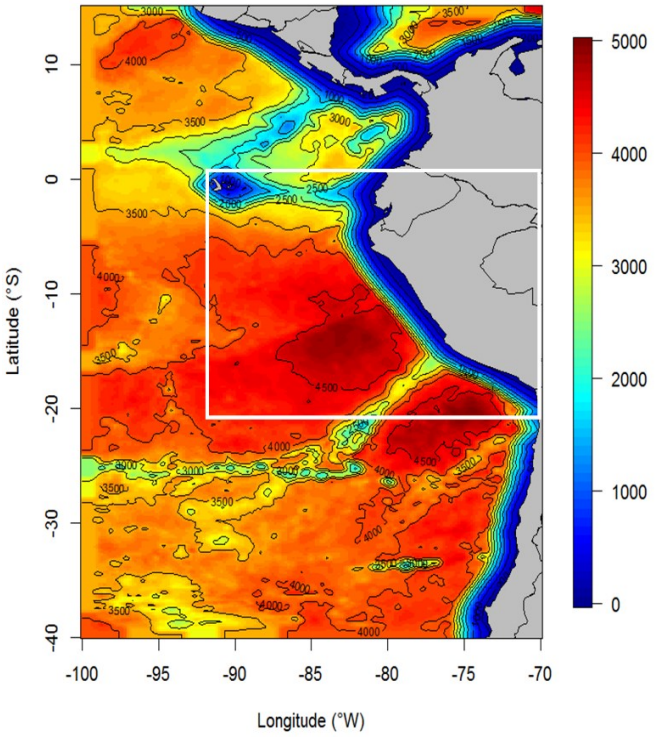

Figure 4. Model domain. The white box represents the PCUS. The model topography (in meters, originally from ETOPO2 before being smoothed) is shown in color scale.

2.3. Atmospheric forcing

The wind fields come from a blended product: SCOW climatological winds [Riesen and Chelton, 2008] and a statistically-downscaled NCEP wind anomalies [Goubanova et al. 2010]. The SCOW climatology is based on 8 years of observations (Sept. 1999 – Aug. 2007). In the

statistical downscaling procedure, the low resolution (2.5°x2.5°) NCEP winds were downscaled at the resolution of QuickSCAT satellite winds (0.5°x0.5°). The methodology described by Goubanova et al. [2010] consists in finding a statistical relationship between regional winds and large-scale climate characteristics:

$$QuickSCAT(wind) \sim \alpha\ NCEP\ (wind) + \beta\ SLP$$

Sea-level pressure (*SLP*) and winds at 10 m came from NCEP. The statistical relationships (α and β coefficients) were computed over the QuickSCAT period (2000 – 2008). Then, they were applied during the entire period of study (1958 – 2008) to infer regional winds. Last, in order to obtain the anomalies, a climatology of the downscaled product over 2000 – 2008 was computed and substracted from interannual downscaled NCEP winds. The reader is referred to Goubanova et al. [2010] for more details on the statistical downscaling methodology. The product is named DwS hereafter.

NCEP anomalies and COADS climatology [Da Silva et al., 1994] are added to construct short wave heat flux and surface air parameters (2m air temperature and humidity) used in the ROMS flux bulk formulation [Liu et al., 1979]. A bulk formulation is used to allow the adjustment between modelled surface ocean fields and the low atmosphere parameters. Furthermore, in the bulk formulation, the wind stress is computed using the winds at 10 m and the modelled SST.

2.4. Open Boundary Conditions of the regional model

A regional model domain has several boundaries which allow the ocean outside the model domain to influence the dynamics inside the model domain. In the case of the PCUS model, there are 3 open boundaries (north, south and west). In this work, we have run two interannual simulations which have the same atmospheric forcing but differ in their open boundary conditions (OBC). Indeed, one crucial forcing of the PCUS dynamics and biogeochemistry is the eastward near-equatorial flow composed by the EUC and subsurface countercurrents. These currents transport momentum, heat, nutrients and oxygen to the PCUS, and their intensities differ depending on the OGCM resolution (Fig. 5). Using different OGCM as OBC allows to evaluate the sensitivity of the regional solutions to the OBC forcing.

2.4.1. The RPSoda simulation

The ROMS-PISCES simulation forced by SODA physical OBC (RPSoda) is used in Chapters three, four and five. It allows to describe and to analyze the impact of El Niño on the productivity (Chapter 3), the oxygen (Chapter 4), and the biogeochemical trends (Chapter 5) in the PCUS. The validation of the simulation is detailed in chapter 3.

Physical boundary conditions (temperature, salinity and velocities) come from an interannual Simple Ocean Data Assimilation (SODA) simulation (version 2.1.6) [Carton and Giese, 2008] which has a horizontal resolution of 0.5° and 40 vertical levels. SODA assimilates hydrographic profiles, moored and satellite data. It is forced with ECMWF ERA-40 atmospheric fluxes [Uppala et al., 2005]. 5-day averaged SODA outputs are used at the ROMS OBC for the period 1958-2008.

Unfortunately, the SODA OGCM is not coupled to a biogeochemical model, thus other products have to be used. Biogeochemical boundary conditions come from CSIRO Atlas of Regional Seas (CARS) 2009 climatological data [Ridgway et al., 2002] for oxygen and nutrients (nitrate, phosphate, silicate; see section 3.1) and from the World Ocean Atlas (WOA) 2005 climatology [Conkright et al., 2002] for dissolved organic carbon (DOC), dissolved inorganic carbon (DIC) and total alkalinity (TALK). The WOA DIC and TALK fields do not vary seasonally. Iron concentrations come from a NEMO-PISCES global simulation climatology [Aumont et al., 2015].

2.4.2. The RPOrca simulation

This ROMS-PISCES simulation forced by ORCA2-PISCES physical and biogeochemical OBC (RPOrca) is used in Chapter 3 in order to complement the impact of El Niño events on the productivity. It allows to investigate the impact of interannual variability of biogeochemical boundary conditions (see supplementary material section in Chapter 3), in contrast with climatological biogeochemical conditions in RPSoda.

Monthly outputs from the ORCA2-PISCES simulation (L. Bopp, pers. comm.) are used for both physical and biogeochemical interannual boundary conditions. ORCA2 has a spatial resolution of 2° and 30 vertical levels. Its atmospheric forcing is constructed from various data sets (*e.g.* NCEP/NCAR for wind stress, see Aumont et al. [2015] for details).

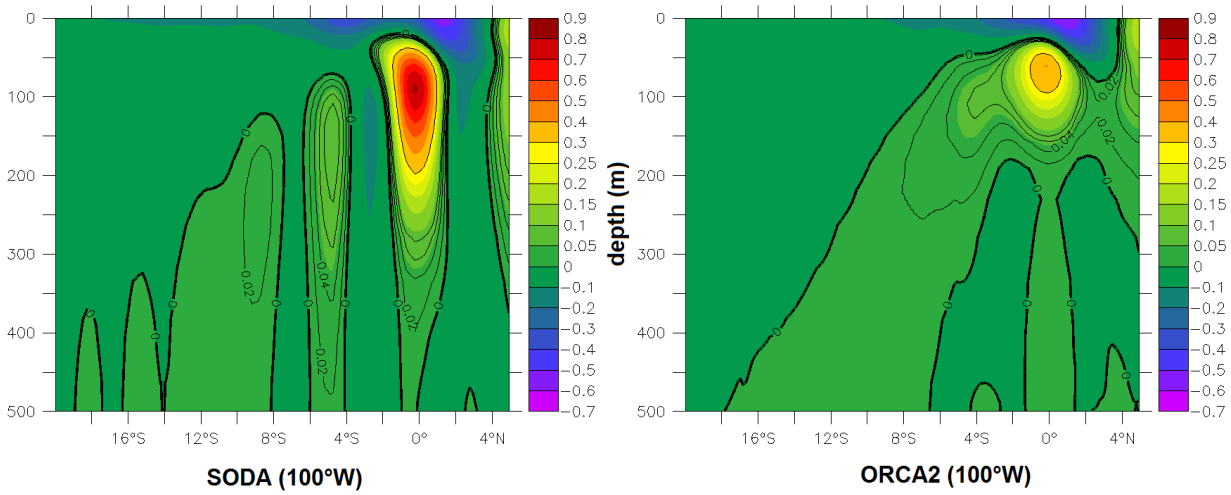

Figure 5. Annual mean (1958-2008) of the zonal currents (cm s^{-1}) at 100°W from SODA (left) and ORCA2 (right) used as OBC in the regional simulations.

2.5. Sensitivity Experiments

Additionally to RPSoda and RPOrca, we run some sensitivity simulations to investigate the impact of a specific forcing. RPSoda is considered the "control run" (CR) to which the sensitivity runs are compared. The different simulations are listed below :

Wclim: It uses SODA interannual OBC and RPSoda monthly climatological atmospheric forcing (see Table 3). It is used to evaluate the role of the oceanic remote forcing, mainly equatorial subsurface currents and equatorial Kelvin waves which generate coastal trapped waves.

Kclim: It uses SODA montly climatological OBC and RPSoda interannual atmospheric forcing (see Table 3). By suppressing the intraseasonal equatorial Kelvin wave, it allows to study the role of variability of the wind forcing.

Due to computational requirements, Kclim and Wclim were run from 1979 to 2008. We performed these simulations in order to investigate: (i) the role of the remote and local forcing during El Niño and La Niña (see chapter 4); and (ii) evaluate which forcing drives the biogeochemical trends in the PCUS.

Although it has been simulated with several global atmospheric models, the surface wind is not well known off Peru over the period 1958-1990, as satellite data were not available. Thus, the influence of different wind intensities on the modelled circulation and its variability

were also studied (Table 3). Additionally to the NCEP downscaled product from Goubanova et al [2010], two other wind products were used. 10-meter wind anomalies were computed from CFSR [Saha et al., 2010] and ERA-Interim reanalysis (Dee et al. [2011]; hereafter ERA). These products are available at a horizontal resolution of ~ 38km (0.33°) and ~ 83 km (0.75°) respectively. In order to compute the wind anomalies, we computed a climatology from 2000 to 2008 for the two wind products. The anomalies were then added to the SCOW climatology and gridded over the ROMS domain, using the interpolation tools from the ROMSTOOLS pre-processing package [Penven et al., 2008].

With these two additional wind products, we performed four simulations, listed in Table 3: CR-CFSR, CR-ERA, Kclim-CFSR and Kclim-ERA. These simulations were run over the period 1979-2008.

Simulations	REMOTE FORCING		ATMOSPHERIC FORCING				
	Physical Boundary Conditions (SODA)	Biogeochemical Boundary Conditions (CARS/WOA)	10m wind Velocity (DwS – CFSR – ERA - SCOW)	2m air temperature (NCEP + COADS)	Relative Humidity (NCEP + COADS)	Precipitation Rate (NCEP + COADS)	Short and Long Wave Radiation (NCEP + COADS)
CR	Inter	clim	inter (DwS)	inter	Inter	Inter	clim
Wclim	Inter	clim	clim (DwS)	clim	Clim	clim	clim
Kclim	Clim	clim	inter (DwS)	inter	Inter	Inter	clim
CR-CFSR	Inter	clim	inter (CFSR + SCOW)	inter	Inter	inter	clim
CR-ERA	Inter	clim	inter (ERA + SCOW)	inter	Inter	inter	clim
Kclim-CFSR	Clim	clim	inter (CFSR + SCOW)	Inter	Inter	inter	clim
Kclim-ERA	Clim	clim	inter (ERA + SCOW)	Inter	Inter	inter	clim

Table 3. Characteristics of the experimental simulations performed in the present study.

2.6. Tracking the upwelling Source Waters using ROMS-OFFLINE (ROFF)

The ROMS-offline tracking module, developped initially by [Capet et al., 2004] and used in several studies [*e.g.* Montes et al., 2010; Albert et al., 2010], was implemented to calculate the trajectories of water parcels (see Chapters 3 and 4). The virtual floats trajectories

were computed using 5-day averaged ROMS velocity fields from the RPSoda simulation (also called CR). The ROMS-offline Fortran 77 code was modified to register water parcels nitrate, iron and oxygen concentrations along their trajectories.

In chapter 3, two experiments were made to study the properties of the upwelling source water (SW), namely the offshore waters which are later upwelled along the Peruvian coasts:

a) SW floats (10 000) were tracked backward in time for one month from the position where they were upwelled near the coast to their offshore position, in order to evaluate the change in depth, nitrate and iron concentration along their pathways towards the upwelling region (Fig. 6a). In this experiment, the floats were released between 0-15 m and 6°S-14°S within the 100 m isobath to the coast.

b) SW were followed (backward in time) and their characteristics registered until they reached an offshore 'equatorial section' (defined by a meridional section at 88°W). In this experiment, the floats were released at the same region in the previous experiment, but only in spring during every LN, neutral and EN event. However, it does not means that floats reached to equatorial section in the same ENSO phase when they were released. Our goal is to understand the changes in the equatorial SW characteristics during ENSO phases (Fig. 6b). The results are presented in Chapter 3.

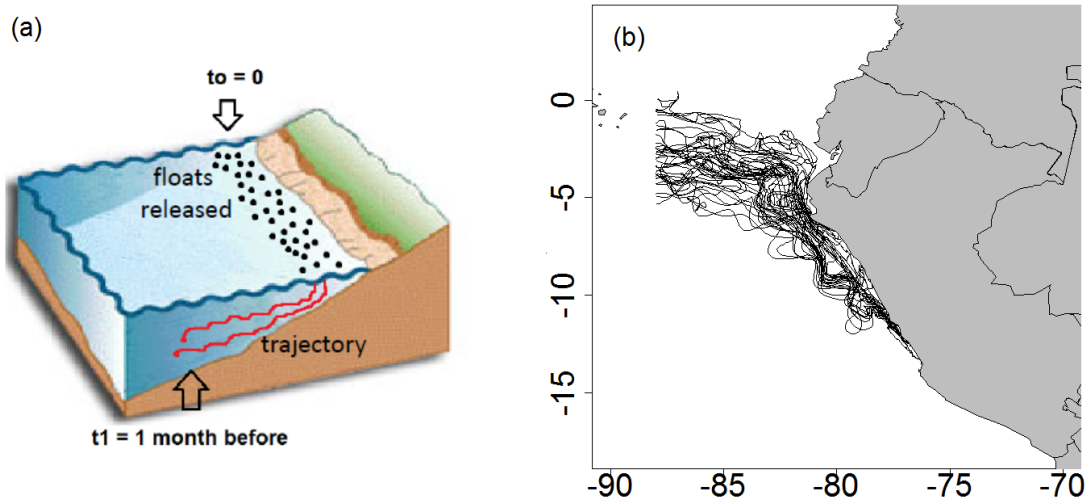

Figure 6. (a) Schematic of virtual floats released in the upwelling region before being transported backward in time (black dots). 2 trajectories are marked by red lines. (b) Float trajectories (black lines) originating from the equatorial region (88°W) and reaching the upwelling region.

In a second experiment, the oxygen concentration from the floats was stored. The floats (2000) were initially launched each spring (between 1958 and 2008) on the shelf and slope at two latitudes (9°S and 12°S) and between the surface and 250 m depth in order to sample the subsurface oxygen minimum zone (Fig. 7), and transported backward in time for a maximum of 2 years. This experiment aims at describing the oxygen changes in the equatorial SW during LN, EN and neutral periods. The results are presented in chapter 4.

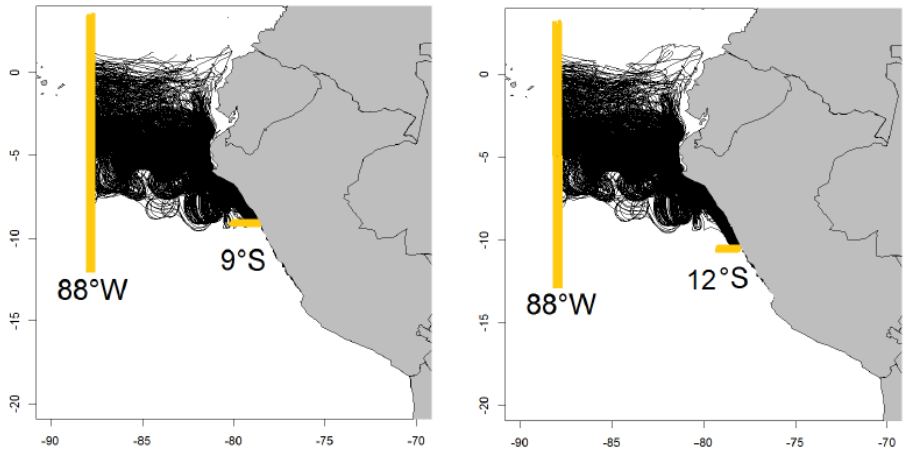

Figure 7. Float trajectories (black lines) originating from the equatorial region (88°W) and reaching the upwelling region at 9°S and 12°S.

3. Observational Data

3.1. CARS

Climatological data from the CSIRO Atlas of Regional Seas (CARS2009; Ridgway et al. [2002]) was also used to evaluate the seasonal variations of temperature, salinity, oxygen and nitrate at the surface and at specific subsurface depths over the entire model domain.

CARS2009 presents a horizontal resolution of 0.5°x0.5° and 79-vertical levels. This product was assembled using the following main data sources: World Ocean Database 2005 (WOD05), CSIRO data, Argo floats, WOCE Global Hydrographic Program, TAO/TRITON data (buoys) and other smaller datasets available up to 2008.

3.2. Sea surface temperature

Two different gridded SST products were used:

The 'Reynolds' daily SST product [Reynolds et al., 2007], also known as Optimal Interpolation Sea Surface Temperature (OISST), has a horizontal resolution of 0.25°x0.25° (~ 25 km). It combines infrared satellite data and *in situ* measurements (*e.g.* ships and buoys), and is a 'level 4' gridded product. The Optimal interpolation statistical method is used to fill the missing values due to the presence of clouds. In the present study, we used the monthly values during the period September 1981-December 2008.

The Pathfinder SST product is a monthly SST satellite data from Pathfinder at ~ 4 km resolution [Casey et al., 2010] over the period January 1984 – December 2008. These SST products from satellite data were used to evaluate the SST from the model.

3.3. Sea level anomalies (SLA)

Gridded satellite altimetry data from AVISO (www.aviso.oceanobs.com) at 1/3° of horizontal resolution was used. This product merges along-track sea level data and merges them into a single gridded product. The SLA fields were then interpolated onto the model grid for comparison purposes. The available data spans from January 1993 to December 2008 (every 5 days). Geostrophic current anomalies were also computed using AVISO data.

3.4. Surface chlorophyll

Monthly mean chlorophyll satellite data from SeaWIFS [O´Reilly et al., 1998] at ~ 9 km resolution (1/12°) from September 1997 to December 2008 were used to evaluate the modelled surface chlorophyll concentration.

3.5. IMARPE *in situ* observations

Surface and subsurface *in situ* data from IMARPE surveys was used to validate the modelled temperature, chlorophyll-a, nitrate and oxygen. The data was collected between 1960 and 2008. Temperature came from Conductivity-Temperature Depth (CTD) and Ocean Station Data (OSD) using reverse thermometers. The chlorophyll-a and nitrate concentrations were measured using the standard fluorometric procedure from Holm-Hansen et al. [1965] and the spectrophotometric method described in Strickland and Parsons [1972], respectively. Dissolved oxygen from Nansen and Niskin bottles was determined by the Winkler method [Carrit and Carpenter, 1966].

Most of the data was collected between 0 and 100 m within 200 km to the coast (see Figures in Appendix). Oxygen was the variable with the larger number of observations (~ 706

000 points), while temperature and nitrate presented ~ 442 000 and ~ 270 000 samples respectively in surface and subsurface (Table 4). At the surface, Chl-a was sampled ~ 20 000 times during the study period (Table 5). The season with more observations (for all variables) was spring.

Depth (m)	Summer			Autumn			Fall			Spring		
	Temp.	NO3	Oxygen	Temp.	NO3	Oxygen	Temp.	NO3	Oxygen	Temp.	NO3	Oxygen
0	15612	5386	15015	13431	5646	11419	25687	5877	13344	18904	7103	14691
<0 - 100]	33077	25727	71619	37883	31601	65182	41493	22584	62079	48070	29923	74589
<100 - 200]	18307	15080	43985	18510	17610	37509	24086	11539	37539	30855	17360	45950
<200 -300]	12696	11321	32402	12051	12318	25815	18073	8551	28988	25050	14084	35650
<300 - 400]	2960	2502	6984	3086	3095	6718	4709	1362	6998	6911	2764	8894
<400 - 500]	2416	2062	6039	2626	2125	5677	3614	811	5610	6128	1847	7524
<500 - 1000]	2055	1588	8273	2521	1777	8312	3465	758	8036	8263	1198	11742

Table 4. Number of IMARPE observations with respect to depth and season for temperature, nitrate and oxygen.

IMARPE data was gridded horizontally at the same resolution as the ROMS grid (1/6°) and vertically (each 10 meters) for each month. Every month, between 1960 and 2008, extreme values were filtered out (in log scale for chlorophyll) before gridding by removing values higher than twice the standard deviation in each spatial bin. In the bins with less than three observations, all values were taken in account to compute the monthly mean.

In order to evaluate the variability of temperature, nitrate and oxygen in the water column, we computed some regional indices: the depth of the 15°C isotherm (ZT15, a proxy of the thermocline depth), the depth of a subsurface nitrate isoline (16 µmol kg^{-1}, ZNO3, a proxy of the nutricline depth) and the depth of a subsurface dissolved oxygen isoline (22 µmol L^{-1}, ZO2, a proxy of the oxycline depth close to the coast). To compute ZT15, ZNO3 and ZO2, the IMARPE profiles of temperature, nitrate and oxygen respectively were linearly interpolated on a vertical grid with a 1 m resolution (Fig. 7).

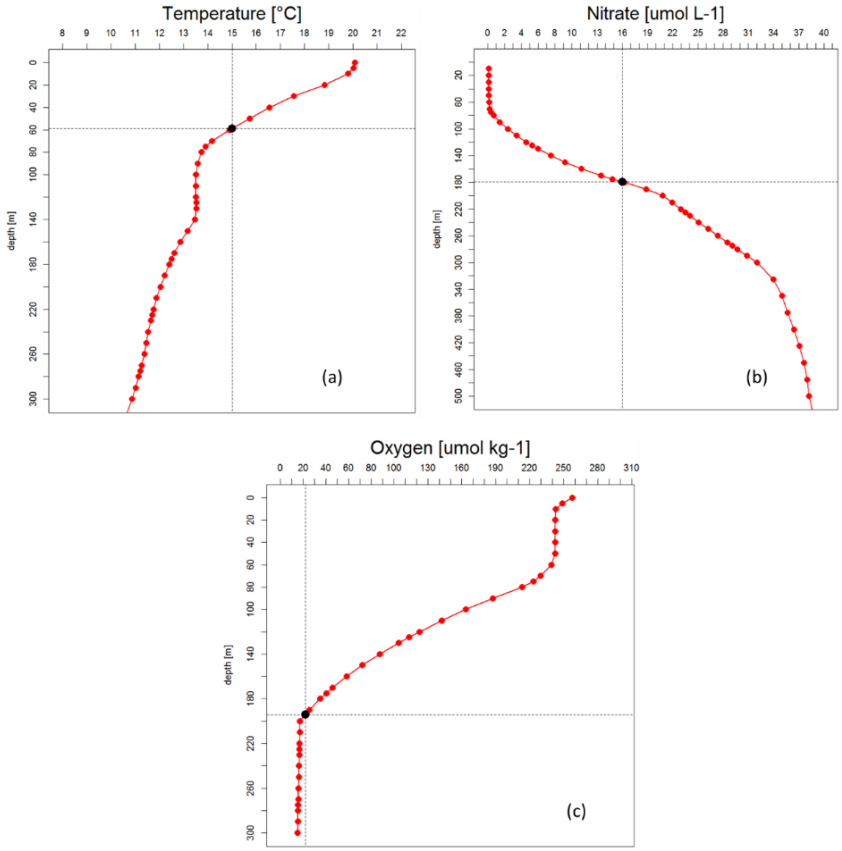

Figure 7. IMARPE typical interpolated profiles of (a) temperature, (b) nitrate and (c) oxygen, localized close to the coast. In each subplot, the black point indicates the depth selected to compute the ZT15, ZNO3 and ZO2.

Approximately 13000, 17000 and 7000 vertical profiles of temperature, oxygen and nitrate were used to compute ZT15, ZNO3 and ZO2 respectively, from 1960 and 2008. More data are available during fall-spring, spring-summer and autumn for ZT15, ZNO3, and ZO2 respectively (Table 5).

Variable	Summer	Autumn	Fall	Spring	TOTAL
Chl-a (0 m)	4866	4476	4758	5364	19464
Thermocline	2254	2396	4151	4174	12975
Oxycline	4416	3666	3846	4832	16760
Nutricline	1647	2155	1514	1986	7302

Table 5. Number of IMARPE sampled points by season for surface Chl-a, ZT15, ZNO3 and ZO2.

4. Computation of Trends

In chapter 5 we computed and analyzed the trends of the main physical and biogeochemical variables. The trend of a given variable was computed by obtaining the linear relationship between the time and the variable, as follows:

$$Variable \sim a + b * time$$

"a" represents the intercept and "b" is the slope in the linear relationship. This slope represents the trend of the analyzed variable. The R software was used to compute the linear relationship and its statistical significance (the function "lm" from the R package "stats" was used to calculate the coefficients by the least square method). The trend was obtained just for the times series that present more than 50% of data during the respective analyzed period i.e. from 1979 to 2008, there is 360 months, therefore only time series with more than 180 points were used to compute trends.

In order to obtain the statistical significance of the trend (b), we used two criteria:

c) When spatial trends were computed (a trend for each grid point), due to computational power limitations and the long processing time, we used the function "anova" to evaluate the statistical significance of "b" in every pixel. In this function, F-test is used to evaluate if the parameter "b" is different to zero (significant). 90 % of confidence level was taken in account to consider the trend was statistically significative. Confidence intervals were not computed for each pixel.

d) When the trend of a single time serie was computed, we used the bootstrap method to compute its significance. With this method, the time serie was first subsampled 1000 times, using the "boot" function in R program, creating 1000 timeseries, which contain the positions in time of the samples. 1000 replicates seem to be enough to compute the confidence intervals. Then "b" was computed for each subsampled time series, producing a histogram. Last, the trend is supposed to be statistically significative if the 0 value is beyond the quantiles 5% (for positive trend, e.g. Fig. 8a) and 95% (for negative trend) (Fig. 8).

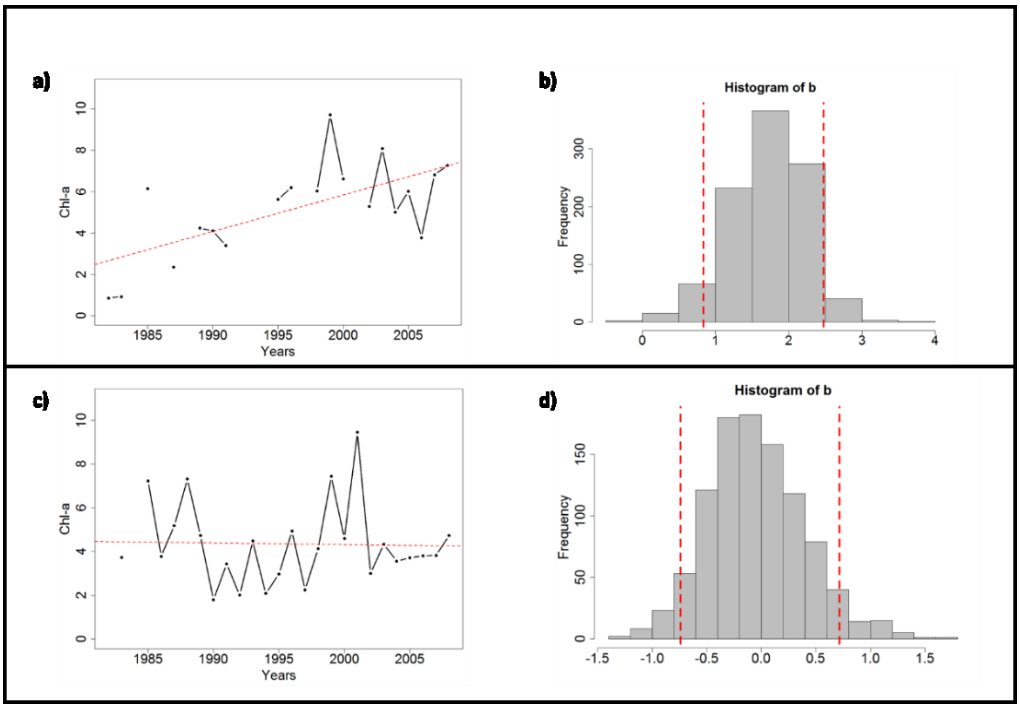

Figure 8. Times series of surface Chl-a (a and c) and histograms of their trend values (b and d). Red lines represent the quantiles 0.05 and 0.95 (90% of confidence level) in (b) and (d). In panel (a), the time series holds 19 observations (in a total of 27 years), and the histogram (b) does not include the 0 value, hence a significant positive trend. In the bottom panels, the time series (c) has more observations (26 out of 27 years) but the histogram of trends (d) includes the 0 value. The trend is hence non significative.

5. Appendix

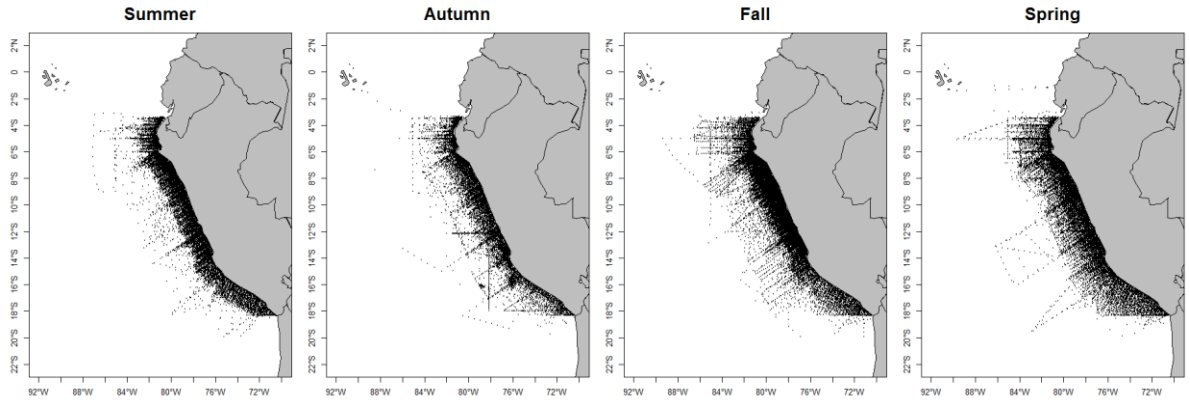

Figure S1. Sampled point of SST from IMARPE by season between 1958 and 2008.

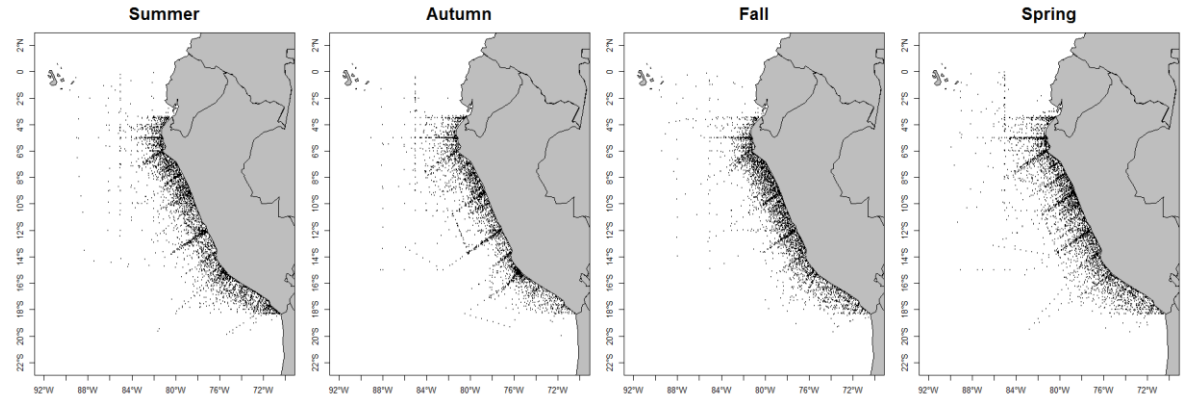

Figure S2. Sampled point of surface Chl-a from IMARPE by season between 1958 and 2008.

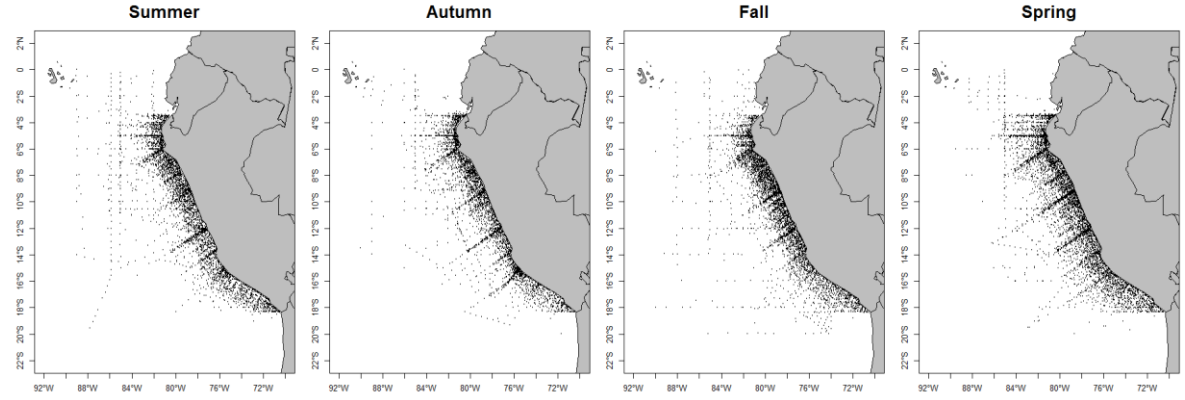

Figure S3. Sampled point of surface NO_3 from IMARPE by season between 1958 and 2008.

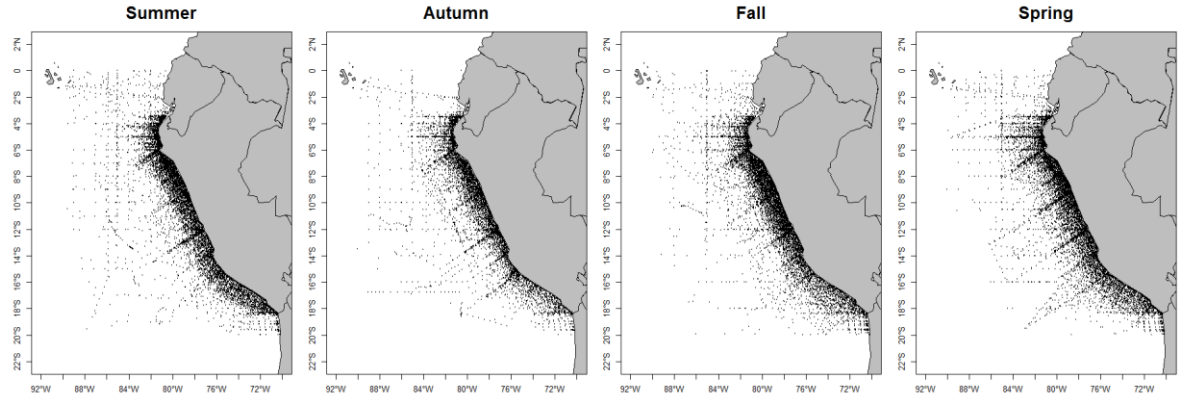

Figure S4. Sampled point of surface O_2 from IMARPE by season between 1958 and 2008.

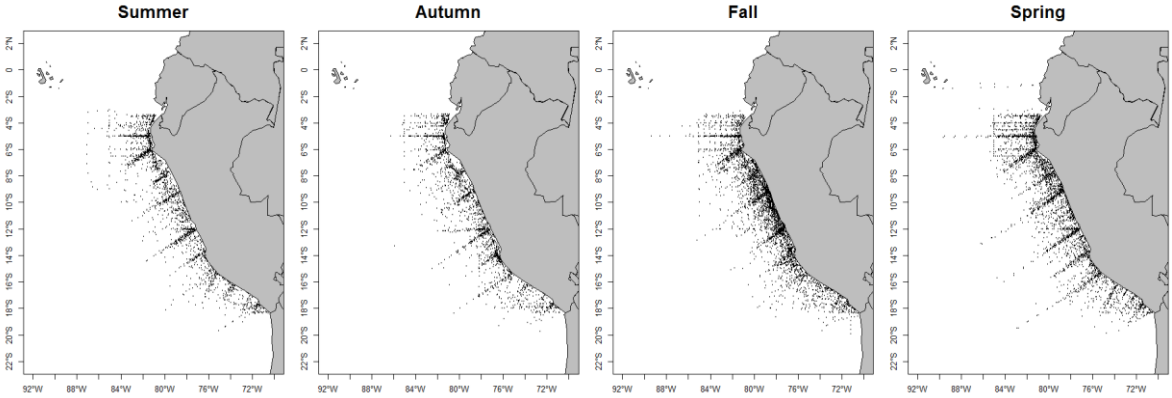

Figure S5. Sampled point of isotherm of 15°C (thermocline) from IMARPE by season between 1958 and 2008.

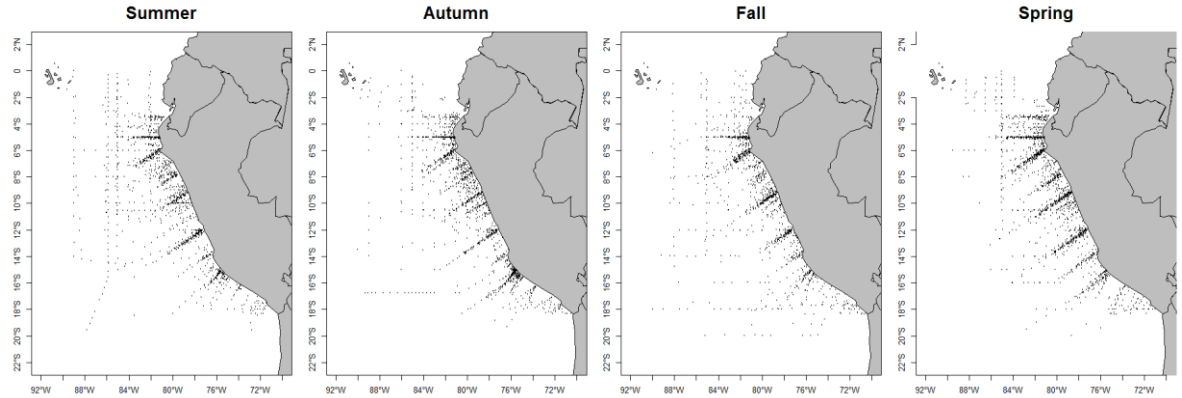

Figure S6. Sampled point of isoline of 16 µmol L^{-1} (nutricline) from IMARPE by season between 1958 and 2008.

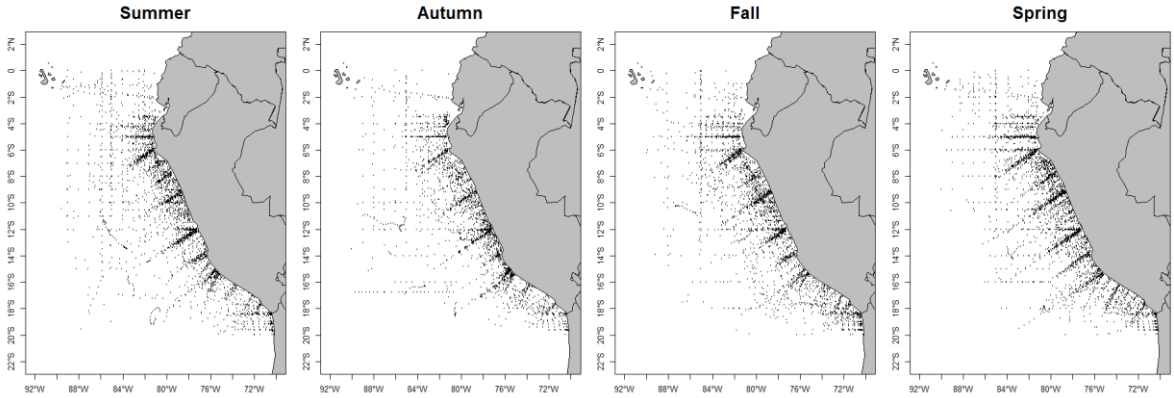

Figure S7. Sampled point of the isoline of 22 µmol kg^{-1} (oxycline) from IMARPE by season between 1958 and 2008.

CHAPTER 3:
IMPACTS OF EL NIÑO ON THE PRODUCTIVITY

Summary

The Peruvian Coastal Upwelling System (PCUS) is dramatically impacted at interannual time scales by El Niño (EN) and La Niña (LN) events. During EN, the sea surface temperature (SST) strongly increases, ventilated and nutrient-depleted waters are found near the coast, along with a surface chlorophyll (Chl) decrease. During LN, negative SST anomalies and a slightly higher phytoplankton and anchovy biomass are observed. The main objective to this chapter is to investigate the involved mechanisms in the decrease of productivity during EN events. For this purpose, the hydrodynamics-biogeochemical ROMS-PISCES coupled model was run for the period 1958-2008, which includes several EN events and in particular the extreme 1972/1973, 1982/1983 and 1997/1998 events.

The model was able to reproduce the main characteristics of different EN events: the SST and Sea Surface Height (SSH) increase, and the Chl and nutrient decrease off Peru. The wind-driven upwelling intensifies, but is partly compensated by an onshore geostrophic flow associated with an alongshore sea-level gradient. The compensating current is intense in winter and spring, and weaker or nonexistent in summer. The nitrate and iron contents of the upwelling source waters (SW) strongly decrease while their depths are little modified in the upwelling region. Besides, the SW properties in the equatorial region away from the coasts (88°W) do not change during neutral, EN moderate and LN period, while during extreme EN events their nutrient content is lower (20%) probably because of the longer duration of the events (~ 16 months).

The passage of a strong downwelling coastal trapped wave (CTW) increases the SSH and the SST, while it deepens the isotherm and nutricline. It triggers strong negative surface Chl anomalies, mainly during summer. Slightly enhanced light limitation in summer and nutrient (nitrate) limitation in winter are found during EN with respect to neutral periods. The nutrient limitation increase is due to the nitrate vertical flux decrease in winter, while it is compensated by the upwelling increase in summer. The light limitation increase in summer can be related to the mixed-layer deepening.

During EN, mesoscale turbulence is stronger, which plays a significant role in nutrient offshore transport and subduction. The nitrate vertical eddy flux, with respect to the mean vertical nutrient flux, increases during EN and is estimated in our simulation to be twice as large as during normal years. However, the magnitude of the nitrate vertical eddy flux could be underestimated due to the relatively low horizontal resolution of our model.

Last, the impact of EN events depends of their intensity. Extreme EN affect the structure of the water column and the Chl surface concentration more than moderate events. Weaker changes are found during LN. In these periods, the chlorophyll slightly increases due to an enhanced upwelling and slightly nutrient-richer source waters.

There results have been published in a research paper in Journal of Geophysical Research Ocean in 2017. The paper is included below.

AGU PUBLICATIONS

JGR

Journal of Geophysical Research: Oceans

RESEARCH ARTICLE
10.1002/2016JC012439

Key Points:
- Deeper nutricline and stronger winds during El Nino lead to reduced productivity due to depleted upwelled waters and thicker mixed layer
- Enhanced wind-driven coastal upwelling during El Nino is compensated by onshore geostrophic current mainly during fall-spring
- Enhanced eddy activity during El Nino drives eddy-driven subduction of nitrate

Supporting Information:
- Supporting Information S1

Correspondence to:
D. Espinoza-Morriberón,
despinoza@imarpe.gob.pe

Citation:
Espinoza-Morriberón, D., V. Echevin, F. Colas, J. Tam, J. Ledesma, L. Vásquez, and M. Graco (2017), Impacts of El Niño events on the Peruvian upwelling system productivity, *J. Geophys. Res. Oceans*, *122*, doi:10.1002/2016JC012439.

Received 10 OCT 2016
Accepted 29 MAY 2017
Accepted article online 2 JUN 2017

Impacts of El Niño events on the Peruvian upwelling system productivity

D. Espinoza-Morriberón[1,2], V. Echevin[2], F. Colas[2], J. Tam[1], J. Ledesma[1], L. Vásquez[1], and M. Graco[1]

[1]Laboratorio de Modelado Oceanográfico, Ecosistémico y de Cambio Climático (LMOECC)/Instituto del Mar del Peru (IMARPE), Esquina general Gamarra y Valle, Callao, Peru, [2]Laboratoire d'Océanographie et du Climat: Expérimentations et Approches Numériques (LOCEAN), IRD/Sorbonne Universites (UPMC Univ Paris 06)/CNRS/MNHN, 4 Place Jussieu, Paris Cedex, France

Abstract Every 2–7 years, El Niño events trigger a strong decrease in phytoplankton productivity off Peru, which profoundly alters the environmental landscape and trophic chain of the marine ecosystem. Here we use a regional coupled physical-biogeochemical model to study the dynamical processes involved in the productivity changes during El Nino, with a focus on the strongest events of the 1958–2008 period. Model evaluation using satellite and in situ observations shows that the model reproduces the surface and subsurface interannual physical and biogeochemical variability. During El Niño, the thermocline and nutricline deepen significantly during the passage of coastal-trapped waves. While the upwelling-favorable wind increases, the coastal upwelling is compensated by a shoreward geostrophic near-surface current. The depth of upwelling source waters remains unchanged during El Niño but their nutrient content decreases dramatically, which, along with a mixed layer depth increase, impacts the phytoplankton growth. Offshore of the coastal zone, enhanced eddy-induced subduction during El Niño plays a potentially important role in nutrient loss.

1. Introduction

The Peru upwelling system (also known as the Northern Humboldt Current System) is one of the most important coastal upwelling systems of the global ocean [*Chavez and Messié*, 2009; *Lachkar and Gruber*, 2012]. Along the coasts of Peru, equatorward winds drive a persistent coastal upwelling of cold and nutrient-rich waters, triggering a high primary productivity [e.g., *Tarazona and Arntz*, 2001; *Pennington et al.*, 2006]. This high productivity supports diverse and abundant fisheries, particularly the Peruvian anchovy [*Chavez et al.*, 2008]. The features of the Peruvian upwelling system are dramatically impacted at interannual time scales by the El Niño-Southern Oscillation (ENSO).

During El Niño (EN), the warm phase of ENSO, a weakening of the trade winds over the equatorial Pacific allows the eastward displacement of West Pacific warm pool [*Picaut et al.*, 1996], generating positive sea surface temperature (SST) anomalies in the Central and Eastern Pacific Ocean. Environmental conditions off Peru change dramatically: SST strongly increases (e.g., $\sim +3$°C SST anomaly in 1997–1998) [*Picaut et al.*, 2002], ventilated and nutrient-depleted waters are found near the coast [*Arntz et al.*, 2006; *Graco et al.*, 2007, 2016], and surface chlorophyll decreases (e.g., ~ -4 mg.m^{-3} anomaly during the extreme 1997–1998 EN) [*Thomas et al.*, 2001; *Carr et al.*, 2002; *Calienes*, 2014]. The planktonic biomass decrease during EN triggers habitat changes and high mortality for several fish populations such as the Peruvian anchovy [*Alheit and Ñiquen*, 2004; *Ñiquen and Bouchón*, 2004] but also for top predators due to reduced food availability [*Tovar and Cabrera*, 1985]. One should keep in mind that the impact of a given EN event on the Peru ecosystem depends on its intensity and spatial structure: the so-called "central Pacific" EN events [e.g., *Takahashi et al.*, 2011] are not likely to have a strong impact near the Peruvian coast in contrast with the "Eastern Pacific" EN events (e.g., 1997–1998).

A pronounced bottom-up mechanism happens during EN owing to the decrease of primary producers [*Tam et al.*, 2008]. The lowest chlorophyll concentrations (a proxy for the phytoplankton biomass) near the coast of Peru in the last 50 years were observed during extreme 1982–1983 and 1997–1998 EN events [*Calienes*, 2014; *Gutiérrez et al.*, 2016]. In climatological conditions, surface chlorophyll off Peru peaks in summer ($\sim$4 mg.m^{-3}) and spring ($\sim$2 mg.m^{-3}) [*Echevin et al.*, 2008]. In contrast, during the 1983 EN chlorophyll-*a*-

AGU Journal of Geophysical Research: Oceans 10.1002/2016JC012439

poor waters (<0.3 mg.m^{-3}) were observed north of 14°S [*Calienes*, 2014], and values of 0.5–1 mg.m^{-3} were recorded along the coast of Peru during the 1997–1998 EN [*Carr et al.*, 2002]. These waters were associated with low nutrient concentrations near the surface [*Barber and Chavez*, 1983].

Different physical processes can have an impact on the productivity of the upwelling system during EN:

1. Intense downwelling equatorial Kelvin waves [e.g., *Kessler and McPhaden*, 1995] trigger coastal trapped waves (CTW) which deepen the nearshore thermocline/nutricline [e.g., *Barber and Chavez*, 1983; *Calienes*, 2014; *Echevin et al.*, 2014; *Graco et al.*, 2016].
2. Changes in equatorial circulation and nutrient concentrations of the upwelling source water (SW) occur during EN. The Peru-Chile Undercurrent (PCUC), a major source water for the Peru upwelling [*Huyer et al.*, 1991; *Albert et al.*, 2010], is fueled by the zonal, eastward Equatorial Undercurrent (EUC) [*Wyrtki*, 1967] and mainly by the Subsurface countercurrents (SSCCs) [*Tsuchiya*, 1975; *Montes et al.*, 2010]. During EN, the position and intensity of the latter are modified [*Montes et al.*, 2011], which may produce changes in the subsurface circulation, water masses, and hence nutrient flux to the upwelling system.
3. Last, mesoscale eddies of higher intensity have been observed during EN [*Chaigneau et al.*, 2008]. This enhanced eddy activity could increase the offshore transport and subduction of nutrients and plankton [*Lathuilière et al.*, 2010; *Gruber et al.*, 2011; *Thomsen et al.*, 2016].

During the cold phase of ENSO (La Niña, LN), the Peru ecosystem is less impacted: upwelling-favorable winds off Peru are intensified, resulting in negative SST anomalies [*Morón et al.*, 2000] and a slightly higher phytoplankton and anchovy biomass [*Calienes*, 2014; *Bouchón and Peña*, 2008].

The main goal of the present study is to investigate the previously mentioned mechanisms and discuss their respective impacts on phytoplankton growth during EN, using a regional physical-biogeochemical coupled model. For this purpose, the 1958–2008 period, which includes several EN events and in particular the extreme 1982–1983 and 1997–1998 events, was simulated. While the study focused on EN events, impacts of LN events are also briefly presented. In the following, we describe the data, model configuration and methods in section 2. Results evaluating the model realism and the main processes at play during EN events are described in section 3. The respective processes that produce the chlorophyll decrease are discussed in section 4. The main conclusions and perspectives of this study are presented in section 5.

2. Material and Methods

2.1. The Coupled Physical-Biogeochemical Model

2.1.1. Model Characteristics

The Regional Oceanic Modeling System (ROMS) resolves the Primitive Equations, based on the Boussinesq approximation and hydrostatic vertical momentum balance. A third-order, upstream-biased advection scheme allows the generation of steep tracer and velocity gradients [*Shchepetkin and McWilliams*, 1998]. For a complete description of the model numerical schemes, the reader is referred to *Shchepetkin and McWilliams* [2005]. The model is used here in its "AGRIF ROMS" version [*Shchepetkin and McWilliams*, 2009].

The Pelagic Interaction Scheme for Carbon and Ecosystem Studies (PISCES) simulates the marine biological productivity and the biogeochemical cycles of carbon and main nutrients (P,N,Si,Fe) [*Aumont and Bopp*, 2006; *Aumont et al.*, 2015]. PISCES has three nonliving compartments which are the semilabile dissolved organic matter, small-sinking particles, and large-sinking particles. It has four living compartments represented by two size classes of phytoplankton (nanophytoplankton and diatoms) and two size classes of zooplankton (microzooplankton and mesozooplankton). The growth of phytoplankton is limited by external nutrients concentration and diatoms differ from nanophytoplankton by their need for silicate and higher iron requirements [*Sunda and Huntsman*, 1997]. Zooplankton feeds on two phytoplankton sizes and their predators are implicitly parameterized by a linear and a quadratic mortality term simulating the predation of an infinite chain of carnivores [*Buitenhuis et al.*, 2006]. The reader is referred to *Aumont et al.* [2015] for a complete description of the model, and to *Echevin et al.* [2014] for a list of biogeochemical parameters values used in the Peru upwelling system.

2.1.2. Model Configuration

The model domain extends from 15°N to 40°N and from 100°W to 70°W. The domain encompasses the Northern and central Chile region; however, our analysis focused on the Peruvian coastal region (Figure 1).

AGU Journal of Geophysical Research: Oceans 10.1002/2016JC012439

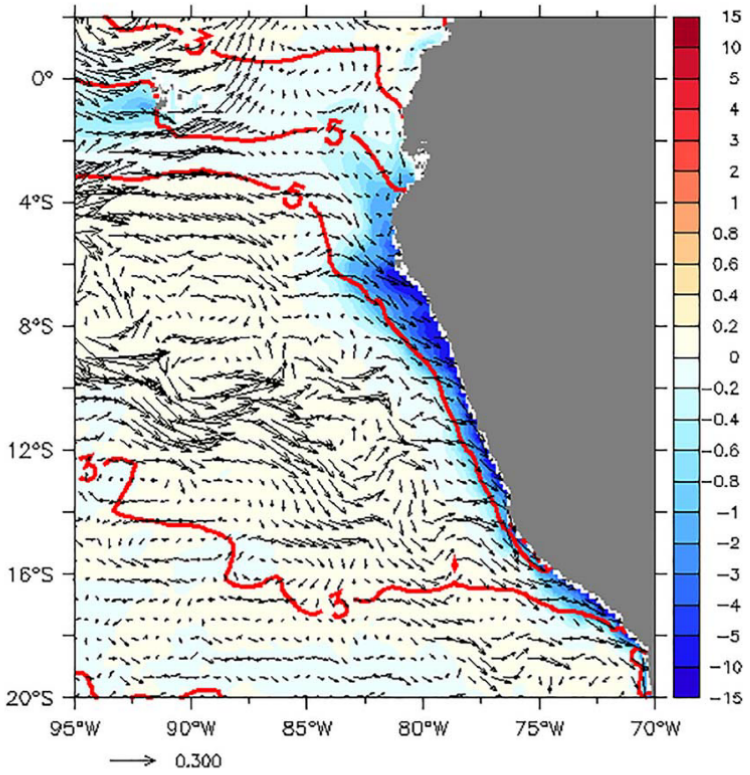

Figure 1. Surface velocity anomalies (arrows, in $m.s^{-1}$), surface chlorophyll anomalies (color scale, in $mg.m^{-3}$), and sea surface temperature anomalies (red lines marking +3 and +5°C) in December 1997 to March 1998 for the simulation. Anomalies were computed with respect to the 1958–2008 climatology.

The horizontal resolution of the grid is 1/6°, corresponding to ~18.5 km. The bottom topography from ETOPO2 [*Smith and Sandwell*, 1997] is interpolated on the grid and smoothed in order to reduce potential error in the horizontal pressure gradient. The vertical grid has 32 sigma levels.

2.1.3. Open Boundary Conditions

Open boundary conditions (OBC) for physical variables (temperature, salinity, velocities, and sea-level) came from an interannual SODA model solution (version 2.1.6) [*Carton and Giese*, 2008] which has a horizontal resolution of 0.5° and 40 vertical levels. Five day-averaged outputs are used for the period 1958–2008. SODA-assimilated hydrographic profiles, moored and satellite data. It was forced with ECMWF ERA-40 atmospheric fluxes [*Uppala et al.*, 2005].

OBC for biogeochemical variables came from CARS2009 climatological data [*Ridgway et al.*, 2002] with a horizontal resolution of 0.5° and 79 vertical levels for oxygen and nutrients (nitrate, phosphate, silicate) and from World Ocean Atlas climatology (WOA2005) [*Conkright et al.*, 2002] for dissolved organic carbon (DOC), dissolved inorganic carbon (DIC), and total alkalinity (TALK). The DIC and TALK from WOA do not have seasonal variation. Iron came from a NEMO-PISCES global simulation climatology [*Aumont and Bopp*, 2006].

2.1.4. Regional Atmospheric Forcing

Statistically downscaled NCEP interannual monthly wind anomalies [*Goubanova et al.*, 2011] and SCOW monthly climatological winds [*Risien and Chelton*, 2008] were added to construct surface wind fields. NCEP monthly anomalies and COADS monthly climatology [*Da Silva et al.*, 1994] were added to construct short wave heat flux and surface air parameters used in ROMS bulk parameterization [*Liu et al.*, 1979].

The atmospheric forcing fields, physical and biogeochemical initial and open boundary conditions were interpolated onto the ROMS grid using the ROMSTOOLS preprocessing package [*Penven et al.*, 2008].

To remove trends induced by the adjustment of the model to initial and boundary conditions, a 20 year spin-up in climatological mode was first run. We used a monthly climatological forcing derived from the

AGU Journal of Geophysical Research: Oceans 10.1002/2016JC012439

atmospheric forcing and monthly climatological OBC from the 5 day SODA OBC. These monthly climatologies were computed over the period 1958–1970. Statistical steady state was reached for physical variables and biogeochemical variables after 3 and 20 years, respectively. Steady state was used as initial condition (1 January 1958) to run the ROMS-PISCES model. The model was run from 1958 to 2008 and the outputs are stored as 5 day averages.

2.2. Lagrangian Analysis

The ROMS-offline tracking module [*Capet et al.*, 2004] was used to calculate the trajectories of water parcels. The virtual float trajectories were computed using the 5 day-averaged ROMS velocity fields. Floats register nitrate and iron concentrations along their trajectories. Two experiments were made to study the properties of the upwelling source water (SW): SW were tracked back 1 month before they were upwelled near the coast, and when they were located in the equatorial zone during LN, neutral, and EN conditions.

In the first experiment, to study the pathways and the characteristics of the SW, 10,000 floats were released every first day of each month from 1958 to 2008 in the surface layer (between 0 and 15 m depth), between the coast and the 100 m isobath in the latitude range 6°–14°S. The floats were then tracked backward in time during 1 month after they had left the mixed layer. In our statistical analysis, we did not take in account the floats that left the mixed layer more than 1 month after being released. From all these floats characteristics, we computed a climatology of the SW depth and nitrate concentration one month before they were upwelled.

In the second experiment, we used the same criterion to select the floats which were tracked backward in time during 2 years. The floats reaching 88°W between 2°N and 10°S (e.g., the typical latitude range of the EUC and SSCCs) [*Montes et al.*, 2010] were used to compute statistics of the SW properties in the equatorial region. In this experiment the floats were released in spring (October, November, December) during every LN, neutral, and EN event.

To compute a probability of presence for a specific depth or concentration range and for a specific month, we counted the particles in the given range and divided this number by the total number of particles upwelled during that month.

2.3. Satellite Data Sets

Monthly mean sea surface temperature from Pathfinder satellite data (~4 km) [*Casey et al.*, 2010] over the period 1984–2008 were used to evaluate SST over the entire model domain. AVISO satellite altimetry data (www.aviso.oceanobs.com) from January 1993 to December 2008 (every 5 days) were used to evaluate the model sea level variability. The 1/3° gridded data were interpolated onto the model grid. Besides, monthly SeaWIFs satellite data [*OReilly et al.*, 1998] at 1/12° (~9 km) resolution were used to validate the model surface chlorophyll concentration from September 1997 to December 2008.

2.4. In Situ Data Sets

Temperature, nitrate, and chlorophyll-*a* (hereafter Chl) data from IMARPE (Instituto del Mar del Peru) sampling were gridded vertically (every 10 m) and then horizontally at the same resolution (1/6°) as the model. Extreme values (in log scale for Chl) were filtered out by removing values higher than twice the standard deviation in each bin. For more details on the Chl and nitrate measurement protocols, the reader is referred to the appendix in *Echevin et al.* [2008]. IMARPE cruises are generally planned twice a year with some exceptions. Gridded (1/2° resolution) surface nitrate concentration from CARS [*Ridgway et al.*, 2002] was also used to evaluate the nitrate concentration model.

2.5. Cross-Shore Sections and Coastal Indices

Alongshore-averaged vertical sections for neutral and EN periods are computed to highlight the mean cross-shore structures. We averaged data between 6°S–16°S and 100 km from the coast (Figure 1; hereafter coastal region), which encompasses most of the IMARPE data.

Due to a subsurface temperature and nitrate bias, thermocline and nutricline depth (hereafter ZT and ZNO_3) were defined as follows: ZT was the depth of the 15°C and 16°C isotherm in IMARPE and model, respectively, and ZNO_3 was the depth of the 16 $\mu mol.L^{-1}$ and 21 $\mu mol.L^{-1}$ nitrate isoline in IMARPE and model, respectively. ZT, ZNO_3, and surface Chl were averaged in the coastal region (see green line in Figure 1) every 6 months to define coastal indices. In order to compute ZT and ZNO_3, the IMARPE profiles of temperature

AGU Journal of Geophysical Research: Oceans 10.1002/2016JC012439

and nitrate were linearly interpolated on a vertical grid with a 1 m resolution. The coastal SST anomalies were computed every month because of their higher sampling in space and time.

To illustrate the data scarcity, we computed for a given variable X an index of Sample Representation ($ISR(x)$) over the Peruvian coastal region: $ISR(x) = |100 * \left(1 - {}^{X_s}/_{X_c}\right)|$, where X_s represents the spatial mean of the model variable sampled using the positions of observational data and X_c represents the spatial mean of the model variable using all the model grid points in the region of averaging. The coverage ratio was computed as ${}^{N_{sampled}}/_{N_{total}}$, where $N_{sampled}$ represents the number of grid points with observations and N_{total} is the total number of grid points in the coastal band ($N_{total} = 438$ points).

2.6. Eddy Subduction During EN

In order to filter the nearshore influence of the CTW and focus on the mesoscale processes related to the formation of eddies and filaments, the eddy kinetic energy (EKE_m) was computed in an offshore band (between 100 and 500 km from the coast and 6°S–14°S). A 60 days moving average filter (labeled $<.>$ in the following) was applied to zonal ($<u>$) and meridional ($<v>$) currents, to compute mesoscale anomalies $u' = u - <u>$ and $v' = v - <v>$. The equation for EKE_m is defined as follows: $EKE_m = \frac{(u')^2 + (v')^2}{2}$.

In order to evaluate nitrate subduction during EN, we estimate the nitrate vertical eddy flux:

$$\overline{w'.N'} = \overline{w.N} - \overline{\langle w \rangle . \langle N \rangle}$$

where w and N are 5 day-averaged vertical velocity and nitrate concentration, respectively, $<w>$ and $<N>$ represent the 60 day filtered values of w and N, and w' and N' are the eddy terms. The overbar represents a spatial average over an offshore band located 100–500 km from the coast and between 6°S and 14°S. We computed the eddy terms every 5 m from 0 to 250 m depth and averaged them for EN and neutral periods.

2.7. Definition of EN Periods

An EN (LN) period is defined when the 3 month-running mean SST anomaly in the Niño 1 + 2 region (0–10°S and 90°W–80°W) is larger (less) than +0.5°C (−0.5°C) for at least five consecutive months, using ERSST.v4 data [*Huang et al.*, 2015]. Neutral periods occur during non-EN and non-LN periods. In addition, we defined different categories of EN events. If the SST anomalies are greater than +1.6°C during at least 3 months the event is considered an "extreme" EN otherwise it is a "moderate" EN. The correlation between model and observed EN 1 + 2 index was 0.9 and both indices detected three EN extremes (1972–1973, 1982–1983, and 1997–1998), and the majority of the EN moderates. Note that in the model solution, the 2002 EN appears as a warm period presenting only 4 months with SST anomalies greater than +0.5°C.

3. Results

3.1. Model Evaluation

3.1.1. Surface Mean State

We compared the mean modeled and observed surface patterns of temperature, nitrate, and Chl (Figure 2). Coastal waters were colder than offshore in the model and observations (Figures 2a–2c) because of the upwelling of subsurface waters. Between 13°S and 16°S, the coldest coastal waters associated with the intense Pisco upwelling (~13.5°S) [*Gutiérrez et al.*, 2011] were seen in both the observations (~16–17°C in IMARPE and ~18°C in Pathfinder) and the simulation (~18°C).

The surface nitrate distribution presented high concentrations near the coast due to the persistent coastal upwelling which brought nutrient-replete subsurface waters to the surface, especially in two regions between 4°S–6°S and 14°S–16°S (Figures2d–2f). The model reproduced the maximum nearshore nitrate concentrations and overestimated the observed values by ~5 $\mu mol.L^{-1}$ (Figure 2f).

The surface Chl concentration presented a marked contrast between the coastal region and the open ocean. The coastal region averaged value was ~4.2 $mg.m^{-3}$ in SeaWIFS, ~3.6 $mg.m^{-3}$ in IMARPE, and ~4.9 $mg.m^{-3}$ in the model, while low values (<1 $mg.m^{-3}$) were encountered offshore (>200 km). The richest nearshore areas (>5 $mg.m^{-3}$) off Peru were located between 8°S and 12°S in IMARPE (Figure 2g), 11°S and 14°S in SeaWIFS (Figure 2h), and between 6°S and 14°S in the simulation (Figure 2i). Computed over the SeaWIFS period (1997–2008), the model coastal average was higher (~6.4 $mg.m^{-3}$) than over the 1958–2008 period. Overall, the nearshore productivity was overestimated by the model, in particular between 6°S

AGU Journal of Geophysical Research: Oceans 10.1002/2016JC012439

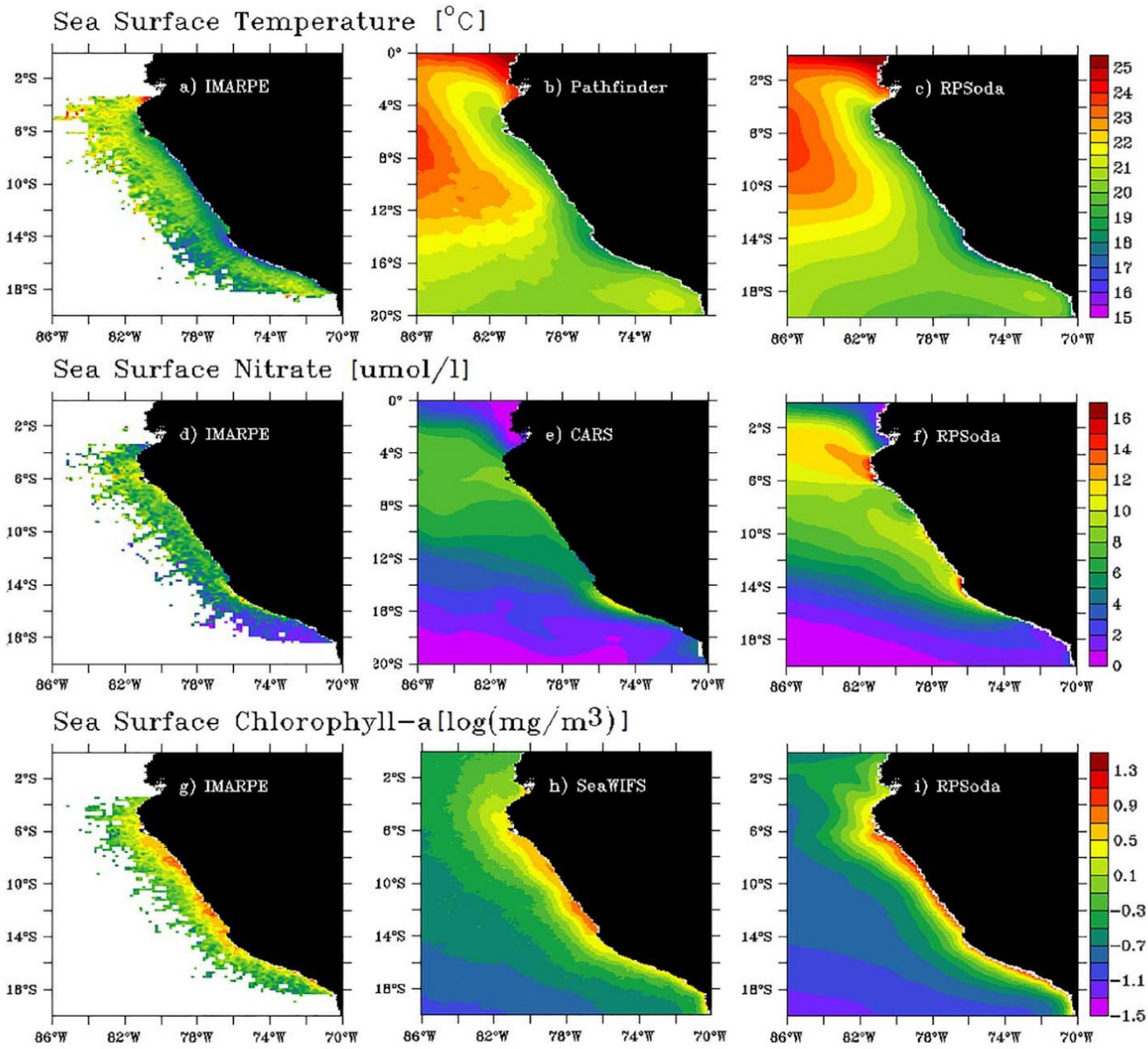

Figure 2. (a–c) Mean sea surface temperature (°C), (d–f) surface nitrate concentration (μmol.L^{-1}), and (g–i) surface chlorophyll (mg.m^{-3}) for observational data and model simulation. IMARPE data were averaged between 1965 and 2008, SeaWIFS data were averaged between 1997 and 2010.

and 10°S and south of 14°S (Figure 2h), probably due to the model high subsurface nitrate concentrations (Figures 2d–2f).

The modeled seasonal cycle of surface Chl was also evaluated in the coastal region (supporting information Figure S1a). Model and observations peaked during late spring-summer, and displayed low values during winter. The model solution overestimated surface Chl by ~4 mg.m^{-3} (75%) during late spring-summer and by ~2 mg.m^{-3} (90%) during the rest of the year with respect to SeaWIFS and IMARPE data, except in late winter-early spring where modeled Chl was close to IMARPE.

3.1.2. Interannual Variability

3.1.2.1. Vertical Structures

Alongshore-averaged vertical sections of temperature, Chl, and nitrate for the model and IMARPE data are shown for neutral and EN periods in Figure 3. Near-surface slanted isotherms (for the model and observations) were present during neutral and EN event, indicating the occurrence of coastal upwelling (Figures 3a,

AGU Journal of Geophysical Research: Oceans 10.1002/2016JC012439

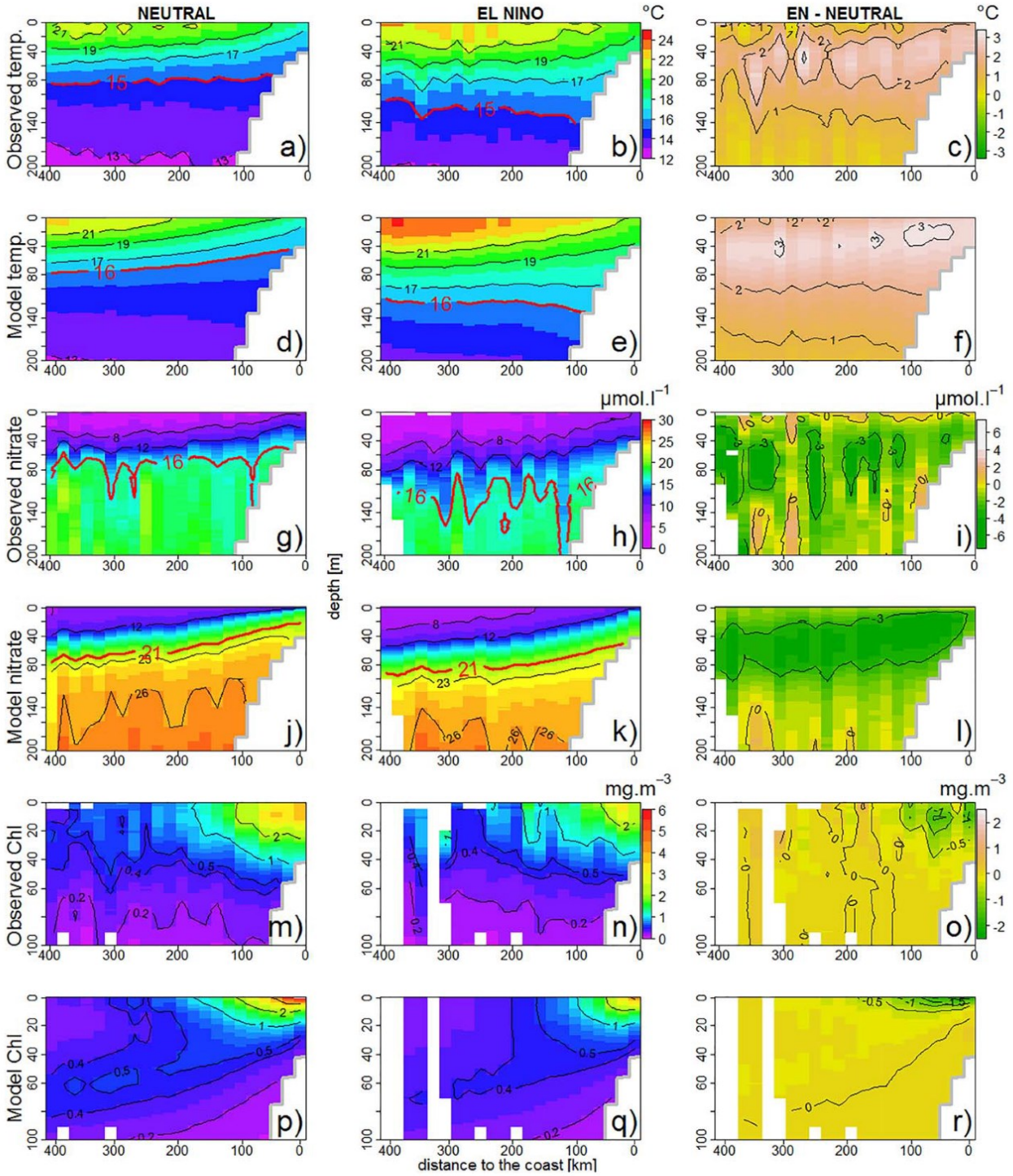

Figure 3. Along-shore averaged vertical section (between 6°S and 16°S) of observational data from IMARPE and model variables: (a–f) temperature (°C), (g–l) nitrate (μmol.L^{-1}), and (m–r) chlorophyll (mg.m^{-3}). (left column) Neutral periods, (middle column) El Niño periods, and (right column) differences between EN and Neutral period are shown. Red lines mark ZT (Figures 3a, 3b, 3d, 3e) and ZNO_3 (Figures 3g, 3h, 3j, 3k).

AGU Journal of Geophysical Research: Oceans 10.1002/2016JC012439

3b, 3d, and 3e). During neutral periods, between the coast and 200 km offshore, ZT was found at ~80 m depth for IMARPE (Figure 3a) and ~60 m depth in the model (Figure 3d). In contrast, during EN periods ZT deepened up to ~130 m depth for IMARPE (Figure 3b) and the simulation (Figure 3e). Despite a slight warm bias, the simulation clearly reproduced the higher temperature anomalies in the surface layer (> +2°C) above 80 m depth (Figures 3c and 3f) and the ZT deepening during EN.

The nitrate vertical sections indicated a model positive bias (~6–8 μmol.L^{-1}) below the surface layer (located below the 17°C and 19°C isotherms during neutral and EN periods, respectively) (Figures3g, 3h, 3j, and 3k). During neutral periods and between the shelf and 200 km, ZNO_3 was localized between ~60 m and 80 m depth for IMARPE (Figure 3g) and between ~30 m and 60 m depth in the model (Figure 3j). During EN, both the model and IMARPE data showed a deepening of ZNO_3. ZNO_3 was highly variable in the observations (Figures3g and 3h) but its mean depth (between the shelf and 200 km) during EN was ~120 m depth for IMARPE (Figure 3h) and ~70 m depth for the model (Figure 3k). Negative anomalies (< −3 μmol.L^{-1}) indicated substantial nitrate loss in both the model (between 5 and 90 m depth) and the observations (between 30 and 125 m depth) (Figures 3i and 3l).

The Chl vertical sections presented high values in the nearshore surface layer, in the model and observations (Figures 3m–3q). During neutral periods the 2 mg.m^{-3} isoline reached the surface 100 km offshore both in IMARPE data (Figure 3m) and the simulation (Figure 3p). Within the first 50 km nearshore, surface mean values were ~3.5 mg.m^{-3} for IMARPE data and ~4.5 mg.m^{-3} for the simulation. Note also the thicker highly productive layer (>2 mg.m^{-3}) in the observations (Figure 3m). The remotely sensed decrease of surface Chl concentration evidenced during EN [e.g., *Carr et al*., 2002] was also found in IMARPE data and the model (Figures 3n and 3q). Within 100 km from the coast, in the surface layer (<10 m depth), a chlorophyll decrease was found in the observations (~ −0.7 mg.m^{-3}) and the model (~ −1.5 mg.m^{-3}). However, the observations showed a deeper Chl decrease: the −0.5 mg.m^{-3} isoline reached ~35 m depth in IMARPE data and ~15 m depth in model (Figures3o and 3r).

3.1.2.2. Interannual Time Series

Interannual variations of the model physical (SSH, SST, and ZT) and biogeochemical (ZNO_3 and surface Chl) variables were evaluated in the coastal region (see Figure 1 and section 2.5). Five day average modeled SSH

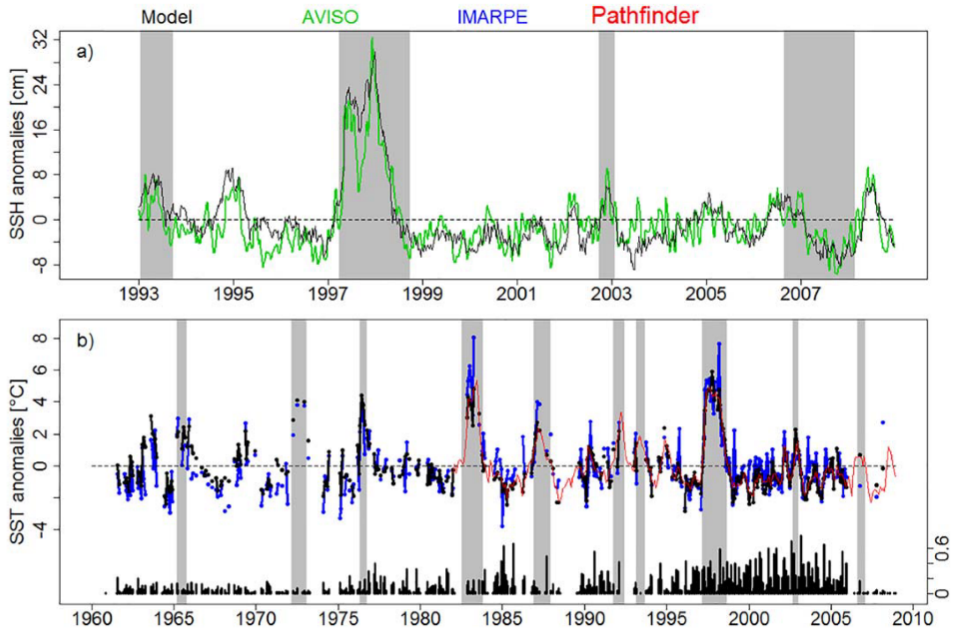

Figure 4. (a) Time series of sea level anomaly (5 day averages, in cm) from AVISO (green line), and model (black line) and (b) monthly SST anomalies (°C) from IMARPE (blue line), model (black line), and Pathfinder data (red line). The averages were computed in a coastal box (see Figure 1). Monthly coverage ratio (see section 2.5) in the coastal box (bottom black bars) is also shown in Figure 7c. Shaded grey boxes represent El Niño periods.

AGU Journal of Geophysical Research: Oceans 10.1002/2016JC012439

anomalies reproduced well the sea level variability during the four EN events from 1993 to 2008 (Figure 4a), in particular the two peaks associated with the passage of CTW trains during the 1997–1998 event [*Colas et al.*, 2008]. The SSH time series anomalies had a correlation coefficient of 0.86.

The model reproduced well the SST variability in particular the SST increase during EN (Figure 4b). Monthly SST anomalies had a high correlation with IMARPE data (~0.8) and with Pathfinder (~0.9). During the 1982–1983 and 1997–1998 events, respectively, mean maximum SST anomalies of ~ +2.9°C and ~ +3.2°C were simulated, weaker than IMARPE anomalies (~ +4.2°C, ~ +3.4°C) but very similar to Pathfinder anomalies (~+2.5°C, ~ +3.2°C). The ISR(SST) presented low values (~2%) indicative of robust estimates (Figure 6a).

Figure 5 shows the interannual variations of ZT, ZNO_3, and surface Chl concentration over 1958–2008. The simulation reproduced the deepening of the thermocline during most EN events (Figure 5a). On average, ZT was found at ~55 m depth in both the observations and the simulation. During the 1997–1998 EN (the best sampled event in terms of temperature), the observed ZT depth was ~120 m and ~140 m in the model. Correlation between modeled and observed ZT is 0.7. Mean ISR(ZT) was ~23% during the studied period (Figure 6b).

The interannual variations of the ZNO_3 are displayed in Figure 5b. Modeled ZNO_3 was slightly shallower (~36 m depth) than the observed (~45 m depth) during study period. The model simulated a strong deepening event during the 1982–1983 (~ +23 m) and 1997–1998 (~ +30 m) events, also found in the observations (~ +25 m in both events). However, modeled and observed ZNO_3 time series were poorly correlated (~0.3) over the entire time period. Mean ISR(ZNO_3) was ~25% (Figure 6c).

Relatively low Chl concentrations were observed during the 1982–1983 (~1.8 $mg.m^{-3}$) and 1997–1998 (~1.7 $mg.m^{-3}$) events, with respect to time periods preceding and following the events, which was

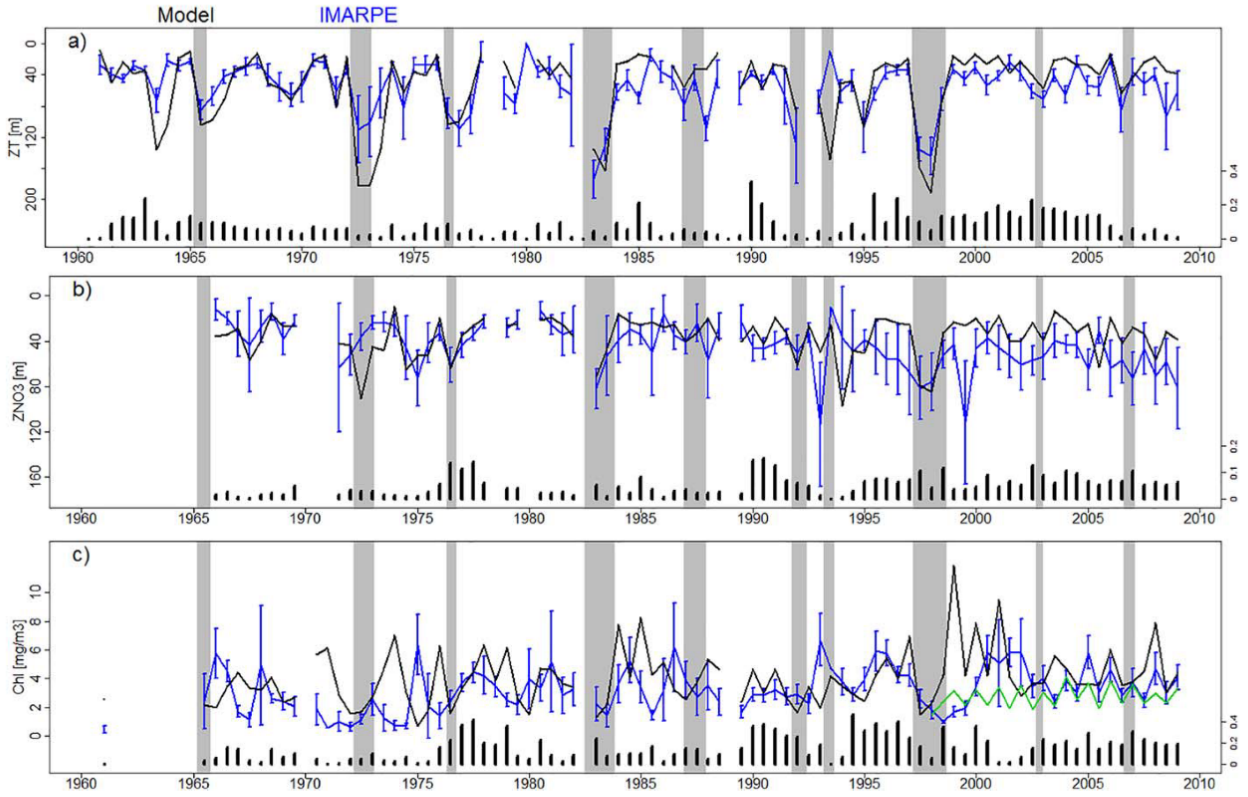

Figure 5. Time series of (a) ZT (in meters), (b) ZNO_3 (in meters), and (c) surface chlorophyll (in $mg.m^{-3}$). Data were averaged each semester for IMARPE (blue line) and model (black line) and SeaWIFS (green line). Error bars represent standard deviation for IMARPE data. Beside, coverage ratio (bottom black bars) is presented. The model mean was computed using the IMARPE sampling (gaps meaning not data), and for SeaWIFS all available data were used.

AGU Journal of Geophysical Research: Oceans 10.1002/2016JC012439

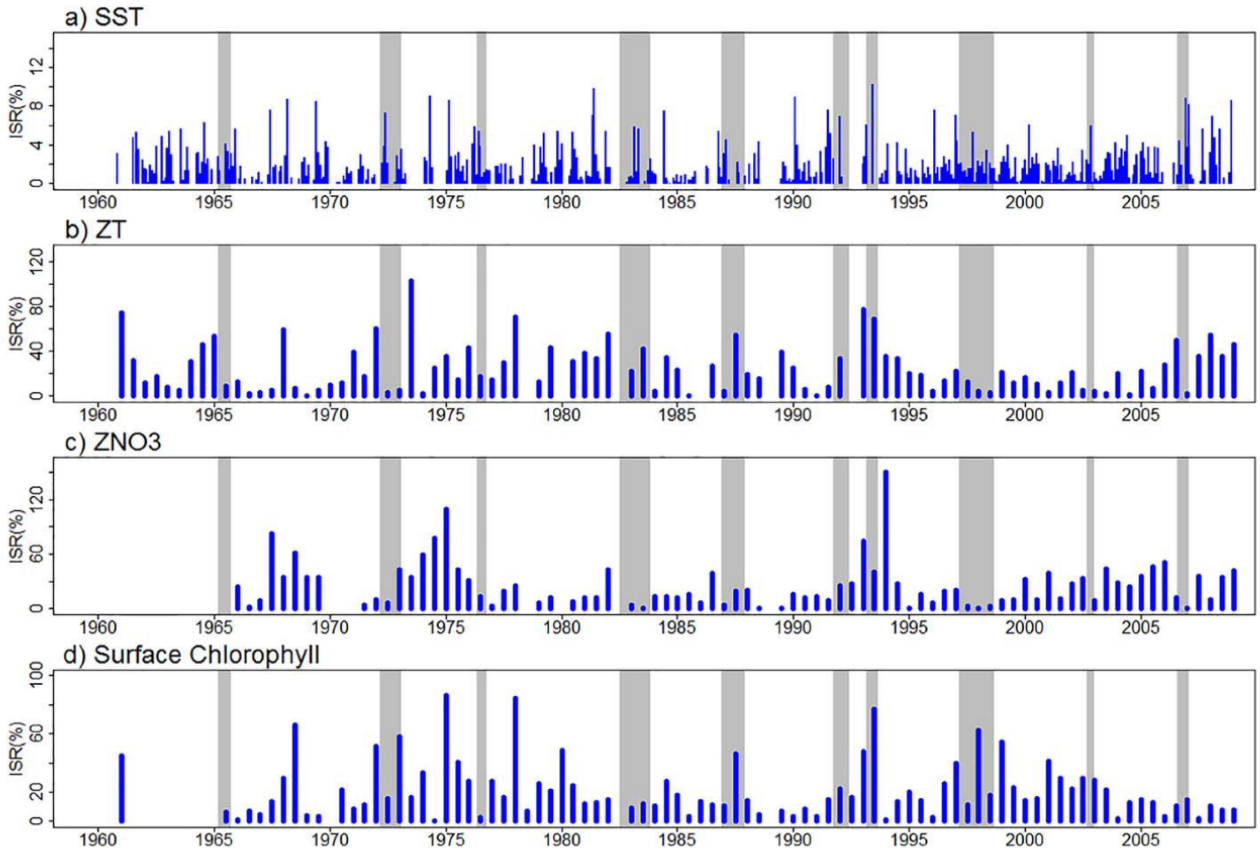

Figure 6. ISR (in %) for (a) SST, (b) ZT, (c) ZNO_3, and (d) Chl. Monthly and 6-month averages are shown in Figures 6a and 6b–6d, respectively. ISR was computed in a coastal band (see Figure 1). Shaded grey boxes represent El Niño events.

reproduced by the simulation. However, there was no correlation between the model and IMARPE observations. The Chl concentration averaged over all EN periods was lower (∼2.5 $mg.m^{-3}$ for both model and data) than the mean over the full time period (∼4 $mg.m^{-3}$ for the model and ∼3.2 $mg.m^{-3}$ for the data). Model and SeaWIFS data confirmed that negative Chl concentration anomalies were found during EN 1997–1998 (supporting information Figure S1b). However a weak interannual variability was evidenced in SeaWIFS in comparison with in situ data. Note that SeaWIFS Chl concentration mean is affected by the presence of important cloud coverage [*Wood et al.*, 2011; *Echevin et al.*, 2014]. ISR was ∼18% during neutral periods and EN events (Figure 6d). However high ISR values in some years (e.g., 60% in the first semester of 1998) suggest that some of the discrepancies between model and data may be attributed to insufficient observational sampling.

3.2. Impact of EN in Phytoplankton Groups

Both diatoms and nanophytoplankton, the two phytoplanctonic groups represented by the model, displayed negative Chl anomalies during EN events. EN events impacted in different proportion the two phytoplankton groups: the Chl loss represented ∼ −50% for diatoms (particularly in late spring-summer) and ∼−20% for nanophytoplankton. The lowest Chl values were found during the 1972–1973, 1982–1983, and 1997–1998 events, with values of ∼ −4 $mg.m^{-3}$ for diatoms and ∼ −0.15 $mg.m^{-3}$ for nanophytoplankton (Figure 7a). EN events also had a different impact on their seasonal cycles. The seasonal cycle of nanophytoplankton during neutral periods presented relatively weak peaks during early autumn and late spring (∼0.6 $mg.m^{-3}$) and low values during late spring-summer (∼0.39 $mg.m^{-3}$) and barely changed during EN (Figure 7b). Diatoms, the dominant species in the Peru upwelling system [*Sánchez*, 2000], were much more impacted, as they are less adapted to nutrient-poor waters [*Irwin et al.*, 2006]. The late spring-early

AGU Journal of Geophysical Research: Oceans 10.1002/2016JC012439

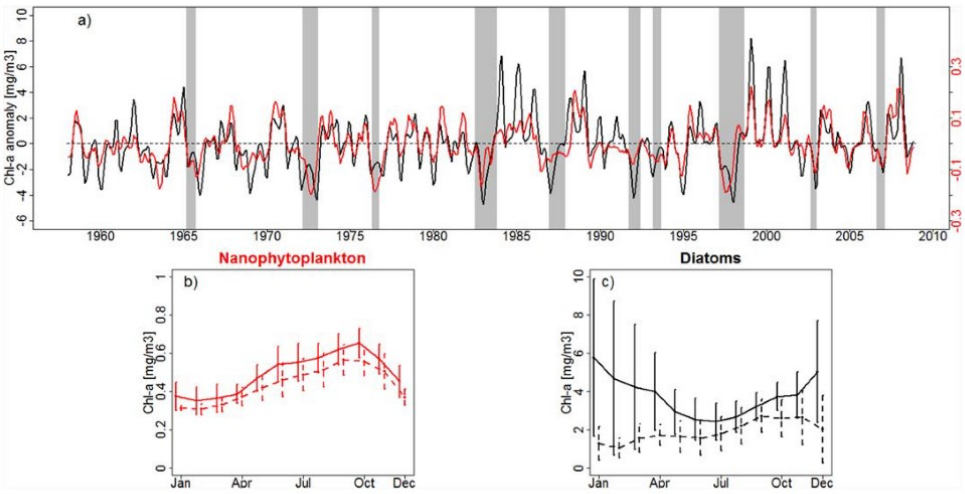

Figure 7. (a) Time series of model nanophytoplankton (red line) and diatoms (black line) surface chlorophyll concentration (in mg.m^{-3}) anomalies. Anomalies were low-pass filtered. Note the different vertical scales for the two time series. Seasonal cycle of (b) nanophytoplankton and (c) diatoms surface chlorophyll concentration (in mg.m^{-3}) during composite El Niño (dashed line) and Neutral (thick line) periods. Error bars represent standard deviation.

summer peak (~ 5 mg.m^{-3}) disappeared completely (~1.5 mg.m^{-3}) and a peak was found in late winter-beginning spring (~2.5 mg.m^{-3}) during EN events. The Chl in diatoms decrease reached ~ −60% during summer and ~ −25% during winter (Figure 7c).

3.3. Processes Driving the Chlorophyll Decrease During EN

3.3.1. Poleward Propagation of CTW

Figure 8 displays the alongshore signature of the poleward propagating CTW on SSH, ZT, ZNO_3, and surface Chl particularly during the two strong EN events (1982–1983 and 1997–1998) simulated by the model. The slanted isolines in each panel indicate southward propagation. Three downwelling EKW in 1982–1983

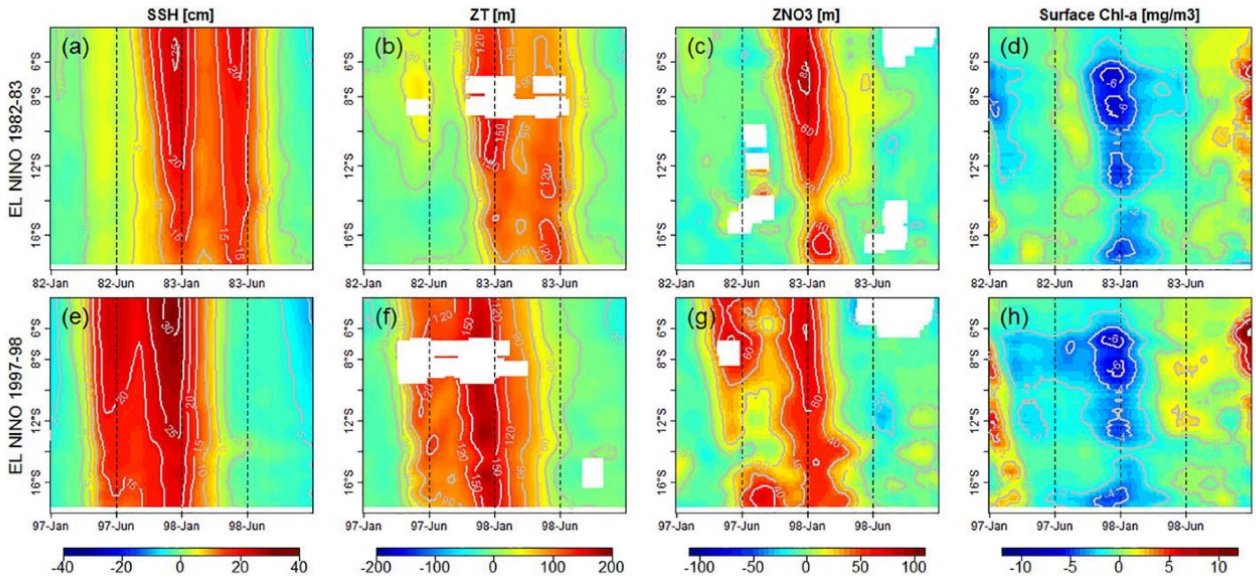

Figure 8. Hovmoller (latitude versus time) of (a, e) model sea level (in cm), (b, f) ZT (in meters), (c, g) ZNO_3 (in meters), and (d, h) surface chlorophyll (in mg.m^{-3}) anomalies during the (top) 1982–1983 and (bottom) 1997–1998 El Niño events. Model values were averaged between the coast and 100 km. All variables were filtered in time (60 days moving average) and space (100 km alongshore). Missing data in Figures 8b, 8c, 8f, and 8g indicate that ZT and ZNO_3 were not detected from 100 km to the coast because of their deepening during EN.

AGU Journal of Geophysical Research: Oceans 10.1002/2016JC012439

(respectively, two in 1997–1998) propagated eastward (supporting information Figure S2) and triggered downwelling CTW upon reaching the Ecuadorian coasts. During both EN events, a more intense CTW is seen during spring-early summer, as well as a weaker CTW in autumn of 1983 and late autumn-early winter of 1997. The passage of the downwelling CTW generated a SSH rise, with maximum values around ∼25 cm and ∼35 cm during the peak of the strongest CTW for the 1982–1983 and 1997–1998 events, respectively (Figures 8a and 8e). The amplitude of SSH anomalies decreased by ∼40–50% between 4°S and 18°S, as the CTW energy dissipated during its poleward propagation.

In association with the sea level rise, ZT deepened during the passage of the CTWs. Anomalies peaked at ∼110 m and ∼160 m in late spring-early summer 1982–1983 and 1997–1998, respectively (Figures 8band 8f). The nutricline depth was also affected: during the 1982–1983 EN ZNO_3 deepening (∼50 m, Figure 8c) was observed in late spring-summer, whereas during 1997–1998 the nutricline deepened during two successive periods, first in autumn-early winter 1997 and then in late spring-summer 1998. The spring-summer CTW had the largest impact (∼55 m; Figures 8c and 8g).

The CTW generated strongly negative surface Chl anomalies. Expectedly, the CTW impact was stronger during late spring-summer (∼ −4.5 $mg.m^{-3}$) than during autumn (∼ −2 $mg.m^{-3}$), due to the higher Chl concentration and greater deepening of the nutricline/thermocline in summer. This increased both nutrient limitation of phytoplankton growth during EN, but light limitation was also increased due to a deepening of the mixed layer during EN (see section 4.2 and supporting information Figure S3). The latitude band between 6°S and 9°S (e.g., the northern shelf region) was mostly affected (anomalies less than −6 $mg.m^{-3}$; Figures 8d and 8h) due to the higher modeled Chl values in this region.

3.3.2. Nearshore Vertical Fluxes

During neutral periods the wind stress had a marked seasonality, with a maximum during late winter (∼5.5 10^{-2} $N.m^{-2}$) and low values during summer (∼1.7 10^{-2} $N.m^{-2}$) in the simulation (Figure 9a) and in observations [*Gutiérrez et al.*, 2011]. The wind stress was roughly in phase with the seasonal cycle of mass vertical

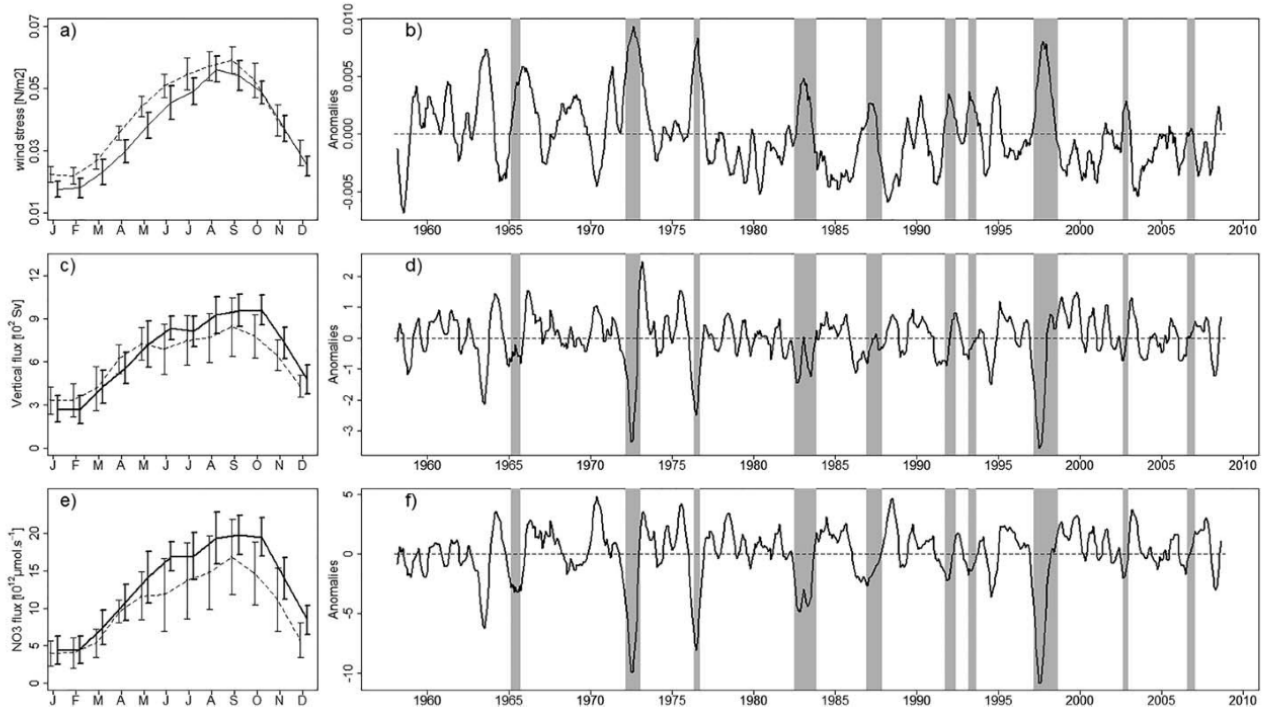

Figure 9. (a, c, e) Seasonal cycle and (b, d, f) interannual time series of low-pass filtered anomalies for (a and b) wind stress ($N.m^{-2}$), (c and d) mass vertical flux (in Sv) at 20 m depth, and (e and f) nitrate vertical advection flux at 20 m depth (in $\mu mol.s^{-1}$) during Neutral (thick line) and EN periods (dashed line). All model variables were averaged in a coastal band (see Figure 1).

AGU Journal of Geophysical Research: Oceans 10.1002/2016JC012439

flux (referred to as the upwelling) and nitrate vertical flux (Figures 9b and 9c). The vertical fluxes were also modulated by seasonal CTW which had different amplitude and timing, as shown in *Echevin et al.* [2011].

During EN, alongshore winds increased off Peru [*Enfield*, 1981; *Kessler*, 2006]. The mean wind stress anomalies were around $\sim$0.35 10^{-2} N.m^{-2} (Figure 9b) with stronger anomalies in summer-autumn (Figure 9a). The strongest anomalies were found during the 1972–1973 and 1997–1998 EN events with $\sim +0.7\ 10^{-2}$ N.m^{-2}. Other EN events presented a $\sim +0.25\ 10^{-2}$ N.m^{-2} anomaly on average. The wind stress increase during EN generated a mixed layer deepening (supporting information Figure S3).

These wind stress positives anomalies suggest that the wind-driven upwelling could be enhanced during EN events. However, the model showed an upwelling decrease during winter-spring (Figure 9c), which was associated to a compensating onshore current during EN (Figure 1 and see section 4.3). The mean upwelling anomalies were $\sim -0.6\ 10^{2}$ Sv and the highest negative anomalies were encountered during the 1972–1973 and 1997–1998 events ($\sim -3.2\ 10^{2}$ Sv; Figure 9d). Expectedly, the nitrate flux decreased during EN due to both a nearshore reduction of the vertical velocity and a deepening of the nutricline, particularly in winter-spring, while summer was less impacted (Figure 9e). The maximum negative anomalies occurred during the 1997–1998 event. The mean modeled nitrate flux anomalies were around $\sim -3.4\ 10^{12}$ µmol.s^{-1} during EN events (Figure 9f).

3.3.3. Modification of the Source Water Properties

Using the virtual floats released in the upwelling region and integrated backward in time, we computed histograms of the source water (SW) depth and nitrate concentration for neutral and EN composite years.

The mean depth of the SW, 1 month before being upwelled, had a marked seasonal pattern (Figure 10a). During austral summer, water parcels were located within the upper 120 m of the water column, with a maximum probability ($\sim$70%) between 25 and 40 m depth. During austral winter the parcels depth spanned a wider depth-range (between the surface and 180 m), and 40% of the upwelled water came from the 60–100 m

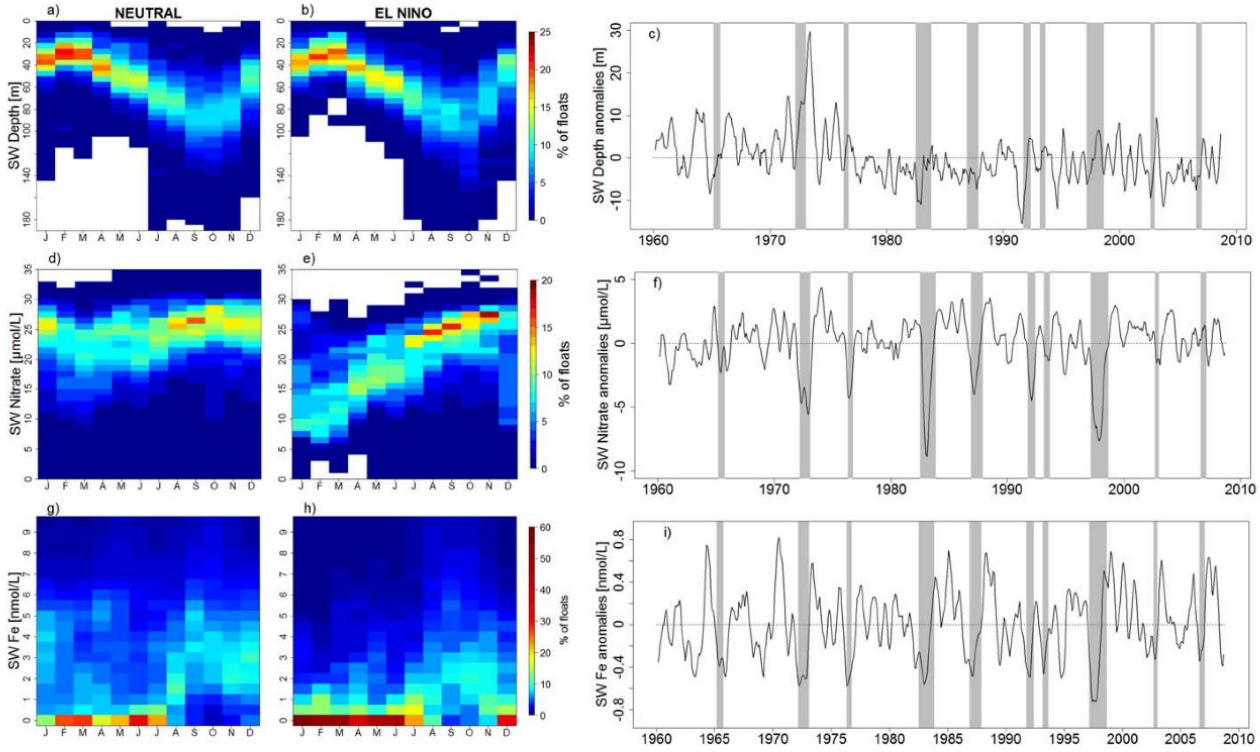

Figure 10. (a and b) Seasonal variation of source water depth (in meters), (d and e) nitrate concentration (in µmol.L^{-1}), and (g and h) iron concentration (in nmol.L^{-1}) 1 month before their upwelling at the coast. Histograms are presented for (left column) Neutral and (right column) El Niño periods. The color scale indicates the percentage of floats in each bin. Time series of (c) SW depth (in meters), (f) nitrate concentration (in µmol.L^{-1}), and (i) iron concentration (in nmol.L^{-1}) anomalies. Times series were low-pass filtered using 6 month moving average filter.

AGU Journal of Geophysical Research: Oceans 10.1002/2016JC012439

depth range. Interestingly, during EN, the SW depth was little modified (Figure 10b): it had the same seasonality, with a slightly narrower vertical range (between 0 and 80 m depth) in summer, likely due to an enhanced stratification caused by the shoreward advection of anomalously warm waters [*Colas et al.*, 2008].

During neutral years, the SW nitrate concentration showed a weak seasonality with a slightly higher concentration (~22–30 μmol.L^{-1}) during winter-early summer than during late summer-autumn (~17–25 μmol.L^{-1}; Figure 10d). During EN events, the percentage of SW parcels with a high concentration of nitrate dropped dramatically in summer and autumn. A large portion (~40%) had concentrations between ~7 and 12 μmol.L^{-1} in summer and ~12 and 17 μmol.L^{-1} in autumn, which represented a 40% decrease. During winter and spring, the SW nitrate content was not significantly altered (Figure 10e). Expectedly, the time series of SW depth anomalies did not exhibit a clear behavior during EN events (Figure 10c). In contrast, the strongest nitrate anomalies were found during the 1972–1973, 1982–1983, and 1997–1998 events with peaks of −5.5 μmol.L^{-1}, −9 μmol.L^{-1}, and −8 μmol.L^{-1}, respectively (Figure 10f).

SW iron (Fe) concentration was also evaluated. The role of iron limitation during EN has been little investigated, however its impact on phytoplankton growth off Peru has been documented [*Hutchins et al.*, 2002; *Bruland et al.* 2005]. Our Lagrangian analysis showed that the SW Fe concentration strongly decreased during EN (Figure 10i), especially during summer – autumn, where ~70% of floats presented concentrations less than 0.5 nmol.L^{-1} (Figures 10g and 10h). During the peak of EN (e.g., January 1998), surface Fe positive anomalies were found offshore (>40 km; Figure not shown). It is likely that the low phytoplankton biomass did not consume the upwelled Fe which accumulated and was transported offshore by Ekman currents. However, to our knowledge there was no available Fe data collected during EN to confirm this mechanism.

In a second experiment (see section 2.2), we focused on the changes in SW characteristics away from the upwelling region, e.g., in the equatorial zone when SW crossed the longitude 88°W. In this experiment, more than 95% of the floats were found between 2°N and 10°S. In Figure 11 we displayed some properties of the floats at 88°W: the time to reach the upwelling region, depth, and nitrate concentration. We also contrasted LN, neutral, moderate, and extreme EN events. During extreme events, water particles reached the coastal zone more rapidly (~6 months) than in neutral conditions (~10 months), and floats during LN periods transited in an even longer time (~14 months; Figure 11a) in line with *Montes et al.* [2011]. In addition, during extreme EN events floats were shallower (~90 m) than during neutral and moderate events (~105 m). Floats were much deeper (~155 m) during LN (Figure 11b).

The SW nitrate content at 88°W were depleted only during extreme EN events. In such conditions, particles carried at least 20% less nitrate (~20 μmol.L^{-1}) than during LN, neutral and EN moderate. Besides, SW nutrient concentration during LN was not very different than during neutral and EN periods (Figure 11c).

3.3.4. Enhanced Mesoscale Turbulence

The EKE increased during EN, particularly during extreme events (1972–1973, 1982–1983, 1997–1998). The amplitude of the modeled EKE increase during the 1997–1998 EN was consistent with the observations (Figure 12a). *Chaigneau et al.* [2008] also found a 40% increase in satellite-derived eddy activity during the 1997–1998 event. We evaluated the nitrate flux in the offshore region. In Figure 12b the mean vertical flux

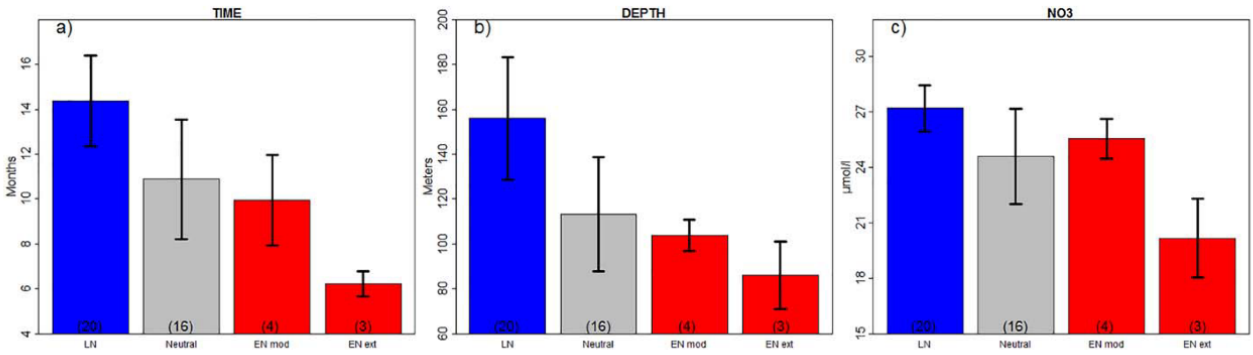

Figure 11. (a) Transit time (from 88°W to the coast) (in months), (b) depth (in meters), (c) nitrate concentration (in μmol.L^{-1}), and (d) iron concentration (in nmol.L^{-1}) of equatorial source waters (at 88°W) during LN events (blue bars), Neutral periods (grey bars), EN moderate and EN extreme events (red bars). Error bars represent standard deviation. Numbers at the bottom of the bars indicate the number of events taken into account to compute the average. Floats were released between October and December.

AGU Journal of Geophysical Research: Oceans 10.1002/2016JC012439

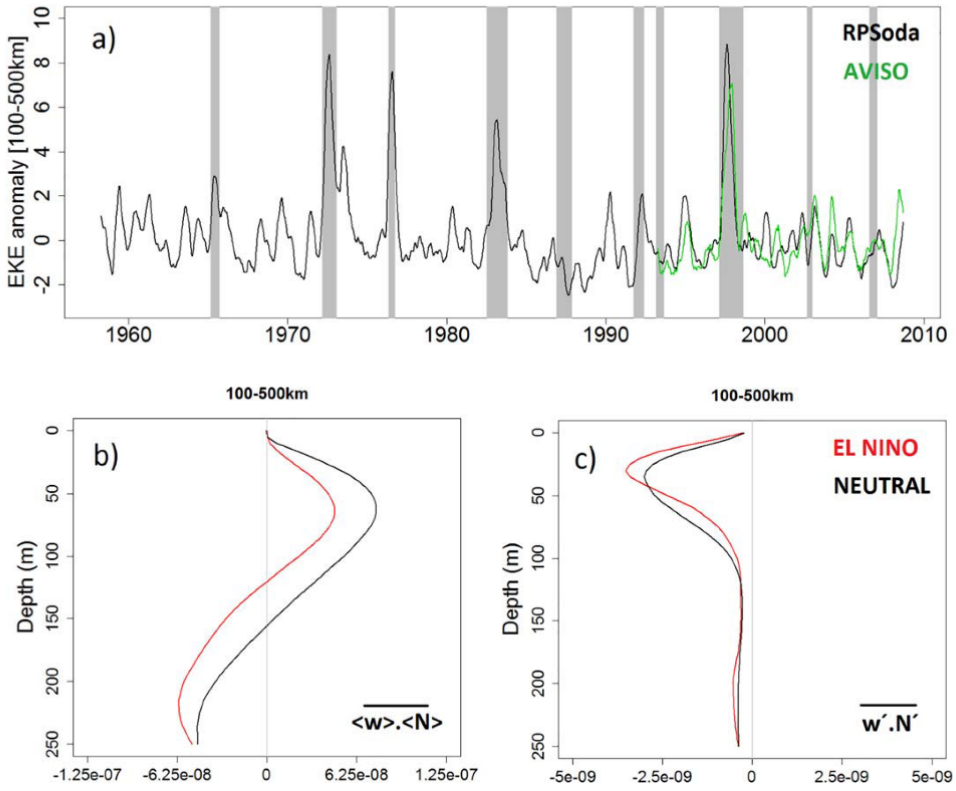

Figure 12. Times series of geostrophic Eddy Kinetic Energy (EKE, in $cm^2.s^{-2}$) anomaly in an offshore oceanic band (100–500 km from the coast and 6°S–14°S). Geostrophic currents anomalies were computed with respect to a 60 days moving average filter for model (black line) and AVISO data (green line). (a) The EKE times series was low-pass filtered using a 6 month moving average filter. (b) Vertical profile of mean vertical nitrate flux (in $\mu mol.m^{-2}.s^{-1}$) and (c) eddy vertical nitrate flux (in $\mu mol.m^{-2}.s^{-1}$) for Neutral (black line) and EN periods (red line). The nitrate fluxes were computed in an oceanic band between 100 and 500 km from the coast and 6°S–14°S.

$(\overline{\langle w \rangle . \langle N \rangle})$ showed positive values between ~5 and ~130 m depth, likely related to Ekman pumping [e.g., *Albert et al.*, 2010]. During EN, the mean flux decreased due to a reduced Ekman pumping [*Halpern*, 2002] and lower nutrient concentration. In contrast, the nitrate eddy flux presented negative values with a maximum at ~40 m depth during neutral ($-3\ 10^{-9}$ $\mu mol.m^{-2}.s^{-1}$) and EN ($-3.5\ 10^{-9}$ $\mu mol.m^{-2}.s^{-1}$) years (Figure 12c). This eddy-driven subduction (or nitrate vertical eddy flux) represents a fraction of the mean vertical flux $(\overline{w'.N'}/\overline{\langle w \rangle . \langle N \rangle})$: ~6% and ~12% (between 30 and 70 m) for neutral and EN periods, respectively.

3.4. Impact of EN Intensity and LN Conditions

In this section we characterized the impact of different EN intensities (moderate and extreme) and the impact of LN on modeled wind stress, upwelling, ZT, ZNO_3, Chl, and SW properties in the coastal region (Figure 13). Expectedly, extreme EN events had the strongest impact on wind stress increase, upwelling decrease, ZT and ZNO_3 deepening, SW nitrate and iron concentration, and surface Chl. The SW depth (one month before upwelling) were unchanged regardless of the event intensity. Interestingly, during LN the coastal system tended to be slightly more productive than during neutral periods, due to an enhanced upwelling (Figure 13b) and slightly nutrient-richer SW (Figures 13f and 13g).

In general EN impacts on physical and biogeochemical variables (negative or positive anomalies) were about twice as strong as LN impact and of opposite sign. However a fully dedicated study would be necessary to investigate further the processes at play during LN events.

3.5. Impacts of EN on Zooplankton and Carbon Export

EN impacted the higher trophic levels of the ecosystem [*Ñiquen and Bouchón*, 2004], as for instance the modeled zooplankton stocks (Figures 14a and 14b). Both mesozooplankton and macrozooplankton showed

AGU Journal of Geophysical Research: Oceans 10.1002/2016JC012439

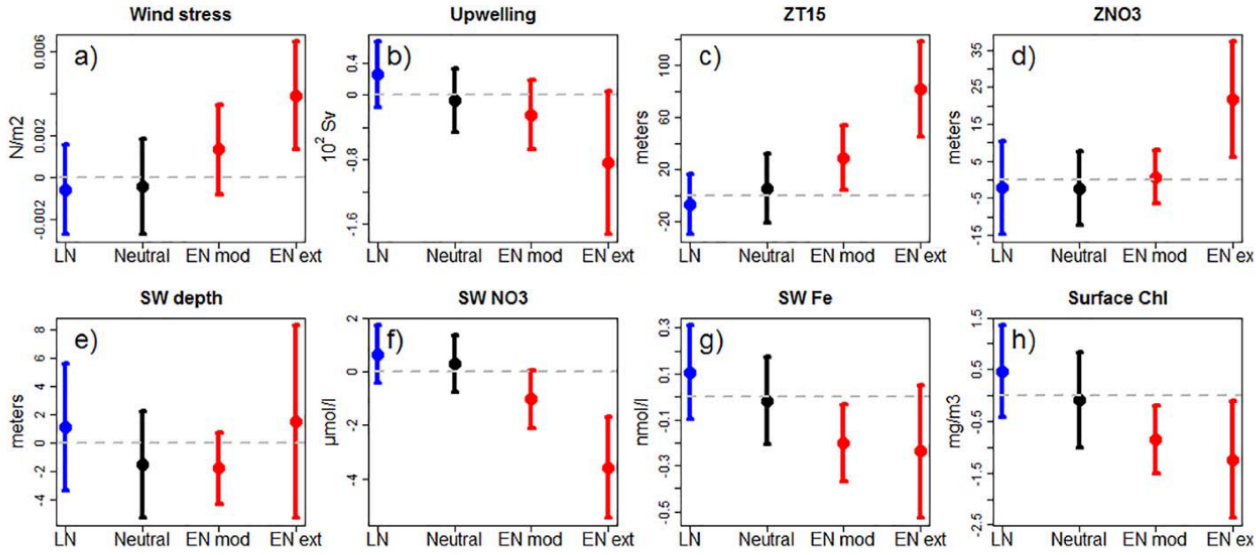

Figure 13. (a) Wind stress (in $N.m^{-2}$), (b) upwelling rate (in 10^2 Sv), (c) ZT (in meters), (d) ZNO_3 (in meters), (e) SW depth (in meters), (f) SW nitrate concentration (in $\mu mol.L^{-1}$), (g) SW iron concentration (in $nmol.L^{-1}$), and (h) Chl concentration (in $mg.m^{-3}$) during LN (blue bar), Neutral (black bar), EN moderate and EN extremes (red bars). All variables are averaged in a coastal band (see Figure 1). Error bars represent the standard deviation.

strongly negative anomalies during EN, reaching 35–40% during extreme events. Nevertheless, observational data in Peru did not show a clear relationship between EN events and a decrease of zooplankton biomass. The observed interannual variability seems dominated by decadal regime shifts [*Ayon et al.*, 2008a] and is supposed to be partly controlled by fish predation at the local scale [*Ayon et al.*, 2008b]. Note that zooplankton predation by higher trophic levels is crudely parameterized in PISCES (see section 2.1.1 and *Aumont et al.*, [2015]). South of the Peru region, off central Chile, a systematic decrease of zooplankton during EN was not observed, as specific types of zooplankton can thrive during EN conditions [*Ulloa et al.*, 2001]. Possibly, the coupling of our model with a higher trophic level model [e.g., *Travers et al.*, 2009; *Hernandez et al.*,2014; *Lefort et al.*, 2015] could help disentangle the bottom-up and top-down mechanisms that control the zooplankton biomass during EN. Besides, export and remineralization of organic matter

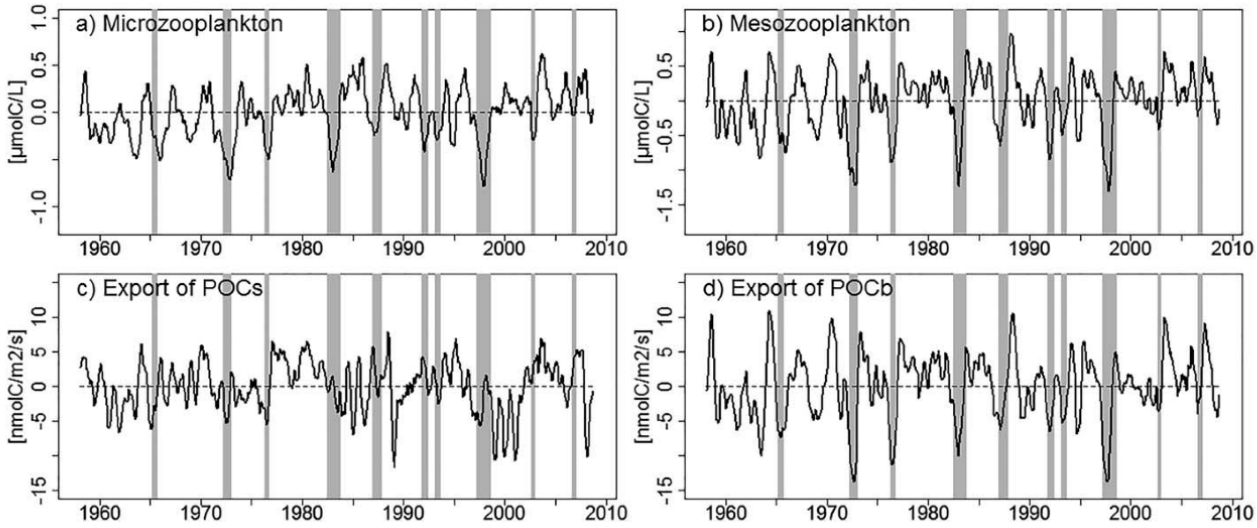

Figure 14. Time series of modelled zooplankton surface concentration (in $\mu molC.L^{-1}$): (a) microzooplankton and (b) mesozooplankton, (c) small and (d) big POC downward flux (in $nmolC.m^{-2}.s^{-1}$) anomalies. All variables were averaged in a coastal band (see Figure 1) and filtered using a s6 month moving average filter.

AGU Journal of Geophysical Research: Oceans 10.1002/2016JC012439

play an important role in the maintenance of the Peru OMZ [*Paulmier et al.*, 2006; *Graco et al.*, 2007]. The simulated export of organic matter, namely through sedimentation of particulate organic carbon (POC) in the form of big (POCb, 100–5000 μm) settling particles, was strongly reduced during EN (Figures 14c and 14d), while the small POC export (POCs, 1–100 μm) did not have a clear relationship with EN events. The average anomaly of POCb export was ~–4.5 nmolC.m^{-2}.s^{-1} during EN, and reached ~–10 nmolC.m^{-2}.s^{-1} (~50% loss) during strong events (e.g., 1997–1998). A strong export decrease was also found by *Carr* [2003] during the 1997–1998 event with minimums values during the passage of CTW.

4. Discussion

4.1. Model-Data Discrepancies

Rather expectedly, the model reproduced more accurately the physical variability than the biogeochemical variability observed from IMARPE surveys. Surface Chl and nutrients have a high variability in space and time due to nonlinear biogeochemical processes involved in primary productivity. Daily variability can reach 1 order of magnitude, e.g., in the case of fast blooms associated with red tides [*Kahru et al.*, 2004]. Also, strong horizontal gradients due to mesoscale and submesoscale features [*Chaigneau et al.*, 2008; *Colas et al.*, 2013; *McWilliams*, 2016] are commonly observed and not well represented in our model because of its relatively low spatial resolution (1/6°).

Estimation of a coastal index for the entire Peru region based on IMARPE in situ data (e.g., Figure 3) could also be partly biased due to the cruises sampling. Low values of ISR for some variables suggest that IMARPE in situ sampling was able to represent the oceanographic conditions along the coasts. Relatively good spatial sampling of SST in situ measurements resulted in low values of ISR (~3%) and hence good representativity (Figure 6a). In contrast, the highly heterogeneous surface Chl produced a higher ISR (~20%, Figure 6d) in spite of a relatively large number of samples. High ISR values (~20%) for the thermocline and nutricline (Figures 6b and 6c) were likely due less numerous subsurface measurements. The IMARPE in situ sampling seemed sufficient to reproduce the SST temporal variability near the coast, while for ZT, ZNO_3, and surface Chl a denser sampling would be needed.

4.2. Seasonal Response of Chlorophyll During EN

During neutral periods, Chl concentration presented a marked seasonality driven by nutrient and light limitation growth factors. Nutrient and light limitation were quantified by computing the limitation terms offline [see *Echevin et al.*, 2008; *Aumont et al.*, 2015, for details]. In the nearshore mixed layer, strong nutrient limitation (~0.2–0.4) was found during late spring-summer and strong light limitation (~0.2) during winter (Figure 15a). Nutrient limitation showed a marked seasonality with nitrate limitation during spring-summer and iron limitation during autumn-winter (Figures 15b and 15c). Using a regional model setting similar to ours, *Echevin et al.* [2008] suggested that iron limitation could occur during winter, in line with *Messié and Chavez* [2015] results based on in situ and satellite observations.

The seasonality of limiting factors did not change during EN. However, slightly enhanced light limitation in summer and nutrient (nitrate) limitation in winter were found during EN with respect to neutral periods (Figure 15a). The nutrient limitation increase was related to the nitrate vertical flux decrease in winter, while it was compensated by the upwelling increase in summer (Figures 9e and 9f). On the other hand, the light limitation increase during EN in summer can be explained by the ML deepening (supporting information Figure S3). To investigate the impact of the model nitrate bias on these results, the light and nutrient limitation terms were computed in a different model run (named RPOrca, see details in supporting information) which simulated a reduced nitrate content. It reproduced the nitrate decrease during EN in the same proportion as the simulation analyzed in the previous sections (supporting information Figure S4a). However, in summer during EN, nutrient limitation was enhanced, whereas light limitation was not changed due to a weak wind increase (supporting information Figure S4b). Thus, our conclusion is that both light and nutrient limitation may play a role in the decrease of Chl during EN, depending on the nutrient subsurface concentration and mixed layer variability.

4.3. Onshore Surface Geostrophic Transport During EN

Using satellite observations, *Thomas et al.* [2009] found strong negative anomalies of Chl concentration during the 1997–1998 EN in the Peru and California systems. They mentioned that the anomalies were

AGU Journal of Geophysical Research: Oceans 10.1002/2016JC012439

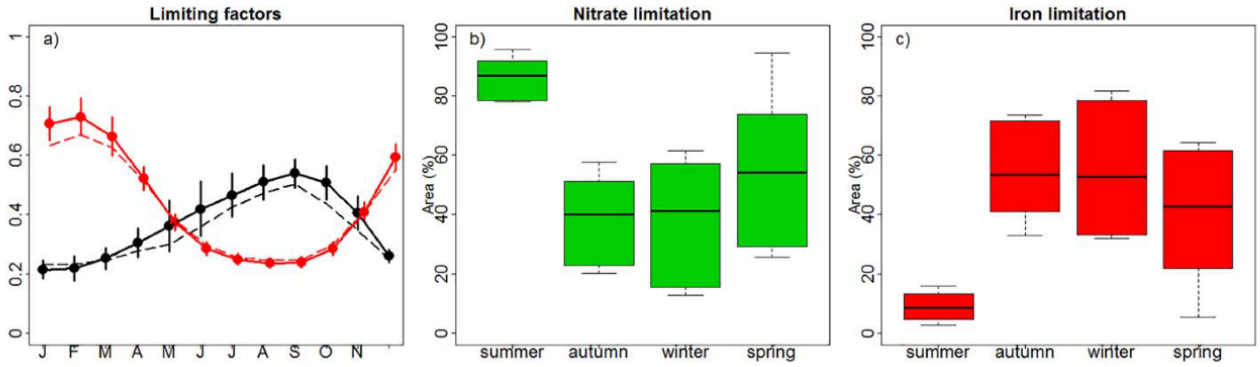

Figure 15. (a) Seasonal cycle of diatoms growth limiting factors during EN (dashed line) and neutral period (thick line). Light limitation is marked in red; nutrient in black. Error bars represent standard deviation. Values were averaged in the mixed layer and in a coastal band. Values close to 1 indicate weak limitation. Seasonal cycle of (b) nitrate and (c) iron limitation for diatoms. The % of limitation was computed as the ratio between the number of pixels with nutrient (nitrate or iron) limitation and the total number of pixels in the coastal band (see Figure 1).

associated with both negative and positive wind-driven upwelling anomalies, but also that anomalous subsurface hydrographic structures may change the canonical relationship between upwelling, nutrient flux and Chl response. In spite of the wind increase during EN [e.g., *Bakun et al.*, 1973; *Enfield*, 1981; *Bakun et al.* 2010; *Kessler*, 2006], a positive correlation between coastal upwelling and alongshore wind stress was only found during summer-early autumn. During the rest of the year, our model reproduced an upwelling decrease despite the wind stress intensification, due to a compensation of the upwelling by an onshore geostrophic flow [*Colas et al.*, 2008; *Marchesiello and Estrade*, 2010]. *Carr et al.* [2002] computed an upwelling index based on the difference between coastal and oceanic SST, which indicated a decrease in upwelling during El Nino north of 15°S. The shutdown of the upwelling during EN was also mentioned by *Zuta and Guillén* [1970], and by *Huyer et al.* [1987] from the observation of cross-shore sections of temperature during 1982–1983 at 10°S.

The decoupling between upwelling-favorable winds and vertical flux during EN was studied by *Huyer et al.* [1987] and by *Colas et al.* [2008]. They showed that the enhanced wind-driven upwelling during EN was partly compensated by an onshore geostrophic flow driven by an alongshore sea-level gradient. To document this process in our simulation, we computed the zonal geostrophic current (u_g) at ~200 km from the coast between 6°S and 16°S and compared it with the surface u_g derived from AVISO data. The zonal geostrophic current presented positives anomalies not only during the 1982–1983 and 1997–1998 events but also during the other EN events in the simulation period (Figure 16a). The compensating current was strong in winter and spring, and weaker or nonexistent in summer (Figure 16b). This explains the EN positive vertical flux forced by enhanced upwelling-favorable winds in summer (Figures 9a and 9c).

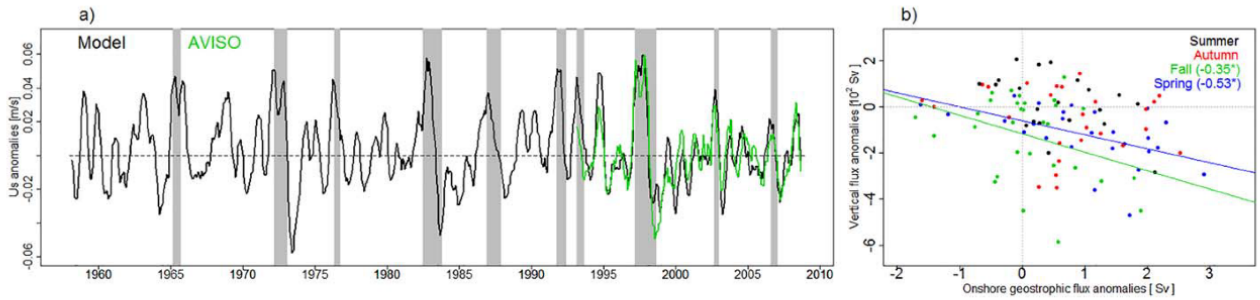

Figure 16. Time series of geostrophic zonal surface currents (in m.s $^{-1}$) derived from the model (black line) and AVISO (green line) sea level. (a) Spatial averaging was performed between 6°S–16°S and 150–200 km from the coast. (b) Scatterplot of the monthly vertical flux anomalies (at 20 m depth) and onshore geostrophic flux anomalies (for 20 m thick surface layer) during EN. Colors and lines represent seasons and significant linear regression, respectively.

AGU Journal of Geophysical Research: Oceans 10.1002/2016JC012439

4.4. Changes in SW During EN

Using a simplified one-dimensional model, *Carr* [2003] hypothesized that the wind-driven upwelling increase during EN may induce a SW deepening and stimulate favorably planktonic growth. In contrast, our results suggested that the SW depth near the upwelling region (e.g., 1 month before they are upwelled) did not exhibit significant changes during EN, in line with *Huyer et al.* [1987].

However, SW characteristics were modified in the equatorial region (88°W), months before being upwelled. During moderate EN events, the SW nutrient content and depth were not significantly different from those during the neutral period, while during extreme events SW were shallower and nutrient-poorer. These differences are likely to be related to the different duration of EN periods as well as regional circulation changes. As a moderate EN event spanned on average ~8 months, the SW at 88°W did not undergo a depressed nutricline typical of EN conditions in the equatorial region, because at the time of their departure from the equatorial region the event had not developed yet. Thus SW encountered a deep nutricline only in the nearshore region during the passage of the CTW. In contrast, during an extreme, much longer (~16 months) EN event, SW transited much more rapidly from 88°W to the upwelling region, and their characteristics (e.g., low nutrient due to a anomalously deep nutricline) were modified in the equatorial region as EN conditions (e.g., deeper nutricline) had fully developed.

4.5. Eddy-Driven Nutrient Subduction During EN

Mesoscale turbulence generated by the alongshore currents instabilities modulates nearshore turbulent fluxes of nutrients and plankton in upwelling systems [e.g., *Lathuilière et al.*, 2010; *Gruber et al.*, 2011; *Renault et al.*, 2016]. Using an eddy-resolving biophysical coupled model coupled in the California Current System, *Gruber et al.* [2011] evidenced coastal nitrate loss by eddy-driven offshore transport and subduction. This process reduces the nearshore primary production due to offshore and downward transport of phytoplankton and upwelled nutrients. In particular, the net effect of downward eddy flux in the offshore region is to deplete the upwelling SW and thus to reduce the coastal productivity. Offshore transport of nutrients within eddy cores [*Stramma et al.*, 2013] and subduction of newly upwelled in submesoscale cold filaments [*Thomsen et al.*, 2016] were previously evidenced in the PCUS. Our results show that the percentage of the nitrate vertical eddy flux with respect to the mean vertical nutrient flux increased during EN. However, the magnitude of the nitrate vertical eddy flux could be underestimated due to the relatively low horizontal resolution (1/6°) of our model [e.g., *Capet et al.*, 2008; *Colas et al.*, 2012]. An underestimated subduction in our simulation could partly explain the overly high surface Chl (Figures 3p and 3q).

Note that in spite of its relatively low resolution, our model represented correctly the spatial (supporting information Figure S5) and interannual (Figure 12a) variability of the EKE. A resolution of 1/6° is eddy-resolving off Peru due to its proximity to the equator, as the typical length scale of mesoscale structures would be covered by ~10 grid points [*Belmadani et al.*, 2012]. Nevertheless, more modeling studies with an increased spatial resolution would be needed to better understand and quantify the role of submesoscale variability on surface productivity off Peru.

5. Conclusions

The main physical and biogeochemical processes acting on the development of phytoplankton biomass off Peru during EN were studied using a three-dimensional, eddy-resolving, coupled physical-biogeochemical regional model, evaluated with in situ and satellite observations. The model was able to reproduce the main characteristics of several EN events (extreme and moderate) occurring between 1958 and 2008: the temperature and sea level increase, the thermocline/nutricline deepening, and the phytoplankton (mainly diatoms) and nutrient concentration decrease along the Peruvian coast.

During EN periods, coastal upwelling intensified (mainly in summer-fall) due to a nearshore wind stress increase, but was partly compensated by an onshore geostrophic flow associated with an alongshore sea-level gradient in winter and spring. CTW propagating along the coast increased dramatically the depth of thermocline and nutricline, particularly in late spring-early summer. Consequently, the nitrate vertical flux into the surface layer decreased, except in summer-early autumn when the subsurface nitrate decrease was mitigated by the wind-driven upwelling increase. In our simulations, the Chl decrease during summer was

AGU Journal of Geophysical Research: Oceans 10.1002/2016JC012439

thus mainly attributed to an increase of light limitation related with a deepening of the mixed layer, while it was caused by nutrient depletion during the other seasons.

The nutrient (nitrate and iron) content of the upwelling source waters strongly decreased in summer-autumn in the region of upwelling during EN, while their depth was little modified. In the equatorial region away from the coasts, the source water properties did not change during neutral, EN moderate, and LN periods, while during extreme EN events their nutrient content was lower (20%) in relation to the longer duration of these events. This sequence of events could be modified under intensified surface warming (e.g., related to regional climate change) as the annual mean upwelling intensity could decrease and source waters may shoal due to much stronger changes in stratification than those occurring during EN [*Oerder et al.* 2015].

The impact of EN events depended of their intensity. Extreme EN affected the structure of the water column and the Chl surface concentration more than moderate events. The impact of LN was opposite and much weaker than the impact of EN.

During EN events mesoscale turbulence was stronger, which played a significant role in nutrient offshore transport and subduction. The nitrate vertical eddy flux with respect to the mean vertical nutrient flux increased during EN and was estimated in our simulation to be twice as large as during normal years. This could however be a lower bound considering the relatively low horizontal resolution of the model. A more accurate assessment of the role of eddy fluxes during EN will be performed in future work.

Acknowledgments

DEM was supported by an individual doctoral research grant from the IRD program "Allocations de Rercherche pour une Thèse au Sud" (ARTS). The authors acknowledge: AVISO for providing the altimeter products (www.aviso.oceanobs.com); SeaWIFS for the chlorophyll satellite data (oceancolor.gsfc.nasa.gov/cms/data/seawifs); NOAA for the satellital Pathfinder SST (www.nodc.noaa.gov/SatelliteData/pathfinder4km); CARS for in situ climatological nutrients data (www.marine.csiro.au/~dunn/cars2009); as well as the IMARPE for providing the in situ oceanographic data, which is available upon request to jledesma@imarpe.gob.pe, mgraco@imarpe.gob.pe, and lvasquez@imarpe.gob.pe. The ERSST.v4 data are provided by NOAA to compute ONI (El Nino 1 + 2) and downloaded from www.esrl.noaa.gov/psd/data/gridded/data.noaa.ersst.html. The model results are available upon request to despinoza@imarpe.gob.pe and vincent.echevin@ird.fr. Numerical simulations were performed on the ADA computer at IDRIS (project i2015011140). This work is a contribution from the cooperation agreement between the Instituto del Mar del Peru (IMARPE) and the Institut de Recherche pour le Développement (IRD), through the LMI DISCOH project. This work was developed in the framework of the BID project "Adaptation to Climate Change Project of the Fisheries Sector and Coastal Marine Ecosystem-Peru."

References

Albert, A., V. Echevin, M. Lévy, and O. Aumont (2010), Impact of nearshore wind stress curl on coastal circulation and primary productivity in the Peru upwelling system, *J. Geophys. Res.*, *115*, C12033, doi:10.1029/2010JC006569.

Alheit, J., and M. Ñiquen (2004), Regime shifts in the Humboldt Current ecosystem, *Prog. Oceangr.*, *60*, 201–222, doi:10.1016/j.pocean.2004.02.006.

Arntz, W. E., V. A. Gallardo, D. Gutïerrez, E. Isla, L. A. Levin, J. Mendo, C. Neir, G. T. Rowe, J. Tarazona, and M. Wolff (2006), El Nino and similar perturbation effects on the benthos of the Humboldt, California, and Benguela Current upwelling ecosystems, *Adv. Geosci.*, *6*, 243–265.

Aumont, O., and L. Bopp (2006), Globalizing results from ocean in situ iron fertilization studies. *Global Biogeochem. Cycles*, *20*, GB2017, doi:10.1029/2005GB002591.

Aumont, O., C. Ethé, A. Tagliabue, L. Bopp, and M. Gehlen (2015), PISCES-v2: An ocean biogeochemical model for carbon and ecosystem studies, *Geosci. Model Dev.*, *8*, 2465–2513, doi:10.5194/gmd-8-2465-2015.

Ayón, P., M. I. Criales-Hernandez, R. Schwamborn, and H. -J. Hirche (2008a), Zooplankton research off Peru: A review, *Prog. Oceanogr.*, *79*, 238–255, doi:10.1016/j.pocean.200810.020.

Ayón, P., G. Swartzman, A. Bertrand, M. Gutiérrez, and S. Bertrand (2008b), Zooplankton and forage fish species off Peru: Large-scale bottom-up forcing and local-scale depletion, *Prog. Oceanogr.*, *79*, 208–214, doi:10.1016/j.pocean.200810.023.

Bakun, A. (1973), Coastal upwelling indices, west coast of North America, 1946–71, *NOAA Tech. Rep., NMFS SSRF-671*, 103 pp., U.S. Dep. of Commer., Wash.

Bakun, A., D. B. Field, A. Redondo-Rodriguez, and S. J. Weeks (2010), Greenhouse gas, upwelling-favorable winds, and the future of coastal ocean upwelling ecosystems, *Global Change Biol.*, *16*, 1213–1228, doi:10.1111/j.1365-2486.2009.02094.x.

Barber, R. T., and F. P. Chavez (1983), Biological consequences of El Niño, *Science*, *222*, 1203–1210, doi:10.1126/science.222.4629.1203.

Belmadani, A., V. Echevin, B. Dewitte, and F. Colas, (2012), Equatorially forced intraseasonal propagations along the Peru–Chile coast and their relation with the nearshore eddy activity in 1992–2000: A modeling study, *J. Geophys. Res.*, *117*, C04025, doi:10.1029/2011JC007848.

Bouchón, M., and C., Peña (2008), Impactos de los eventos La Niña en la pesquería peruana, *Inf. Inst. Mar Perú.*, *35*(3), 193–198.

Bruland, K. W., E. L. Rue, G. J. Smith, and G. R. DiTullio (2005), Iron, macronutrients and diatom blooms in the Peru upwelling regime: Brown and blue waters of Peru, *Mar. Chem.*, *93*, 81–103.

Buitenhuis, E., C. Le Quéré, O. Aumont, G. Beaugrand, A. Bunker, A. Hirst, T. Ikeda, T. O'Brien, S. Piontkovski, and D. Straile (2006), Biogeochemical fluxes through mesozooplankton, *Global Biogeochem. Cycles*, *20*, GB2003, doi:10.1029/2005GB002511.

Calienes, R. (2014), Producción primaria en el ambiente marino en el Pacífico sudeste, Perú, 1960–2000, *Bol. Inst. Mar Perú*, *29*(1–2), 232–288.

Carr, M.-E. (2003), Simulation of carbon pathways in the planktonic ecosystem off Peru during the 1997–1998 El Niño and La Niña, *J. Geophys. Res.*, *108*(C12), 3380, doi:10.1029/1999JC000064.

Carr, M.-E., P. T. Strub, A. C. Thomas, and J. L. Blanco (2002), Evolution of 1996–1999 La Niña and El Niño conditions off the western coast of South America: A remote sensing perspective, *J. Geophys. Res.*, *107*(C12), 3236, doi:10.1029/2001JC001183.

Capet, X., J. C. McWilliams, M. J. Molemaker, and A. F. Shchepetkin (2008), Mesoscale to submesoscale transition in the California Current System. Part I: Flow structure, eddy flux, and observational tests, *J. Phys. Oceanogr.*, *38*(1), 29–43.

Capet, X. J., P. Marchesiello, and J. C. McWilliams (2004), Upwelling response to coastal wind profiles, *Geophys. Res. Lett.*, *31*, L13311, doi:10.1029/2004GL02123.

Carton, J. A., and B. Giese (2008), A Reanalysis of Ocean Climate Using Simple Ocean Data Assimilation (SODA), *Mon. Weather Rev.*, *136*, 2999–3017.

Casey, K. S., T. B. Brandon, P. Cornillon, and R. Evans (2010), The past, present and future of the AVHRR Pathfinder SST Program, in *Oceanography from Space: Revisited*, edited by V. Barale, J. F. R. Gower, and L. Alberotanza, Springer, Dordrecht, Heidelberg, London, New York, doi:10.1007/978-90-481-8681-5_16.

Chaigneau, A., G. Arnaud Gizolme, and C. Grados (2008), Mesoscale eddies off Peru in altimeter records: Identification algorithms and eddy spatio-temporal patterns, *Prog. Oceanogr.*, *79*, 106–119, doi:10.1016/j.pocean.2008.10.013.

Chavez, F., and M. Messié (2009), A comparison of Eastern Boundary Upwelling Ecosystems, *Prog. Oceanogr.*, *83*, 80–96, doi:10.1016/j.pocean.2009.07.032.

AGU Journal of Geophysical Research: Oceans 10.1002/2016JC012439

Chavez, F., A. Bertrand, R. Guevara-Carrasco, P. Soler, and J. Csirke (2008), The northern Humboldt Current System: Brief history, present status and a view towards the future, *Prog. Oceanogr.*, *79*, 95–105, doi:10.1016/j.pocean.2008.10.012.

Colas, F., X. Capet, J. C. McWilliams, and A. Shchepetkin (2008), 1997–98 El Niño off Peru: A numerical study, *Prog. Oceanogr.*, *79*, 138–155.

Colas, F., J. C. McWilliams, X. Capet, and J. Kurian (2012), Heat balance and eddies in the Peru-Chile current system, *Clim. Dyn.*, *39*, 509–529, doi:10.1007/s00382-011-1170-6.

Colas, F., X. Capet, J. C. McWilliams, and Z. Li (2013), Mesoscale eddy buoyancy flux and eddy-induced circulation in eastern boundary currents, *J. Phys. Oceanogr.*, *43*, 1073–1095, doi:10.1175/JPO-D-11-0241.

Conkright, M., R. Locarnini, H. Garcia, T. D. O'Brien, T. P. Boyer, C. Stephens, and J Antononov (2002), World Ocean Atlas 2001: Objectives, analyses, data statistics and figures [CD-ROM], *NOAA Atlas NESDIS 42*, Int. Report 17, Silver Spring, Md.

Da Silva, A. M., C. C. Young, and S. Levitus (1994), Atlas of surface marina data 1994, technical report, Natl. Oceanogr. And Atmos. Admin, Silver Spring, Md.

Echevin, V., O. Aumont, J. Ledesma, and G. Flores (2008), The seasonal cycle of surface chlorophyll in the Peruvian upwelling system: A model study, *Prog. Oceanogr.*, *79*, 167–176.

Echevin, V., F. Colas, A. Chaigneau, and P. Penven (2011), Sensitivity of the Northern Humboldt Current System nearshore modeled circulation to initial and boundary conditions, *J. Geophys. Res.*, *116*, C07002, doi:10.1029/2010JC006684.

Echevin, V., A. Albert, M. Lévy, O. Aumont, M. Graco, and G. Garric, (2014), Remotely-forced intraseasonal variability of the Northern Humboldt Current System surface chlorophyll using a coupled physical-ecosystem model, *Cont. Shelf Res.*, *73*, 14–30, doi:10.1016/j.csr.2013.11.015.

Enfield, D. B. (1981), Thermally driven wind variability in the planetary boundary layer above Lima, Peru, *J. Geophys. Res.*, *86*(C3), 2005–2016, doi:10.1029/JC086iCO3p02005.

Goubanova, K., V. Echevin, B. Dewitte, F. Codron, K. Takahashi, P. Terray, and M. Vrac (2011), Statistical downscaling of sea-surface wind over the Peru-Chile upwelling region: Diagnosing the impact of climate change from the IPSL-CM4 model, *Clim. Dyn.*, *36*, 1365, doi:10.1007/s00382-010-0824-0.

Graco, M., J. Ledesma, G. Flores, and M. Girón (2007), Nutrientes, oxígeno y procesos biogeoquímicos en el sistema de surgencias de la corriente de Humboldt frente a Perú, *Rev. Per. Biol.*, *14*(1), 117–128.

Graco, M., S. Purca, B. Dewitte, O. Morón, J. Ledesma, G. Flores, C. Castro, and D. Gutiérrez (2016), The OMZ and nutrients features as a signature of interannual and low frequency variability off the peruvian upwelling system, *Biogeosci. Discuss.*, doi:10.5194/bg-2015-567, in press.

Gruber, N., Z. Lachkar, H. Frenzel, P. Marchesiello, M. Munnich, J. McWilliams, T. Nagai, and G. Plattner (2011), Eddy-induced reduction of biological production in eastern boundary upwelling systems, *Nat. Geosci.*, *4*, 787–792.

Gutiérrez, D., et al. (2011), Coastal cooling and increased productivity in the main upwelling zone off Peru since the mid-twentieth century, *Geophys. Res. Lett.*, *38*, L07603, doi:10.1029/2010GL046324.

Gutiérrez, D., M. Akester, and L. Naranjo (2016), Productivity and Sustainable Management of the Humboldt Current Large Marine Ecosystem under climate change, *Environ. Dev.*, *17*, 126–144, doi:10.1016/j.envdev.2015.11.004.

Halpern, D. (2002), Offshore Ekman transport and Ekman pumping off Peru during the 1997–1998 El Niño, *Geophys. Res. Lett.*, *29*(5), 1075, doi:10.1029/2001GL014097.

Hernandez, O., P. Lehodey, I. Senina, V. Echevin, P. Ayón, A. Bertrand, and P. Gaspar (2014), Understanding mechanisms that control fish spawning and larval recruitment: Parameter optimization of an Eulerian model (SEAPODYM-SP) with Peruvian anchovy and sardine eggs and larvae data, *Prog. Oceanogr.*, *123*, 105–122.

Huang, B., V. F. Banzon, E. Freeman, J. Lawrimore, W. Liu, T. C. Peterson, T. M. Smith, P. W. Thorne, S. D. Woodruff, and H. -M. Zhang (2015), Extended Reconstructed Sea Surface Temperature version 4 (ERSST.v4): Part I. Upgrades and intercomparisons, *J. Clim.*, *28*, 911–930, doi:10.1175/JCLI-D-14-00006.1.

Hutchins, D. A., et al. (2002), Phytoplankton iron limitation in the Humboldt Current and Peru Upwelling, *Limnol. Oceanogr.*, *47*, 997–1011, doi:10.4319/lo.2002.47.4.0997.

Huyer, A., R. L. Smith, and T. Paluszkiewicz (1987), Coastal upwelling off Peru during normal and El Niño times, *J. Geophys. Res.*, *92*(C13), 14,297–14,307, doi:10.1029/JC092iC13p14297.

Huyer, A., M. Knoll, T. Paluszkiewic, and R. L. Smith (1991), The Peru Undercurrent: A study of variability, *Deep Sea Res., Part A*, *38*, S247–S271.

Irwin, A. J., Z. B. Finkel, O. M. E.Schofield, and P. G. Falkowsky (2006), Scaling-up from nutrient physiology to the size-structure of phytoplankton communities, *J. Plankton Res.*, *28*(5), 459–471, doi:10.1093/plankt/fbi148.

Kahru, M., B. G. Mitchell, A. Diaz, and M. Miura (2004), MODIS Detects a Devastating Algal Bloom in Paracas Bay, Peru. *Eos Trans. AGU.*, *85*(45), 465–472, doi:10.1029/2004EO450002.

Kessler, W. S. (2006), The circulation of the eastern tropical Pacific: A review, *Prog. Oceanogr.*, *69*, 181–217.

Kessler, W. S., and M. J. McPhaden (1995), Oceanic equatorial waves and the 1991–1993 El Niño, *J. Clim.*, *8*, 1757–1774.

Lachkar, Z., and N. Gruber (2012), A comparative study of biological production in eastern boundary upwelling systems using an artificial neural network, *Biogeosciences*, *9*, 293–308, doi:10.5194/bg-9-293-2012.

Lathuilière, C., V. Echevin, M. Lévy, and G. Madec (2010), On the role of the mesoscale circulation on an idealized coastal upwelling ecosystem, *J. Geophys. Res.*, *115*, C09018, doi:10.1029/2009JC005827.

Lefort, S., O. Aumont O., L. Bopp, T. Arsouze, M. Gehlen, and O. Maury (2015), Spatial and body-size dependent response of marine pelagic communities to projected global climate change, *Global Change Biol.*, *21*(1), 154–164.

Liu, W., K. B. Katsaros, and J. A. Businger (1979), Bulk parameterization of the air-sea exchange of heat and water vapor including the molecular constraints at the interface, *J. Atmos. Sci.*, *36*, 1722–1735.

Marchesiello, P., and P. Estrade (2010), Upwelling limitation by onshore geostrophic flow, *J. Mar. Res.*, *68*, 37–62, doi:10.1357/002224010793079004.

McWilliams, J. C. (2016), Submesoscale currents in the ocean, *Proc. R. Soc. A*, *472*, 20160117, doi:10.1098/rspa.2016.0117.

Messié, M., and F. P. Chavez (2015), Seasonal regulation of primary production in eastern boundary upwelling systems, *Prog. Oceanogr.*, *134*, 1–18, doi:10.1016/j.pocean.2014.10.011.

Montes, I., F. Colas, X. Capet, and W. Schneider (2010), On the pathways of the equatorial subsurface currents in the eastern equatorial Pacific and their contributions to the Peru-Chile Undercurrent, *J. Geophys. Res.*, *115*, C09003, doi:10.1029/2009JC005710.

Montes, I., S. Wolfgang, F. Colas, B. Blanke, and V. Echevin (2011), Subsurface connections in the eastern tropical Pacific during La Niña 1999–2001 and El Niño 2002–2003, *J. Geophys. Res.*, *116*, C12022, doi:10.1029/2011JC007624.

Morón, O. (2000), Características del ambiente marino frente a la costa peruana, *Bol. Inst. Mar Perú*, *19*(1–2), 179–204.

Ñiquen, M., and M. Bouchón (2004), Impact of El Niño event on pelagic fisheries in Peruvian waters, *Deep Sea Res., Part II*, *51*, 563–574, doi: 10.1016/j.dsr2.2004.03.001.
Oerder, V., F. Colas, V. Echevin, F. Codron, J. Tam, and A. Belmadani (2015), Peru-Chile upwelling dynamics under climate change, *J. Geophys. Res. Oceans*, *120*, 1152–1172, doi:10.1002/2014JC010299.
OReilly, J. E., S. Maritorena, B. G. Mitchell, D. A. Siegel, K. L. Carder, S. A. Garver, M. Kharu, and C. McClain (1998), Ocean color chlorophyll algorithms for SeaWIFS, *J. Geophys. Res.*, *103*(C11), 24,937–24,953, doi:10.1029/98JC02160.
Paulmier, A., D. Ruiz-Pino, V. Garçon, and L. Farías (2006), Maintaining of the Eastern South Pacific Oxygen Minimum Zone (OMZ) off Chile, *Geophys. Res. Lett.*, *33*, L20601, doi:10.1029/2006GL026801.
Pennington, J. T., K. L. Mahoney, V. S. Kuwahara, D. D. Kolver, R. Calienes, and F. P. Chavez (2006), Primary production in the eastern tropical Pacific: A review, *Prog. Oceanogr.*, *69*, 285–317, doi:10.1016/j.pocean.2006.03.012.
Penven, P., P. Marchesiello, L. Debreu, and J. Lefèvre (2008), Software tools for pre- and post-processing of oceanic regional simulations, *Environ. Modell. Software*, *23*, 660–662, doi:10.1016/j.envsoft.2007.07.004.
Picaut, J., M. Ioualalen, C. Menkes, T. Delcroix, and M. J. McPhaden (1996), Mechanisms of the zonal displacements of the Pacific warm pool: Implications for ENSO, *Science*, *274*, 1486–1489, doi:10.1126/science.274.5292.1486.
Picaut J., E. Hackert, A. J. Busalacchi, R. Murtugudde and G. S. E. Lagerloef (2002), Mechanisms of the 1997–1998 El Niño–La Niña, as inferred from space-based observations, *J. Geophys. Res.*, *107*(C5), 3037, doi: 10.1029/2001JC000850.
Renault, L., C. Deutsch, J. C. McWilliams, H. Frenzel, J.-H. Liang, and F. Colas (2016), Partial decoupling of primary productivity from upwelling in the California Current system, *Nature*, *46*, 273–289.
Ridgway, K. R., J. R. Dunn, and J. L. Wilkin (2002), Ocean interpolation by four-dimensional least squares-Application to the waters around Australia, *J. Atmos. Oceanic Technol.*, *19*(9), 1357–1375.
Risien, C. M., and D. B. Chelton (2008), A Global Climatology of Surface Wind and Wind Stress Fields from Eight Years of QuikSCAT Scatterometer Data, *J. Phys. Oceanogr.*, *38*, 2379–2413.
Sánchez, S. (2000), Variación estacional e interanual de la biomasa fitoplanctónica y concentraciones de clorofila frente a la costa peruana durante 1976–2000, *Bol. Inst. Mar Perú*, *19*(1–2), 29–43.
Shchepetkin, A. F., and J. C. McWilliams (1998), Quasi-monotone advection schemes based on explicit locally adaptive dissipation, *Mon. Weather Rev.*, *126*, 1541–1580.
Shchepetkin, A. F. and McWilliams J.C. (2005), The regional oceanic modeling system: A split-explicit, free-surface, topography-following-coordinate ocean model, *Ocean Modell.*, *9*, 347–404.
Shchepetkin, A. F. and J. C. McWilliams (2009), Computational kernel algorithms for fine-scale, multiprocess, longtime oceanic simulations, *Handb. Numer. Anal.*, *14*, 121–183, doi: 10.1016/S1570-8659(08)01202-0.
Smith, W. H. F., and D. T. Sandwell (1997), Global sea floor topography from satellite altimetry and ship depth soundings, *Science*, *277*, 1957–1962.
Stramma, L., H. W. Bange, R. Czeschel, A. Lorenzo, and M. Frank (2013), On the role of mesoscale eddies for the biological productivity and biogeochemistry in the eastern tropical Pacific Ocean off Peru, *Biogeosciences*, *10*, 7293–7306, doi:10.5194/bg-10-7293-2013.
Sunda, W. G., and S. A. Huntsman (1997), Interrelated influence of iron, light and cell size on marine phytoplankton growth, *Nature*, *390*, 389–392.
Takahashi, K., A. Montecinos, K. Goubanova, and B. Dewitte (2011), ENSO regimes: Reinterpreting the canonical and Modoki El Niño, *Geophys. Res. Lett.*, *38*, L10704, doi:10.1029/2011GL047364.
Tam, J., et al. (2008), Trophic modeling of the Northern Humboldt Current Ecosystem, Part I: Comparing trophic linkages under La Niña and El Niño conditions, *Prog. Oceanogr.*, *79*, 352–365, doi:10.1016/j.pocean.2008.10.007.
Tarazona, J., and W. Arntz (2001), The Peruvian Coastal Upwelling System, *Coastal Mar. Ecosyst. Latin Am.*, *144*, 229–244, doi:10.1007/978-3-662-04482-7_17.
Thomas, A. C., M. E. Carr, and P. T. Strub (2001), Chlorophyll variability in eastern boundary currents, *Geophys. Res. Lett.*, *28*(18), 3421–3424, doi:10.1029/2001GL013368.
Thomas, A. C., P. Brickley, and R. Weatherbee (2009), Interannual variability in chlorophyll concentrations in the Humboldt and California Current Systems, *Prog. Oceanogr.*, *83*, 386–392, doi:10.1016/j.pocean.2009.07.020.
Thomsen, S., T. Kanzow, F. Colas, V. Echevin, G. Krahmann, and A. Engel (2016), Do submesoscale frontal processes ventilate the oxygen minimum zone off Peru?, *Geophys. Res. Lett.*, *43*, 8133–8142, doi:10.1002/2016GL070548.
Tovar, H., and D. Cabrera (1985), Las aves guaneras y el fenómeno "El Niño", in *El fenómeno "El Niño" y su impacto en la fauna marina, extraordinary* vol. 181–186, edited by W. F. Arntz, A. Landa, and J. Tarazona, Bol. Inst. Mar Perú, Callao, Peru.
Travers, M., Y. J. Shin, S. Jennings, E. Machu, J. A. Huggett, J. G. Field, and P. Cury (2009), Two-way coupling versus one-way forcing of plankton and fish models to predict ecosystem changes in the Benguela, *Ecol. Modell.*, *220*(21), 3089–3099, doi:10.1016/j.ecolmodel.2009.08.016.
Tsuchiya, M. (1975), Subsurface countercurrents in the eastern equatorial Pacific, *J. Mar. Res.*, *33*, 145–175.
Ulloa, O., R. Escribano, S. Hormazabal, R. A. Quiñones, R. R. González, and M. Ramos (2001), Evolution and biological effects of the 1997–98 El Niño in the upwelling ecosystem off northern Chile, *Geophys. Res. Lett.*, *28*(8), 1591–1594, doi:10.1029/2000GL011548.
Uppala, S. M., et al. (2005), The ERA-40 re-analysis, *Q. J. R. Meteorol. Soc.*, *131*, 2961–3012, doi:10.1256/qj.04.176.
Wood, R., et al. (2011), The VAMOS Ocean-Cloud-Atmosphere-Land Study Regional Experiment (VOCALS-REx): Goals, platforms, and field operations, *Atmos. Chem. Phys.*, *11*(2), 627–654, doi:10.5194/acp-11-627-2011.
Wyrtki, K (1967), Circulation and water masses in the eastern equatorial Pacific Ocean, *Int. J. Oceanol. Limnol.*, *1*, 117–147.
Zuta, S., and O. G. Guillén (1970), Oceanografía de las aguas costeras del Perú, *Bol. Inst. Mar Perú*, *2*, 157–324.

Journal Geophysical Research Oceans

Supporting Information for

Impacts of El Niño Events on the Peruvian Upwelling System Productivity

Espinoza-Morriberón D.[a,b], V. Echevin[b], F. Colas[b], J. Tam[a], J. Ledesma[a], L. Vásquez[a], M. Graco[a]

[a]Instituto del Mar del Peru (IMARPE), Esquina general Gamarra y Valle, Callao, Peru, [b]UMR LOCEAN, IRD/Sorbonne Universités (UPMC Univ Paris 06)/CNRS/MNHN, 4 Place Jussieu, Paris Cedex 75252, France.

Contents of this file

Figures S1 to S5

Introduction

This supporting information provides figures in order to support the validation of the model used in the study: Fig.S1 shows the validation of the seasonal variation of the surface chlorophyll of the model with respect to satellite and *in situ* data. Besides, the comparison between Chl anomalies from the model and SeaIWFS during EN 1997-98 is shown;

Fig.S2 shows the Coastal Trapped Wave (CTW) sea level signal during two extreme El Niño in order to demonstrate that the alongshore propagations reproduced by the model result from Equatorial Kelvin Waves reaching the South American coasts and triggering CTWs.

Fig.S3 shows the increase of the mixed layer depth (MLD) during EN, which plays an important role in the light limitation. Note that the MLD mainly increases during summer – winter.

Fig.S4 displays results from a different model simulation (RPOrca), in particular the nitrate content and phytoplankton growth limitation terms during EN. The simulation RPOrca has reduced subsurface nitrate concentrations than the one (RPSoda) presented in the manuscript. RPOrca has a negative nutrient bias of ~ -5 $\mu mol.l^{-1}$ with respect to our simulation. It reproduced the decrease of nitrate concentration during in the same proportion as RPSoda. The same seasonality for nutrient and light limitation are found during EN, but enhanced nitrate limitation is observed in summer, in contrast with RPSoda (Fig. 15a).

RPOrca had the same atmospheric forcing as RPSoda. Monthly outputs from an ORCA2-PISCES ocean global model (L.Bopp, pers. comm.) from 1958-2008 were used for both physical and biogeochemical interannual boundary conditions. ORCA2 had a spatial resolution

of 2° and 30-vertical levels. Its atmospheric forcing is constructed from various data sets (e.g., NCEP/NCAR for wind stress), see Aumont et al. [2015] for details.

Fig.S5 shows the Eddy Kinetic Energy during El Niño and neutral periods with respect to observational altimetry data from AVISO.

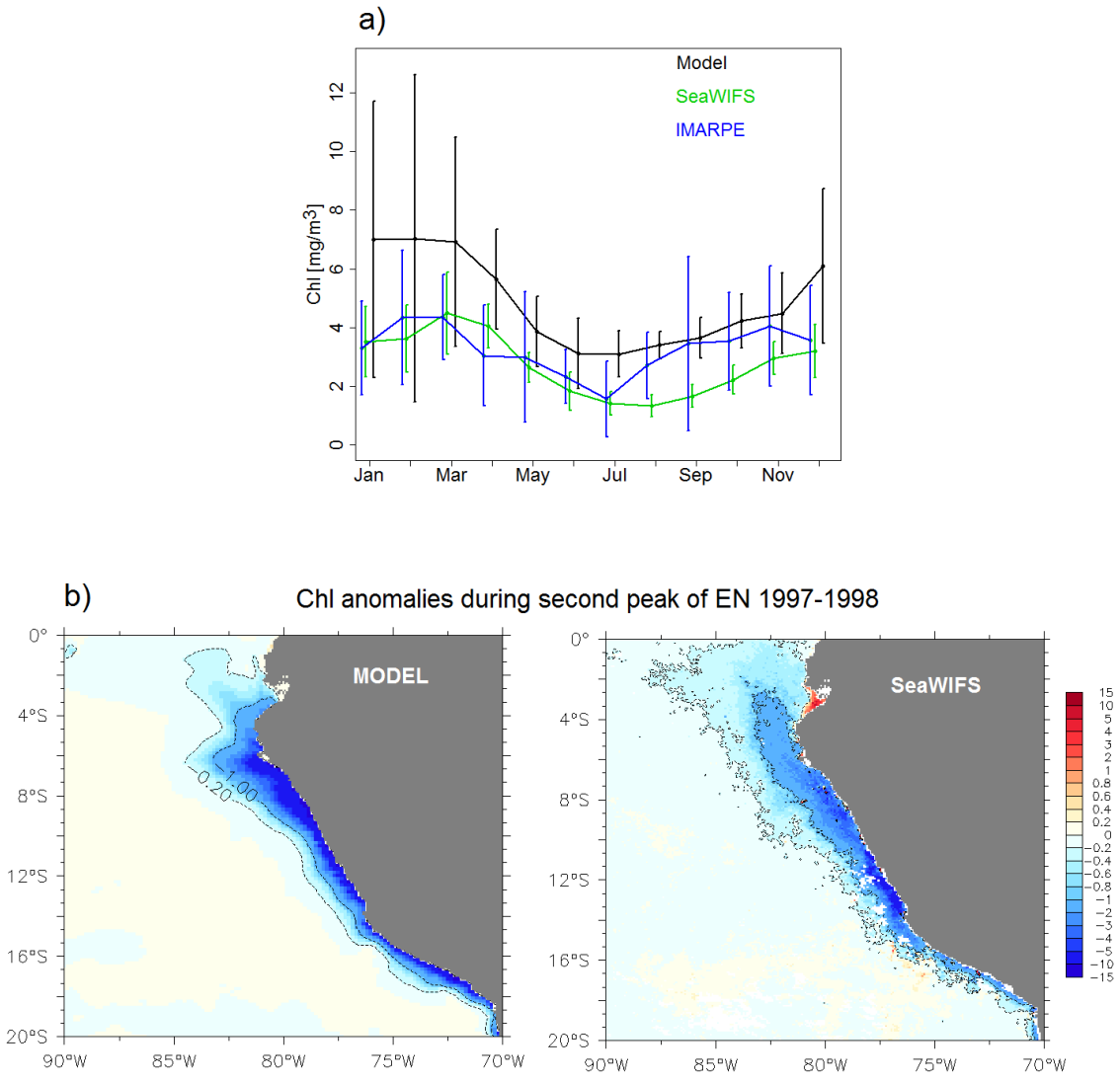

Figure S1. Monthly climatological Chl from IMARPE (blue lines), SeaWIFS (green lines) and model (black lines) in the coastal region. Error bars represent standard deviation associated with interannual variability. Mean Chl anomalies (in $mg.m^{-3}$) from model and SeaWIFS during the second peak of EN 1997-98 (Nov-Dec 1997) (b). In (b) isolines of -0.2 and -1 $mg.m^{-3}$ are plotted.

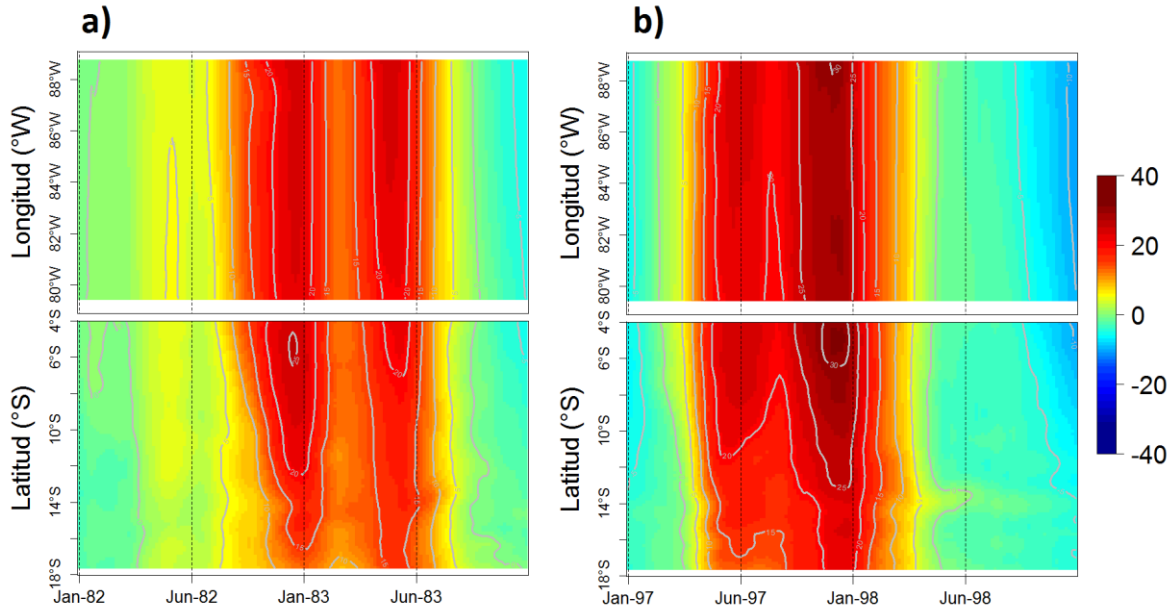

Figure S2. Hovmoller of longitude (top panel) and latitude (bottom panel) vs time for model sea level anomalies (cm) during the 1982-83 (a) and 1997-98 (b) EN events. Sea level was averaged between 0.5°N and 0.5°S in the top panels and between the coast and 100 km in the bottom panels. Sea level is filtered in time (60 days moving average) and space (100 km moving average).

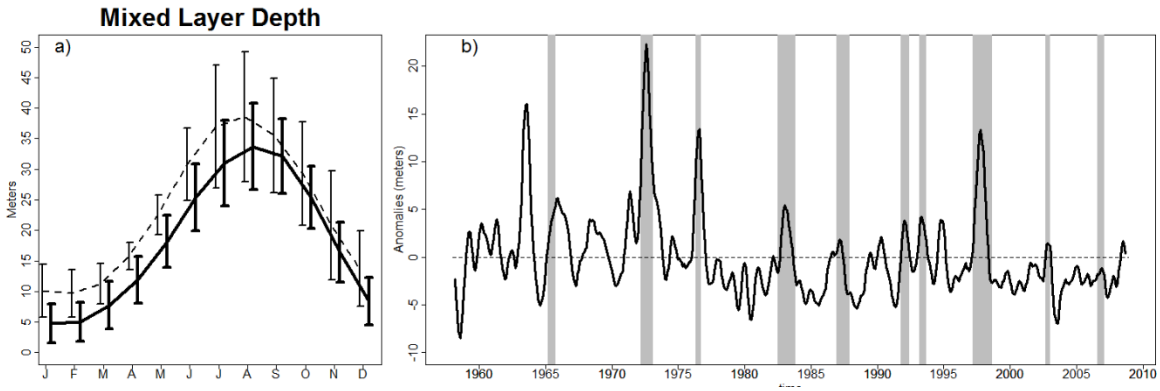

Figure S3. Seasonal cycle (a) and interannual time series of low-pass filtered anomalies (b) of mixed layer depth during neutral (thick line) and EN periods (dashed line). MLD is averaged between 6°S to 16°S and 100 km from the coast. Shadow boxes represent EN periods.

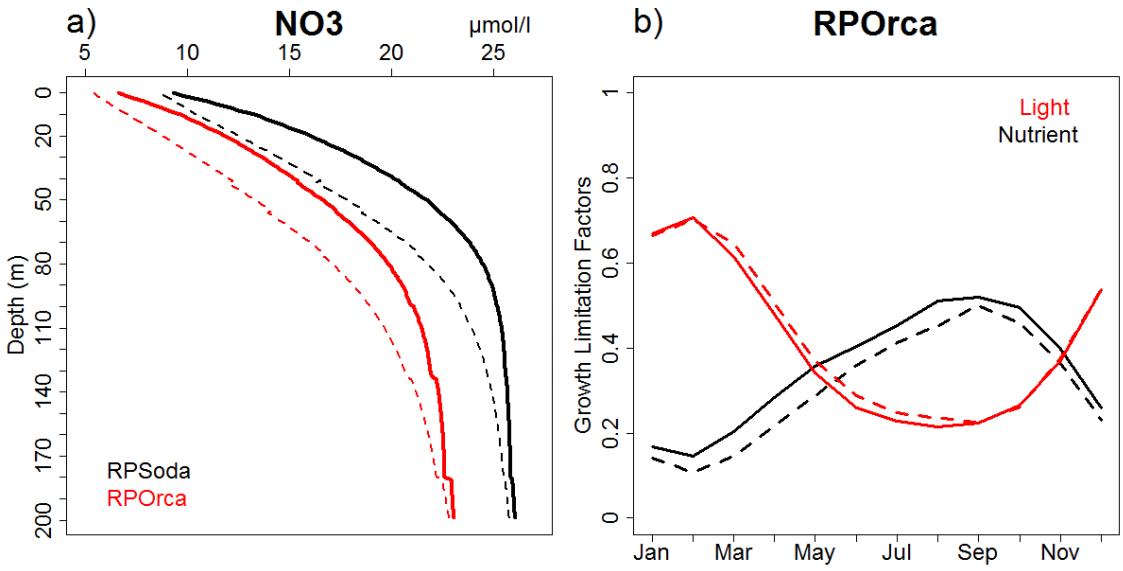

Figure S4. Annual mean of nitrate profile for RPOrca (red lines) and studied simulation (black lines) during EN (dashed lines) and neutral period (thick lines). In (a), to compute the profile we averaged the nitrate concentration between 6°S-16°S and from 200 km to the coast. Monthly climatology of diatoms growth limiting factors (b) during EN (dashed line) and neutral period (thick line) from RPOrca simulation. Light limitation is marked in red; nutrient in black. Values are averaged from the mixed layer to surface and in a coastal band (same criterion in Fig.15 in the main text). Values close to 1 indicate low limitation.

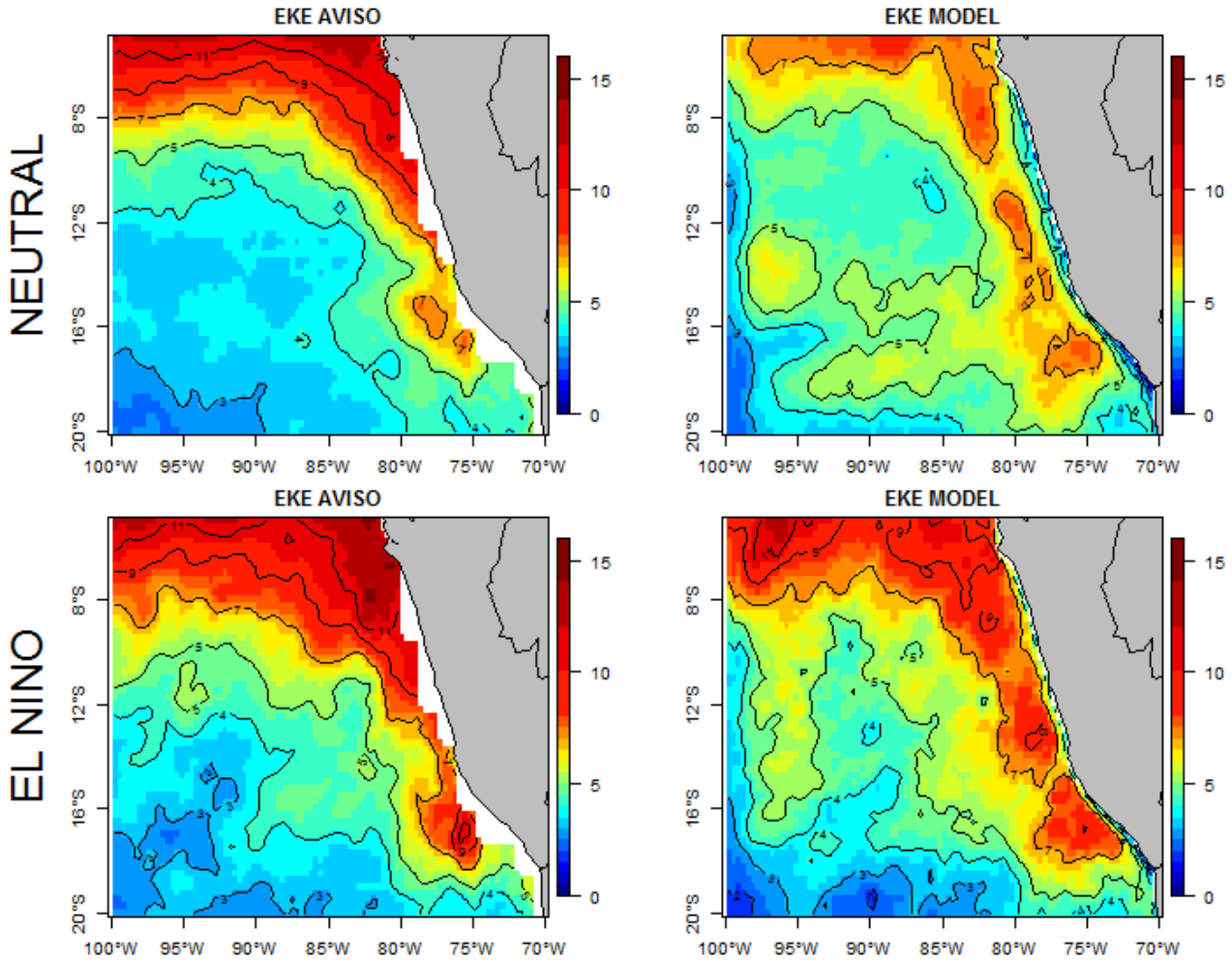

Figure S5. Mean eddy kinetic energy ($cm^2.s^{-2}$) during neutral (top panel) and EN periods (bottom panel) for AVISO data (left side) and model (right side). The 1993-2008 period is taken in account for the analysis.

CHAPTER 4:
IMPACTS OF EL NIÑO ON THE OXYGEN

Summary

The OMZ of the Tropical South Eastern Pacific is one of the most intense OMZ of the open ocean**.** At interannual time scales, the OMZ is mainly affected by El Niño (EN) and La Niña (LN). During EN, coastal-trapped waves (CTWs) propagate poleward and impact the vertical structure of physical and biogeochemical variables along the coasts of Peru. The water column becomes more oxygenated during EN and a deeper oxycline is observed, while during LN a shallower oxycline is described. The main goal of this chapter is to study the physical and biogeochemical processes involved in the OMZ variability during EN and LN phases. The hydrodynamics-biogeochemical ROMS-PISCES coupled model was run for the period 1958-2008 in order to simulate the OMZ variability. The model reproduces well the variability of the oxycline depth, however within the OMZ the model underestimates the observed concentration.

The passage of a downwelling and upwelling CTW during EN and LN trigger a deepening and shoaling of the oxycline, respectively. A high correlation is found between the depth of the isotherm and the oxycline in the nearshore region (~ 0.8), and drops offshore and south of 18°S, where the OMZ vanishes.

The equatorial source waters (SW) are mainly transported eastward by the secondary Tsuchiya jet and the EUC during LN and EN, respectively, before reaching the Peru coast. During EN the SW are more oxygenated as they originate from the north of the OMZ and transit faster to the coastal region than during LN.

Regarding the vertical eddy flux, it decreases during EN, while during LN it is not affected. The horizontal eddy flux tends to inject oxygen into the OMZ at its boundaries (mainly at the southern one). During EN, this horizontal eddy flux strongly increasesdue to the eddy activity increase, intensifying eddy-driven horizontal ventilation. However, during LN, it is not modified.

Remineralization is the main process consuming oxygen in the water column, followed by zooplankton respiration and nitrification. Nearshore, negative and positive anomalies predominate during LN and EN respectively, while ~ 30 km offshore and above 15 m, opposite sign patterns are found. Indeed, dissolved oxygen (DO) changes during LN and EN are influenced not only by physical processes but also by changes in DO production related to primary productivity changes above the upper limit of the OMZ, between 0 and ~ 20 m. The nearshore DO changes induces an oxygen increase (decrease) consumption by remineralization and respiration during EN (LN). Nitrification is enhanced at depth (50 – 150 m) due to DO availability during EN.

Sensitivity experiments performed to evaluate the influence of the equatorial remote (e.g. CTWs) and local forcing (e.g. wind), demonstrate that the equatorial remote forcing is the main driver of changes in the ZO2 and OMZ core during both EN and LN. During LN, the local wind fluctuations play a minor role, slightly increasing the ventilation of the surface layer and biological production of oxygen due to more upwelling and vertical mixing. During EN, the effect of the wind variability is slightly stronger: coastal upwelling is enhanced due to the alongshore wind increase associated to the SST warming, which partly compensates the ZO2 deepening driven by the downwelling CTWs.

There results have been submitted in a research paper in Frontiers in Marine Sciences in 2018, it is currently under revision (with very minor corrections asked by the reviewers and the editor). The paper is included below.

Oxygen variability during ENSO in the Tropical South Eastern Pacific

Dante Espinoza-Morriberón[1,2*], Vincent Echevin[2], Francois Colas[2], Jorge Tam[1], Dimitri Gutiérrez[1,3], Michelle Graco[1,3], Jesús Ledesma[1], Carlos Quispe-Ccalluari[1]

[1]Instituto del Mar del Peru (IMARPE), Esquina general Gamarra y Valle, Callao, Perú.
[2]Laboratoire d'Océanographie et de Climatologie: Expérimentation et Analyse Numérique (LOCEAN), Institut Pierre-Simon Laplace (IPSL), IRD/CNRS/UPMC/MNHN, 4 Place Jussieu, Case 100, 75252, Paris, France.
[3]Laboratorio de Ciencias del Mar, Universidad Peruana Cayetano Heredia, Lima, Perú. Corresponding Author: despinoza@imarpe.gob.pe

Abstract

The Oxygen Minimum Zone (OMZ) of the Tropical South Eastern Pacific (TSEP) is one of the most intensely deoxygenated water masses of the global ocean. It is strongly affected at interannual time scales by El Niño (EN) and La Niña (LN) due to its proximity to the equatorial Pacific. In this work, the physical and biogeochemical processes associated with the subsurface oxygen variability during EN and LN in the period 1958 – 2008 were studied using a regional coupled physical-biogeochemical model and *in situ* observations. The passage of intense remotely forced coastal trapped waves caused a strong deepening (shoaling) of the OMZ upper limit during EN (LN). A close correlation between the OMZ upper limit and thermocline depths was found close to the coast, highlighting the role of physical processes. The subsurface waters over the shelf and slope off central Peru had different origins depending on ENSO conditions. Offshore of the upwelling region (near 88°W), negative and positive oxygen subsurface anomalies were caused by Equatorial zonal circulation changes during LN and EN, respectively. The altered properties were then transported to the shelf and slope (above 200 m) by the Peru-Chile undercurrent. The source of nearshore oxygenated waters was located at 3°S – 4°S during neutral periods, further north (1°S – 1°N) during EN and further south (4°S – 5°S) during LN. The offshore deeper (< 200 – 300 m) OMZ was ventilated by waters originating from ~ 8°S during EN and LN. Enhanced mesoscale variability during EN also impacted OMZ ventilation through horizontal and vertical eddy fluxes. The vertical eddy flux decreased due to the reduced vertical gradient of oxygen in the surface layer, whereas horizontal eddy fluxes injected more oxygen into the OMZ through its meridional boundaries. In subsurface layers,

remineralization of organic matter, the main biogeochemical sink of oxygen, was higher during EN than during LN due to oxygenation of the surface layer and in spite of a reduced primary production. Sensitivity experiments highlighted the larger impact of equatorial remote forcing with respect to local wind forcing during EN and LN.

1. Introduction

Oxygen Minimum Zones (OMZ) are large water bodies of the open ocean with low concentrations of dissolved oxygen (DO < 22 μmol kg^{-1}) at subsurface depths (~ 50 – 900 m; Levin, 2003; Kartensen et al., 2008). Low DO has a strong impact on the nitrogen cycle: a significant portion (35%) of the nitrogen loss in the global ocean occurs in these regions (Devol et al., 2006) due to denitrification and anammox (Babbin et al., 2014). The oxycline, which separates the well-mixed surface waters with the low-oxygenated subsurface waters, also impacts marine life by limiting the habitat of several species in the water column (Gutiérrez et al., 2008; Diáz and Rosenberg, 2008; Bertrand et al., 2011). These features, along with the recently observed increase of their vertical extent (Stramma et al., 2008, 2010; Ito and Deutsch, 2013; Schmidtko et al., 2017; Breitburg et al., 2018) have made OMZ studies an oceanographic hot topic in the recent decades.

The OMZ of the Tropical South Eastern Pacific (TSEP; Fig. 1) is one of the most intense OMZ of the open ocean (Paulmier and Ruiz–Pino, 2009; Fuenzalida et al., 2009; Ulloa and Pantoja, 2009; Graco et al., *in press*). DO concentrations in its core can be lower than 5 μmol kg^{-1} or totally depleted (*e.g.* Czeschel et al., 2015; Thomsen et al., 2016). Off Peru the OMZ extends vertically between ~ 50-100 and 600-700 m depth on average (Helly and Levin, 2002; Fuenzalida et al., 2009), being deeper offshore (Kartensen et al., 2008). Near the coast, the oxycline is found at 20 – 50 m water depth (Graco et al., 2007; Gutiérrez et al., 2008; Fuenzalida et al., 2009).

Complex physical and biogeochemical processes are involved in the TSEP OMZ formation and maintenance. Vertical mixing between the shallow, oxygenated, surface mixed layer and subsurface OMZ waters is reduced due to the relatively weak alongshore winds. A sharp permanent pycnocline also mitigates vertical mixing and prevents local ventilation of subsurface waters (Fielder and Talley, 2006). Furthermore, it is located in the poorly ventilated "shadow zone" of the Subtropical South Eastern Pacific, out of reach of the ventilated water masses pathways which subduct in the thermocline (Luyten et al., 1983). Indeed, the residence time of OMZ waters can be very long: water masses may recirculate within the OMZ during

more than a year (*e.g.* ~ 15 months at 8°S, Czeschel et al., 2011). On other hand, as it is relatively close to the equatorial region, the northwestern boundary of the OMZ is ventilated by the equatorial current system and is sensitive to its variability. In particular, equatorial subsurface undercurrents (SSCCs) or Tsuchiya jets (Tsuchiya, 1975) transport relatively DO-rich waters eastward (Montes et al., 2014). The nearshore OMZ is then ventilated by the poleward Peru-Chile Undercurrent (PCUC), which connects the offshore equatorial region to the Peruvian coastal upwelling system (PCUS) (Zuta and Guillén, 1970; Codispoti et al., 1989; Chaigneau et al. 2013). The PCUC is recognized as the main source of the upwelling waters (Huyer et al., 1991). It is mainly fueled by the primary (2°S – 6°S, pSSCC) and secondary (6°S – 10°S, sSSCC) subsurface undercurrents (Montes et al., 2010), and to a much lesser extent by the Equatorial Undercurrent (2°N – 2°S, EUC; Wyrtki, 1967).

The very high PCUS productivity also impacts the OMZ. The large amount of organic matter (OM) eventually sinks into the OMZ, and oxygen is consumed by microbial respiration during OM remineralization (*e.g.* Paulmier et al., 2006; Cavan et al., 2017). Overall, the temporal variability of the OMZ extension is assumed to be mainly driven by physical processes (*e.g.* Xu et al., 2015), but its maintenance is due to the oxygen respiration (Paulmier et al., 2006).

The OMZ is variable over a wide range of temporal and spatial scales. At seasonal time scales, its variability is related to the local wind forcing, remineralization and mesoscale circulation (eddies and filaments; Vergara et al., 2016; Thomsen et al., 2016). At interannual time scales, the OMZ is mainly affected by the warm (El Niño, EN) and cold (La Niña, LN) phases of the El Niño Southern Oscillation (ENSO). During EN, intraseasonal Equatorial Kelvin Waves (IEKW) are generated by wind anomalies in the Equatorial Pacific region (*e.g.* Kessler et al., 1995). They propagate eastward and reach the western coasts of America. There, they trigger coastal trapped waves (CTWs) which propagate poleward and impact the vertical structure of physical and biogeochemical variables alongshore off Peru (Gutiérrez et al, 2008; Echevin et al., 2014; Graco et al. 2017) and Chile (Ulloa et al., 2001). The water column thus becomes oxygenated during EN and a deeper oxycline (> 100m) is observed (Gutiérrez et al., 2008, 2016), while during LN (*e.g.* 1999–2000), a shallower oxycline is described (Graco et al., 2007, 2017). These DO changes are strongly linked with the physical variability, as both the thermocline and oxycline are displaced vertically during the passage of downwelling (warm) and upwelling (cold) CTWs (Echevin et al., 2014; Graco et al., 2017).

Besides, the DO content of the PCUC could also be modified during ENSO. As it is fed mainly by the pSSCC and the EUC during LN and by the sSSCC during EN (Montes et al., 2011), variability in DO concentrations in the equatorial region could impact differently the ventilation

of the OMZ.

Few modelling works have described the OMZ variability at interannual time scales. Using a regional model, Mogollón and Calil (2017) simulated the impact of the strong 1997–98 EN and 1999–2000 LN events on the OMZ. They found a deepening (~ 150 m) of the OMZ during 1997–1998 EN respect to neutral condition, while a shallower OMZ (~ 50 m) was observed during LN in the main coastal upwelling centers of the PCUS. Using a global model, Yang et al. (2017) found that the denitrifying SETP OMZ core volume expanded during LN (*e.g.* ~ + 35 % in 1999–2000 LN) and shrinked during EN (*e.g.* ~ – 75 % in 1982–1983/1997–1998 EN). Note that in these recent works, few *in situ* oxygen measurements were used to validate the simulations during ENSO.

In the present work, we make use of a unique interannual DO *in situ* data set and of a regional physical-biogeochemical coupled model to study the physical and biogeochemical processes involved in the OMZ variability during EN and LN phases. Unlike previous studies, we simulated a large number of ENSO events from 1958 to 2008, which allows a comparison of the impact of extreme and moderate events. After carefully evaluating the model with *in situ* data, we used the model to investigate the role of the CTWs, the impact of the equatorial circulation and the ventilating eddy fluxes due to the variable mesoscale activity during EN and LN events. Finally, we performed sensitivity experiments forced by contrasted atmospheric and open boundary forcing to investigate the impact of the local (*e.g.* wind and heat fluxes) and remote forcing (*e.g.* coastal waves) on the DO changes during EN and LN.

2. Material and Methods

2.1. The ROMS-PISCES coupled physical-biogeochemical model

The Regional Oceanic Modeling System model (Shchepetkin and McWilliams, 2005) was used to simulate the ocean dynamics. The ROMS-AGRIF code (version 3.1) was used (Penven et al. 2006). ROMS resolves the Primitive Equations, based on the Boussinesq approximation and hydrostatic vertical momentum balance (Shchepetkin and McWilliams, 1998). ROMS is coupled to the Pelagic Interaction Scheme for Carbon and Ecosystem Studies (PISCES) biogeochemical model to simulate the marine biological productivity and the biogeochemical cycles of carbon and main nutrients (P, N, Si, Fe; Aumont et al., 2015) as well as DO (*e.g.* Resplandy et al., 2012). PISCES has three non-living compartments which are the semi-labile dissolved organic matter, small sinking particles and large sinking particles, and four living compartments represented by two size classes of phytoplankton (nanophytoplankton and

diatoms) and two size classes of zooplankton (microzooplankton and mesozooplankton).
This coupled model has been used to study the climatological (Echevin et al., 2008; Albert et al., 2010), intraseasonal (Echevin et al., 2014) and interannual (Espinoza-Morriberón et al., 2017) variability of the surface productivity in the PCUS.

2.1.1. The Oxygen cycle in the PISCES model

The oxygen evolution in PISCES is computed taking into account the dynamical transport, biogeochemical processes (sources and sinks) and air-sea fluxes, as follows:

$$\partial tO_2 = \underbrace{-u_H.\nabla_H O_2 \; - w.\nabla_H O_2 \; + \frac{\partial K_z \partial O_2}{\partial z^2}}_{Dynamical\ transport} + \underbrace{\left(\frac{\partial O_2}{\partial t}\right)_{Bio}}_{Biogeochemical\ processes} + \underbrace{J_{flux}}_{air-ocean\ exchange}$$

u_H and w represent the horizontal (zonal and meridional) and vertical currents, respectively. K_z represents the vertical diffusivity. The last term on the right hand side represents the air-sea oxygen flux, which depend on the partial pressure air-sea difference, solubility and velocity transfer of oxygen. The atmospheric oxygen concentration is constant throughout the simulation.
Besides, the biogeochemical processes which produce and consume oxygen are parametrized as follows (see also Resplandy et al., 2012):

$$\left(\frac{\partial O_2}{\partial t}\right)_{Bio} = R^1_{O/C}.\underbrace{\left(\mu^P_{nh4}P + \mu^D_{nh4}D\right)}_{New\ Production} + \left(R^1_{O/C} + R^2_{O/C}\right).\underbrace{\left(\mu^P_{no3}P + \mu^D_{no3}D\right)}_{Regenerated\ Production}$$
$$- R^1_{O/C}.\underbrace{\left(\lambda^*_{DOC}\left(1-\Delta(O_2)\right)DOC + G^Z Z + G^M M\right)}_{Remineralization\ and\ Respiration} - R^2_{O/C}.\underbrace{Nit}_{Nitrification}$$

Diatoms (D) and nanophytoplankton (P) produce oxygen during photosynthesis through new and regenerated production. The corresponding production rates are μ_{nh4} and μ_{no3}. Oxygen consumption is due to remineralization of Dissolved Organic Carbon (DOC), respiration of mesozooplankton ($G^Z Z$) and microzooplankton ($G^M M$), and nitrification. λ^*_{DOC} represents the remineralization rate. $\Delta(O_2)$ varies between 0 (in oxic conditions) and 1 (anoxia), mimicking the suppression of remineralization in anoxic conditions. $R^1_{O/C}$ (131/122) represents the change in oxygen relative to carbon when ammonium is converted to organic matter during new production and when DOC is being respired. $R^2_{O/C}$ (32/122) represents the change in oxygen

relative to carbon during nitrification (*Nit*). More detail about the model structure and parameterizations can be found in Aumont et al. (2015).

2.1.2. Model configuration

The model domain spanned from 15°N to 40°S and from 100°W to 70°W (Fig. 1). Due to the extension of the model area and computational requirements, the horizontal resolution of the grid was 1/6° (~ 18 km). It allowed to reproduce mesoscale structures off Peru owing to the proximity of the region to the equator (see section 4.2). The bottom topography from ETOPO2 (Smith and Sandwell, 1997) was used, and the vertical grid had 32 sigma levels.

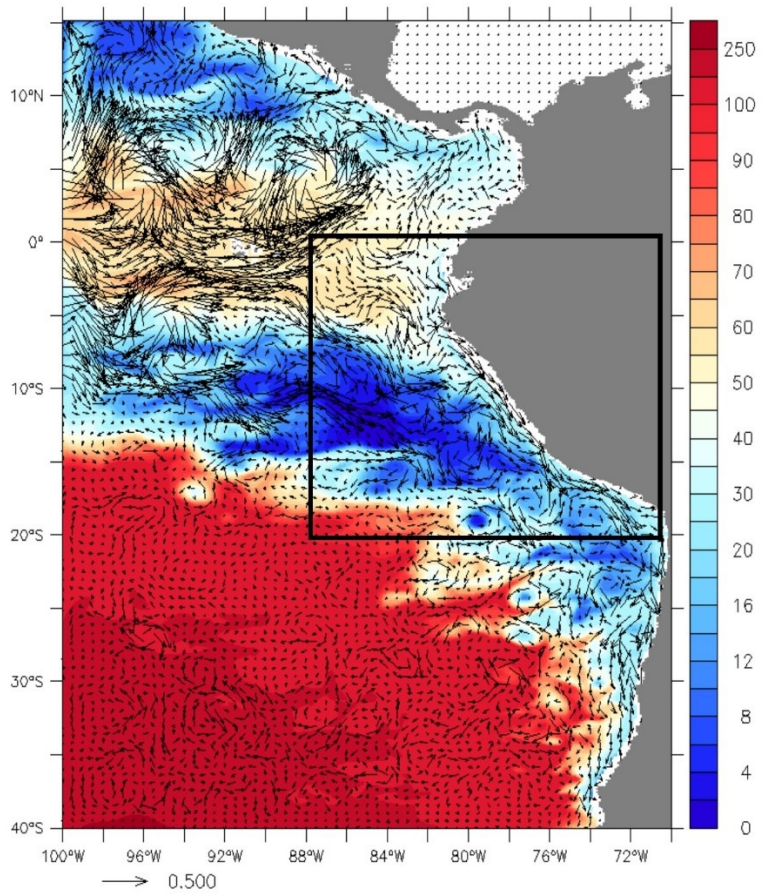

Figure 1. Modelled Velocity current (arrows, in m s^{-1}) and DO mean (color scale, µmol kg^{-1}) between 200 – 300 m depth during December 1997 – March 1998. The black box marks the studied area.

Open boundary conditions (OBC) for physical variables came from an interannual SODA model solution (version 2.1.6; Carton and Giese, 2008) over the period 1958-2008. As an interannual global simulation of the biogeochemical conditions was not available during the

period of study (1958-2008), climatological OBC from CARS2009 climatology (Ridgway et al., 2002) were used for nutrients (nitrate, silicate, phosphate) and oxygen and from World Ocean Atlas climatology (WOA2005; Conkright et al., 2002) for DOC, dissolved inorganic carbon and total alkalinity. As a gridded climatology of iron measurements does not exist, iron OBC from a climatology of a NEMO-PISCES global simulation were used (Aumont et al., 2015).

Wind stress, fresh water, sensible and latent heat fluxes were computed using the bulk parameterization of Liu et al. (1979). The surface wind fields were obtained by summing statistically-downscaled NCEP daily wind anomalies (Goubanova et al., 2010) and the SCOW monthly climatology (Risien and Chelton, 2008). NCEP daily anomalies and COADS monthly climatology (Da Silva et al., 1994) were summed to obtain surface air parameters. Climatologies of short (COADS) and downward long wave (NCEP) heat fluxes were used. The forcing characteristics of the different simulations are listed in Table 1.

Simulations	REMOTE FORCING		ATMOSPHERIC FORCING				
	Physical Boundary Condition	Biogeochemical Boundary Condition	Winds Velocity	Surface Air Temperature	Relative Humidity	Precipitation Rate	Short and Long Wave Radiation
CR	inter	clim	inter	inter	inter	inter	clim
Wclim	inter	clim	clim	clim	clim	clim	clim
Kclim	clim	clim	inter	inter	inter	inter	clim

Table 1. Characteristics of the model simulations. The Control Run (CR) uses interannual forcings over 1958–2008. Wclim simulation used climatological atmospheric forcing and interannual remote oceanic forcing. Kclim simulation used interannual atmospheric forcing and climatological remote oceanic forcing. Both runs were run over 1979–2008.

2.2. Model Experiments

The interannual simulation which is mainly described and studied in the following sections is named the control run (CR) and covers the period 1958–2008. It was forced by interannual atmospheric forcing and boundary conditions. The circulation, productivity and nutrient fluxes during ENSO were evaluated in Espinoza-Morriberón et al. (2017).

Two additional simulations were performed and analyzed (Table 1):

- The Wclim simulation, forced by interannual OBC and monthly climatological atmospheric forcing, was used to evaluate the role of the oceanic remote forcing, *e.g.* equatorial subsurface currents, equatorial Kelvin waves and coastal trapped waves.
- The Kclim simulation, forced by monthly climatological OBC and interannual atmospheric forcing, allowed to study the role of the wind forcing.

Due to computational requirements Kclim and Wclim were run from 1979 to 2008, a period which included two extreme EN events (1982–1983/1997–1998) and one strong LN event (1999–2000). 5 day-averaged outputs were stored for each simulation.

2.3. Lagrangian Analysis

The ROMS-offline tracking module (Capet et al., 2004) was used to calculate the trajectories of virtual floats simulating water parcels. The floats trajectories were computed using the 5-day averaged velocity fields. Oxygen concentration were registered along the trajectories. In order to describe the source waters (SW) characteristics reaching the nearshore OMZ, 2000 floats were released over the shelf and slope, between the surface and 350 m depth within ~ 150 km from the coast on the first day of each month of spring (October, November, December), during each LN and EN events and during neutral periods. The floats were released from a zonal section at 9°S, but other sections (*e.g.* 12°S) were tested. The floats were then tracked backwards in time during two years. The floats reaching the so-called offshore equatorial region (defined by a meridional section at 88°W, 2°N – 10°S) were used to compute statistics. The characteristics of these waters (DO concentration and depth in the equatorial region, duration of the transit from the equatorial section to the cross-shore coastal section (at 9°S) were mapped onto the cross-shore section where the water parcels were released (see section 3.2.2).

2.4. Eddy fluxes

The oxygen vertical eddy flux was computed as $\overline{w'.O_2'} = \overline{w.O_2} - \overline{\langle w \rangle.\langle O_2 \rangle}$, where w and O_2 are the 5 day-averaged vertical velocity and oxygen concentration, respectively. $\langle . \rangle$ denotes a moving filter with a 60 days' window. The mean profiles of oxygen mean vertical flux and eddy vertical flux were obtained by averaging values horizontally (horizontal averaging is marked by an overbar) in an offshore box (between 100 and 500 km from the coast and between 6°S and 16°S). We chose to average profiles in an offshore box in order to discard the effect of nearshore upwelling and downwelling velocities associated with the CTWs and to retain the role of eddies and filaments.

The meridional ($v'.O_2'$) and zonal ($u'.O_2'$) eddy oxygen fluxes were computed using the same

time filter. Maps of the intensity and direction of the horizontal eddy fluxes ($\sqrt{(u'.O_2')^2 + (v'.O_2')^2}$) at 100 m and 400 m during neutral, LN and EN events are described in section 3.2.3.

2.5. ENSO index

ENSO phases are defined when the 3-month-running mean SST anomaly in the 'Niño1+2' region (0 – 10°S, 90°W – 80°W) is higher or less than +/- 0.5 °C for at least five consecutive months for EN and LN, respectively (as in Espinoza-Morriberón et al., 2017). The ERSST.v4 SST product of Huang et al. (2015) was used. Neutral periods correspond to non-EN and non-LN periods. For EN events, if the SST anomalies are greater than + 1.6 °C during at least three months the event is categorized as "extreme", otherwise it is a "moderate" EN (see Table in Suppl. Material). The correlation between the Niño1+2 index computed from the model SST and observations was 0.9, thus the majority of EN and LN events were represented by the model.

2.6. Oxygen *in situ* observations

Approximately ~ 20 000 DO vertical profiles collected by the Peruvian Marine Institute (IMARPE) between 1960 and 2008 (Bertrand et al., 2011; Ledesma et al., 2011) were used to evaluate the modelled OMZ. DO was determined by the Winkler method (Carrit and Carpenter, 1966). Observations (Nansen and Niskin bottles) were collected during surveys and at fixed stations along the coast. The data was gridded at the same resolution as the model (1/6°). Composite alongshore-averaged cross-shore sections for neutral and ENSO phases between 6°S and 16°S and 100 km from the coast (hereafter coastal region) were computed.

The depth of the upper limit of the OMZ (*i.e.* where DO is equal to 22 µmol kg^{-1}) was computed from each IMARPE profile (linearly interpolated on a vertical grid with a 1 meter resolution). These values were then averaged horizontally in the coastal region to produce an index (ZO2) characterizing oxygenation in the nearshore region.

In addition, CARS2009 DO observations (Ridgway et al., 2002) were used to evaluate the spatial distribution of the simulated oxygen over the entire model domain. The CARS 1/2° gridded data was interpolated onto the 1/6° model grid.

3. Results

3.1. Evaluation of the modelled OMZ

3.1.1. Mean state

The mean modelled and observed OMZ are shown in Figure 2. ZO2 presented a marked cross-shore gradient, with shallower depths (< 25 m) near the coast than offshore (~ 100 m at 100 km from the coast off the central shelf), likely associated with coastal upwelling. The nearshore ZO2 was deeper in the model (~ 50 – 70 m between 6°S and 14°S), than in the observations (~ 30 m in IMARPE and ~ 50 m in CARS). The shoaling of ZO2 towards the coast (~ 50 m depth) was also observed between 14°S – 16°S by Graco et al. (2007). ZO2 reached 150 m depth at 86°W between 6°S and 14°S (Fig. 2 a–c), highlighting the offshore deepening and westward extent of the OMZ.

Figures 2d, e display a meridional section of the OMZ at 86°W, more than 1500 km east of the model western boundary. The modelled and observed OMZ boundaries were rather similar between 6°S – 14°S. Although ZO2 was relatively similar in the model and CARS observations, the maximum OMZ thickness (found near 8°S – 10°S at 86°W) was larger in the model than CARS due to the OMZ deeper (by ~ 100 m) lower limit in the model. In the core of the OMZ between 8°S – 11°S and 200 – 500 m depth, modelled DO concentrations were lower than 5 μmol kg^{-1}, lower than CARS (~ 10 μmol kg^{-1}), but in agreement with previous observations (Kartensen et al., 2008). Between 2°S and 2°N the modelled OMZ vanished, while a thin (~ 100 m) OMZ remained between 300 and 450 m depth in CARS, pointing to a likely overestimation of the modelled oxygen westward flux driven by the equatorial currents.

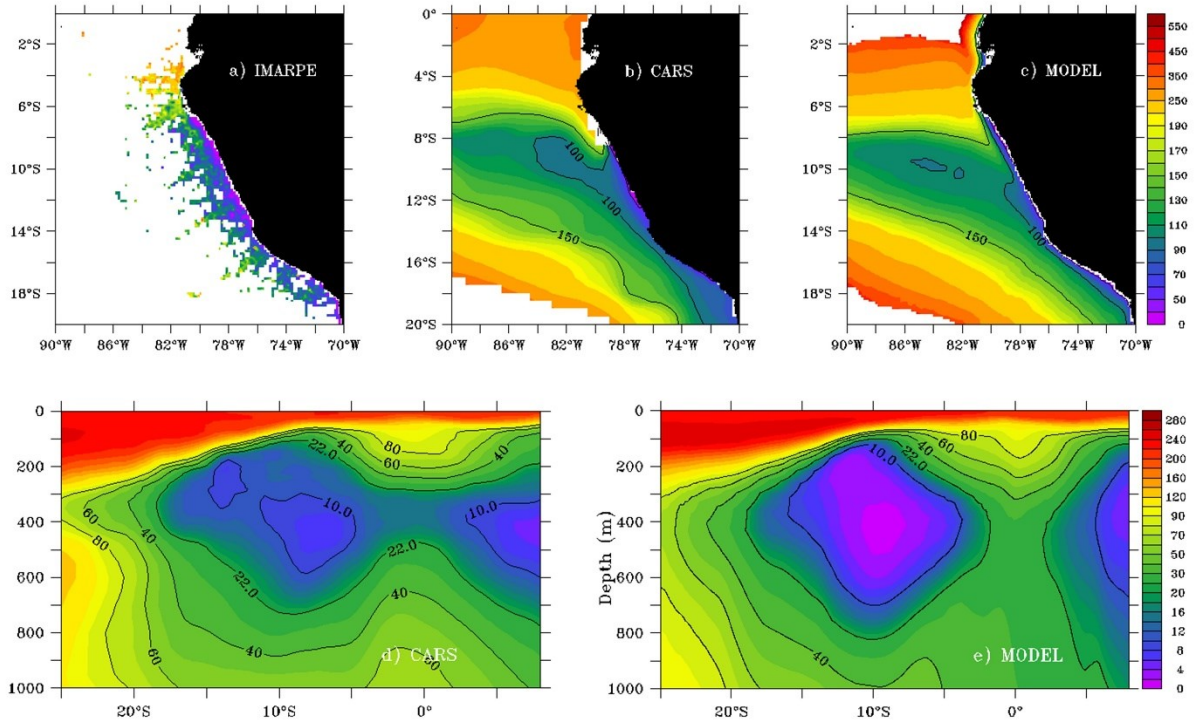

Figure 2. Annual ZO2 mean (in meters) from IMARPE (a), CARS (b) and model (c). Meridional section (86°W) of the annual DO mean (in µmol kg^{-1}) from CARS (d) and model (e). Annual means were computed over 1958-2008 using the model and IMARPE data.

3.1.2. Interannual Variability

Due to the relative scarcity of *in situ* data, it was impossible to compute cross-shore sections of DO at distinct latitudes, therefore we present alongshore-averaged cross-shore sections between 6°S and 16°S (see section 2.6) representative of averaged DO conditions near the Peru shelf and slope (*e.g.* Espinoza-Morriberón et al., 2017). The model and data sections are shown for neutral, EN and LN phases (Fig. 3). Near-surface slanted isolines of oxygen were evidenced in the model and IMARPE sections during neutral, EN and LN events, indicating the occurrence of coastal upwelling during each phase (Figs. 3a–c, f–h). During neutral periods, between the coast and 200 km offshore, the observed ZO2 was located at ~ 180 m depth and the modelled ZO2 at ~ 150 m depth (Figs. 3a, f). In contrast, during EN (LN) a deeper (slightly shallower) ZO2 was observed in the model (Figs. 3b, c). These features were well reproduced by the model (Figs. 3g–h). The main differences between model and observations were found in the OMZ core and near its lower limit. In the model, DO values less than 5 µmol kg^{-1} were observed in the OMZ core (between 300 – 450 m depth) during neutral and LN periods. During EN, the thickness of lowest DO (< 5 µmol kg^{-1}) layer was reduced, a result also found in another modelling study (Yang et al., 2017). In contrast, the observations presented a slightly more

oxygenated core than in the model during neutral (~ 8 µmol kg^{-1}), EN (~ 15 µmol kg^{-1}) and LN (~ 12 µmol kg^{-1}) periods. Moreover, the modelled OMZ lower limit was deeper than that of the observed OMZ, in particular during LN (Fig. 3c–h). During EN, both observations and model presented a thinner OMZ than during neutral periods, owing to a deepening of its upper limit and a shoaling of its lower limit. In contrast, the model was not able to simulate the observed OMZ thinning during LN. Indeed, the modelled OMZ was thicker during LN with respect to neutral conditions due to little change of its lower limit, whereas the shoaling of the lower limit was strong in the observations.

In terms of magnitude, the DO changes in the surface layer (0 – 150m) during ENSO phases were qualitatively reproduced by the model. The highest DO anomalies were observed between 10 m and 150 m (Figs. 3d–i) both in the model (+ 40 µmol kg^{-1}) and in observations (+ 25 µmol kg^{-1}) during EN. During LN, negative anomalies of similar amplitude in the model and observations (~ – 10 µmol kg^{-1}; Fig. 3e, j) were found in the same layer between the coast and 150 km offshore.

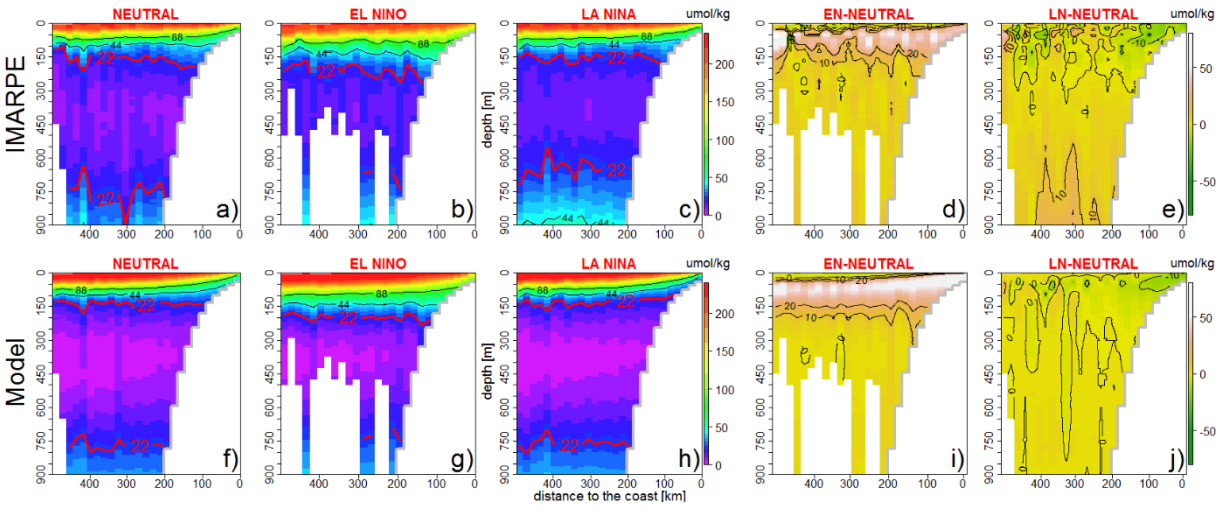

Figure 3. DO (in µmol kg^{-1}) alongshore-averaged (6°S – 16°S) vertical sections during neutral, EN and LN periods, from IMARPE data (a–c) and model output (f–h). DO anomaly alongshore–averaged vertical sections (6°S – 16°S) for EN and LN periods from IMARPE (d–e) and model output (i–j).

Interannual variations of the nearshore modelled and observed ZO2 were highly correlated over 50 years (0.72, $p < 0.05$, Fig. 4). During each EN event, ZO2 increased strongly. The maximum ZO2 (~ 300 m) was attained during the peak of the extreme 1982–83 EN for model and observations. During neutral periods, the observed and modelled ZO2 were ~ 120 m depth on

average. No significant differences between LN and neutral periods were found in the model and in the observations time series. In conclusion, in spite of the discrepancies in DO concentration within the OMZ (Figs. 3–5), the model represented realistically the oxygen changes during ENSO phases.

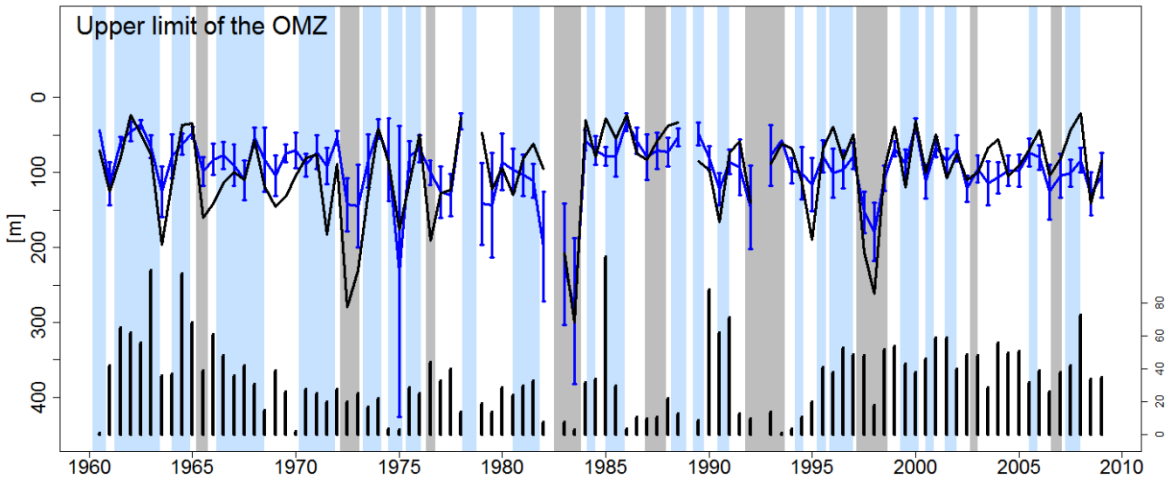

Figure 4. ZO2 time series (in meters). Data was averaged each semester for IMARPE (blue line) and model output (black line) in a coastal box (6°S – 16°S and 100 km from the coast). Error bars represent the standard deviation from IMARPE data. Black bars (at the bottom of the figure) represent the coverage ratio (number of sampled points/ total number of points). The modelled ZO2 was computed using the same sampling as IMARPE observations (gaps mean there is no data). Gray and blue shading represent EN and LN period respectively.

3.2. Physical drivers of OMZ variability during ENSO

3.2.1. Coastal Trapped Waves

The impacts of the downwelling and upwelling CTWs during an extreme EN (1997–1998) and a strong LN (1999–2000) are highlighted in Figure 5. During the 1997–1998 EN the poleward propagation of two downwelling CTWs was evidenced on the Sea Surface Height (SSH) signal, which showed positive anomalies. The thermocline depth (defined by the position of the 15°C isotherm, Z15) deepened during the first (~ + 80 m) and second (~ + 150 m) peak (Fig. 5a, b; Espinoza-Morriberón et al., 2017). The slightly tilted isolines indicate poleward propagation of the signals. ZO2 deepened strongly during EN (Fig. 5c). The deepest anomalies (+ 200 m) were observed during the second peak of the event.

During the strong 1999–2000 LN, two strong upwelling IEKW crossed the Central Pacific

provoking the shoaling of the 20°C isotherm (figure not shown). They triggered two CTWs which impacted the alongshore SSH, thermocline depth (ZT15) and ZO2 during the summer–autumn of 1999 and 2000 (Fig. 5d–f), with magnitudes weaker than those of the EN downwelling CTWs. The SSH anomalies presented negative values (Fig. 5 d) and a shallower ZT15 was observed, associated with negative anomalies of ~ 50 m north of 6°S, and ~ 30 – 40 m between 10°S – 15°S (Fig. 5e). A shoaling ZO2 was also observed during the passage of both upwelling CTWs. Negative anomalies of ~ 45 m were found between 8°S – 14°S during the passage of the CTW (Fig. 5f). Note that the upwelling CTW during LN occurred during the same season (summer) in 1999 and 2000.

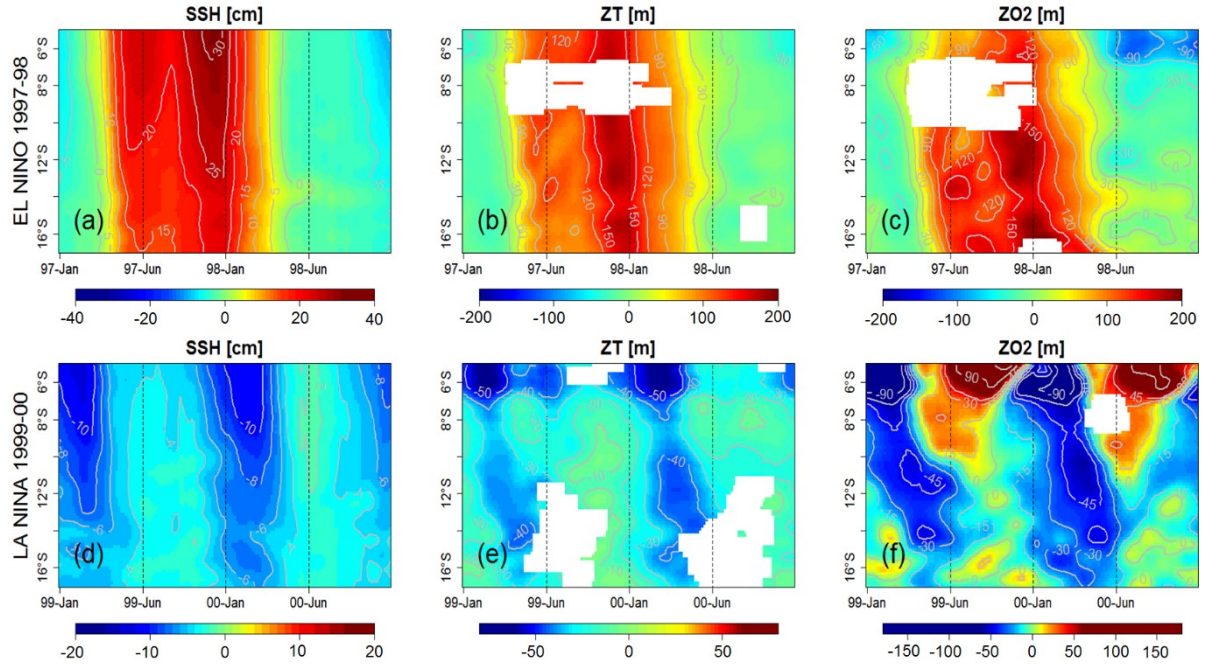

Figure 5. Hovmoller (latitude vs time) of modelled SSH anomalies (a, d, in cm), ZT15 anomalies (b, e, in meters) and ZO2 anomalies (c, f, in meters) during EN 1997-98 (top) and LN 1999 (bottom) events. Model values were averaged within 100 km to the coast. All variables were filtered in time (60 days moving average) and space (100 km alongshore). Empty data in (b, c, e, f) means that ZT15 and ZO2 were not detected.

The strong relationship between the variability of ZT15 and ZO2 is well known locally at specific coastal sites off Peru (*e.g.* 12°S, Gutiérrez et al., 2008; Graco et al., 2017), but also in other regions where CTWs play an important role, *e.g.* Vallivattathillam et al. (2017) for the western coast of India. These authors mentioned that the effects of biogeochemical processes (*e.g.* remineralization and respiration) and of vertical mixing were smaller than those due to

advection (*e.g.* CTW). This strong relationship is highlighted in Figure 6a, which shows the spatial pattern of correlation between ZT15 and ZO2 monthly anomalies over the entire PCUS. The correlation was highest (~ 0.8) nearshore (between the coast and 50 km offshore) and dropped offshore and south of 18°S, where the OMZ vanishes. The high correlation pattern extended westward until 350 km offshore along 10°S. North of 10°S, the correlation decreased due to a ZO2 deepening larger than that of ZT15. Figures 6b–c show cross-shore sections of the correlation between ZO2 and ZT15 and the depth difference at 7°S and further south, at 10°S. The ZO2 was shallower at 10°S than at lower latitudes (Figs. 2b, c) as it was less impacted by the oxygen-rich waters transported eastward by the EUC and SSCCs. At 7°S (Fig. 6b), the OMZ was more impacted by ENSO (Mogollón and Calil, 2017) and by the eastward SSCCs transporting oxygen-rich waters (Montes et al., 2014), leading to the increasing distance between ZO2 and ZT15 and correlation decrease west of 81°W. Note that the correlation was very high along the coasts of Colombia and Central America. This indicates that the nearshore interannual variability of ZO2 in the northern hemisphere is also controlled by the shoaling and deepening of isotherms during the poleward propagation of CTWs.

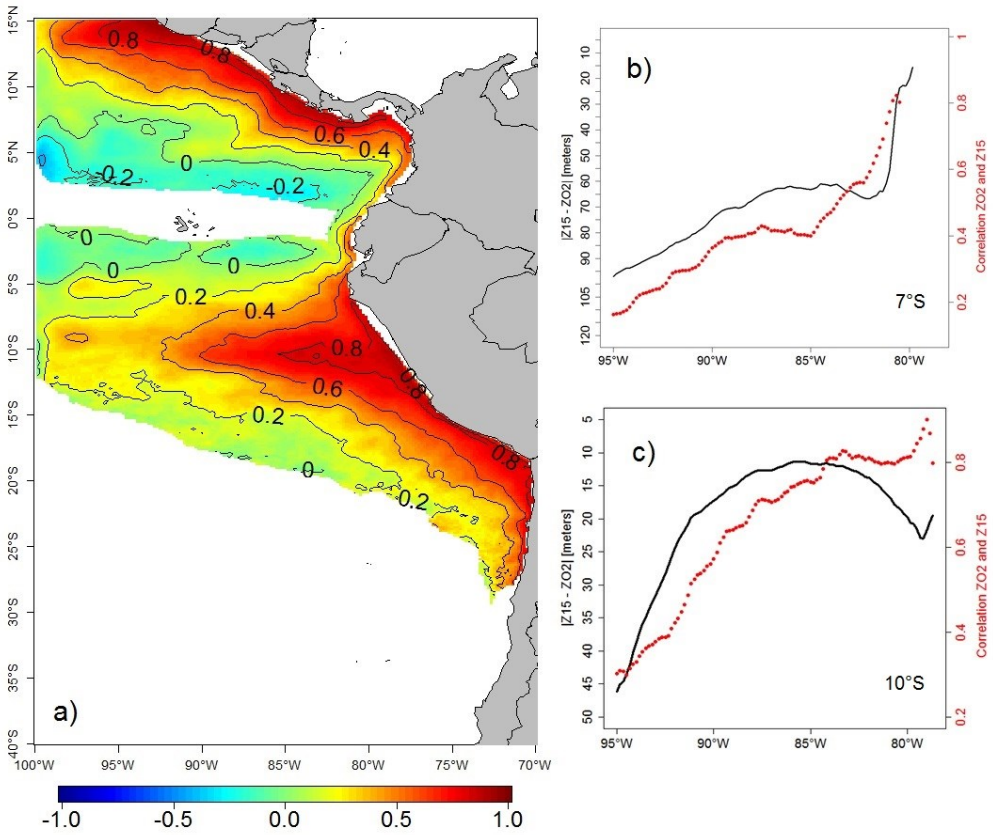

Figure 6. Spatial correlation between modelled ZT15 and ZO2 monthly anomalies in the period 1958-2008 (a). Mean absolute difference (|ZT15–ZO2|, black line, in meters) and correlation (red line) between ZO2 and Z15, from the coast to 95°W, at 7°S (b) and 10°S (c).

3.2.2. Changes in the origin of the shelf and slope waters during ENSO

A modification of the pathways of equatorial water masses (hereafter source waters, SW) reaching the PCUS during ENSO phases was first evidenced by Montes et al. (2011). Given the offshore DO meridional gradients (Figs. 2d, e), this could have consequences on the OMZ ventilation. In this section, we characterize the properties of the offshore (88°W) waters that reached the Peruvian shelf and slope (at 9°S) during EN and LN. Note that modifying the latitude of the cross-shore section (*e.g.* 12°S) did not modify substantially the results presented below.

Expectedly, the DO nearshore section displayed a deeper and shallower ZO2 during EN and LN, respectively (Figs. 7a, f, k, p). The equatorial SW were impacted during ENSO phases. During neutral periods the SW DO concentration was ~ 60 µmol kg^{-1} in average (Fig. 7g), while SW were slightly less oxygenated (~ 40 µmol kg^{-1}) during LN (Fig. 7b). In contrast, SW were more oxygenated (~ 80 to 120 µmol kg^{-1}) during EN depending on the intensity of the events (Figs. 7l, q).

The changes in offshore oxygen content were related to changes in the location of the SW, associated with the modified SSCCs fluxes during ENSO (Montes et al., 2011). Within 100 km from the coast, during neutral periods, the SW originated from 3.5°S – 4°S (Fig. 7h) and 110 – 140 m depth (Fig. 7j). SW were then transported towards the coast for ~ 12 months (Fig. 7i). During LN, SW were located south of 4.5 °S (Fig. 7c) and at greater depths (~ 160 – 180 m; Fig. 7e), thus were less oxygenated (Fig. 7b). Moreover, they were older since it took them more time (~ 15 months; Fig. 7d) to reach the coastal section. This longer transit may partly explain the nearshore oxygen deficit during LN due to microbial respiration in the transported water mass. In contrast, during EN, the SW were initially closer to the equator (3°S – 1°S; Figs. 7m, r), shallower (~ 100 – 120 m depth; Figs. 7o, t) and thus more oxygenated (Figs. 7l, q) than during LN and neutral periods. The SW transit time to the coastal region was much shorter (5 – 10 months; Figs. 7n, s). Note that a fast pathway (~ 2 – 4 months) from the equatorial regions to the coastal range was also found by Montes et al. (2011) for the 2002–2003 EN. In agreement with these results, our model simulated a fast (~ 6 months) and a slow (~ 12 months) pathway during EN 2002–2003 and LN 1999–2000 respectively (Figure not shown).

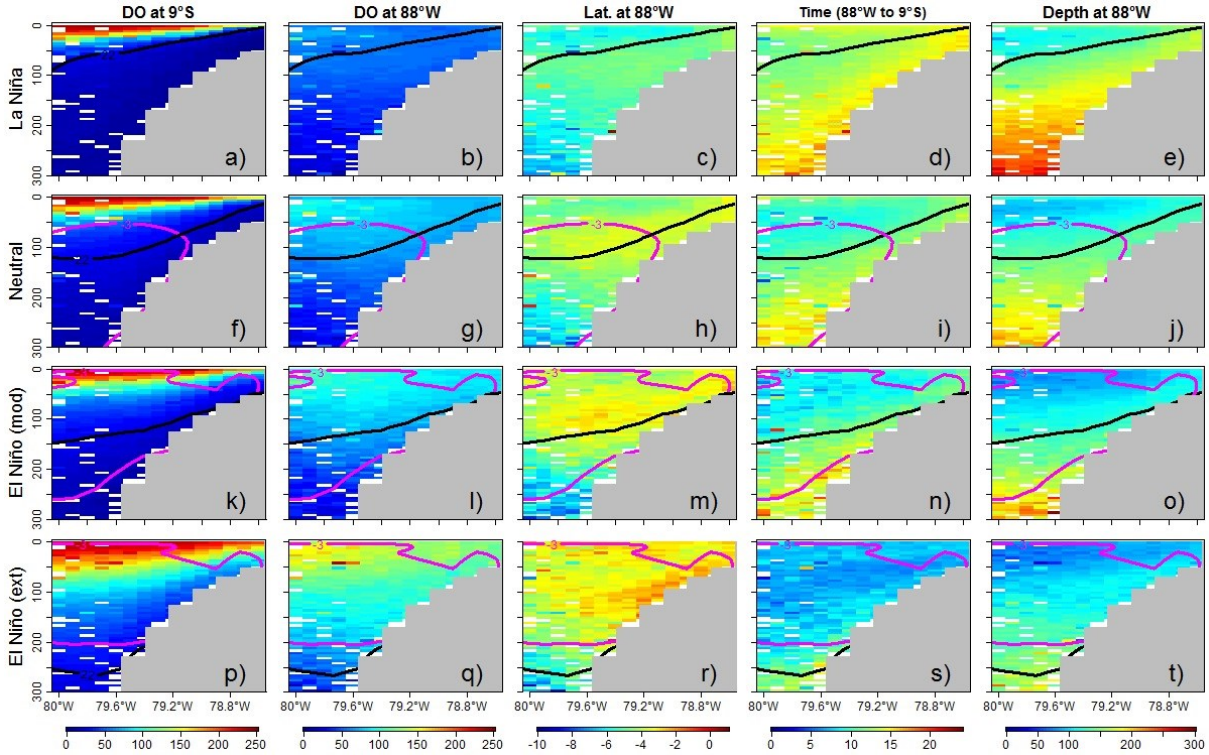

Figure 7. DO cross-shore section (9°S) during LN (a), Neutral (f), moderate (k) and extreme (p) EN. Equatorial (from 88°W) SW properties: DO concentration (b, g, l, q), latitude (c, h, m, r), travel time from 88°W to 9°S (d, i, n, s) and depth (e, j, o, t) during LN, Neutral, moderate and extreme EN periods. The properties were derived from floats released during spring of the ENSO phases. The PCUC (pink line) and ZO2 (black line) also are presented.

3.2.3. Eddy oxygen fluxes

The TSEP OMZ is embedded in a region of intense mesoscale activity (Chaigneau et al., 2008) due to the presence of unstable boundary currents (Echevin et al, 2011; Colas et al. 2012). These eddies generate horizontal (*e.g.* Vergara et al, 2016) and vertical eddy fluxes which impact the OMZ structure. As eddy activity is enhanced during ENSO (Chaigneau et al, 2008; Espinoza-Morriberón et al, 2017), we investigate the impact of EN and LN events on the oxygen vertical and horizontal fluxes.

The mean oxygen vertical flux ($\overline{\langle w \rangle . \langle O_2 \rangle}$) presented positive values with a peak at ~ 40 m depth (Fig. 8a). As the input of oxygen due to the mean flux is equal to - $\partial_z(\langle w \rangle . \langle O_2 \rangle)$, it adds oxygen above ~ 40 m (mainly due to the decrease of mean vertical velocity near the surface, Fig. 8d) and takes out oxygen in the subsurface layer between 40 m and 150 m depth (due to the upwelling of less-oxygenated deep water from the OMZ core, Fig. 8c). At the maximum flux depth (~ 40 m), the mean fluxes did not present strong differences (~ 0.3 µmol m^{-2} s^{-1}) between

neutral and LN periods, while a decrease was observed (~ 0.24 µmol m^{-2} s^{-1}, ~ 20 % reduction) during EN. This flux reduction was partly driven by the reduction of the vertical velocity (Fig. 8d), which counteracted the impact of the subsurface oxygen increase (Fig. 8c). Note that the modelled vertical velocity decrease (~ 40 % at 50 m depth, Fig. 8d) cannot be fully attributed to a decreased Ekman pumping during EN (*e.g.* Halpern, 2002, Chamorro et al., 2018, for the 1997–1998 EN), as it was only ~ 5 % in our simulation (Figure not shown).

The vertical eddy flux also presented positive values with a maximum at ~ 60 m depth (Fig. 8b), which corresponds to the depth of maximum oxygen vertical gradient ($\partial_z O_2$) (Fig. 8c). In the stratified interior, mesoscale eddy fluxes tend to flatten the tilted upper thermocline (Colas et al. 2013) and hence the oxycline. Consequently, the vertical eddy flux brings oxygen into the layer above ~ 60 m, while below it acts as an oxygen sink and reinforces the OMZ. As for the mean flux, weak differences were found between neutral and LN (~ 0.2 10^{-1} µmol m^{-2} s^{-1} at 60 m depth), while an important decrease during EN (~ 0.06 10^{-1} µmol m^{-2} s^{-1}, ~ 70 % decrease) can be seen between 50 m and 70 m depth. This was likely due to a reduction of the oxygen mean vertical gradient during EN (Fig. 8c). As a consequence, the vertical gradient of the vertical eddy flux ($-\partial_z(w'O_2')$) was also much weaker during EN than during LN and neutral periods. This highlights the much weaker role of the eddies as sink/source of oxygen below/above the oxycline during EN periods. At depths greater than 100 m, the vertical eddy flux reached values close to zero during neutral and LN periods, whereas slightly positive values (~ 0.02 10^{-1} µmol m^{-2} s^{-1}) were found during EN.

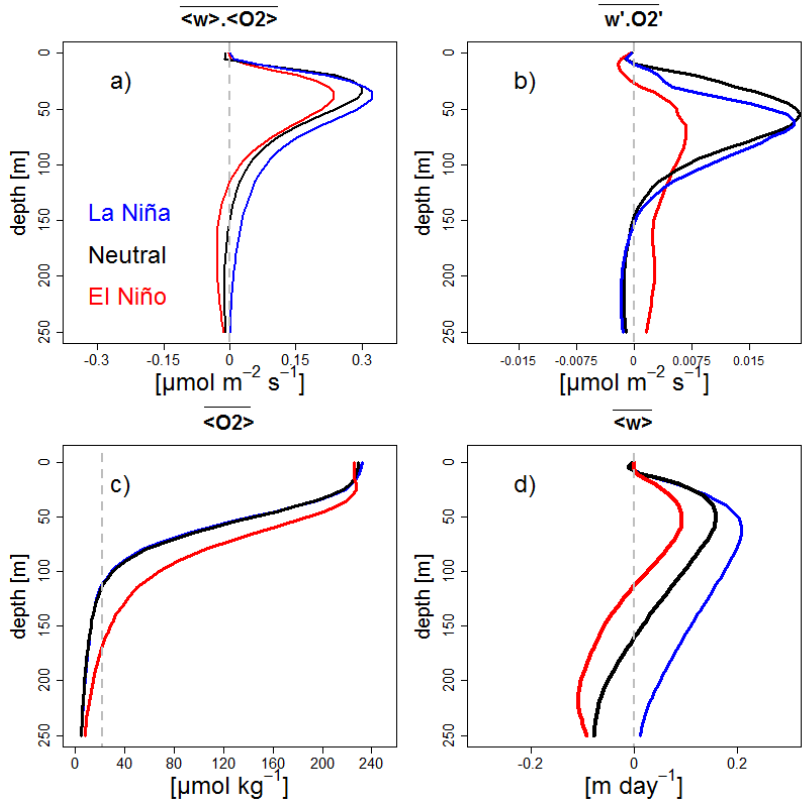

Figure 8. Vertical profile of DO mean vertical flux (a, in µmol O_2 m^{-2} s^{-1}) and DO eddy vertical flux (b, in µmol O_2 m^{-2} s^{-1}), DO concentration (c, in µmol O_2 kg^{-1}) and vertical velocity (d, in m day^{-1}) for Neutral (black line), LN (blue line), EN periods (red line). Profiles were computed in an oceanic band between 100 – 500 km from the coast and 6°S – 14°S. In (c) dashed gray line represents the depth of the OMZ upper limit (22 µmol O_2 kg^{-1}).

The horizontal eddy fluxes play an important role in structuring the OMZ lateral extent (Vergara et al., 2016). Figure 9 shows the horizontal oxygen eddy fluxes at 100 m and 400 m during ENSO phases and neutral periods. Intense eddy fluxes are found in the vicinity of the OMZ boundaries, mainly along the southern limit of the OMZ at 100m depth and in the equatorial region (4°N – 4°S) at 400 m depth. It is well-known that eddy tracer fluxes are downgradient (and pronounced) when there is a strong sink in the tracer distribution (*e.g.* Wilson and Williams, 2006). Hence this is logically the case at the lateral boundaries of the OMZ, especially at its southern limit where the horizontal gradient of DO is intense at 100 m depth. Eddy advection tends to inject oxygen into the OMZ, and it is more intense at shallower depths. During EN, the horizontal oxygen eddy fluxes increased almost by a factor of 3 in comparison with neutral periods, at 100 m depth along the OMZ southern boundary and alongshore (~ 5°S – 18° S) from the coast to 200 km offshore (Fig. 9c). This indicates that eddy fluxes contributed

to oxygenate the coastal region. At 400 m, fluxes were much weaker than at 100 m but also enhanced during EN periods (+ ~ 40%), both at the southern and the northern limits of the OMZ and along the northern shelf (Fig. 9f). Eddy fluxes were quite similar during LN and neutral periods. Overall, the OMZ ventilation at its lateral boundaries by mesoscale eddy advection increased during EN, whereas ventilation due to vertical eddy fluxes reduced.

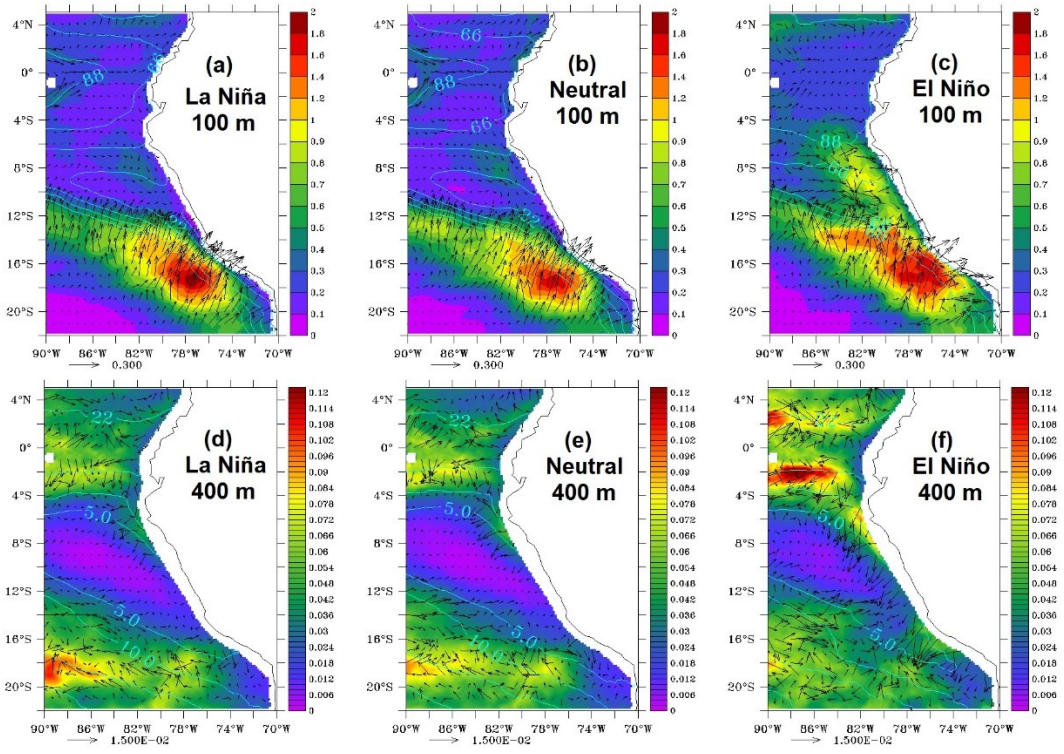

Figure 9. Intensity (colors) and direction (arrows) of the horizontal eddy fluxes ($\sqrt{(u'.O_2')^2 + (v'.O_2')^2}$) at 100 m (top) and 400 m (bottom) averaged during LN (a, d), Neutral (b, e) and EN (c, f) events.

3.3. Biologeochemical drivers of O2 changes during ENSO

The OMZ changes due to biogeochemical processses is investigated. The vertical profiles of biogeochemical source and sinks of oxygen (see Eq. 2 in section 2.1.1) were averaged horizontally within 200 km to the coast (Figure 10). Most of the modelled biogeochemical processes related to the oxygen cycle take place in the near-surface layers and impact the OMZ indirectly through subduction of oxygen-enriched/depleted waters into the oxycline (*e.g.* Thomsen et al., 2016). The annual mean profiles of DO production and consumption had an exponential decrease with depth, with the exception of nitrification. The new and regenerated production (through photosynthesis) provided oxygen to the upper ocean above the ZO2 (~ 100

m depth). Remineralization was the main process consuming oxygen in surface and subsurface water, above 300 m. Microzooplankton respiration consumed oxygen above the upper limit of the OMZ, while mesozooplankton respiration was also found at depth. Oxygen consumption by nitrification peaked at 30 m in oxygen-repleted waters, as it is inhibited by light (Yoshioka and Saijo, 1984) near the surface (0 – 10 m depth). Nitrification decreased in the subsurface layer due to oxygen limitation (see Eq. 2 in section 2.1.1). Within the OMZ (below 120 m depth), only oxygen consumption was observed (due to remineralization, mesozooplankton respiration and nitrification).

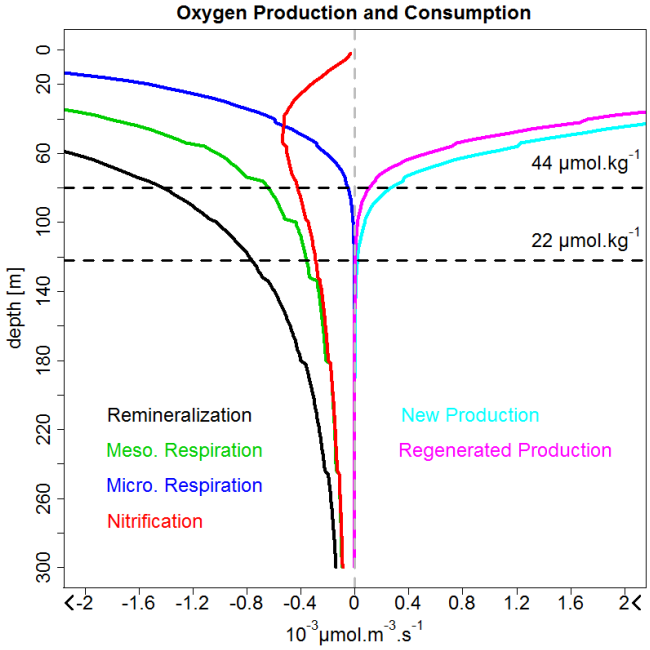

Figure 10. Mean vertical profiles of the DO biogeochemical sources and sinks (in 10^{-3} µmol O2 m^{-3} s^{-1}): new (cyan line) and regenerated (magenta line) production, remineralization (black line), respiration by microzooplankton (blue line) and microzooplankton (green line), and nitrification (red line). The profiles were computed from 6°S – 16°S and with 200 km from the coast. Negative and positive values indicate DO consumption and production respectively.

The impacts of EN and LN on the oxygen sources and sinks were diagnosed in the surface layer (above 100 m depth) and within ~60 km from the coast (Fig. 11). Note that the sinks (*i.e.* negative terms in Eq. 1, section 2.1.1) are shown here with a positive sign, meaning that positive (resp. negative) sink anomalies (e.g. Fig. 11c–f, i–l) indicate an increase in oxygen consumption.

During LN, a positive anomaly (> 2 10^{-3} µmol m^{-3} s^{-1}) produced by the increase in new and

regenerated production was found in a very thin surface layer (above ~ 10 m) and ~ 20 km offshore. In contrast, just below (10 – 80 m depth) and nearshore (within 20 km from the coast), new and regenerated production were weaker by ~ – 0.45 10^{-3} µmol m^{-3} s^{-1} and ~ – 0.8 10^{-3} µmol m^{-3} s^{-1} respectively (Fig. 11a, b). This is due to the thinner mixed layer during LN, in which primary production was confined (Espinoza-Morriberón et al., 2017).

During EN, the nutricline depth increased and photosynthesis decreased in the surface layer (Espinoza-Morriberon et al., 2017), producing less oxygen (< – 6.5 10^{-3} µmol m^{-3} s^{-1}), while new (~ + 0.46 10^{-3} µmol m^{-3} s^{-1}) and regenerated (~ + 0.73 10^{-3} µmol m^{-3} s^{-1}) productions were enhanced in the subsurface layer between 10 and 80 m depth nearshore and within 60 km from the coast (Figs. 11 g, h).

During ENSO phases, oxygen consumption was also strongly modified during ENSO (*e.g.* Yang et al., 2017) with anomalies of DOC remineralization and zooplankton respiration presenting marked cross-shore patterns. Nearshore, negative and positive anomalies predominated during LN and EN respectively, while ~ 30 km offshore and above 15 m, opposite sign patterns were found. Nitrification anomalies presented a pronounced vertical gradient. Below ~ 30 m depth, the nitrification decreased and increased during LN and EN respectively, due to the presence/absence of oxygen.

During LN, remineralization, mesozooplankton and microzooplanton respiration within ~ 20 km from the coast were characterized by negative anomalies of – 0.29 10^{-3} µmol m^{-3} s^{-1}, – 0.28 10^{-3} µmol m^{-3} s^{-1} and – 0.16 10^{-3} µmol m^{-3} s^{-1} respectively (Figs. 11c–e), likely due to the stronger offshore advection of properties. A deficit of nitrification (– 0.13 10^{-3} µmol m^{-3} s^{-1}) was found above the shelf (20 – 60 m; Fig. 11f), due to the ZO2 shoaling and decrease of DO. In contrast, remineralization decreased in a thin surface layer (0 – ~ 10 m) but strongly increased below, down to 100 m depth during EN, due to the production decrease (increase) in the (sub-) surface layer. Positive anomalies of + 1.6 10^{-3} µmol m^{-3} s^{-1} were found nearshore (within ~ 80 km from the coast and between 10 – 80 m, Fig. 11i). Expectedly, meso and microzooplankton respiration reduced in a thin surface layer and increased at depth above the shelf, producing positive anomalies of + 0.55 10^{-3} µmol m^{-3} s^{-1} and + 0.31 10^{-3} µmol m^{-3} s^{-1}, respectively, between 10 – 80 m and from 0 to 80 km to the coast (Figs. 11j, k). Last, nitrification was less intense between the surface and 40 m depth and increased near the bottom over the shelf (+ 0.21 10^{-3} µmol m^{-3} s^{-1} between 40 – 100 m and 0 – 80 km from the coast; Fig. 11l). Nitrification, which was switched off in this depth range during neutral and LN conditions due to the lack of oxygen, took place during EN as shelf waters became oxygenated.

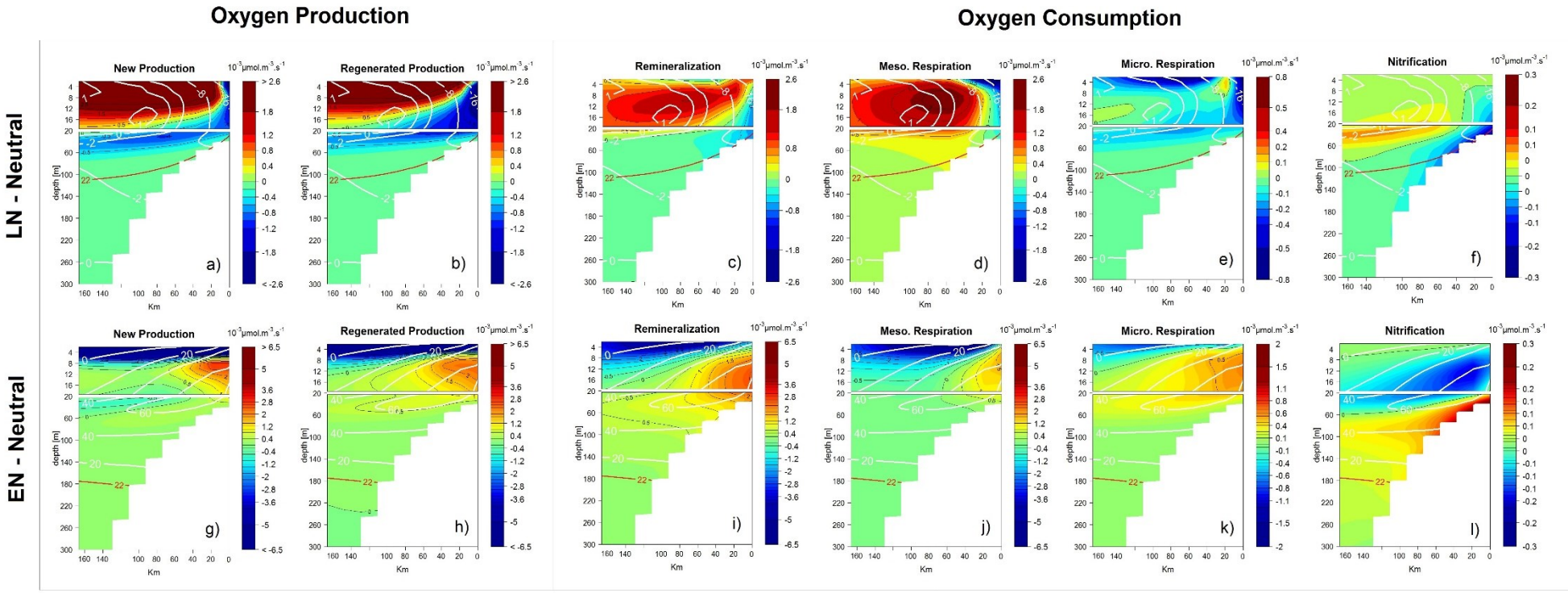

Figure 11. Alongshore-averaged vertical sections of DO sources (by new and regenerated production) and sinks (remineralization, respiration by zooplankton and nitrification) (in 10^{-3} µmol O_2 m^{-3} s^{-1}) during LN (top) and EN (bottom) periods. The sign of the sink terms has been changed to positive. DO anomalies (black lines) and the isoline of 22 µmol O_2 kg^{-1} (red lines) are presented.

In summary, DO changes during LN and EN were influenced not only by physical processes but also by changes in DO production related to primary productivity changes above the upper limit of the OMZ, between 0 and ~ 20 m. The nearshore DO changes induced an increased (decrease) oxygen consumption by remineralization and respiration during EN (LN). Nitrification was enhanced at depth (50 – 150 m) due to DO availability during EN. The relationship between the oxygen consumption and DO availability was also evidenced offshore (86°W) using *in situ* data during the 2009 LN (Llanillo et al., 2013). The authors found an increase of the oxygen consumption by respiration and remineralization within the OMZ due to the presence of the oxygen-rich Antarctic Intermediate Waters (AAIW).

3.4. Impact of the remote and local forcing during ENSO

Sensitivity experiments (see section 2.2 and Table 1) were performed to investigate the impact of remote (Kclim) and local forcing (Wclim) on the OMZ during ENSO. Figure 12 shows the oxygen changes (in %), in Kclim and Wclim with respect to CR, in an alongshore- averaged (between 6°S – 16°S) cross-shore section (see also Fig. 3).

During LN, the oxygen content increased slightly (~ 10 %, + 10 μmol kg^{-1}) in Kclim with respect to CR in the surface layer (between 0 – 50 m depth and within 200 km from the coast, Fig. 12a). In this experiment, the ZO2 shoaling forced by the LN upwelling CTW was absent. In contrast, a moderate DO decrease (10 – 20 %, – 2 μmol kg^{-1}) was found below the upper limit of the OMZ. There, the absence of remotely-forced deep coastal waves (*e.g.* Pietri et al., 2014) may have reduced the equatorward transport of the oxygenated AAIW, which ventilates the deep OMZ between ~ 150 – 350 m and 6°S – 14°S during LN respect to EN (*e.g.* LN 2009; Llanillo et al., 2013). When the interannual wind variability is suppressed (Wclim), a moderate oxygen decrease (~ 3 %, ~ – 8 μmol kg^{-1}) was found above the ZO2 (Fig. 12 b). This may be related to a reduction of vertical mixing between the surface and subsurface layers induced by the much less intense wind variability in Wclim. Besides, primary production was also reduced with respect to CR, thus less oxygen was produced by photosynthesis above 30 m within 200 km to the coast. Below the ZO2, the DO concentration increased offshore by 10% (~ + 2 μmol kg^{-1}). This is possibly related to the reduced offshore Ekman pumping during LN (~ + 20 %) in Wclim, which transports less oxygen-poor waters upward than in CR.

During EN, a strong DO reduction was found over the entire water column in Kclim. It was strongest between 90 m and 150 m depth, where DO was ~ 60 % (~ – 55 μmol kg^{-1}) lower than in CR (Fig. 12c). As expected, the absence of downwelling CTWs in KCLIM prevented deepening events of the OMZ upper limit and maintained low DO concentrations at depth. In

contrast, more oxygen was found (12 %, + 10 µmol kg^{-1}) in Wclim than in CR between 40 – 130 m depth and 50 – 250 km offshore (Fig. 12d). This relatively weak subsurface oxygen increase can be explained as follows: as the alongshore wind increases during EN (see Fig. 9 in Espinoza-Morriberon et al., 2017; Enfield, 1981; Chamorro et al., 2018), the coastal upwelling intensifies. This partly compensates the ZO2 deepening, bringing deep oxygen-poor waters in this depth range. As the EN enhanced wind-driven upwelling was absent in Wclim, the ZO2 was deeper and DO higher than in the CR.

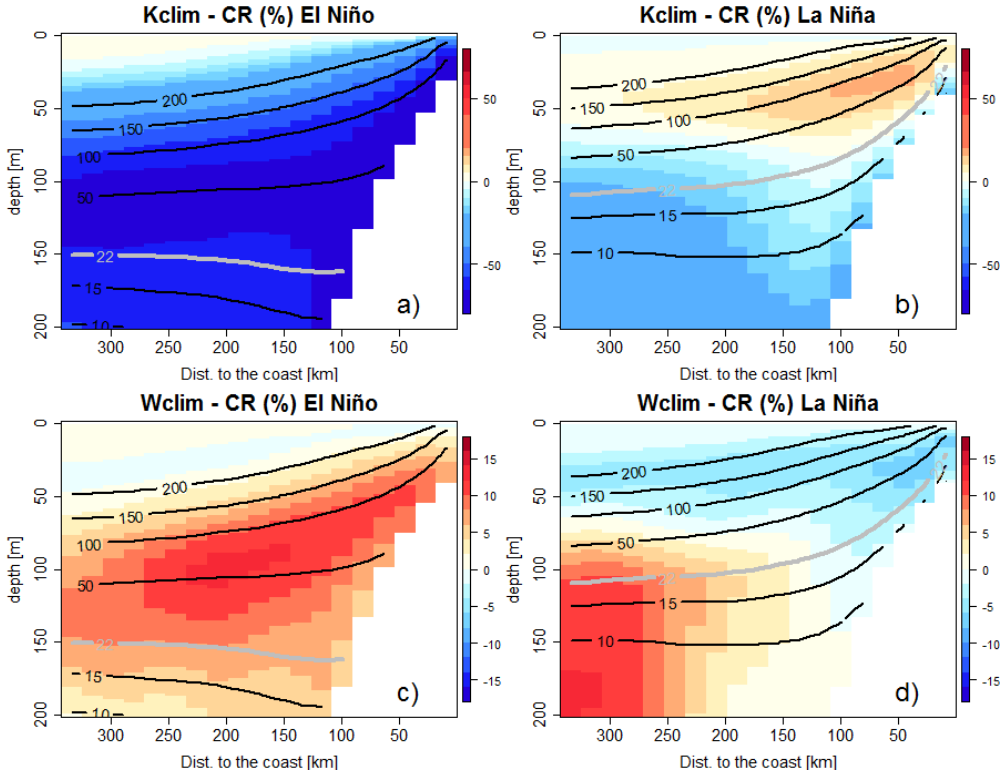

Figure 12. Alongshore-averaged vertical sections of DO concentration change (in %) for Kclim (a, c) and Wclim (b, d) with respect to CR, during LN (top) and EN (bottom). Black isolines mark DO concentration during LN (a, b) and EN (c, d) in the CR simulation. Note the different scale for Kclim and Wclim due to the stronger DO changes in Kclim.

In conclusion, the equatorial remote forcing was the main driver of changes in the ZO2 and OMZ core during both EN and LN. The local wind fluctuations played a minor role, slightly increasing the ventilation of the surface layer and biological production of oxygen due to more upwelling and vertical mixing during LN. During EN, the effect of the wind variability was slightly stronger: coastal upwelling was enhanced due to the alongshore wind increase associated to the SST warming (Chamorro et al., 2018), which partly compensated the ZO2 deepening driven by the downwelling CTWs.

4. Discussion

4.1. Bias of the modelled OMZ

The interannual variability of the main physical parameters, surface productivity and nutrients simulated by our model were validated in Espinoza-Morriberón et al. (2017). The model reproduced well the changes of SSH, temperature, nutrients and chlorophyll-a (Chl) in surface and subsurface waters during both EN and LN phases. Here, we show that the model reproduced deoxygenation and oxygenation during LN and EN respectively, in agreement with previous studies based on *in situ* data analysis (Graco et al., 2007; Gutiérrez et al., 2008; Graco et al., 2017). Nevertheless, some discrepancies were observed. First, between 2°N and 2°S, observational data evidenced a thin and coastal OMZ (*e.g.* Kartensen et al., 2008; Czeschel et al., 2015; Llanillo et al., 2018), that is not reproduced by our simulation. This may be due to the intense EUC simulated by the SODA model (used as the physical OBC forcing in our simulation) which ventilates the equatorial region (Montes et al., 2014). Off Peru, overly low DO (< 5 μmol kg^{-1}) was found within the modelled OMZ core (Figs. 2, 3). This bias with respect to the CARS climatology and IMARPE observations could be partly due to the numerical artefacts during the construction of the 3D fields and/or to the inclusion of records from old instruments which were not sufficiently accurate at low DO values (Bianchi et al., 2012). Underestimation of OMZ volumes slightly more oxygenated than the core was also reported *i.e.* Fuenzalida et al. (2009). Blending vertical high-resolution CTDO profiles with quality-controlled bottle casts from WOD01, Fuenzalida et al. (2009) found that the extent of hypoxic areas (< 60 μmol kg^{-1}) in the TSEP was underestimated in global databases such as WOA01. Note that the more recent WOA 2013 DO climatology (Garcia et al., 2013) did not display lower values than CARS (Figure not shown), so for that reason we chose the latter.

Crude parameterization of the oxygen cycle in the PISCES model, due to the fixed-in-time values of biogeochemical parameters (*e.g.* remineralization rate of DOC and nitrification rate) throughout the interannual simulation may also impact the modelled OMZ. For example, the remineralization rate of DOC only takes into account a proxy of bacterial concentration and DOC concentration in PISCES (Aumont et al., 2015), even though temperature changes (which are particularly strong during EN) impact the bacterial metabolic rates involved in the oxygen cycle (López–Urrutia et al., 2016), an effect seldom included in biogeochemical models (Segschneider and Bendtsen, 2013). Note also that previous regional models of the OMZ using the nitrogen-based BioEBUS model (Gutknecht et al. 2013) also produced a more intense OMZ than the observations (Montes et al. 2014; Vergara et al. 2016; Mogollón and Calil 2017).

Last, we cannot exclude the possibility that our boundary forcing (SODA) may have partly induced the very low OMZ concentrations simulated by our model. Indeed, Montes et al. (2014) showed that using different sets of physical OBCs, which differed in the SSCCs vertical structure intensity, could modify the shape and intensity of the OMZ.

4.2. Impact of eastward fluxes from the equatorial region

The equatorial circulation was impacted during ENSO, which modified the eastward oxygen fluxes in the equatorial region offshore of the PCUS. To illustrate it, the intensity of the zonal currents (EUC, pSSCC and sSSCC) and associated oxygen fluxes at 88°W between 50 m and 200 m were computed (Table 2). The EUC was weaker during EN and LN than during neutral conditions. Stramma et al. (2016) also found a strong weakening of the EUC velocity during the onset (October) of the 2015–2016 EN. In contrast, the SSCCs intensity increased during EN with respect to LN and neutral conditions. These results are in line with Montes et al. (2011), who simulated the circulation during the moderate 2002–2003 EN and 1999–2000 LN. Even though stronger SSCCs were observed during EN, the nearshore water column (*e.g.* at 9°S, Fig. 7) was mainly fed by waters initially transported by the EUC. The water masses transit time from 88°W to the nearshore region ranged from ~ 15 months during LN to ~ 6 months during EN (Montes et al., 2011; Espinoza-Morriberón et al., 2017). This shows that not all particles released in the equatorial zone reached the nearshore regions during the same ENSO phase. In the equatorial region, in our simulation, the oxygen fluxes variability is driven by the equatorial currents variability, and not by oxygen variability as oxygen western boundary conditions are climatological. Thus, the oxygen fluxes from the SSCCs and the EUC were less intense during LN than during EN (an exception is the EUC flux during moderate EN; see Table 2). During EN, enhanced SSCCs oxygen contributed to reduce the OMZ volume and displace its offshore boundaries eastward (Montes et al., 2014).

	Oxygen zonal flux at 88°W (10^4 µmol m^{-2} s^{-1})				Zonal current at 88°W (cm s^{-1})			
	La Nina	Neutral	El Nino (moderate)	El Nino (extreme)	La Nina	Neutral	El Nino (moderate)	El Nino (extreme)
EUC	5.80	7.59	4.59	6.61	5.80	7.48	4.20	5.43
pSSCC	2.34	2.65	4.08	3.99	2.94	3.21	3.87	3.74
sSSCC	0.58	0.89	1.48	2.22	1.55	2.10	2.17	2.00

Table 2. DO mean zonal fluxes (in 10^4 µmol m^{-2} s^{-1}) and intensity of the zonal currents (in cm s^{-1}) from the EUC, pSSCC and sSSCC during LN, Neutral and, moderate and extreme EN periods. The EUC, pSSCC and sSSCC DO and velocity were averaged between 2°N – 2°S, 2°S – 6°S and 6°S – 10°S respectively and from 50 m to 200 m depth at 88°W.

4.3. Ventilation by eddy fluxes

Horizontal eddy fluxes also play an important role near the OMZ boundaries where strong oxygen horizontal gradients are found. In a recent modelling study, Vergara et al (2016), showed that horizontal eddy fluxes through the OMZ coastal boundary attains its maximum in winter in association with a maximum seasonal Eddy Kinetic Energy (EKE). Similarly, the EKE increase during EN induces a large interannual horizontal eddy flux which ventilates the nearshore OMZ. The magnitude of this enhanced interannual ventilation by horizontal eddy fluxes could be underestimated due to the relatively low horizontal resolution (1/6°) of our model (*e.g.* Capet et al., 2008; Colas et al., 2012). However, a resolution of 1/6° is considered eddy-resolving off Peru: due to its proximity to the equator, the typical length scale of mesoscale structures would be covered by ~ 10 grid points (Belmadani et al., 2012). Indeed, in spite of this caveat, our model represented correctly the spatial and interannual variability of the EKE (Espinoza-Morriberón et al., 2017). Nevertheless, a more complete modeling study with an increased spatial resolution would be needed to better understand and quantify the role of submesoscale variability on the OMZ (Thomsen et al., 2016).

4.4. Impact of ENSO Diversity

It is important to mention that our analysis did not take into account the diversity of EN events. Indeed, a Central-Pacific (CP) EN (Modoki; *e.g.*, Takahashi et al., 2011) is likely to impact the OMZ differently than a canonical Eastern Pacific (EP) EN. CP EN events are frequently

associated to upwelling CTWs during fall and winter, in contrast with the more frequent downwelling CTWs observed during EP EN (Dewitte et al., 2012). Thus, during EN Modoki poor oxygen waters could be more present than during a canonical EN, due to a shoaling of the ZO2 triggered by the passage of the upwelling CTWs (*e.g.* Fig. 5f). Besides, in early 2017 a 'coastal El Niño' occurred (Takahashi and Martínez, 2017; Garreaud et al., 2018), which also had a different impact on the DO. In fact, during canonical EN (*e.g.* 2015–2016 EN) a deepening of the ZO2 occurred, while during the summer of 2017 (Coastal EN) the impact was greater in the surface layer but the ZO2 stayed shallower (ENFEN, 2017).

4.5. Biological Processes

Remineralization is the major oxygen sink in the water column (Paulmier and Ruiz-Pino, 2009) and is mainly produced by bacterial respiration off Peru (Kalvelage et al., 2015). This is reproduced in our modelling results (Fig. 10). Furthermore, zooplankton respiration has been little studied in the PCUS in spite of its high oxygen demand in the water column. Global estimates of mesozooplankton respiration (in fraction of body carbon respired daily) indicated that it represents ~ 17 – 32 % of the photosynthetic carbon produced in the open ocean (Hernández-León and Ikeda, 2005; underestimated in previous works *e.g.* del Giorgo and Duarte, 2002). In our configuration, the zooplankton respiration represented ~ 33 % of the oxygen produced by photosynthesis (between 6°S – 16°S and 0 – 200 m depth), close to global estimates. High biomass of zooplankton has been found in the PCUS, showing that zooplankton can adapt to low-oxygen conditions at great depths (Ayón et al., 2008a; Ballón et al., 2011). This implies a high oxygen consumption at greater depths due to the mesozooplankton respiration, which is more tolerant to suboxic condition than microzooplankton (this is explicitly included in PISCES). However due to a lack of data, the zooplankton biomass in PISCES (see Fig. 14 in Espinoza-Morriberón et al., 2017) could not be evaluated, which is needed to estimate reliable respiration rates.

Our model setting has also some limitations, as the nitrogen cycle is crudely parameterized in PISCES (Aumont et al., 2015). High concentrations of nitrous oxide (N_2O), a potent greenhouse gas produced during nitrification (Codispoti and Christensen, 1985), have been observed off the Peruvian coasts (Kock et al., 2016), especially during pulses of oxygenation. Although not simulated by our model, production of nitrous oxide is likely to occur during EN due to enhanced nitrification in subsurface layers (Fig. 11l). Using the nitrogen-cycle-based ROMS-BioEBUS coupled model, Mogollón and Calil (2017) found a decrease (80 %) of nitrification between the peaks of 1997–1998 EN and 1999–2000 LN and production of nitrous oxide during

EN. In line with this study, our model simulated a nearshore nitrification decrease of ~ 60 % between EN and LN (within 20 km from the coast and between 20 and 80 m depth). Furthermore, under suboxic conditions (< 5 – 10 µmol kg^{-1}), both anammox (Lam et al., 2009) and denitrification could produce N loss (Dalsgaard et al., 2012). The percentage of N loss contribution by both processes depends on ENSO phases. During 1997-98 EN, anammox and denitrification contribute to N loss of 40 % and 60 %, respectively, while during 1999–2000 LN the contribution of anammox increase of 70 % (Mogollón and Calil, 2017). In PISCES, anammox is not included, which could explain the overestimation of nitrate in our simulation (see Fig. 3 in Espinoza-Morriberón et al., 2017).

In PISCES, denitrification occurred in regions of DO less than 6 µmol kg^{-1} (hereafter ODZ) and was simply parameterized using DOC and a remineralization rate (Aumont et al., 2015):

$$Denit = R_{NO3} * \lambda^{*}_{DOC} * \Delta(O_2) * DOC$$

Where R_{NO3} represents the N/C stoichiometric ratio. Our model simulated an increase of the denitrification in nearshore and shallower waters during LN (e.g. during the 1999–2000 LN, Fig. 13a), due to the shoaling of the ODZ, despite of the unchanged ODZ volume. This is likely due to a shoaling of the OMZ (Fig. 3j), which allowed denitrification to occur at shallower depths, and enhanced remineralization (Fig. 11c). In contrast, during EN, the ventilated water column inhibited denitrification above ~ 200 m, and a deeper offshore ODZ was observed (*e.g.* during the 1997–1998 EN, Fig. 13b). Overall, denitrification within the ODZ (defined between 6°S – 16°S, 0 – 500 km and 0 – 500 m depth) increased by ~ 25 % during LN and decreased by ~ 60 % during EN (moderate or extreme), with respect to neutral periods (Fig. 13c). Using a global biogeochemical model, Yan et al. (2017) found a denitrification increase of ~ 70 % between the peak of 1997–1998 EN and 1999–2000 LN, which is close to our estimate (~ 85 %).

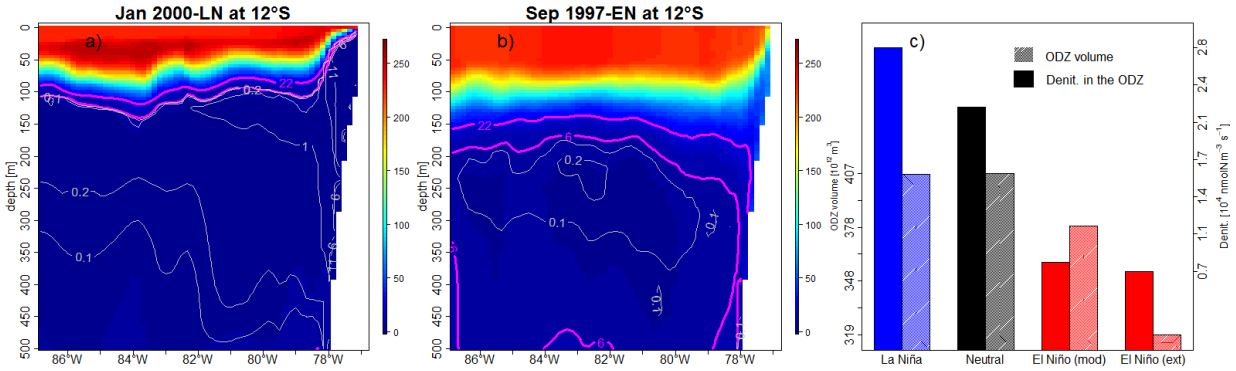

Figure 13. Cross-shore vertical sections (12°S) of DO concentration (colour shading and magenta lines, in µmol O_2 kg^{-1}) and denitrification (gray lines, in 10^4 nmolN m^{-3} s^{-1}) during the peak of 1997–1998 EN (a) and 1999–2000 LN (b) at 12°S. (c) WDC volume and mean denitrification during LN (blue bar), Neutral (black bar), moderate and extreme EN (red bars).

5. Conclusions and perspectives

In the present work, the physical and biological processes that drive the interannual variability of the TSEP OMZ were studied using the physical-biogeochemical ROMS-PISCES coupled model. First, an evaluation of our interannual simulation over the period 1958-2008 showed that, despite a reasonable bias in the representation of the modelled OMZ, the phases of oxygenation and deoxygenation during EN and LN were qualitatively well reproduced. During EN, the nearshore ZO2 deepened due to the passing of remotely-forced intense 'downwelling' CTWs. During LN, the ZO2 shoaled due to the less intense 'upwelling' CTWs, enabling oxygen-depleted waters to accumulate on the shelf. The remote equatorial forcing (IEKWs) was responsible for the tight correlation between the thermocline and ZO2 close to the coasts.

Furthermore, the characteristics of the equatorial SW which were transported towards the coast and fueled the nearshore water column were investigated. SW were mainly transported eastward by the SSCCs (located south of the equator) and EUC during LN and EN, respectively, before reaching the Peru coast. During EN the SW were more oxygenated as they originated from the north of the OMZ and transited faster to the coastal region than during LN.

The vertical and horizontal oxygen eddy fluxes were also evaluated. On average, the offshore (between 100 – 500 km from the coast and 6°S – 14°S) vertical eddy flux brings oxygen to the surface layer (above ~ 60 m), while it removed oxygen below. This flux was not modified during LN, but during EN a very strong decrease was observed, due to the reduced oxygen vertical gradient resulting from the deepening of the ZO2. Horizontal eddy fluxes tended to inject oxygen into the OMZ from its lateral boundaries, especially at its southern limit where

the horizontal gradient of O2 is intense. This was not modified during LN with respect to neutral period. However, during EN, the horizontal oxygen eddy fluxes strongly increased due to the increase of eddy activity, intensifying eddy-driven horizontal ventilation.

Regarding the biogeochemical processes, remineralization was the main process consuming oxygen in the water column, followed by zooplankton respiration and nitrification. These oxygen sinks were strongly altered during ENSO phases, depending on oxygen availability in the water column.

Sensitivity experiments performed to evaluate the influence of the equatorial remote (i.e. CTWs) and local forcing (*e.g.* wind), demonstrated that the equatorial forcing had a greater impact than local winds on the DO changes, in particular during EN.

Future studies will address the mechanisms which drive the DO changes off Peru over the last decades. While a deoxygenation trend has been observed in the open ocean (Stramma et al., 2008; Breitburg et al., 2018), a nearshore shoaling of the TSEP OMZ has also been described in the late 2000s (Bertrand et al., 2011). In contrast, a relative oxygenated-water column was observed in the last decade on the Peru central shelf, likely due to more frequent downwelling CTW (Graco et al., 2017). Future studies will also address the impact of climate change in the PCUS. As downscaled projections of climate scenarios in the PCUS simulated a strong near-surface stratification increase (Echevin et al., 2011, Oerder et al., 2015), this could hamper ventilation and intensify the OMZ. However, further deep and poleward proxy data and instrumental observations suggest ventilation of the OMZ core overthe last decades (Gutiérrez et al., *in prep*).

6. Appendix

Table 1. La Niña and El Niño periods between 1958 and 2008.

LA NIÑA		EL NIÑO	
Period	**Duration (months)**	**Period**	**Duration (months)**
Mar. 1960 - Nov. 1960	9	Mar. 1965 - Oct. 1965	10
Apr. 1961 - Jun. 1963	27	Mar. 1972 - Feb. 1973 (*)	12
Jan. 1964 - Dec. 1964	12	May 1976 - Oct. 1976	6
Mar. 1966 - Jul. 1968	29	Jul. 1982 - Nov. 1983 (*)	17
Mar. 1970 - Nov. 1971	22	Dec. 1986 - Dec. 1987	13
Apr. 1973 - Mar. 1974	12	Oct. 1991 - Jun. 1992	9
Jul. 1974 - Mar. 1975	9	Mar. 1993 - Sep. 1993	7
May 1975 - Feb. 1976	10	Mar. 1997 - Sep. 1999 (*)	19
Feb. 1978 - Oct. 1978	9	Sep. 2002 - Jan. 2003	5
Jul. 1980 - Nov. 1981	17	Aug. 2006 - Feb. 2007	7
Feb. 1984 - Jul. 1984	6		
Jan. 1985 - Dec. 1985	12		
Mar. 1988 - Dec. 1988	10		
Apr. 1989 - Oct. 1989	7		
Jun. 1990 - Jan. 1991	8		
Mar. 1994 - Aug. 1994	6		
Apr. 1995 - Sep. 1995	6		
Nov. 1995 - Jan. 1997	15		
Apr. 1999 - Mar. 2000	12		
Jul. 2000 - Dec. 2000	6		
Jun. 2001 - Jan 2002	8		
Jul. 2005 - Dec. 2005	6		
Apr. 2007 - Jan. 2008	10		

(*) Extreme El Niño period

CHAPTER 5:
OCEANOGRAPHIC TRENDS DURING THE LAST DECADES

Biogeochemical trends in the Peruvian Upwelling System: what are the involved mechanisms?

1. Introduction

In the last 50 years, global SST has increased because of anthropogenic climate change. In contrast, during the last three decades (1980-2010), satellite and in situ data collected by IMARPE have shown a negative SST trend off Peru [Gutiérrez et al., 2011a, 2011b; Dewitte et al., 2012], a deoxygenation trend [Graco et al., 2017; Yang et al., 2017] and an increase in primary productivity [Gutiérrez et al., 2011a; Demarcq et al., 2009] (see section 3 in chapter 1). Few studies have explored the processes involved in the physical and biogeochemical trends off the Peruvian sea, such as the wind influence [e.g. Gutiérrez et al., 2011a] and the remote equatorial forcing associated with Equatorial Kelvin waves [e.g. Dewitte et al., 2012].

The main objective of the present chapter is to evaluate the capability of the model to reproduce the observed trends in the PCUS using IMARPE in situ data and satellite data. Then, we focus on explaining the processes involved in the the subsurface deoxygenation and increase in primary productivity, which may enhance oxygen consumption by increasing subsurface remineralization of organic matter. Furthermore, the shoaling of OMZ upper limit could reduce the habitat of many species [Diaz and Rosenberg et al., 2008], such as the anchovy of high commercial value [Bertrand et al., 2011]. Thus, understanding the processes that generate these biogeochemical trends is important in the context of present and future climate change.

2. Evaluation of Surface and Subsurface Trends

In the previous chapters (3 and 4), the capability of the model to reproduce interannual variability is evaluated for the main physical and biogeochemical variables. In this section the SST, SSH, Chl, Nitrates and OMZ depth trends are computed and compared to observations. Although the control simulation (CR, see sections 2.2 and 2.5 in the Methodology chapter 2 and CR validation in chapter 3) covers the period from 1958 – 2008, only the trends over the last 30 years are evaluated (from 1979 – 2008). Indeed, the ecosystem exhibited a regime shift (e.g. Alheit and Ñiquen [2004]) at the end of the 80's, as shown by Gutiérrez et al. [2011a] using paleoceanographic proxies ($U_{37}^{k'}$,based on alkenone) and ICOADS SST data (from different observing systems) for the SST trend in the Pisco area (~ 13°S). Figure 1 shows that these databases exhibit a slight SST increase from 1960 – 1980, however shifting to coastal cooling

after beginnings of 80´s (more marked in the $U_{37}^{k'}$ SST proxy). In contrast, the model simulation does not represent a regime shift from warming to cooling conditions (between 6°S – 16°S and within 100 km to the coast). Before the 80's no significant trends of SST and thermocline are observed. However, between the 80's and 2008, a significant coastal cooling was reproduced in surface and subsurface (Fig. 2). For this reason and the fact that contrasted wind forcings are available after 1979, we decided to focused on the last 3 decades of simulations.

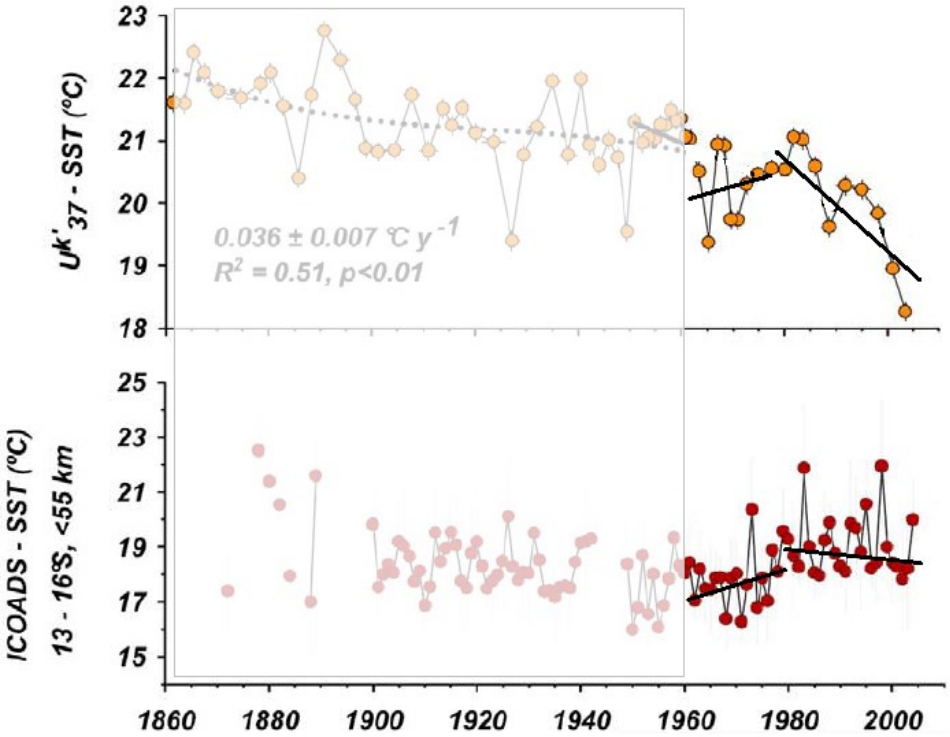

Figure 1. Coastal SST from a paleoceanographic proxy ($U_{37}^{k'}$, top) and ICOADS (bottom) near Pisco (~ 13°S). Figure modified from Gutiérrez et al. [2011a]

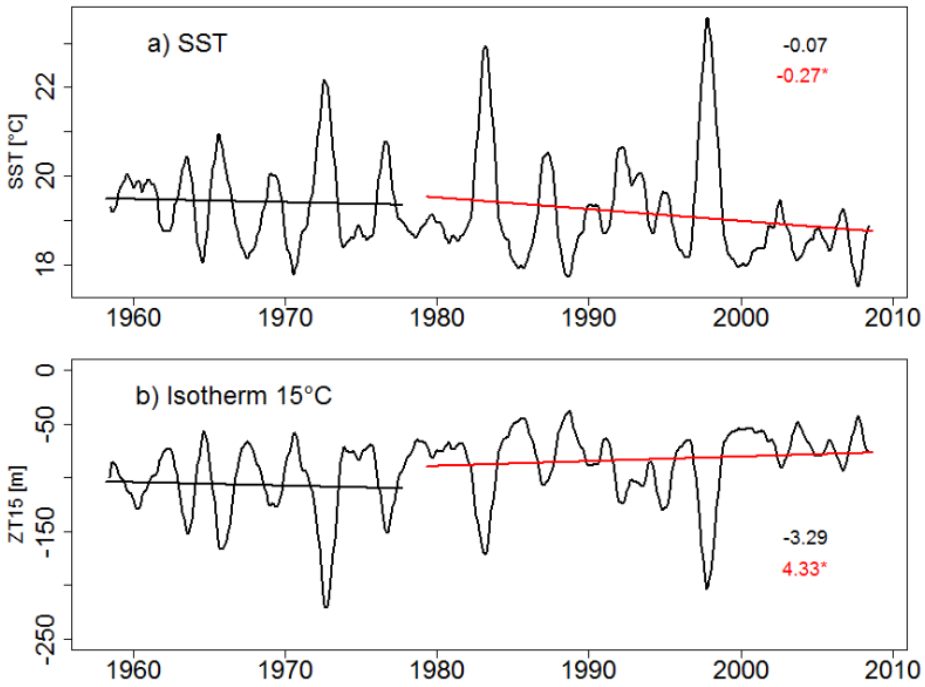

Figure 2. Times series of SST and thermocline depth (ZT15) averaged in a coastal box (6°S – 16°S and 100 km from the coast) for RPSoda (CR simulation). Linear trends are plotted for the two periods: 1958 – 1979 (black line) and 1979 – 2008 (red line). The trends also showed in °C dec-1 and meter dec-1 for SST and ZT15 respectively. (*) indicates that the trend was significant.

In addition, Bertrand et al. [2011] evidenced a deepening of the oxycline before the 80's and a shoaling after the 1982–1983 EN. Furthermore a thickening of the oxygen-poor layers in the eastern equatorial Pacific has been observed (Fig. 12). Such shoaling of the oxycline (proxy of the OMZ upper limit) is usually associated with an increase of the OMZ thickness, as the deeper limit of the OMZ does not present strong variations (see chapter 4). This may thus indicate that deoxygenation occurred during the last decades over a large portion of the water column. Last, it must be noted that the model trends are computed from timeseries that mimick the in situ timeseries, i.e. the model output is sampled at the same locations in time and space as the in situ observations were collected during IMARPE oceanographic cruises.

2.1. Temperature

Figure 3 shows that both the model and AVHRR data present a negative trend along the coast (over 1979-2008). The model overestimates the negative trend observed in AVHRR. The pattern of negative trend in the model extends further offshore and towards the equator, e.g. the

isoline of – 0.2 °C dec^{-1} is located 100 and 500 km offshore at 17°S and 7°S respectively. In AVHRR, trends lower than – 0.2 °C dec^{-1} are found within 150 km from the coast between 10°S – 14°S and within 20 km from the coast between 6°S – 10°S. The core of the negative trend pattern is observed at ~ 12°S for the model (– 0.5 °C dec^{-1}) and AVHRR (– 0.3 °C dec^{-1}).

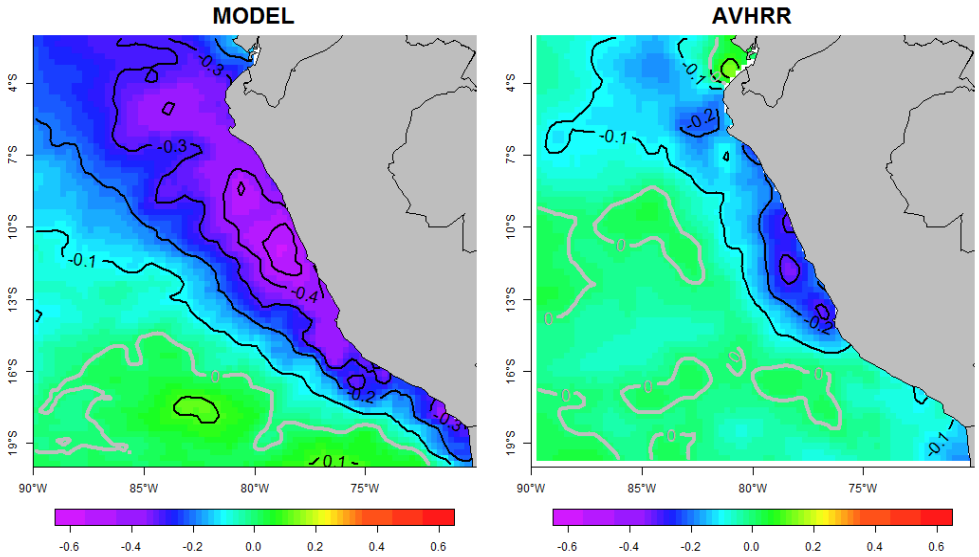

Figure 3. SST trend (°C dec^{-1}, over 1979-2008) from model (left) and AVHRR (right).

The SST trend from IMARPE data, AVHRR and model are shown in Figure 4, as a function of latitude and averaged in a coastal band (within 100 km from the coast). The three datasets show that stronger negative trends between 6°S – 14°S (where the data sampling is larger), although the trends are not significant at some latitudes (see section 4 in Methodology section). Trends of the model and IMARPE data have the same order of magnitude (~ – 0.6 °C) and both are greater than AVHRR (~ – 0.2 °C). It could be due to the scarce in situ data nearshore in AVHRR, as it may come from interpolation due to the high cloud coverage [Reynolds et al., 2007]. North of 5°S, a positive trend is observed, also shown by Gutiérrez et al. [2011a] using SST data at a pier off Paita (~ 5°S) in 1960-2010.

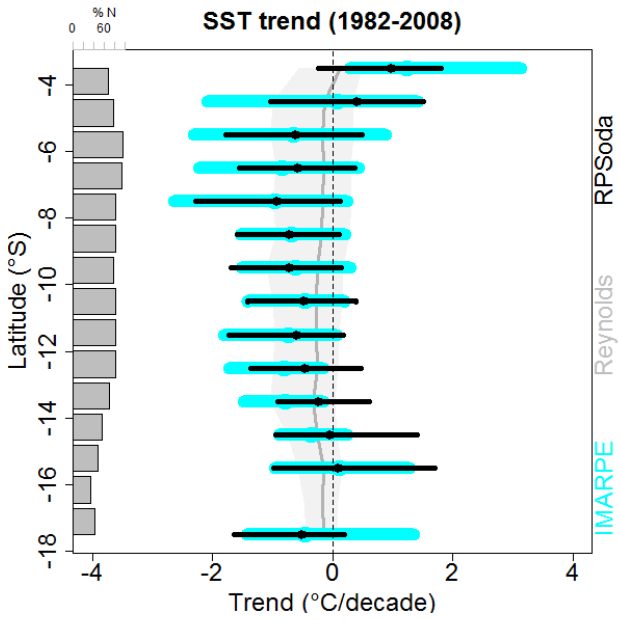

Figure 4. Latitudinal variation of SST trend (°C dec-1) in a coastal band (100 km from the coast) for the model (black), IMARPE (cyan) and Reynolds data (gray). Errors bar are computed with bootstrap. Gray bars represent the percentage of data taken into account to compute the trend. 100 % = 30 points, i.e. one data point per year over 1979 – 2008.

Three regions are defined to contrast the trends in different latitude bands: north-central (6°S – 16°S), north (6°S – 11°S) and central region (11°S – 16°S). As shown in Table 1 (see also Fig. S1), the SST trend is negative (however not significant) in the north-central (~ – 0.2 °C dec^{-1}) and north (~ – 0.3 °C dec^{-1}) regions for both the model and IMARPE data. Nevertheless, in the central zone where a greater amount of sampled observations was collected, a significant negative trend (~ – 0.5 °C dec^{-1}) for both the model and IMARPE data is found. Gutiérrez et al. [2011a] mentioned that the negative SST trend off Peru could be related to the wind increase during the last decades [Bakun et al., 2008, 2010], which could generate a wind-driven upwelling increase during spring. Nevertheless, in our model simulation, the upwelling, diagnosed by the vertical velocity (w) at the depth of the mixed layer, did not present a significant trend for both the north and central zones (Fig. 5).

	6°S - 11°S (North)		11°S - 16°S (Center)		6°S - 16°S (North-center)	
	IMARPE	**MODEL**	**IMARPE**	**MODEL**	**IMARPE**	**MODEL**
SST (°C dec^{-1})	-0.26	-0.32	-0.49	-0.51	-0.22	-0.25
ZT15 (m dec-1)	-1.89	-5.87	-8.42	-9.87	-4.17	-6.9

Table 1. SST and ZT15 trends in different latitude ranges (within 100 km from the coast). Gray shading mark significant trends.

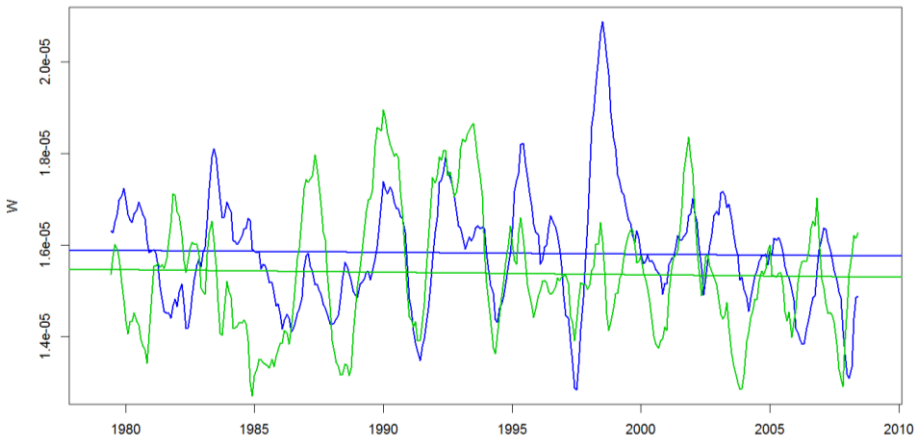

Figure 5. Model vertical velocity (in m s^{-1}) for north (6°S-10°S, blue line) and central (10°S-16°S, green line) regions. The vertical velocity at the depth of the mixed layer was averaged within 100 km from the coast in each region.

The statistically downscaled wind [Goubanova et al., 2010] was used to force our CR simulation using bulk formulae (Liu et al., [1979]). This implies that the model SST is used in the wind stress formulation, taking in account the air-sea interaction. In this formulation, the SST strongly impacts the wind stress amplitude. Therefore, the wind used as input can have a different variability (in space and time) with respect to the wind stress (see the contrasted trends in Fig. 6). In our case, the wind stress seasonal cycle is strongly correlated with the wind speed (cor = 0.95, pvalue < 0.05), however no correlation is found at interannual time scales (Fig.6).

The model simulated a positive trend for the nearshore wind stress (between 10°S – 15°S within 150 km to the coast) north of 6°S (Fig. 7), which may generate an upwelling increase. Nevertheless, between 10°S – 15°S, there was no upwelling increase (Fig.5) in spite of the wind stress increase (Fig. 6b), which would have enhanced the coastal cooling. This

suggests that the remote forcing (equatorial forcing) may be the main driver of the negative SST trend (Dewitte et al. [2012]). The mechanisms will be more detailed in section 3.

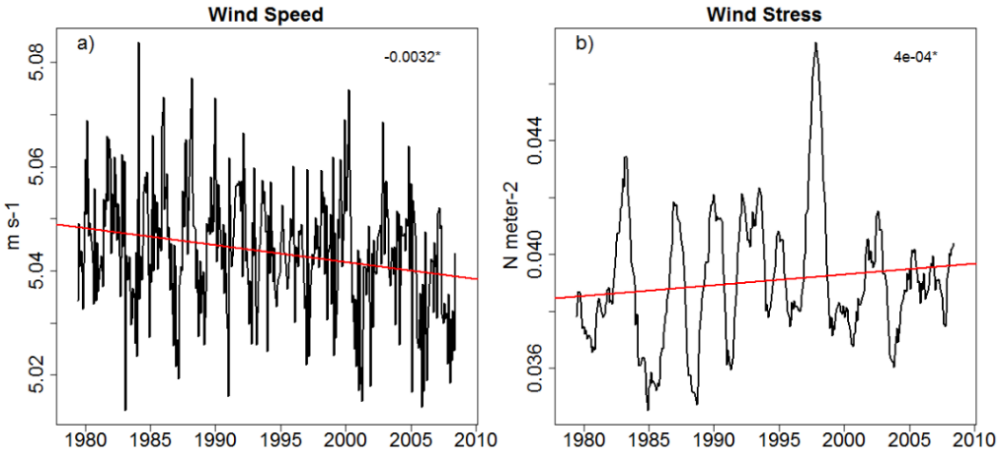

Figure 6. Time series of wind speed from Goubanova et al. [2010] and wind stress computed from the model's bulk formulation. The variables were averaged between 10°S–15°S and 0–100 km to the coast. Red lines represent the linear trend.

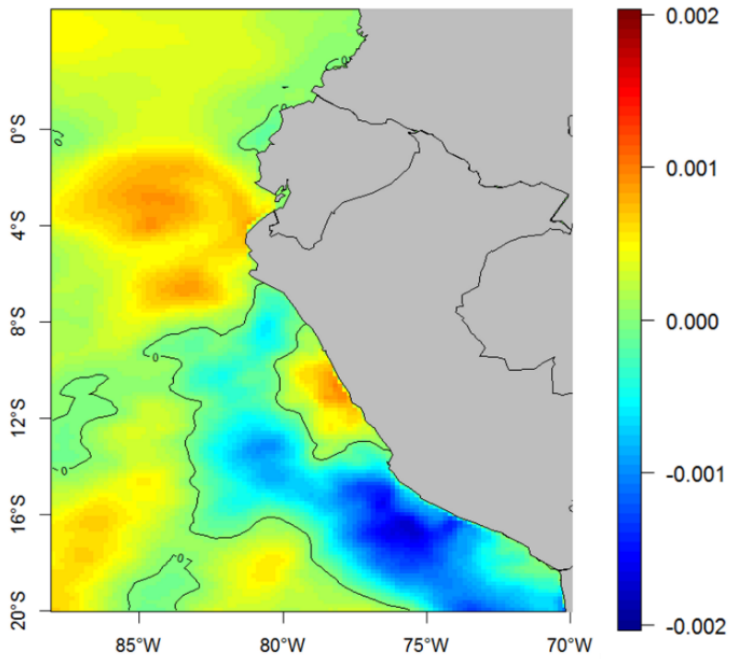

Figure 7. Spatial trend of the wind stress (N m^{-2} dec^{-1}) derived from the model bulk formulae.

In the subsurface layer, the depth of the thermocline (defined by the isoline of 15°C; ZT15) shows a shoaling trend over 1979-2008 (Table 2 and Fig. S2). In the north-central zone ZT15 presents a negative trend (shoaling) of - 4.2 m dec^{-1} and - 6.9 m dec^{-1} for IMARPE data

and the model respectively, the trend being significant only for the latter. The north zone presents a negative trend for the model and IMARPE data, however neither are significant. In the central zone (where more data were collected), a significant ZT15 shoaling of - 9.9 m dec^{-1} and - 8.4 m dec^{-1} was found for the model and IMARPE, respectively.

2.2. Sea Surface Height

Sea Surface Height (SSH) decreased in the last decades (Fig. 8). SSH generally mimics the thermocline variations. The negative SST and SSH trend spatial patterns are similar in the model, suggesting that the SST decrease is associated to a shoaling of the thermocline and SSH decrease. In contrast, satellite data from AVISO (available since 1993) showed a negative SSH trend along the coast (with equatorward offshore extension) with a lower magnitude than in the model. The SSH trend was less than –4 cm dec^{-1} north of 10°S in the model, whereas AVISO data presented a negative core at ~ 9°S (~ – 2 cm dec^{-1}). The SSH decrease off Peru (10°S – 20°S; – 3 cm dec^{-1}) has been previously studied for the 1992-2005 period by Qiu and Chen [2006], using information from a merged satellite product (T/P, Jason-1 and ERS – ½) and a simple "Baroclinic Rossby wave" model. They showed that the equatorial forcing is crucial at low frequencies (ENSO time scales, e.g. during 1997-1998 EN) and explains 54% of the SSH negative trend in the central-south region.

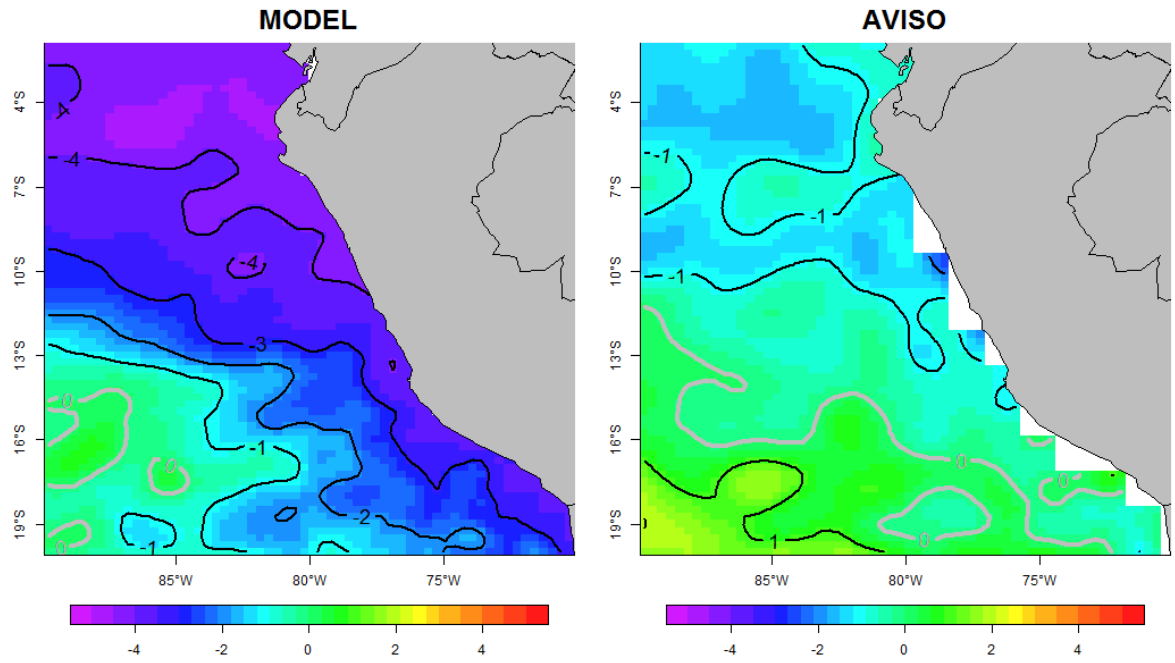

Figure 8. SSH trend (cm dec^{-1}) from model (left) and AVISO (right) between 1993 and 2008.

2.3. Surface Chlorophyll-a

Figure 9 displays the Chl positive trend in different latitude bands within 100 km from the coast, for the model, IMARPE and SeaWIFS satellite data. Note that the SeaWIFS trend is computed over a shorter period (1998-2008). The model and IMARPE observations show a significant positive trend from 1979 to 2008 between 6°S – 8°S and 13°S – 14°S, two latitude ranges where trends were calculated with more than 90% of the available data (30 years). The model trend between 6°S – 8°S (~ + 1 mg m^{-3} dec^{-1}) is slightly higher than the IMARPE trend (~ + 0.8 mg m^{-3} dec^{-1}). In contrast, between 13°S and 14°S, the trend is higher (~ + 1.5 mg m^{-3} $dec^{-1)}$ in the observations than in the model (~ + 0.3 mg m^{-3} dec^{-1}). The SeaWIFS trend presents a different latitudinal pattern, showing a higher value off central Peru at ~ 12°S (~ + 1.8 mg m^{-3} dec^{-1}). This discrepancy could result from the different time windows used to calculate the trends in the model and IMARPE data (1982 – 2008) and in SeaWIFS (1998 – 2008). Because of the relatively low data coverage for IMARPE data over 1998-2008, a trend was only calculated for SeaWIFS and the model over 1998-2008 from monthly Chl mean. Model was regrided to SeaWIFS resolution (~ 9 km) in order to compute the modeled Chl trend with and without the influence of the clouds (called Chl-cloud and Chl-non-cloud, respectively). Figure 10 shows that the model (cloud and non-cloud) and the satellite trends present very different patterns. SeaWIFS displays a positive trend (confirming the findings of Demarcq et al. [2009]) with values higher than + 0.5 mg m^{-3} dec^{-1} between 6°S – 16°S, and with two cores (+ 2 mg m^{-3}) between 8°S – 10°S and 12°S – 13°S . In contrast, the model presents an alternation of negative and positive patterns along the coast. Chl-cloud and non-cloud show the same spatial pattern trend, although Chl-non-cloud presents a weaker negative trend. Chl-cloud negative trends between 6°S – 8°S and between 12°S – 13°S had values of ~ – 2 mg m^{-3} dec^{-1}. The strongest positive trends were found further south, between 15°S - 18°S (> + 2 mg m^{-3} dec^{-1}). From 9°S to 11°S, trends were between 0.5 – 1.6 mg m^{-3} dec^{-1}. Thus, the model was not able to reproduce the positive trend observed during SeaWIFS period. This may be due to the few number of years covered by the satellite and the presence of clouds.

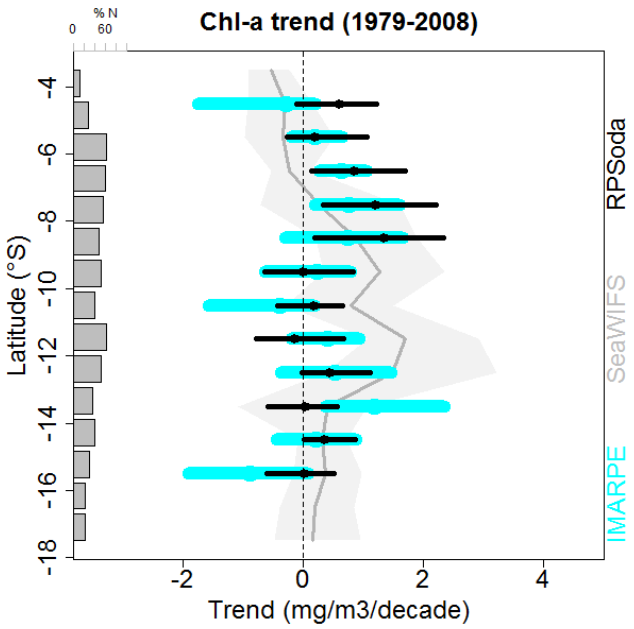

Figure 9. Surface Chl trend (mg m^{-3} dec-1) as a function of latitude and within 100 km from the coast for model (black), IMARPE (cyan) and SeaWIFS (gray). Note that the SeaWIFS period spans over 1998 – 2008, while the other period spans over 1979 – 2008. Error bars are computed with bootstrap. Bars in gray represent the % of data take in account to computed the trend, where 100 % = 30 points (1979 – 2008).

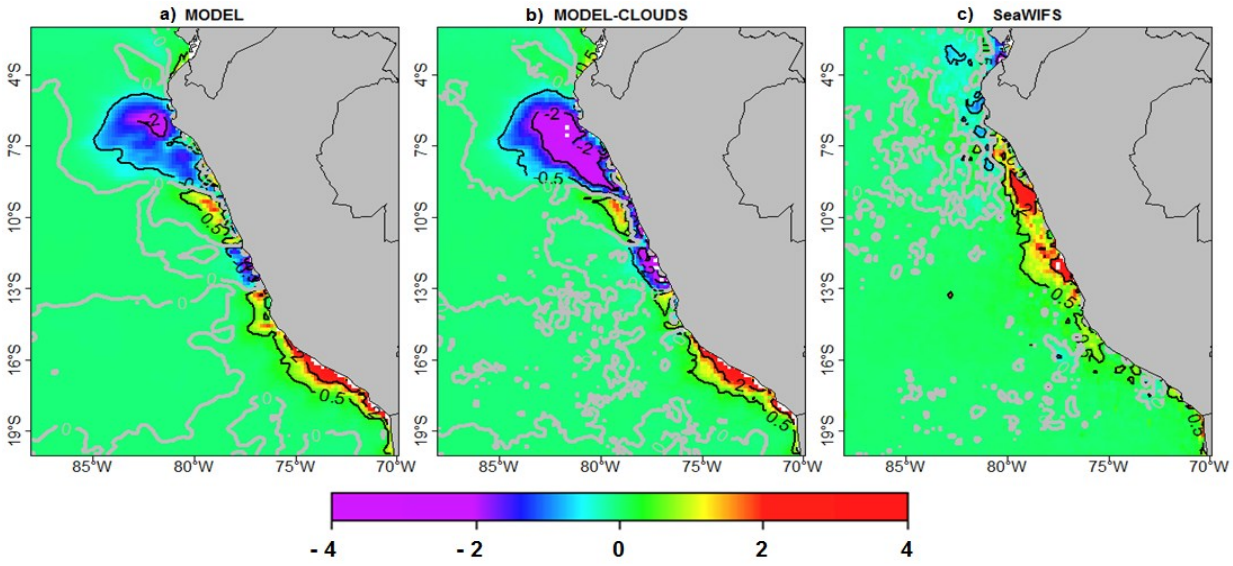

Figure 10. Surface Chl trend (mg m^{-3} dec^{-1}) from model without clouds (a), model with clouds (b) and SeaWIFS (c). The trends were computed during the SeaWIFS period (see also Fig. 13).

We now investigate the trends over a longer time period using IMARPE data and model output. The monthly time series of IMARPE and model Chl in the three coastal regions are

poorly correlated (Table 2 and Fig. S3). However, the north-central zone showed a positive trend of + 0.93 and + 0.62 mg m^{-3} dec^{-1} for the model and IMARPE respectively. In the northern region, the model (IMARPE) also presents a positive trend of + 0.87 (+ 0.53) mg m^{-3} dec^{-1}. The trend is stronger in the central zone (model: + 0.89 mg m^{-3} dec^{-1}; IMARPE: + 0.78 mg m^{-3} dec^{-1}) than in the north zone. Our results for the central region are comparable to those presented in Gutiérrez et al. [2011a]. They found near Pisco (~13.5°S) a Chl increase of 0.7 mg m^{-3} dec^{-1} between 1965 and 2005. This increase was corroborated with a corresponding increase of Total Organic Carbon during this period.

In conclusion, the model reproduced the positive Chl trend observed by in situ data from 1979 – 2008, although the model trend slightly overestimated the in situ Chl trend. However, the model was not able to capture the Chl increase alongshore during the SeaWIFS periods (1998 – 2008).

	6°S - 11°S (North)		**11°S - 16°S (Center)**		**6°S - 16°S (North-center)**	
	IMARPE	**MODEL**	**IMARPE**	**MODEL**	**IMARPE**	**MODEL**
Surface Chl (mg m^{-3} dec^{-1})	0.53	0.87	0.78	0.89	0.62	0.93

Table 2. Surface Chl trends in different coastal regions off Peru. Gray shading represent significant trends.

2.4. Nitrate

We now study the long-term evolution of surface and subsurface nitrate. The depth of the nutricline was calculated using subsurface in situ nitrate data. Whereas it is defined by the isoline of 16 µmol L^{-1} in the observations, we used the 21 µmol L^{-1} isoline in the model due to the overestimation of subsurface nitrate (~ 5 µmol L^{-1}). Figure 11 shows that model and IMARPE data present (non statistically significant) positive trends alongshore. The model presents a significant positive trend at 6°S and south of 16 °S, whereas the in situ trend is positive south of 13°S (except locally at ~16°S).

When decomposed in subregions, the nitrate surface data (see Table 3) evidenced a significant positive trend in the north-central (+ 0.66 µmol L^{-1} dec^{-1}), north (+ 0.73 µmol L^{-1} dec^{-1}) and central zone (+ 0.8 µmol L^{-1} dec^{-1}) for IMARPE in situ data (Figure S4). In contrast, the model trends were not significant in the northern (– 0.07 µmol L^{-1} dec^{-1}) and central zone

(+ 0.19 µmol L^{-1} dec^{-1}). Observations showed a deepening of the nutricline in the northern (+ 5.84 m dec^{-1}, significant) and central (+ 3.76 m dec^{-1}, not significant) zones, whereas the model trends were not significant in both areas (- 2.08 m dec^{-1} in the north and + 0.48 m dec^{-1} in the center). Note that the scarcity of subsurface nitrate observations is more important during the first years of the period of study (i.e. less than five measurements per month before 1995). Moreover, the observed deepening of the nitracline is somehow at odds with the SST decrease (see Fig. S1) and thermocline shoaling (section 1.1).

The scarcity of observations could partly explain the discrepancy between the observed and the model trends. Furthermore, it must be noted that the nitrate concentration is positively biased in the model. Nitrate is impacted by nitrification and denitrification, and these processes have not been evaluated in the model due to lack of data.

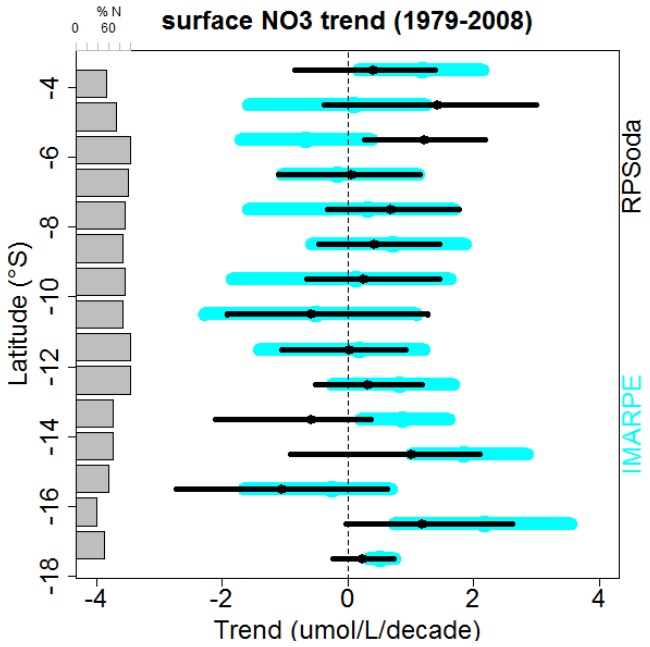

Figure 11. Surface nitrate trend (µmol L^{-1} dec-1) as a function of latitude and within 100 km from the coast for the model (black) and IMARPE data (cyan). Error bars are computed with bootstrap. Gray bars represent the percentage of data taken in account to compute the trend (100 % = 30 points corresponding to one data point per year for the period 1979–2008).

The model nutricline (21 µmol L^{-1}) and surface concentration do not follow a clear trend. However, the shoaling of nitrate isolines is found for other isolines corresponding to lower nitrate values and shallower depths (i.e. 10 and 15 µmol L^{-1}). This means that the model nitrate content increases in the upper water column, mainly in the north region (Table 3). On the other

hand, IMARPE data shows an increase in surface nitrate and a deeper nutricline (i.e. deepening of the 16 µmol L^{-1} isoline; Table 3). The trend of shallower isolines (i.e. 5 and 10 µmol L^{-1}; Table 3) in IMARPE data also indicates a shoaling of the upper part of the nitracline, which seems to be at odds with the deepening of the lower part of nutricline (see Table 3 and Fig. S5). The differences between IMARPE and model in subsurface layer might be related to the few number of sampled data (less than 15 points by months, Fig. S4 and S5) and the annamox process, which contributes to N loss, is not included in PISCES.

The hypothesis of an increase of nutrients at the coast is supported by recent work. An increase of nutrients (nitrates, silicates and phosphates) in subsurface layers (50 – 300 m) was found in the latitude ranges of the EUC (2°S – 2°N) and Tsuchiya Jests (2°S – 8°S) and between 84°W – 87°W and from 1976 to 2012 [Czeschel et al., 2015]. As the eastward jets transport water masses towards the coast, this result supports the concept of a nearshore nutrient increase.

	6°S - 11°S (North)		**11°S - 16°S (Center)**		**6°S - 16°S (North-center)**	
	IMARPE	**MODEL**	**IMARPE**	**MODEL**	**IMARPE**	**MODEL**
surface NO3 (mL L^{-1} dec^{-1})	0.73	-0.07	0.8	0.19	0.66	0
ZNO3 [5/10 umol/L] (m dec^{-1})	-0.43	-3.16	-0.89	-0.63	-0.85	-1.38
ZNO3 [10/15 umol/L] (m dec^{-1})	1.12	-7.55	2.68	-1.8	1.99	-2.25
ZNO3 ([16/21 umol/L] (m dec-1)	5.84	-2.08	3.76	0.48	5.44	0.53

Table 3. Trend of surface NO3 and depth of the nitracline (defined by the isoline of 21 and 16 µmol L^{-1} in the model and IMARPE data, respectively) in different latitudinal coastal regions (within 100 km from the coast). Trends of the depths of the 10 (5) and 15 (10) µmol L^{-1} isolines (i.e. shallower surfaces than ZNO3) from the model (IMARPE data) are also shown. Gray shading indicates significant trends.

2.5. Oxygen

To evaluate the oxygen long term evolution (see table 4 and Fig. S6), we computed trends for the surface O2 concentration and the depth of the upper limit of the OMZ (ZO2), defined as the depth of the 22 µmol kg^{-1} isosurface (see chapter 4). The model and observations present a negative surface trend in all the subregions, although the trends are not significant (except in the north from the model, -2.69 µmol kg^{-1} dec^{-1}). In subsurface layers, the model simulates a weak but not significant shoaling of ZO2 in the northern (- 1.13 m dec^{-1}) and central (- 2.94 m dec^{-1}) regions. Observations also display a shoaling of ZO2, which is significant only

in the central region (- 9.98 m dec^{-1}). The interannual fluctuations of the ZO2 are well represented by the model, as shown in Chapter 4. However, the non-significant model trends, which were computed using the same sampling as the data, could be influenced by the subsurface data scarcity.

	6°S - 11°S (North)		11°S - 16°S (Center)		6°S - 16°S (North-center)	
	IMARPE	**MODEL**	**IMARPE**	**MODEL**	**IMARPE**	**MODEL**
surface O2 (µmol kg^{-1} dec^{-1})	-2.51	-2.69	-2.6	-2.77	-0.04	-1.47
ZO2 (m dec-1)	6.06	-1.13	-9.98	-2.94	-3.79	-3.89

Table 4. Trends of surface O2 concentration and oxycline (22 µmol kg^{-1}) depth in the different latitudinal coastal regions (within 100 km from the coast). Gray shading indicates significant trends.

Stramma et al. [2008] showed the temporal variation between 1960 - 2005 of an oxygen profile between 5°S - 5°N and 105°W - 115°W, located offshore of the PCUS, evidencing the expansion of the OMZ in the Eastern Equatorial Pacific. They showed that OMZ expansion began in the early 80's and that the upper and lower limit of the OMZ were respectively shoaling and deepening. Figure 12 shows the temporal evolution of a modelled oxygen profile between 5°S - 5°N at 88°W, in the western part of the model domain, east of the box shown in Stramma et al. [2008]. In line with Stramma et al. [2008], the modelled OMZ is expanding, although the shoaling and deepening of the upper and lower limits are weaker than those shown by the in situ data west of this location. In addition, the depth range with O_2 values lower than 10 µmol kg^{-1} also expands from the early 80's, which is consistent with the findings of Stramma et al. [2008].

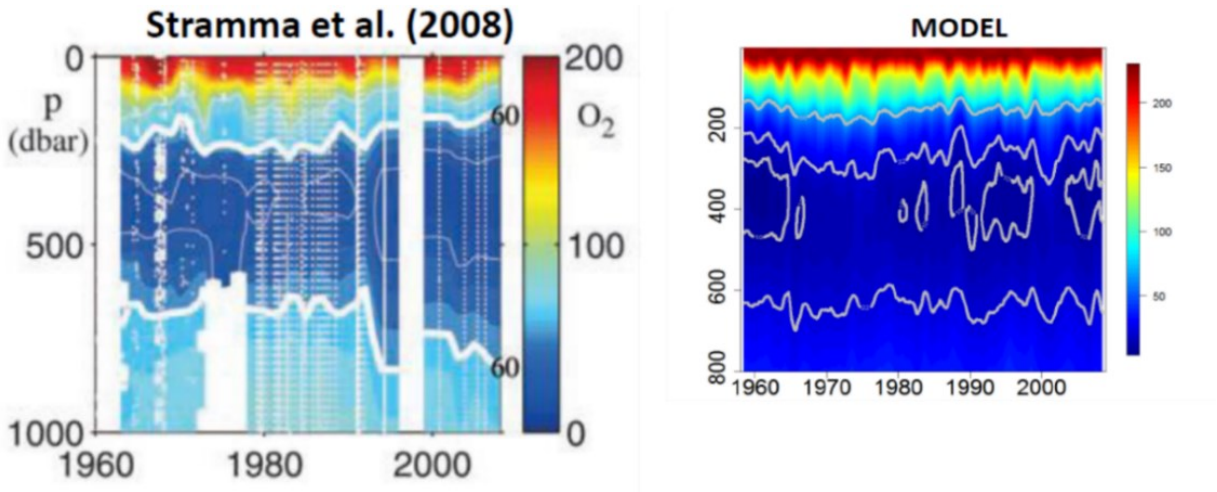

Figure 12. (left) Evolution of the oxygen concentration in the Eastern Equatorial Pacific (5°S – 5°N, 105°W-115°W) offshore of the PCUS between 1960 and 2008 (in contour the isoline of 66 µmol kg^{-1}, adapted from Stramma et al. [2008]). (right) same as left in the model domain (5°S – 5°N, 88°W). The model isolines indicate 66, 22, 10 µmol kg^{-1}.

3. Modelled Trends

In the previous section, we focused on the validation of the model respect to in situ (IMARPE) and satellite data. In this section, we analyze in more details the modelled trends of surface Chl and dissolved oxygen. As the Chl seasonality is large, the Chl trend is computed for each season and the terms limiting phytoplankton growth are studied. Furthermore, the processes involved in the nearshore deoxygenation are described.

3.1. Modelled Chl trend

The model simulated a Chl increase between 1979 and 2008 (Fig. 13). The model trend (> + 0.1 mg m^{-3} dec^{-1}) is significant nearshore and along the coast, overall in three regions: 5°S – 10°S, 11°S – 14°S and 16°S – 18°S. The trend is most intense in the northern region (between 6°S – 9°S), reaching maximum values between + 0.5 and + 0.7 mg m^{-3} dec^{-1} within 200 km from the coast. A weaker positive trend (~ + 0.2 mg m^{-3} dec^{-1}) is found within 100 km from the coast in the two other regions (Fig. 13a). In the following, we attempt to explain the intense positive trend found in the northern region. On average, the nearshore surface Chl (between 6°S – 10°S and 100 km from the coast) presents an interannual variability driven by ENSO phases, with a decrease and increase of productivity during EN and LN respectively (see chapter 3; Figure 13b). Furthermore, the surface Chl presents a significant positive trend of + 0.3 mg m^{-3}

dec^{-1} in average (Fig. 13b). In the time series, we can identify three distinct regimes between 1979 and 2008. First, during the 80's, a high productivity (~ 3.8 mg m^{-3}) is triggered by the frequent LN events, but this productivity is also partly compensated by low productivity during EN periods (1982–1983 EN and 1987 EN). Then, during the 90's, the low productivity (~ 2.9 mg m^{-3}) is mainly due to the moderate 1992–1993 and extreme 1997–1998 EN events. During the last period (between 2000 and 2008), high values (~ 4 mg m^{-3}) were found during the 1999 – 2000 LN and Chl remains relatively high due to the absence of strong EN events.

Figure 14 shows the vertical structure of the modeled Chl trend, averaged between 6°S – 16°S. We found a positive Chl trend from the coast to 200 km offshore and above 20 m depth. The most intense positive trend (~ + 0.2 mg m^{-3} dec^{-1}) is located between 50 – 110 km and 5 – 10 m depth. Nearshore, the Chl trend presents values of + 0.1 – 0.15 mg m^{-3} dec^{-1}, in surface, however below 10 m, a slightly negative trend (~ – 0.02 mg m^{-3} dec^{-1}) is observed.

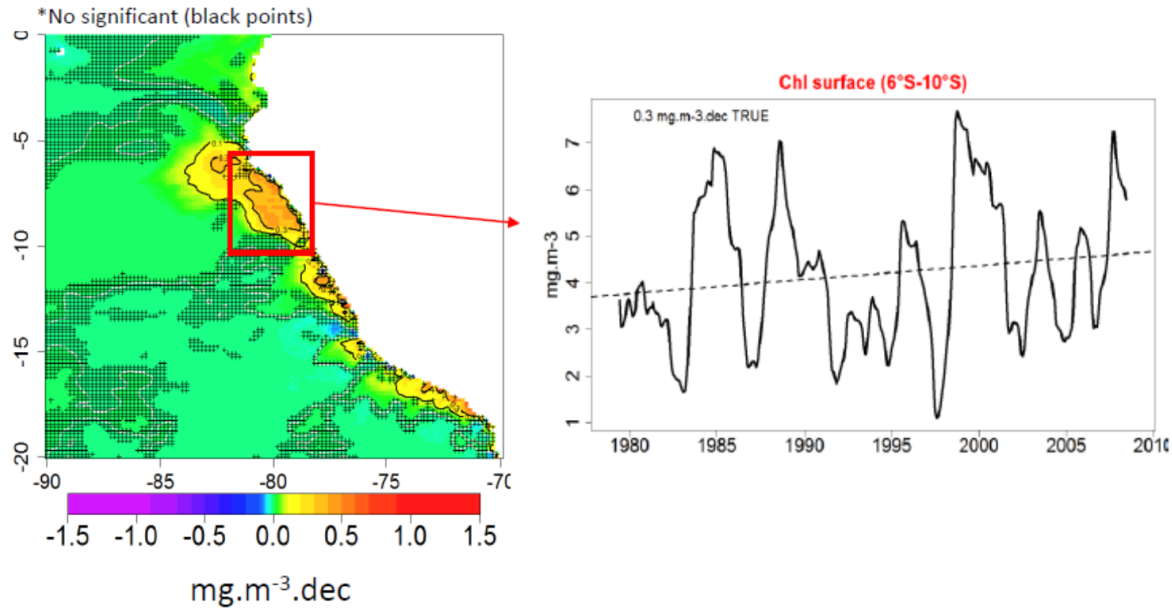

Figure 13. Spatial pattern of the trend (left panel) and time series (right panel) of modelled surface Chl. The timeseries is computed in a coastal box (6°S – 16°S and within100 km from the coast). Stippling in (a) indicates regions of non significant trend. In right panel, the "TRUE"/"FALSE" labels significant/ non-significant trends using bootstrapping.

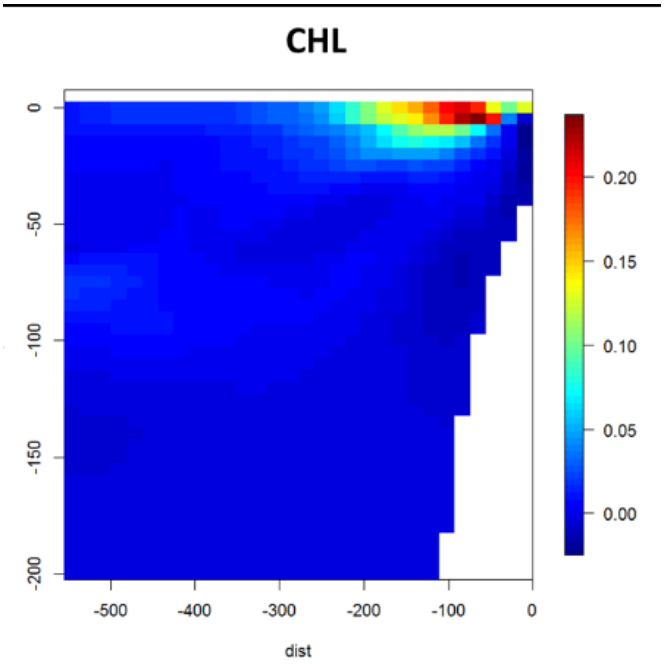

Figure 14. Vertical section (6°S – 16°S) of Chl trend (mg m^{-3} dec^{-1}) between 1979 and 2008.

In conclusion, the model simulates a significant positive Chl trend in surface and subsurface waters (mainly in the northern region). This trend could be associated with a specific season as Chl off Peru presents a marked seasonality [Gutiérrez et al., 2011a]. This is investigated in the next section.

3.1.1. Chl seasonal trends

The seasonalilty and alongshore variability of the trends is examined. Chl peaks in late austral summer – early autumn and decreases during winter owing to the interplay between the light and nutrient limitation [Calienes et al., 1985; Echevin et al., 2008; Messié and Chavez, 2015] (see section 1.4 in Introduction chapter). Gutiérrez et al. [2011a] hypothesized that a deeper mixed layer depth (MLD) associated to a wind increase during summer – spring (found in ERA-interim data) in the last decades drives the observed positive in situ Chl trend (see 3.2 in Introduction chapter).

The trend are computed for each seasons, in order to evaluate if the annual positive trend is maintained during each season (see also Fig. S7) or emerges from specific seasons. The most intense positive trend is found in summer (Fig. 15). It reaches + 0.3 mg m^{-3} dec^{-1} ,mainly within 100 km from the coast, but positive values are found as far as ~ 200 km from the coast (between 5°S and 9°S). The highest positive trend is found at ~ 8°S (+ 1–1.5 mg m^{-3} dec^{-1}). The autumn

trends are also positive but slightly less intense. The most intense trends in this season are found between 8°S and 14 °S within 100 km from the coast (+ 0.3 – + 0.5 mg m^{-3} dec^{-1}). In contrast, a negative trend is predominant within 50 km from the coast (~ – 0.1 mg m^{-3} dec^{-1}) during winter, and the strongest Chl decrease is found at 6°S (~ – 0.3 mg m^{-3} dec^{-1}). Last, both positive and negative trends are found nearshore during the transitional spring season. A positive trend dominates north of 10°S and at ~16°S (+ 0.1 – + 0.3 mg m^{-3} dec^{-1}), while a negative trend pattern is found between 10°S and 15°S (~ – 0.2 mg m^{-3} dec^{-1}).

In conclusion, the Chl positive trend found during 1979 – 2008 in annual means is mainly driven by the Chl increase in summer and autumn, whereas a systematic decrease of Chl is found in winter. Gutiérrez et al. [2011a] suggested that the spring Chl positive trend (between 1958 and 2001) could be related to the alongshore wind increase during warming seasons, which would enhance the upwelling of nutrients. In contrast, our model simulates a stronger Chl increase during summer. This increase could be related to the shoaling nutricline in summer as phytoplankton growth is limited by nutrient availability rather than by light during the warm seasons [Echevin et al., 2008; sea also chapter 3].

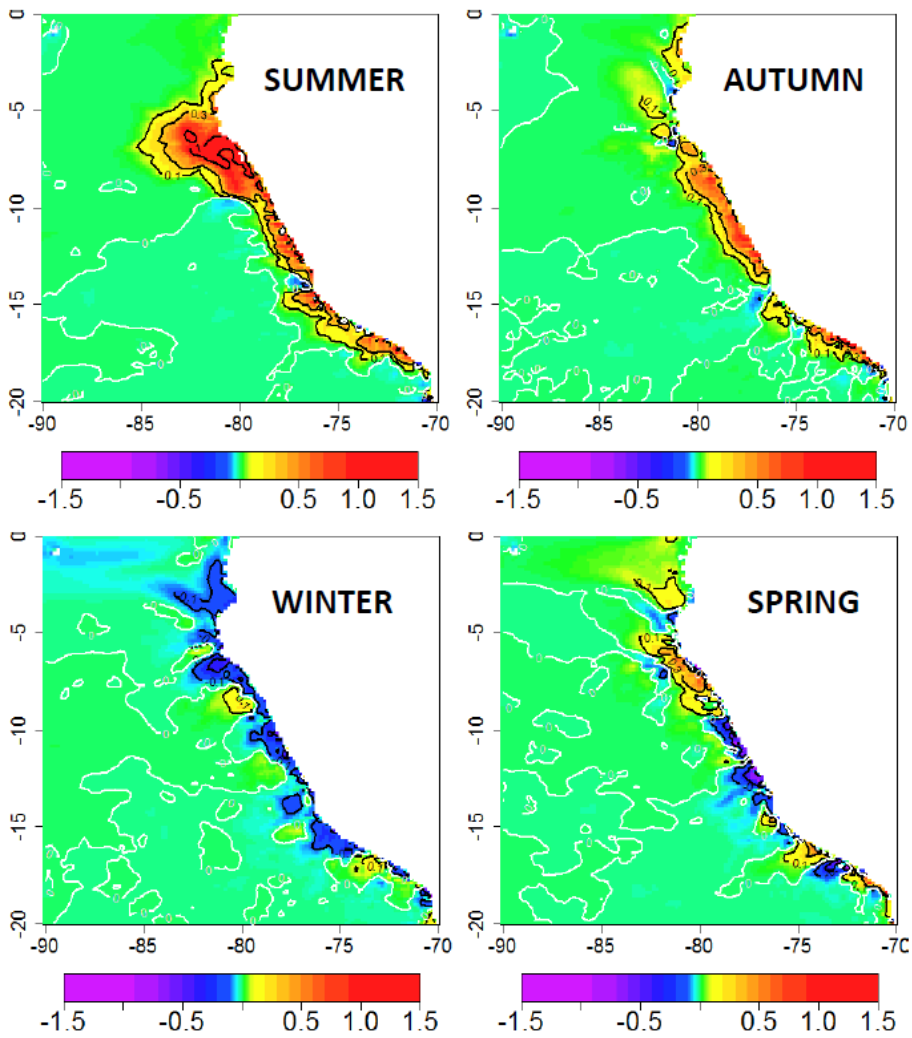

Figure 15. Seasonal trend from the model in mg m^{-3} dec^{-1} between 1958 and 2008. White line represents the isoline of 0 mg m^{-3} dec^{-1}.

Even though the seasonal trends of modelled Chl were computed from 1978 to 2008, they present relatively similar spatial patterns as those found in SeaWIFS. Indeed, SeaWIFS data presents positive trends (from 1998 and 2009) alongshore during summer, autumn and spring, albeit more intense than the model trends (Figure 16). Furthermore, SeaWIFS trends during winter are negative, mainly south of 10°S. In conclusion, the seasonal Chl trend from model and SeaWIFS are in line, both showed positive trends during warming season, while negative trends are found during winter.

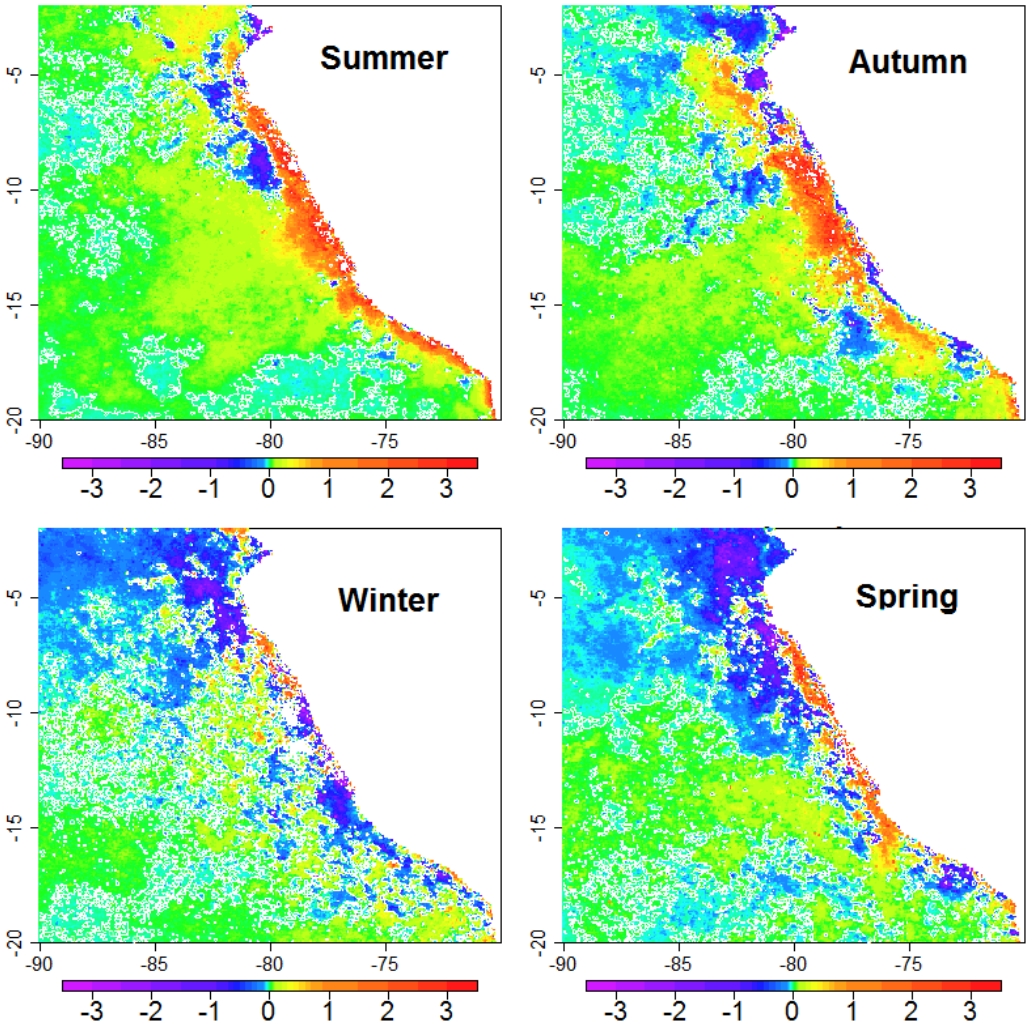

Figure 16. Seasonal trends (in n mg m^{-3} dec^{-1}) from SeaWIFS data between 1998 and 2008. The white line marks the isoline of 0 mg m^{-3} dec^{-1}.

3.1.2. Trends in nutrient and light limitation of phytoplankton growth

The trends of the limiting growth factors were computed in order to investigate the alongshore positive trend. The nutrient and light limititation factors are computed offline using the from PISCES model equations [Aumont et al., 2015].

The nutrient limitation for diatoms (N_{lim}^{D}), the more abundant phytoplankton off Peru [Sanchez et al., 2000], is defined as follows:

$$N_{lim}^{D} = min(N_{po4}^{D}, N_{Fe}^{D}, N_{no3}^{D} + N_{nh4}^{D}, N_{si}^{D})$$

N_{lim}^{D} is the minimum value of the limitation by phosphate (N_{po4}^{D}), iron (N_{Fe}^{D}), nitrogen ($N_{no3}^{D} + N_{nh4}^{D}$) and silicate ($N_{si}^{D}$). In nanophytoplankton, silicate limitation is not taken into account. Each nutrient limitation is computed as: $N_{nut}^{D} = Nut/(K_{nut}^{D} + Nut)$, where K_{nut}^{D} is the half-saturation constant of the nutrient.

The light limitation for diatoms (same for nanophytoplankton) is defined as follows:

$$L_{lim}^{D} = 1 - e^{\frac{\alpha^{D} \cdot (\frac{Chl}{C})^{D} \cdot PAR}{\mu_{D} \cdot N_{lim}^{D}}}$$

Where α^{D} is the initial slope of P–I curve, $\frac{Chl}{C}$ is the ratio between chlorophyll and carbon in the diatom, and PAR is the photosynthetic available radiation. Last, $\mu_{D} = ab^{cT}$, where a is the growth rate at 0°C, b is temperature sensitive of growth, c is temperature dependence of growth and T the water temperature.

Figure 18 shows the time series (from 1979 to 2008) of the nutrient and light limitation factors for diatoms, averaged between 6°S – 16°S and within 100 km from the coast and in the mixed layer, in the region where the positive Chl trend is intensified (Fig. 13). Values close to 1 indicate less limitation. The intensification of nutrient limitation is clear during EN events (e.g. 1997-1998 EN; Figure 17a), due to the nutricline deepening at the passage of downwelling Kelvin waves and coastal trapped waves (Graco et al. [2017]; see also Chapter 3). Beyond the EN events, nutrient limitation shows a significant positive trend (+ 0.01 dec^{-1}), which suggests that a relaxation of nutrient limitation occurs as more nutrient s become available in the surface layer. Light limitation, related to the insolation and MLD variability [Calienes et al., 1985; Echevin et al., 2008], displays a weakly negative, non-significant trend (Fig. 17b).

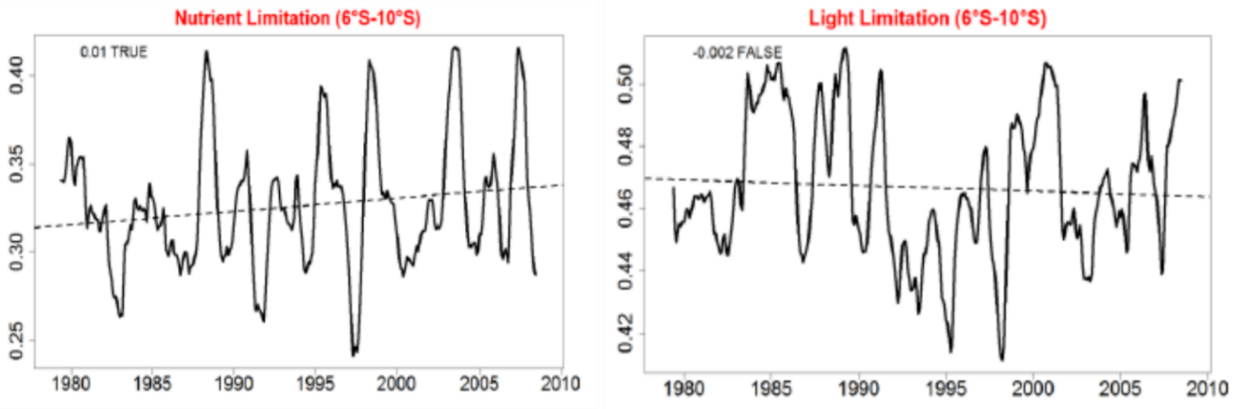

Figure 17. Timeseries (full line) and trends (dashed line) of nutrient (left panel) and light (right panel) limitation terms for diatoms. Values are averaged between 6°S – 16°S and within 100 km from the coast, in the surface mixed layer. The "TRUE"/"FALSE" labels significant/ non-significant trends using bootstrapping.

In order to understand the relaxation of nutrient limitation driving the positive Chl trend, the vertical structure of the nitrate trend is investigated. There is a strong positive trend above 100 m depth (Fig.18b). Close to the coast, the highest trend (~ + 1 µmol L^{-1} dec^{-1}) is found between 10 – 50 m and 80 – 200 km from the coast, while it is located at 50 – 75 m offshore (further than 300 km from the coast). Interestingly, the temperature trend (Fig. 18a) follows the same pattern as the nitrate trend. The link between the water masses in the upwelling region and those in the equatorial region has been highlighted in the previous chapters (3 and 4). The similar spatial patterns for the trends suggest that water masses from the offshore equatorial zone with a higher nutrient content and colder temperature may have reached the coastal region, subsequently decreasing the SST and increasing primary productivity. Furthermore, the spatial pattern of the surface nitrate trend (from 1979 to 2008) shows positive values between 4°S and 12°S (in line with Czeschel et al. [2015]), while negative values are observed south of 12°S (Fig. 19a). In subsurface, there is a clear shoaling (deepening) of the nutricline north (south) of 12°S (19b). In addition, if we focus in the region where the most intense positive Chl trend (6°S – 10°S, see Fig. 13) is found, the nutricline depth presents a significant shoaling (- 1.75 m dec^{-1}), despite the nutricline depth is strongly impacted by EN events, i.e. reaching ~ 100 m during 1997-1999 (Fig. 20).

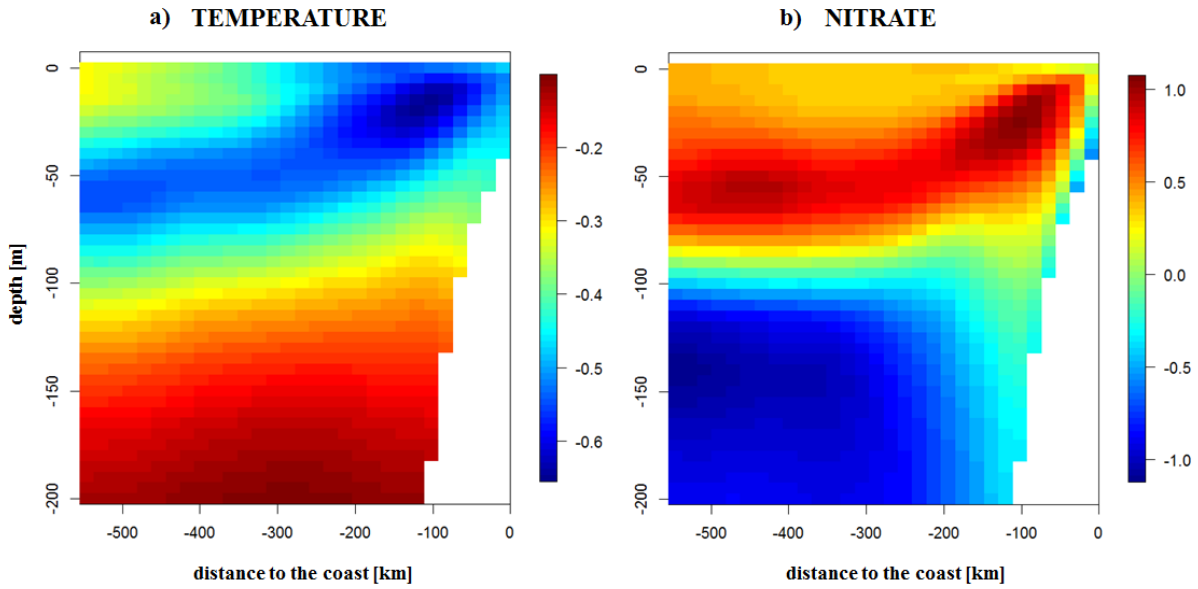

Figure 18. Vertical sections (averaged alongshore between 6°S – 16°S) of temperature (a, °C dec^{-1}) and nitrate (b, µmol L^{-1} dec^{-1}) trends between 1979 and 2008.

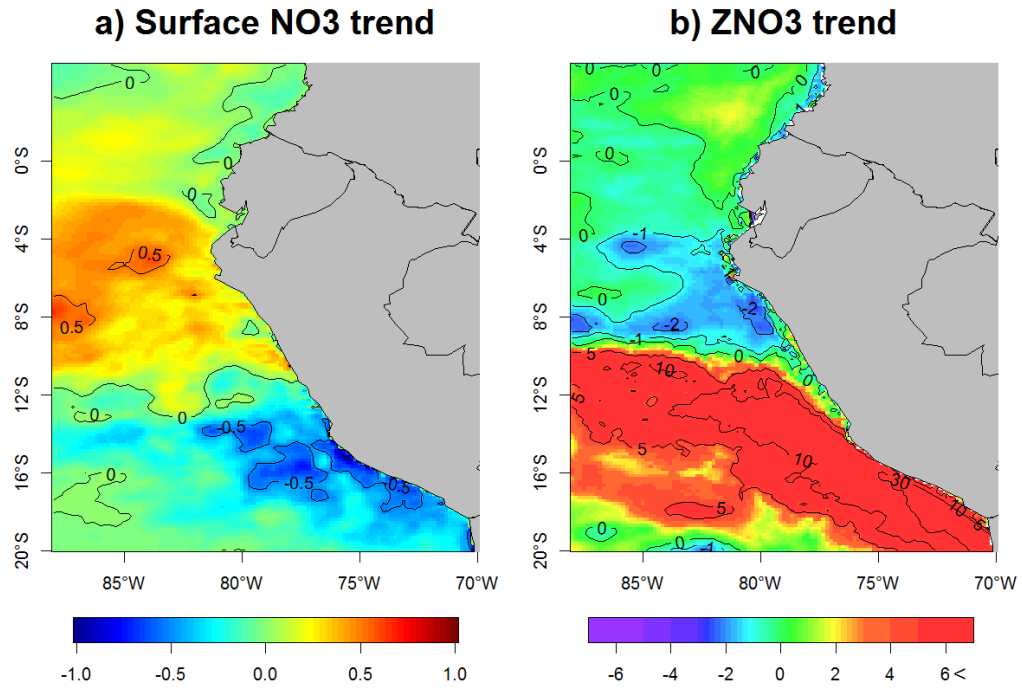

Figure 19. Spatial pattern of surface nitrate (a, µmol L^{-1} dec^{-1}) and ZNO3 (b, m dec^{-1}) model trends between 1958 and 2008.

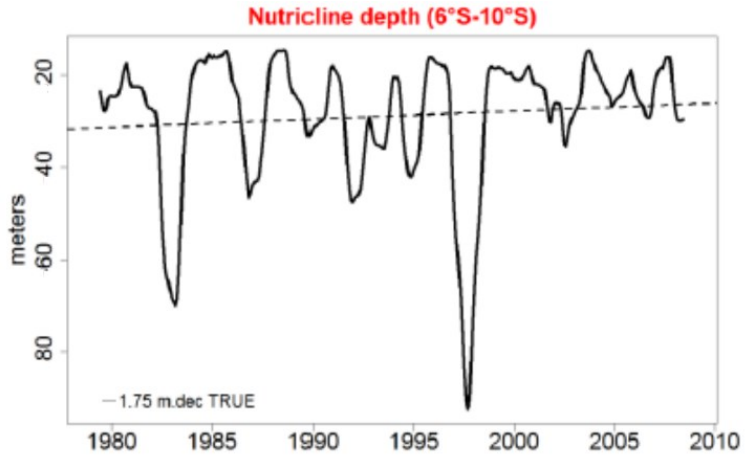

Figure 20. Time series of the nitracline depth. The time series was computed from 6°S – 10°S within the 100 km to the coast. The "TRUE"/"FALSE" labels significant/ non-significant trends using bootstrapping.

Nutrient and light limitation trends are computed for each season. Table 5 shows that a relaxation of nutrient limitation occurs only in autumn and spring, when the nutricline shoals. In contrast, a slight increase of nutrient limitation is observed in summer in spite of the strong nitracline shoaling. In this season, the relaxation of light limitation (+15, Table 5) is the main driver of the increase of productivity. It is consistent with the greater thinning of the ML during summer. Last, during winter, both the nutrient and light limitation influence in the productivity decrease, due to both a ML and nitracline deepening.

	Summer	**Autumn**	**Winter**	**Spring**
Light limitation (L_{lim}) (10^{-3} dec^{-1})	15	-4	-2	-12
Nutrient limitation (N_{lim}) (10^{-3} dec^{-1})	-1	9	-3	15
L_{lim}*N_{lim} (10^{-3} dec^{-1})	2	1	-2	2
Mixed Layer Depth (m dec^{-1})	-0.8	-0.3	0.6	0.6
ZNO3 (m dec^{-1})	-3.8	-0.5	1.2	-1.1

Table 5. Seasonal trends for light (L_{lim}) and nutrients (L_{nut}) limitation, and L_{lim}*L_{nut} in dec^{-1}. MLD and ZNO3 seasonal trend (m dec^{-1}) are also showed. Gray shading indicates statistically significant trends.

To conclude, we found a positive Chl trend during summer, autumn and to a lesser extent, spring, and a decrease in winter. The positive Chl trend in summer could be driven by a relaxation of light limitation associated with a shoaling of the MLD. The shoaling of the

nutricline during autumn and spring could relax nutrient limitation. On the other hand, both nutrient and light limitation increase in winter, triggering a negative Chl trend.

3.2. Oxygen Trends

In order to analyze the model oxygen trends, we computed the spatial linear trend of ZO2 (from 1979 to 2008) in each pixel in the area between 4°N - 4°S and 70°W - 90°W (Fig. 21). In the case of ZO2, values are not always available as ZO2 may reach the surface. Thus, only the pixels that presented more than 50% of the monthly data (> 180 months) in the studied period were taken into account. The model simulated a shoaling of ZO2 (i.e. negative trend), which suggests that deoxygenation occurs in the coastal (north of 18°S) and oceanic region (north of ~ 12°S), with more intensity in the latter. The too strong ventilation of the equatorial region (defined between 2°N and 2°S) by the EUC [Stramma et al., 2010; Montes et al., 2014; Llanillo et al., 2018] in our model generates the fading of the OMZ, thus it was not possible to calculate the ZO2 trend in this region. The strongest ZO2 shoaling (with values greater than -20 m dec^{-1}) is observed offshore (200 km from the coast) between 4°S – 8°S. This offshore region is under the influence of the eastward sSSCCs [Montes et al., 2010], thus changes in the dynamics of the jets could explain this pattern. A latitudinal gradient of the negative ZO2 trend is observed nearshore. Between 6°S – 12°S, the trend varies between - 2 to - 10 m dec^{-1}, while it is weaker between 13°S – 18°S (- 2 m dec^{-1}; Fig. 21). As the largest negative trends (shoaling) are found in the north-central region off Peru, the timeseries of the coastal ZO2 (averaged between 6°S - 14°S within 200 km from the coast) is shown in Figure 22. As shown in chapter 4, ZO2 presents interannual variations associated with ENSO phases. It reached its maximum depth during the 1982–1983 and 1997–1998 EN events [Gutiérrez et al., 2008, Graco et al., 2017; see chapter 4]. However, in spite of the presence of these strong events, a long-term shoaling of ZO2 was observed between 1979 – 2008, corresponding to a significant trend of -7.28 m dec^{-1}.

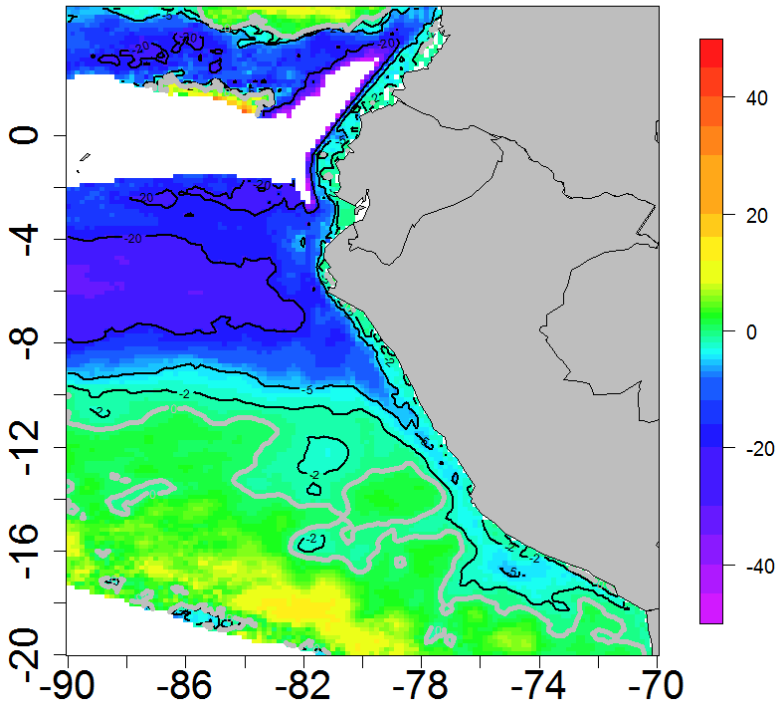

Figure 21. Spatial trend of the ZO2 from the model between 1979 and 2008.

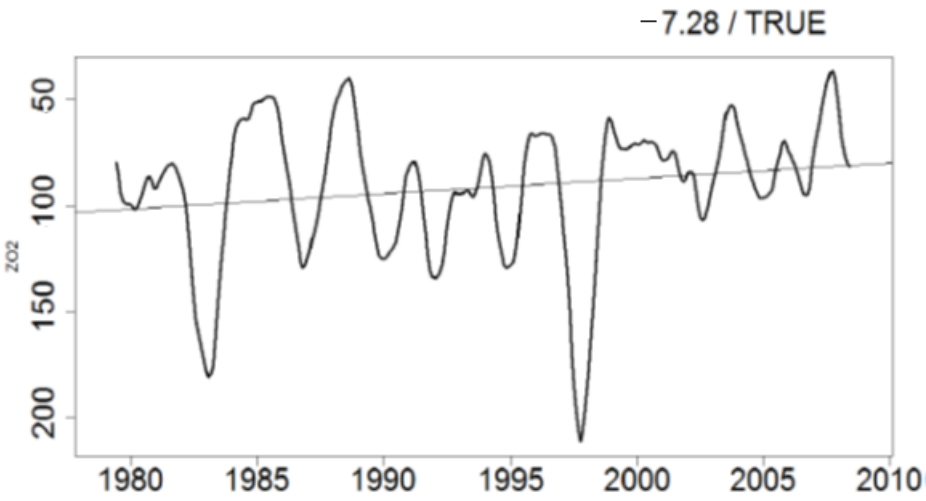

Figure 22. ZO2 timeseries. The timeseries is computed by averaging ZO2 values between 6°S – 14°S and within 200 km from the coast. The trend value is indicated in the top right corner and the "TRUE" label indicates that the trend is statistically significant.

To assess whether nearshore deoxygenation takes place in the entire water column, the temporal variation of an average oxygen profile (computed between 6°S – 16°S within the 200 km to the coast) is shown in Figure 23. As previously mentioned, an oxygenation of the water column was observed during the 70's, associated with a reduction of the water volume with

concentrations lower than 5 µmol kg^{-1}. However, after the 80's the water column lost oxygen between 100 to 900 m (with different intensities). This shift in oxygen variability off Peru was described by Bertrand et al. [2011], who, using the same IMARPE in situ data as in our study, found a deepening of the OMZ (defined in their study as the isoline of 44 µmol kg^{-1}) before 1982–1983 and a shoaling after 1983 until 2008. In the model, a thickening of the OMZ due to a shoaling and deepening of its upper and lower limits is observed since the early 80's. In addition, the OMZ core (< 5 µmol kg^{-1}) also expands vertically (both its upper and lower limits are modified). The upper limit of the OMZ core was found at ~ 250 m during 1980 – 2000, while during 2000-2008 it was found at ~ 200 m (Fig. 23a). The deoxygenation trend is shown in the top 1000m-deep layer in Figure 23b. The strongest deoxygenation (~ – 4 µmol kg^{-1} dec^{-1}) is encountered between 50 and 100 m, whereas oxygen trend values are near – 1.5 µmol kg^{-1} dec^{-1} between 800 and 900 m. The trend is weakest (– 0.2 µmol kg^{-1} dec^{-1}) between 300 and 500 meters, where the lowest oxygen values are found. However, this trend represents a loss of ~ 10% of the oxygen mean in this depth range.

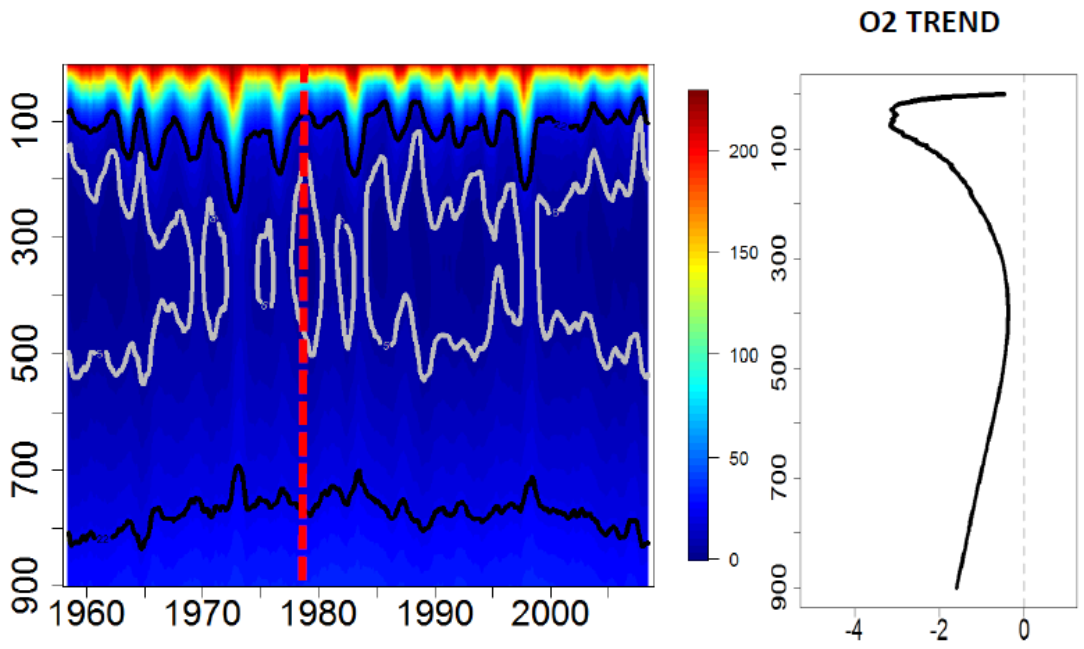

Figure 23. Nearshore modelled oxygen profile evolution between 1958 and 2008 (left panel). The mean profile is obtained by averaging between 6°S – 16°N and 0 – 200 km. Red dashed line indicates the timing of the regime shift. Vertical structure of the oxygen trend (in µmol kg^{-1} dec^{-1}) (right panel).

3.2.1. Processes involved in the deoxygenation

Both biogeochemical and physical processes can generate a progressive deoxygenation in the coastal region. Among the modelled biogeochemical processes, remineralization is the main sink of dissolved oxygen off Peru (Paulmier and Ruiz Pino [2009]; see chapter 4). Remineralization at depth is related to the surface production and export of Particulate Organic Carbon, which is respired by the bacterial pool [Kalvelage et al., 2015]. Therefore, an increase in surface production, export and remineralization could drive subsurface deoxygenation.

Figure 24a shows the evolution of the mean profile of remineralization, averaged between 6°S – 16°S and 0 – 100 km from the coast. The isoline of 1 and 0.1 μmol m^{-3} s^{-1} are shoaling in the last period (~1995-2008). Figure 24b shows the trend of the remineralization profile. Remineralization intensifies above 10 m depth, and reduces below, with a maximum between 20 and 40 m. There is thus a tendency to reduce remineralization in subsurface water in spite of the surface Chl increase during the last years (Fig. 24b). The presence of more suboxic waters in subsurface could influence this process due to its dependence on oxygen availability [Llanillo et al., 2013]. Above 10 m, the increase of surface Chl induces more oxygen consumption by remineralization as it is not limited by the availability of oxygen. Note that enhanced oxygen consumption in the surface layer due to stronger surface productivity is partly compensated by the decrease of SST during the last years, which increases oxygen solubility [Walczyńska and Sobczyk, 2017] and by the oxygen production by photosynthesis. However these effects are not strong enough to compensate for the oxygen decrease. Indeed, a nearshore deoxygenation is evident (within the 50 km and from 7°S to 12°S, Fig.25), but the oxygen decrease rate (~ – 2 μmol kg^{-1} dec^{-1}) is very weak (Fig. 25).

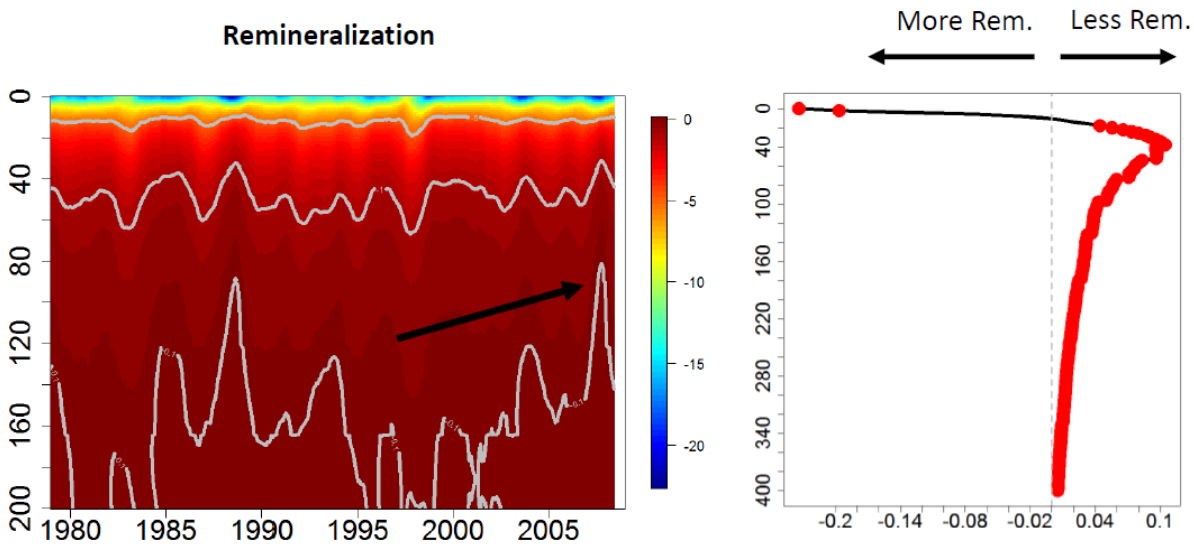

Figure 24. Evolution of model remineralization mean profile between 1958 and 2008 (averaged between 6°S – 16°N and 0 – 200 km) (left panel). Vertical structure of the remineralization trend (right panel, in µmol m^{-3} s^{-1} dec^{-1}). Red points mark significant trend values.

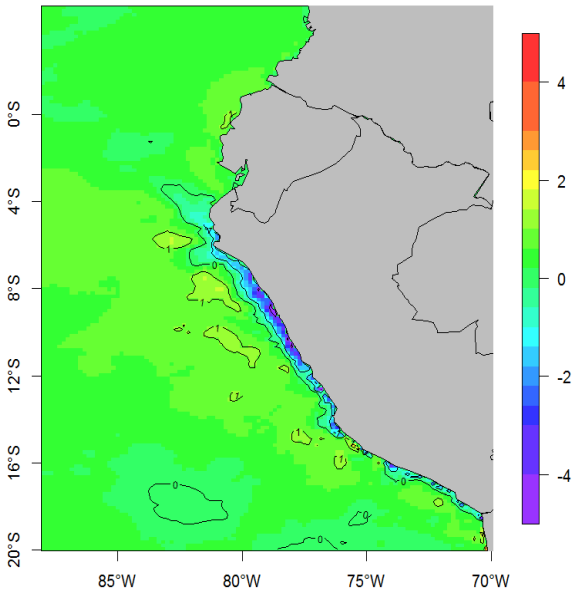

Figure 25. Spatial structure of the modelled surface dissolved oxygen trend (µmol kg^{-1} dec^{-1}).

As neither the remineralization decrease nor the upwelling variability (Fig.5) can not explain in the modelled deoxygenation trend, we now focus on the oxygen content of the upwelling source waters. The time series of the current intensity and oxygen fluxes associated with the EUC (2°N – 2°S), pSSCC (2°S – 6°S) and sSSCC (6°S – 10°S), averaged between 50 and 350 m, are shown in Figure 26. All currents decrease over time (EUC: ~ – 0.24 cm s^{-1} dec^{-}

[1]; SSCCs: ~ – 0.36 cm s^{-1} dec^{-1}, trends are significant for the SSCCs). These subsurface currents show a lower mean after 1997–1998 than before. The oxygen fluxes also decrease and the negative trends are significant for EUC (– 0.03 µmol m^{-2} s^{-1} dec^{-1}), pSSCC (– 0.026 µmol m^{-2} s^{-1} dec^{-1}), sSSCC (– 0.012 µmol m^{-2} s^{-1} dec^{-1}). The latter presents the weakest flux decrease. These results are in line with Stramma et al. [2010] and Czeschel et al. [2015], who found a deoxygenation in the EUC and pSSCC during the last three decades. Due to the connections between the equatorial and coastal zone (see section 3.3.3 and 3.2.2 in Chapters 3 and 4, respectively), this suggests that deoxygenation in the coastal region may be driven by a decrease in the equatorial oxygen supply.

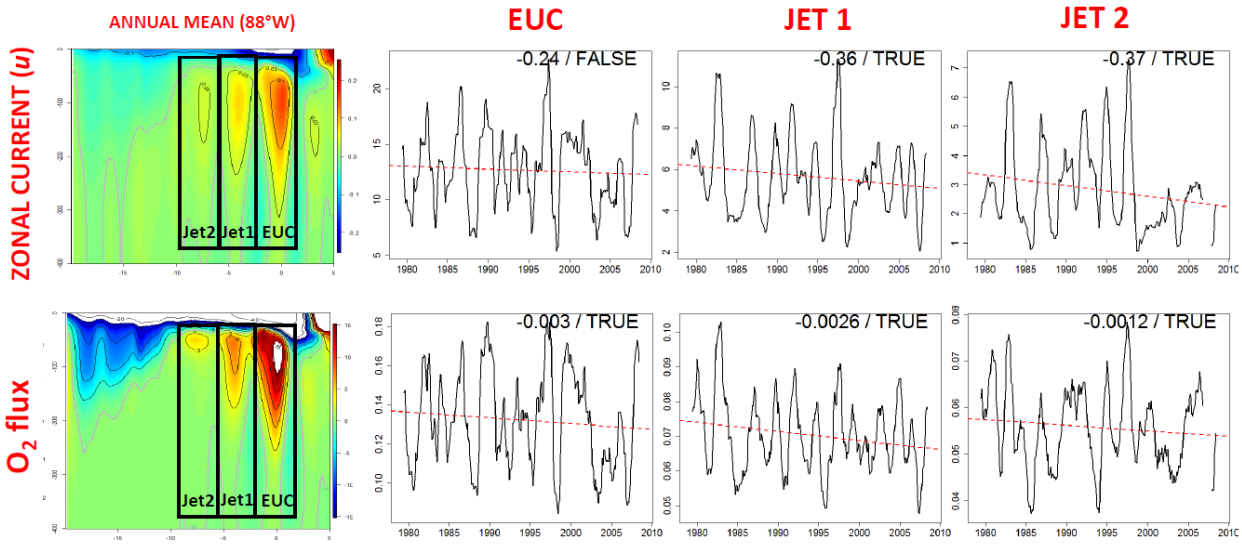

Figure 26. Mean modeled zonal current (cm s^{-1}) and O2 flux (µmol m^{-2} s^{-1}) (left panel). Black rectangles indicates the regions over which spatial averaging was computed. Time evolution of the zonal current (upper right panel) and O2 fluxes (bottom right panel) for EUC, sSSCC, pSSCC. The linear trend units are cm s^{-1} dec^{-1} and 10^{-1} µmol m^{-2} s^{-1} dec^{-1} for zonal current trend and O2 flux trend, respectively. The trend values are indicated in the top righ corner of the right panels. The "TRUE"/"FALSE" labels significant/ non-significant trends using bootstrapping.

4. Impact of Remote versus Local Forcing on the Biogeochemical Trends

In this section we analyze the impact of the remote (e.g. KW) and local (winds) forcing on the trends previously described. The configurations of the simulations were described in methodology section (see Methodology Chapter 2). Two simulations are analyzed: the Kclim simulation is forced by interannual atmospheric (wind, short wave and air parameters) forcing and climatological OBC. The Wclim simulation is forced by interannual OBC and

climatological atmospheric and wind forcing. These two simulations are compared to the CR simulation analyzed in the previous sections, forced by interannual OBC, atmospheric and wind forcing.

4.1. SST and surface productivity

A negative SST trend is observed alongshore (~ – 0.2 °C dec^{-1}, Figure 27) in Wclim, although less intense than in the CR simulation (~ – 0.4 °C dec^{-1}). In contrast, no trend is observed in Kclim in the 50 km coastal band. However, a weak negative trend is found (~ – 0.1 °C dec^{-1}) offshore and north of 13°S. The Chl trend spatial pattern is similar to the SST pattern in Wclim: an increase of the surface Chl is found, with almost the same magnitude as in CR between 5°S – 14°S and within the 100 km from the coast (~+ 0.3-0.5 mg m^{-3} dec^{-1}). In contrast, an alternation of negative and positive patterns are observed alongshore in a thin coastal band in Kclim. These results suggest that the remote oceanic forcing is the main driver of the SST and surface Chl trends along the Peruvian coasts in our model configuration.

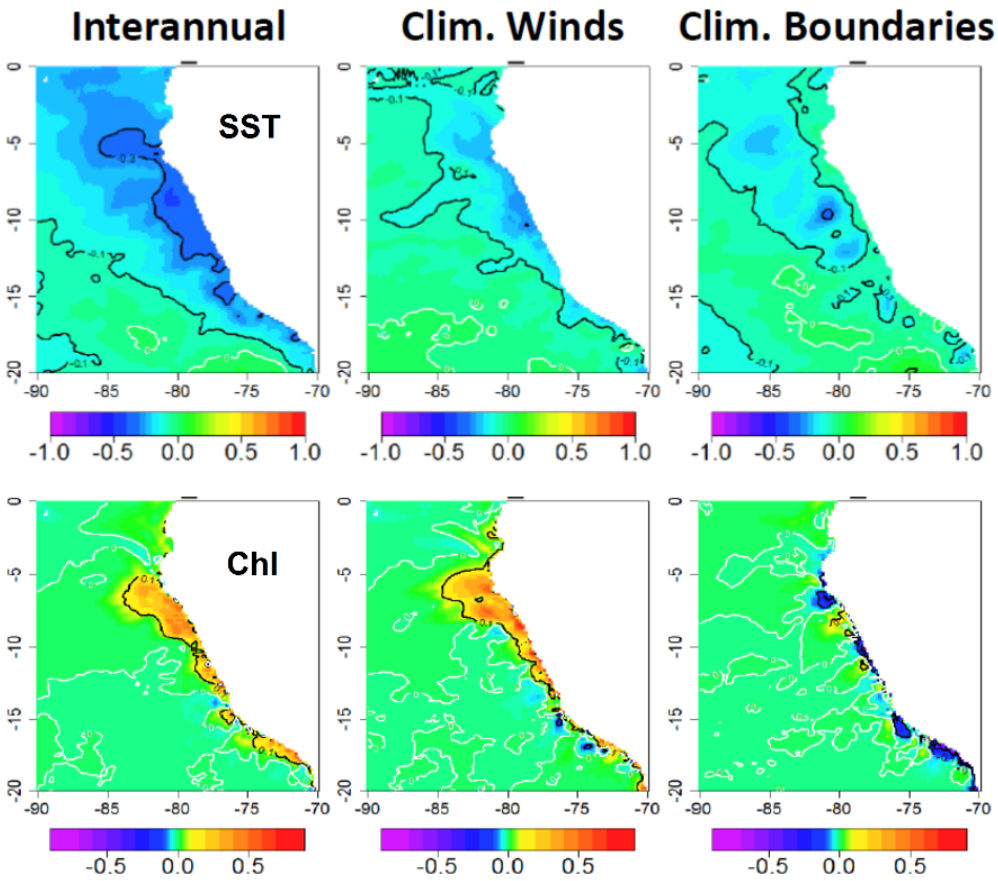

Figure 27. SST (upper panel; in °C dec^{-1}) and Chl (bottom panel; in mg m^{-3} dec^{-1}) trend for CR (left panel), Wclim (middle panel), Kclim (right panel) over 1979-2008.

However, this result may depend on the quality of the atmospheric forcing. In the following, the impact of a different wind forcing is investigated. We used 2 different wind products: CFSR and ERA-interim (hereafter ERA; see description in Methodology section). The statistically downscaled nearshore winds [Goubanova et al., 2010] used in CR simulations (~ 5.0 m s^{-1}), are lower than the CFSR (~ 5.9 m s^{-1}) and ERA (~ 5.5 m s^{-1}) winds (within the 100 km to the coast and from 6°S – 16°S). Moreover, these products have very different trends. CFSR and ERA-interim trends are respectively significantly positive (+ 6 10^{-2} m s^{-1} dec^{-1}) and negative (- 7 10^{-2} m s^{-1} dec^{-1}), while the CR winds have a weaker (significant) negative trend (- 0.3 10^{-2} m s^{-1} dec^{-1}). The wind stress, which results from the interaction of surface wind and the surface ocean layer as it was computed by bulk formulation, presents negative trends in CR, CR-CFSR and CR-ERA (see table 3 in methodology chapter) but with different intensities (-7 10^{-4}, -2 10^{-4}, -9 10^{-4} N m^{-2} dec^{-1}, respectively). Furthermore, the modeled wind stress underestimate the satellite data from ERS (1°x1°; Bentamy et al., 1999) and QuikSCAT (0.25°; from http://www.ifrem er.fr/cersat) (Figure 28).

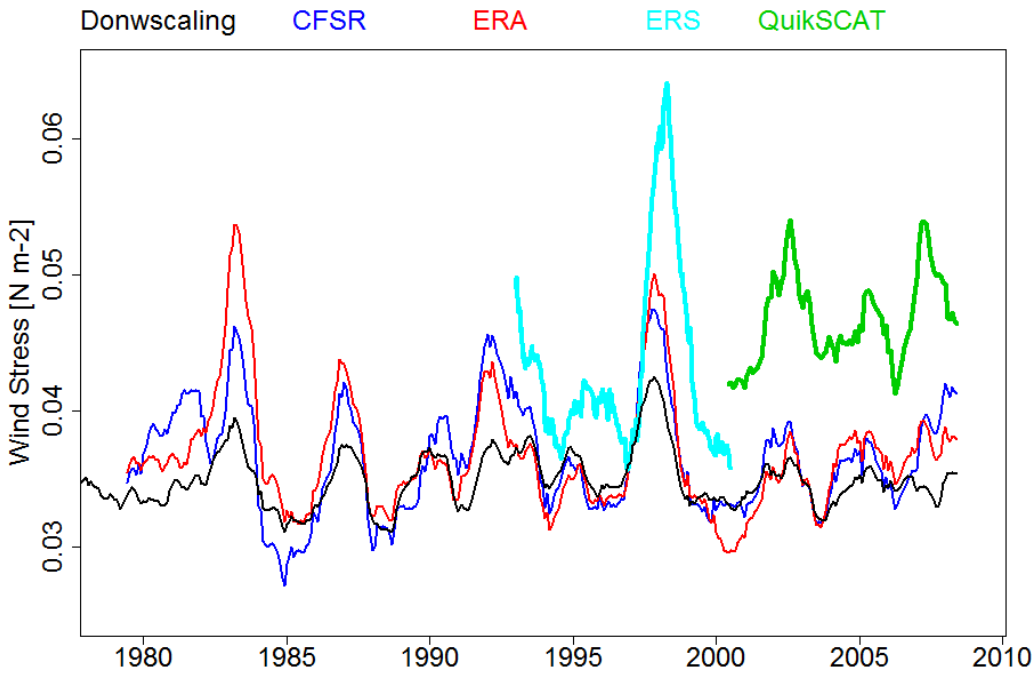

Figure 28. Timeseries of wind stress (in N m^{-2}) for CR, CR-CFSR, CR-ERA simulations, averaged in a coastal box (6-16°S, within 100 km from the coast). Wind stress is computed using a bulk formulation. Wind stress from satellite data as ERS and QuikSCAT are shown.

In order to evaluate the impact of ERA and CFSR winds in the system, we repeated the Kclim simulations using these wind forcings. Kclim-CFSR generates an intense negative SST trend alongshore north of 10°S (~ – 0.5 °C dec^{-1}), while Kclim-ERA produces a weakly negative SST trend (< – 0.1 °C dec^{-1}) north of 11°S, with a negative core (~– 0.1 °C dec^{-1}) between 5°S – 6°S and within 150 km from the coast. The Kclim-CFSR Chl trend was positive north of 10°S, reaching values of + 0.75 mg m^{-3} dec^{-1} at ~ 7°S. The Kclim-ERA Chl trend was less marked, with weak positive (+ 0.1 mg m^{-3} dec^{-1}) and negative (– 0.1 mg m^{-3} dec^{-1}) values in 5°S – 11°S and south of 16°S respectively, within ~ 40 km from the coast.

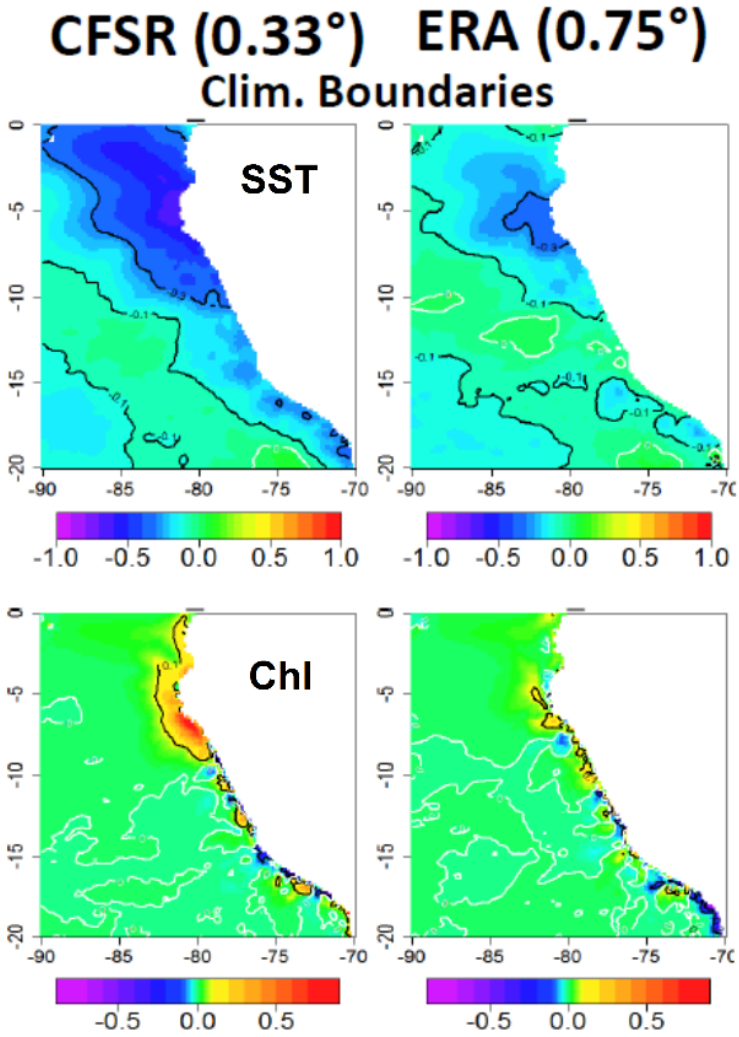

Figure 29. SST (upper panel; in °C dec^{-1}) and Chl (bottom panel; in mg m^{-3} dec^{-1}) trend from Kclim-CFSR (left panel) and Kclim-ERA (right panel) during 1979 to 2008.

These sensitivity experiments demonstrate that the model robustly simulates an increase in surface Chl, independently of the choice of wind forcing, in the absence of remotely forced

coastal waves. This Chl increase is likely due to an enhanced wind-driven upwelling, bringing more nutrient to the surface, and thus relaxing nutrient limitation. The spread between the simulations driven by the different wind products, which have different trend magnitude, informs on the range of uncertainty of the computed SST and Chl trends. We can conclude from this sensitivity study that both the remote and the local forcings contribute to the positive Chl trend. Unfortunately, there is no clear consensus on whether there was or not a wind increase off the Peruvian coasts during 1979-2008, due to large discrepancies in the reanalysis products [Narayan et al., 2010].

4.2. Drivers of deoxygenation

The drivers of upper OMZ variability (ZO2 depth) are investigated using the Kclim and Wclim sensitivity simulations. Figure 30 displays the time series of ZO2, averaged between 6°S – 16°S and 0 – 200 km from the coast. Wclim and CR simulations display the same interannual variability. A significant negative ZO2 trend (- 7.28 m dec^{-1}, shoaling) is found in CR, whereas a weaker (significant) negative ZO2 trend (- 3.41 m dec^{-1}) is found in Wclim. In contrast, the ZO2 interannual variability is very different in the absence of coastal trapped waves in Kclim. As expected, the OMZ deepening, typical of EN, e.g. during 1997–1998 EN is no longer observed. In contrast with CR, Kclim simulates a weak positive ZO2 trend (+ 0.66 m dec^{-1}, deepening). This shows that the remote forcing (e.g. by CTW activity and frequency) drives the interannual variability (ENSO phases) and trend (deoxygenation) of ZO2.

The response of ZO2 trend to different wind forcings is also evaluated using Kclim-CFSR and Kclim-ERA. The ZO2 trends are weak and not significant in both simulations (Kclim-CFSR: - 0.09 m dec^{-1}; Kclim-ERA: - 0.19 m dec^{-1}, Fig. 31). This shows that in spite of and enhanced wind trend, which impacts the productivity and respiration, the long-term deoxygenation is mainly driven by the remote equatorial forcing.

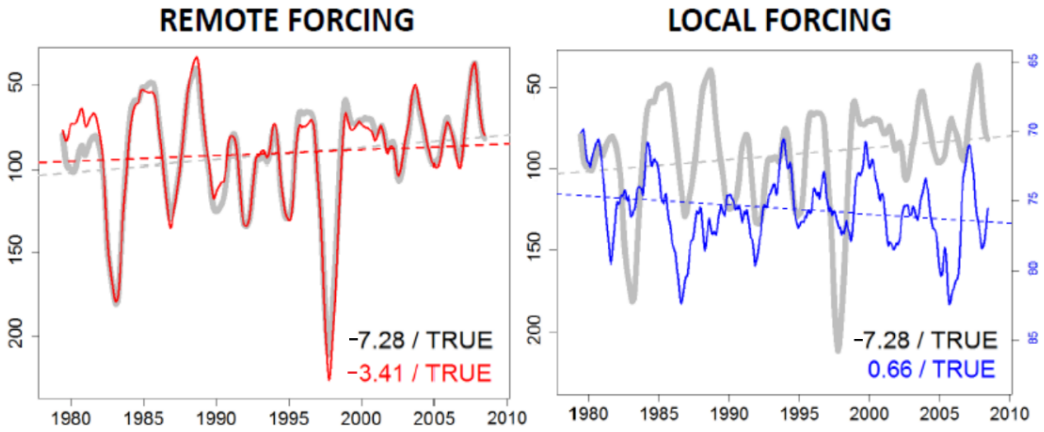

Figure 30. ZO2 timeseries (full line) and trends (dashed line) for CR (gray line), Wclim (red line) and Kclim (blue line) simulations (see table 3 in Chapter 2 for a detailed description of the simulations). ZO2 was computed from 6°S – 16°S and 0 – 200 km. The trend values are indicated in the bottom right corner of the panels. The "TRUE"/"FALSE" labels indicate significant/non-significant trends using bootstrapping.

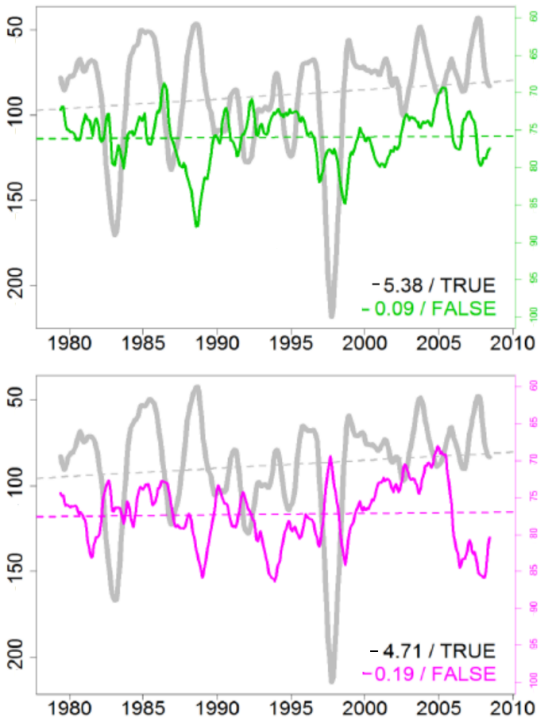

Figure 31. ZO2 timeseries (full line) and trends (dashed lines) for CR, Kclim-CFSR and Kclim-ERA simulations (see table 3 in Chapter 2 for a detailed description of the simulations). ZO2 was computed from 6°S – 16°S and 0 – 200 km. The trend values are indicated in the bottom right corner of the panels. The "TRUE"/"FALSE" labels significant/ non-significant trends using bootstrapping.

5. Analysis of the Equatorial Forcing over 1979-2008

Our results suggest that the equatorial remote forcing is the main driver of the physical and biogeochemical modelled trends between 1979 and 2008. However, the mechanisms remain to de deciphered. The main mechanism described in section 3 to explain the SST, Chl and deoxygenation trends is related to the changing characteristics of the equatorial source waters. Over time, their nutrient content increase, while their temperature and oxygen content decrease. The other mechanism is related to the CTW forced by the EKW variability, which modify the nutricline depth. Lee and McPhaden [2010] observed an increase in the intensity and frequency of the Central Pacific El Niño (CP El Niño or modoki EN) over the last decades. CP El Niño is characterized by highest SST anomalies in the central equatorial Pacific (region El Niño 3.4; Fig. 32). The increase in modoki EN frequency could be associated to the natural multidecadal variability and to the anthropogenic climate change [Yeh et al., 2009].

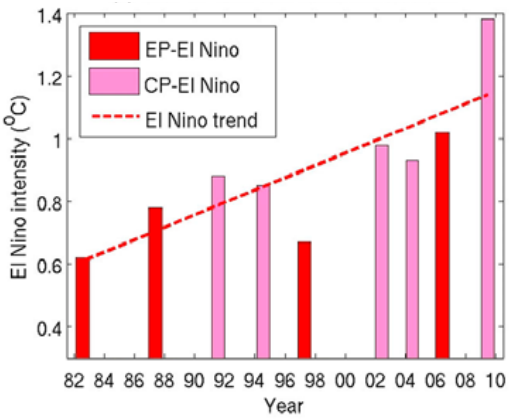

Figure 32. El Niño intensity in the region El Niño 4 from Lee and McPhaden [2010].

Dewitte et al. [2012] described the development of EP and CP EN events by decomposing the equatorial dynamics in the form of mode 1 and mode 2 Equatorial Kelvin waves (mode 2 having a more complex vertical structure than mode 1). Using the SODA reanalysis, they found that the CP El Niño is associated with the propagation of a mode 2 upwelling (cold) EKW a few months before and after the peak of EN, whereas a mode 2 downwelling (warm) EKW are predominant during EP El Niño (Fig. 33). As upwelling CTWs (triggered by upwelling EKWs) induce a shoaling of the main physical and biogeochemical clines during their alongshore poleward propagation [Echevin et al., 2014; see also chapters 3 and 4], this implies that more frequent and more intense CP El Niño could be associated to more frequent upwelling CTWs and shoaling events of the main clines (thermocline, nutricline

and oxycline). Dewitte et al. [2012] computed the SST composite in the autumn fllowing the peak of CP El Niño in summer, using a regional model configuration and observations [Reynolds et al., 2007]. This SST composite is characterized by negative anomalies in both model and observations (– 0.5 to – 1 °C), between 5°S and 14°S. The spatial pattern extends equatorward, suggesting a link with remotely-forced upwelling CTW (Fig. 34).

In conclusion, the more frequent Central Pacific El Niño events (or Modoki El Niño), which typically present the propagation of mode 2 upwelling Kelvin Waves, may have triggered the shoaling of the nearshore thermocline, nutricline and oxycline. The shallower nutricline increases the productivity, while the shoaling of the oxycline could influence coastal deoxygenation.

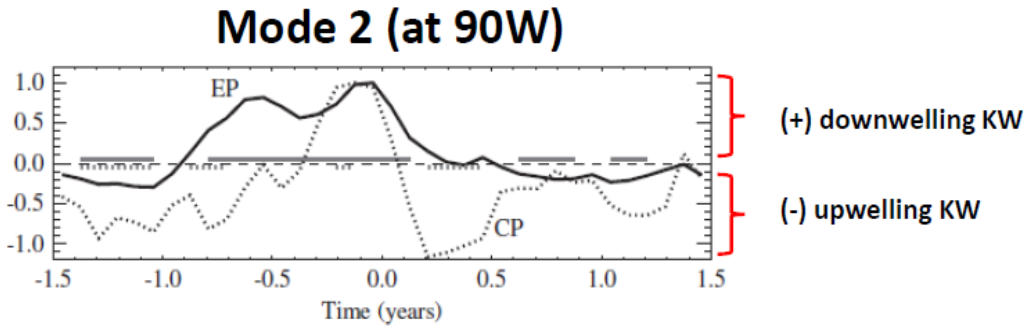

Figure 33. Mode 2 during CP EN and EP EN from Dewitte et al. [2012].

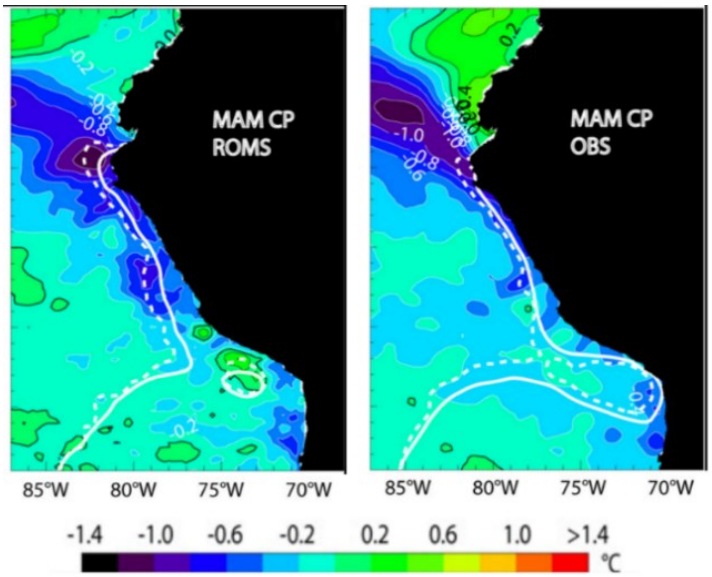

Figure 34. Autumn SST anomalies composite during CP El Niño from model (left) and Reynolds (right). From Dewitte et al. [2012].

6. Appendix

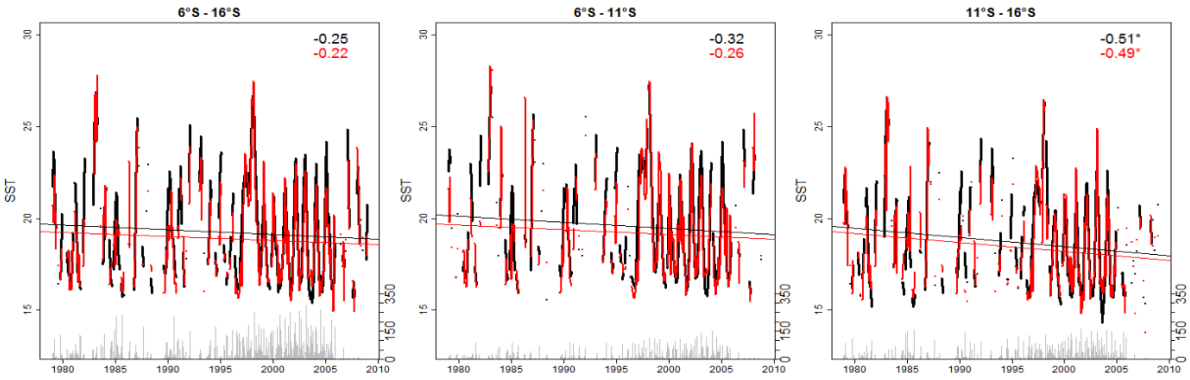

Figure S1. Monthly time series of SST from model (black) and IMARPE data (red) for north-central (left), north (middle), central (right) regions. The asterisk means that the trend is significant by bootstrap. The time series were computed from 6°S – 16°S and within 100 km from the coast. Linear trend were added. Grays bar represent the number of data for each year.

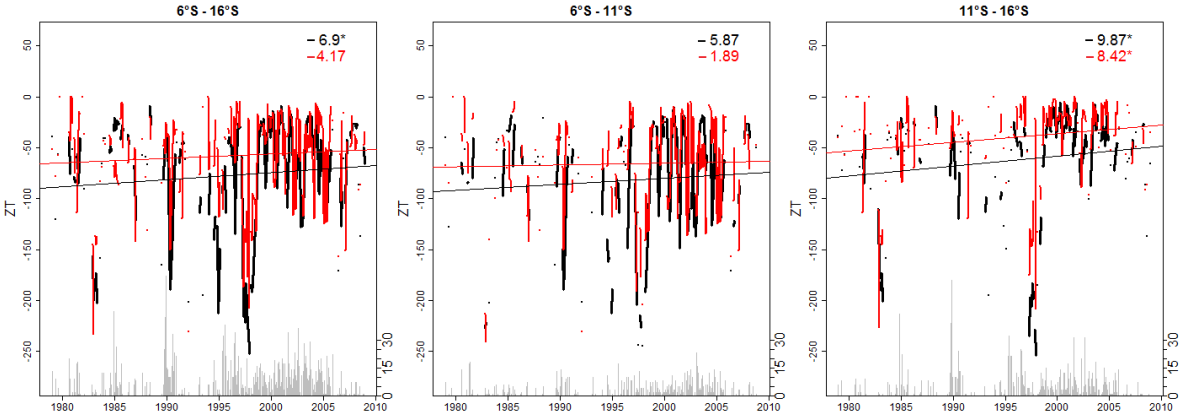

Figure S2. Monthly time series of ZT15 from model (black) and IMARPE data (red) in the north-central (left), north (middle), central (right) regions. The asterisk means significant values by bootstrap. The time series were computed from 6°S – 16°S and within 100 km to the coast. Linear trend were added. Grays bar represent the number of data.

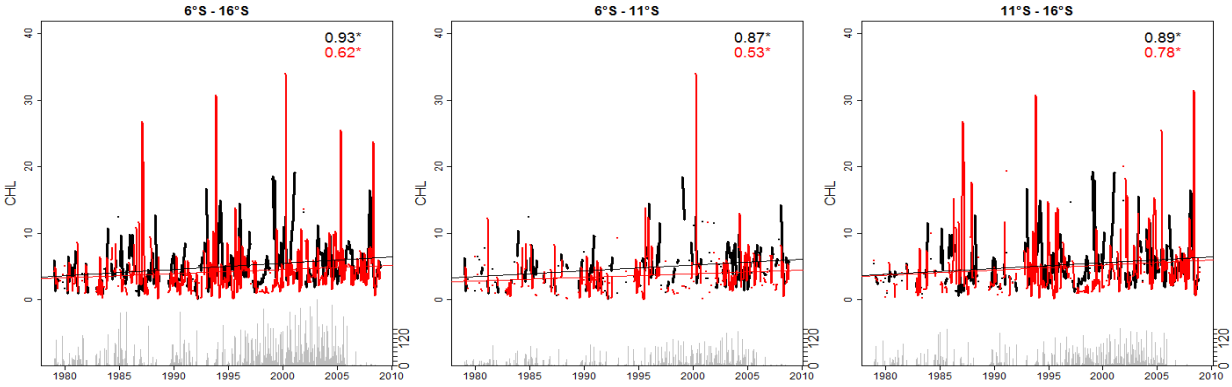

Figure S3. Surface Chl Monthly time series for model (black) and IMARPE data (red) in the north-central (left), north (middle), central (right) regions. The asterisk indicates a significant trend tested using by bootstraping. The time series were computed between 6°S – 16°S and within 100 km from the coast. Linear trends were added. Grays bar represent the number of data.

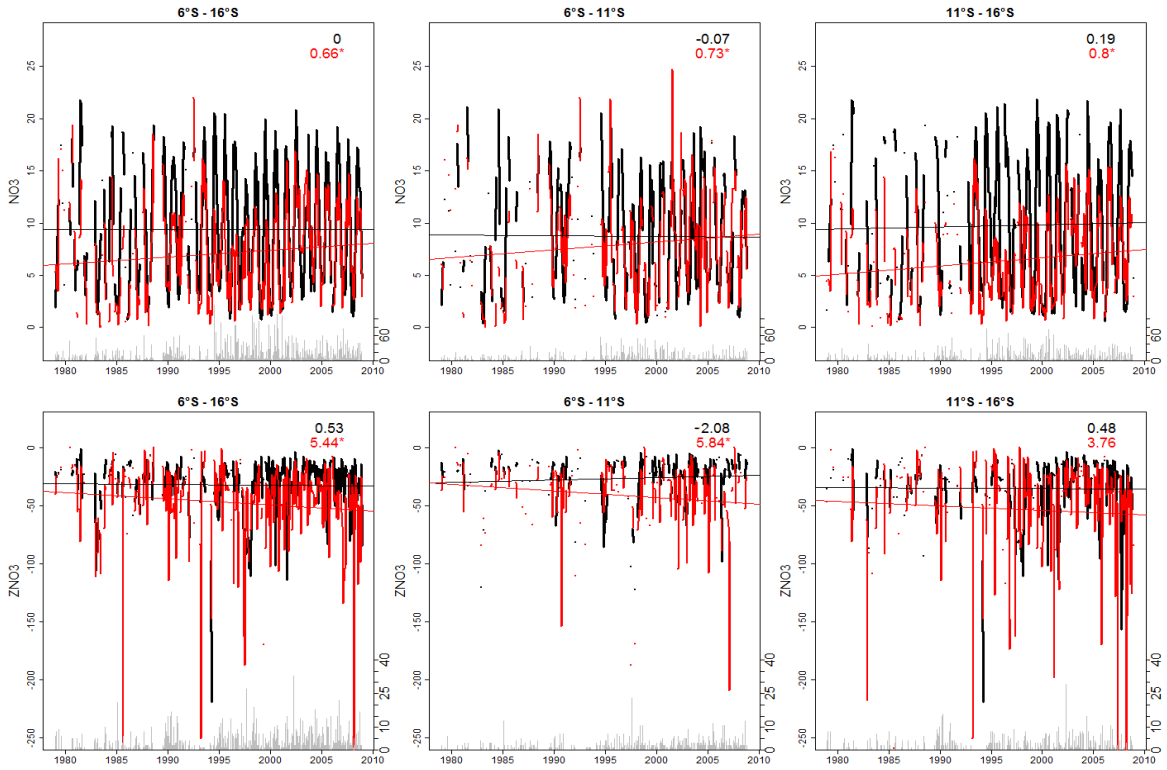

Figure S4. Monthly time series of surface nitrate (upper panel) and nutricline depth (bottom panel) from model (black) and IMARPE data (red) for north-central (left), north (middle), central region (right). * means significant by bootstrap. The time series were computed from 6°S – 16°S and within 100 km to the coast. Linear trend were added. Grays bar represent the number of data.

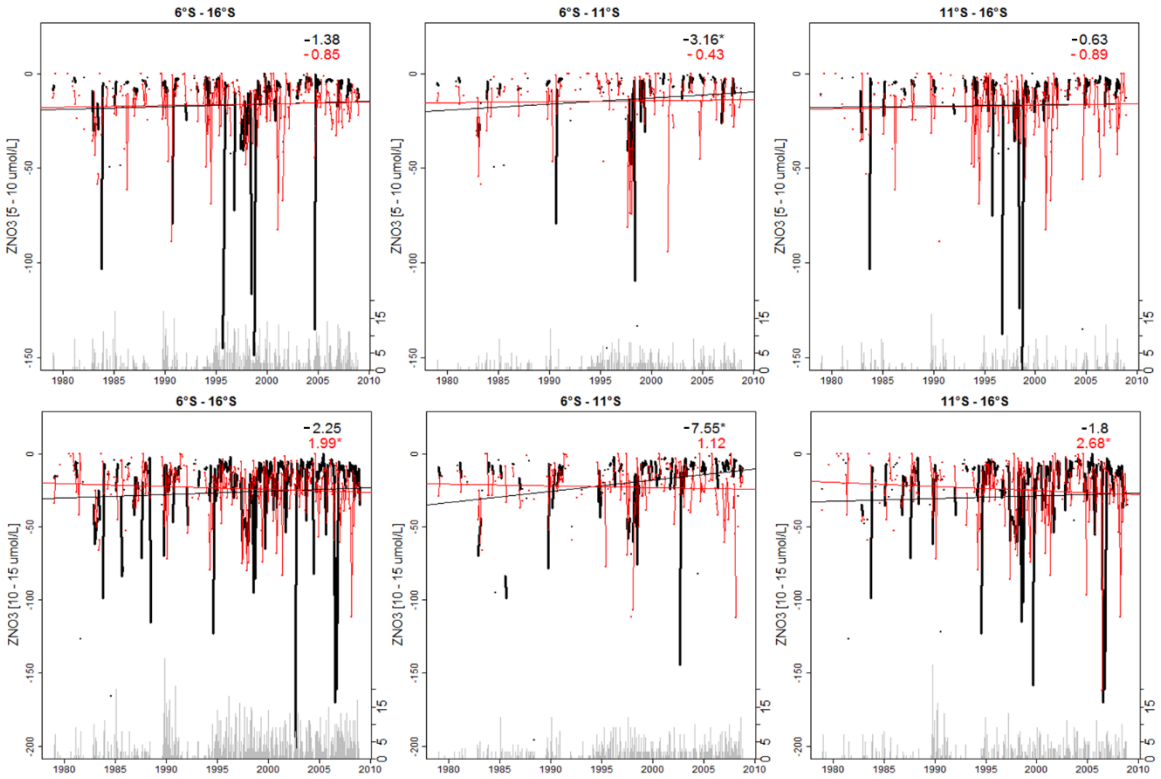

Figure S5. Monthly time series of the isolines depth of 10 (5) and 15 (10) µmol L^{-1} from the model (IMARPE) in the top and bottom panel. Black and red lines represent model and IMARPE data, respectively. * means significant by bootstrap. The time series were computed from 6°S – 16°S and within 100 km to the coast. Linear trend were added. Grays bar represent the number of data.

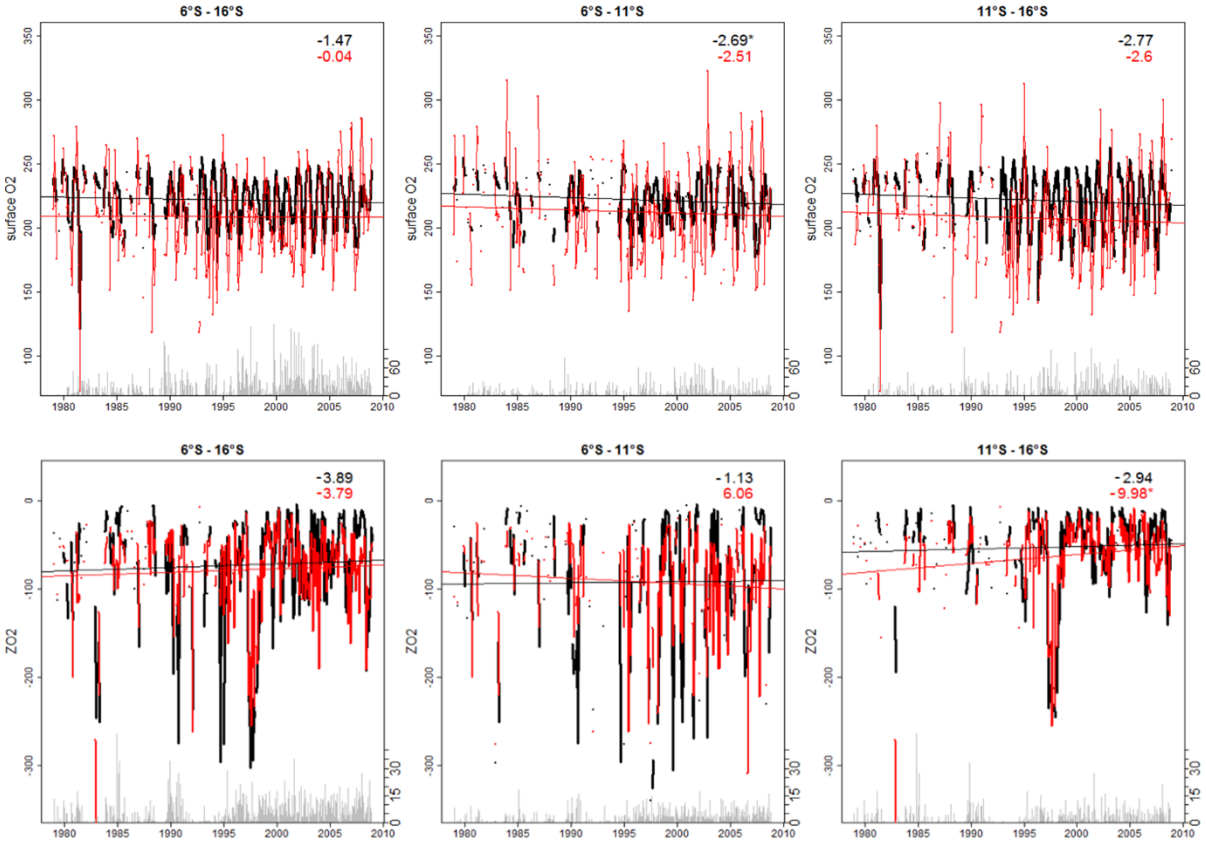

Figure S6. Monthly time series of surface oxygen dissolved (upper panel) and ZO2 (bottom panel) from model (black) and IMARPE data (red) for north-central (left), north (middle), central region (right). * means significant by bootstrap. The time series were computed from 6°S – 16°S and within 100 km to the coast. Linear trend were added. Grays bar represent the number of data.

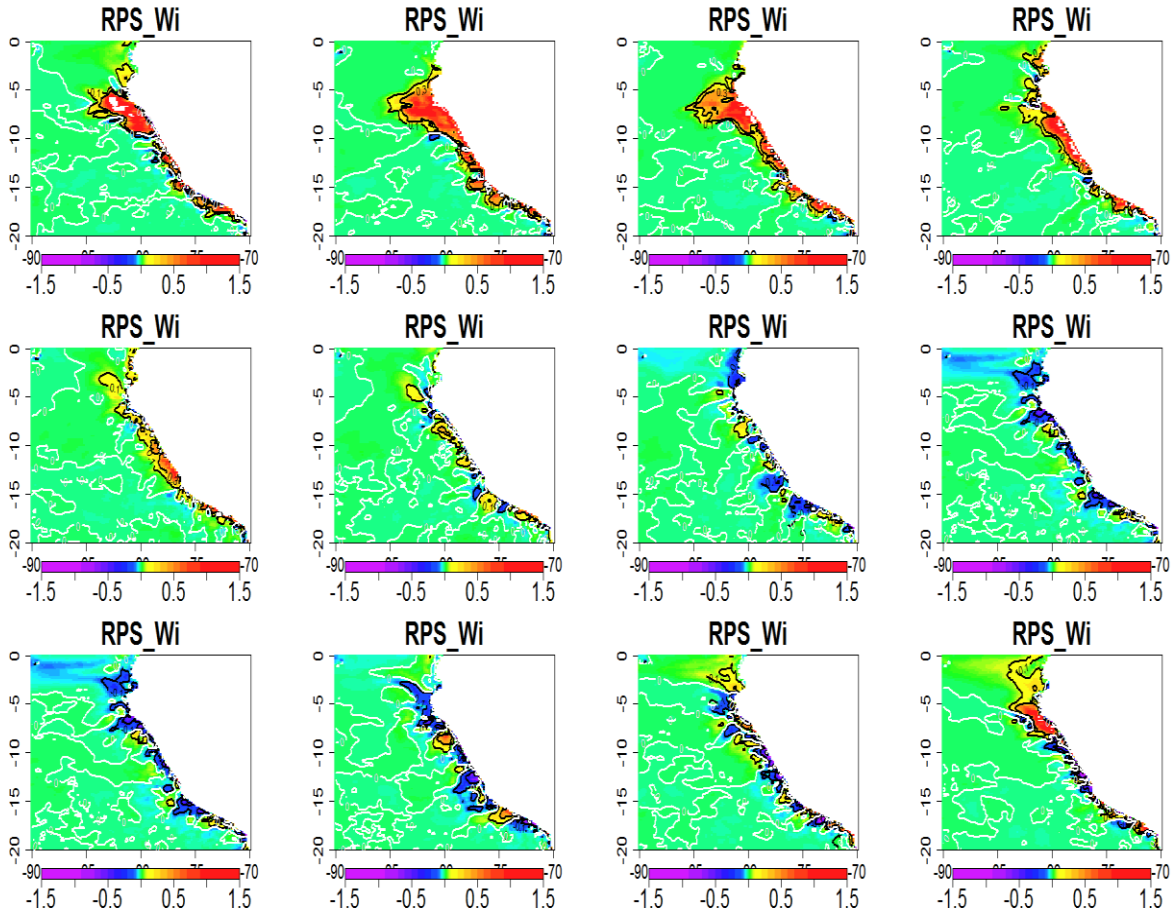

Figure S7. Monthly spatial surface Chl trend (mg m^{-3} dec^{-1}) from 1979 to 2008.

CHAPTER 6:
CONCLUSIONS

Conclusions and Perspectives

1. Conclusions

The Peruvian upwelling System is one of the most productive regions in the global ocean [Chavez et al., 2008] and encompasses a very intense and shallow Oxygen Minimum Zone (OMZ). Furthermore, due to its proximity of the equatorial Pacific, it is strongly impacted by ENSO (El Niño and La Niña events). In the present thesis, we attempted to describe and understand the main mechanisms associated with the impact of El Niño (EN) and La Niña (LN) events on (1) primary productivity and surface chlorophyll concentration and (2) dissolved oxygen content in the upper part of the OMZ. To this aim, we used a physical-biogeochemical coupled model, representing adequately the regional scales of the circulation and biogeochemical cycles. In the last chapter, we studied the recent physical and biogeochemical trends observed in the surface and subsurface layers. The model allowed us to investigate the respective influence of the equatorial circulation decadal variability and that of the local upwelling-favorable wind on these trends. The main conclusions of the thesis are summarized in the following:

a) Our regional model was able to reproduce the main oceanic surface and subsurface conditions in the period 1958 – 2008 as long as their variability associated with ENSO. The model and observations (in situ and satellite) showed the development of warming conditions during EN events, with a notable SST increase and a deepened thermocline. Nutrients were also impacted, as a nitracline deepening and a silicate decrease were found. The surface Chl decreased strongly and an oxygenation of the upper water column was observed. In contrast, cooler water and enhanced nutrient concentrations (than during normal conditions) associated with a shoaling of the nutricline, and a slight increase of surface Chl were encountered during LN along the coast. Furthermore, a shoaling of the OMZ and a decrease of dissolved oxygen concentrations in the upper layer were observed.
b) Moreover, the model was able to reproduce the variability at longer time scales, namely the main physical and biogeochemical trends between 1979 and 2008. A significant coastal cooling was found from 6°S to 14°S. The observed and simulated surface Chl increased during the last decades, mainly between 6°S and 10°S. Last, model and observations displayed a shoaling of the oxycline, indicative of a deoxygenation of the upper layers of the water column.

c) In chapter 3 we described and analyzed the processes driving the decrease and increase of the productivity during EN and LN, respectively. During EN periods, the nearshore wind stress increase (see Chamorro et al. [2018] for a detailed study of this phenomenon) triggered an intensification of the coastal upwelling (mainly in summer – fall), partly compensated by a strong onshore geostrophic flow (mainly in winter and spring). The downwelling Coastal Trapped Waves (CTW), forced by the arrival of eastward propagating Equatorial Kelvin waves at the coasts of South America, propagate poleward along the coast and drive a nitracline deepening. Thus, the upwelling of nitrate into the surface layer decreased, except in summer – early fall as it was mitigated by the wind-driven upwelling increase. The Chl decrease was caused by nutrient depletion during most of the EN period, except during summer, as it was attributed to an enhanced light limitation related with a deepening of the mixed layer. Eddy-driven fluxes were also impacted by the enhanced eddy activity during EN: the downward nitrate vertical eddy flux increased and was estimated to be twice as large as during normal years. Weaker changes were found during LN. In these cold periods, the chlorophyll slightly increased due to an enhanced upwelling and slightly nutrient-richer source waters.

d) The impacts of EN and LN phases on the oxygenation of the upper water column and depth of the upper limit of the OMZ (ZO2) were analyzed in chapter 4. During EN, the OMZ deepened due to the passing of intense downwelling CTWs, whereas it shoaled during LN due to the upwelling CTWs. The source water (SW) of the coastal upwelling were mainly transported eastward from the equatorial regions towards the coasts by the SSCCs and EUC during LN and EN, respectively. During EN, the SW were more oxygenated than during LN as they originated from the more ventilated region north of the OMZ and transited faster towards the coastal region due to stronger onshore currents. Furthermore, the vertical eddy flux, which brings oxygen to the surface layer above ~ 60 m and removes it below, decreased during EN. Horizontal eddy fluxes, which inject oxygen into the OMZ at its lateral boundaries, strongly increased during EN. Modifications of biological consumption of oxygen (mainly remineralization, zooplankton respiration and nitrification in our model) were also estimated. These sinks were strongly altered during ENSO phases, depending on oxygen availability in the water column. During EN, close to the coast, the remineralization, zooplankton respiration and nitrification tended to increase, while during LN, the opposite occured.

e) The processes involved in the biogeochemical trends (especially Chl and oxygen) in the period 1979-2008 were analyzed in detail in chapter 5. The simulated productivity increase was significant in the north-central region (6°S–10°S). The limiting factors of diatoms (i.e. the phytoplankton species contributing mostly to chlorophyll content) growth indicated that the productivity increase was due to a relaxation of nutrient limitation attributed to the nutricline shoaling (and subsequent increase of nutrient in the near-surface layers). In contrast, light limitation was not modified. Furthermore, the positive Chl trend was explained by a strong increase of productivity during summer-autumn, partly compensated by a negative trend in winter.

   Our model also reproduced a progressive shoaling of the upper OMZ in the studied period. The strongest shoaling was observed offshore and between 4°S and 8°S. We found that it could be related to the decreasing oxygen fluxes associated with the equatorial subsurface currents, the EUC and Tsuchiya jets. Nearshore deoxygenation occurred over the entire OMZ but was stronger in the oxycline between 20–100 m depth. Model sensitivity experiments demonstrated that the remote forcing (e.g. Equatorial Kelvin waves in the equatorial latitude band) drove the trends, whereas the local forcing (nearshore winds) did not have a strong impact. One hypothesis to explain this trend is the occurrence and intensification of Central Pacific EN events with respect to Eastern Pacific EN events in the last decades. As suggested by Dewitte et al. [2012], whereas mode 1 downwelling Kelvin wave induces a deepening of the thermocline during Eastern pacific and Central pacific EN events, the mode-2 upwelling Kelvin Waves propagating during CP events causes the shoaling of the nearshore thermocline, possibly impacting the nutricline and oxycline.

2. Limitations of the Study

We discuss the limitations of our modelling approach in the following paragraphs:

a) The biogeochemical model used in this thesis has several ill-constrained parameters. Most parameters used in our regional configuration are identical to those in the default version of the PISCES model which was initially adapted for the global ocean at 2° resolution. Some of them have been modified (see Table in Echevin et al. [2014]). Most of these values have been derived from the literature (laboratory experiments and models). However, they were computed from results and observations in different

regions than Peru. More laboratory studies are needed to obtain more accurate parameters values for the Peruvian coastal region. Besides, due to the large number of PISCES parameters and computational time requirements, simple models (e.g. 1D model) could be used in order to adjust the parameters (e.g. using data assimilation techniques). Indeed, the OMZ and the nitrate concentration are highly sensitive to parameters such as remineralization and nitrification rates. Thus, sensitivity studies of PISCES model to different values of these parameters need to be done in the future. Figure 1 illustrates how different values of remineralization and nitrification rates can impact the nitrate and oxygen concentration, with respect to the RPSoda control simulation.

b) Some processes of the nitrate cycle are not explicitly modeled in PISCES. For example, anammox is not included in PISCES, because the bacterial pool is simplified. The current model may thus overestimate nitrate concentration as anammox contributes to nitrate loss. Including these nitrate cycle processes (i.e. as in the BioEBUS model, Gutknecht et al. [2013]) will be necessary to improve the simulations of the system productivity.

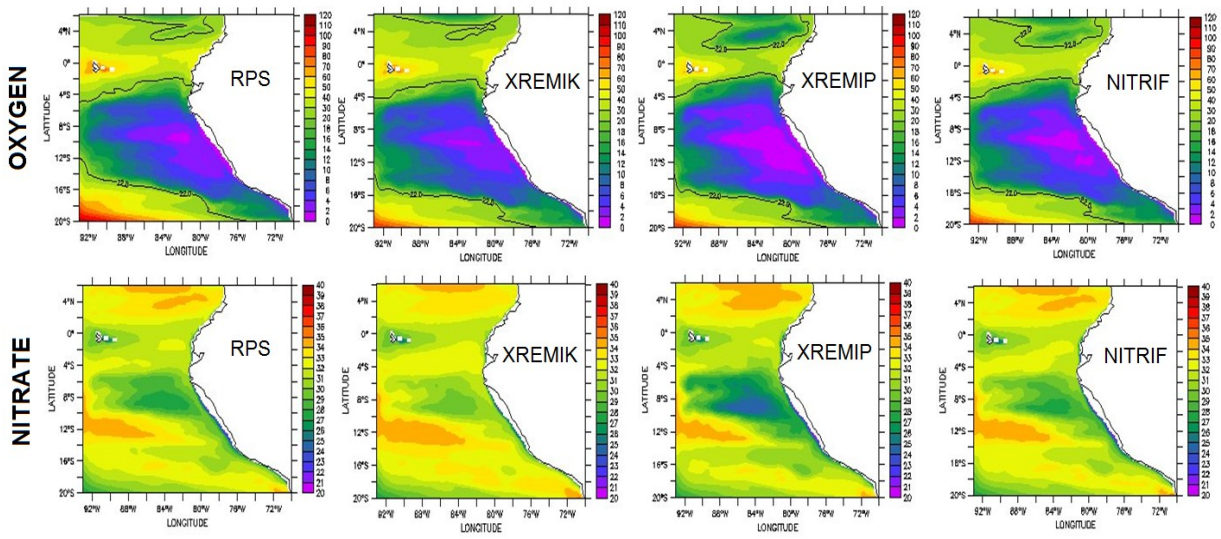

Figure 1. Oxygen and nitrate at 200 m depth from RPSoda, XREMIK, XREMIP, NITRIF with different values of the parameters: remineralization rate (λ_{DOC}), nitrification rate (λ_{NH4}) and degradation rate of Particulate Organic Carbon (λ_{POC}). RPSoda (control run) parameter values were 0.3 d^{-1}, 0.025 d^{-1} and 0.05 d^{-1} for λ_{DOC}, λ_{POC} and λ_{NH4}respectively. In XREMIK, XREMIP and NITRIF simulations, paramater values differed from RPSoda as follows: λ_{DOC} (0.15 d^{-1}), λ_{POC}(0.012 d^{-1}) and λ_{NH4} (0.02 d^{-1}). In this comparison, RPSoda (1/6° of resolution) is a climatological simulation forced by climatological forcing from ECMWF (heat fluxes) and QuikSCAT (winds). The physical and biogeochemical climatological OBC originate from the SODA model and the WOA database, respectively.

c) At the beginning of this thesis, a realistic enough global interannual simulation including biogeochemistry, which could have been used to force variable boundary conditions, was not available for the period 1958 - 2008. In chapter 3, the ORCA2-PISCES global model (C. Ethée, pers. Comm.) was used to force a regional simulation (RPOrca). However, ORCA2-PISCES did not present a realistic distribution of some of the biogeochemical variables. The OMZ (between 5°S – 12°S) from ORCA2-PISCES displays a strong bias (Fig. 2) : there was no nearshore OMZ in ORCA2-PISCES, likely due to a too strong oxygenation by the equatorial subsurface currents (see also Fig. 5 in Methodology chapter). Thus, we had to use a hybrid OBC forcing: WOA climatological conditions for oxygen and ORCA2-PISCES for nutrients and physics. Due to biases in the physical forcing, this simulation was not as realistic as RPSoda (Fig. 3) and thus was not presented in detail in the manuscript, except in chapter 3.

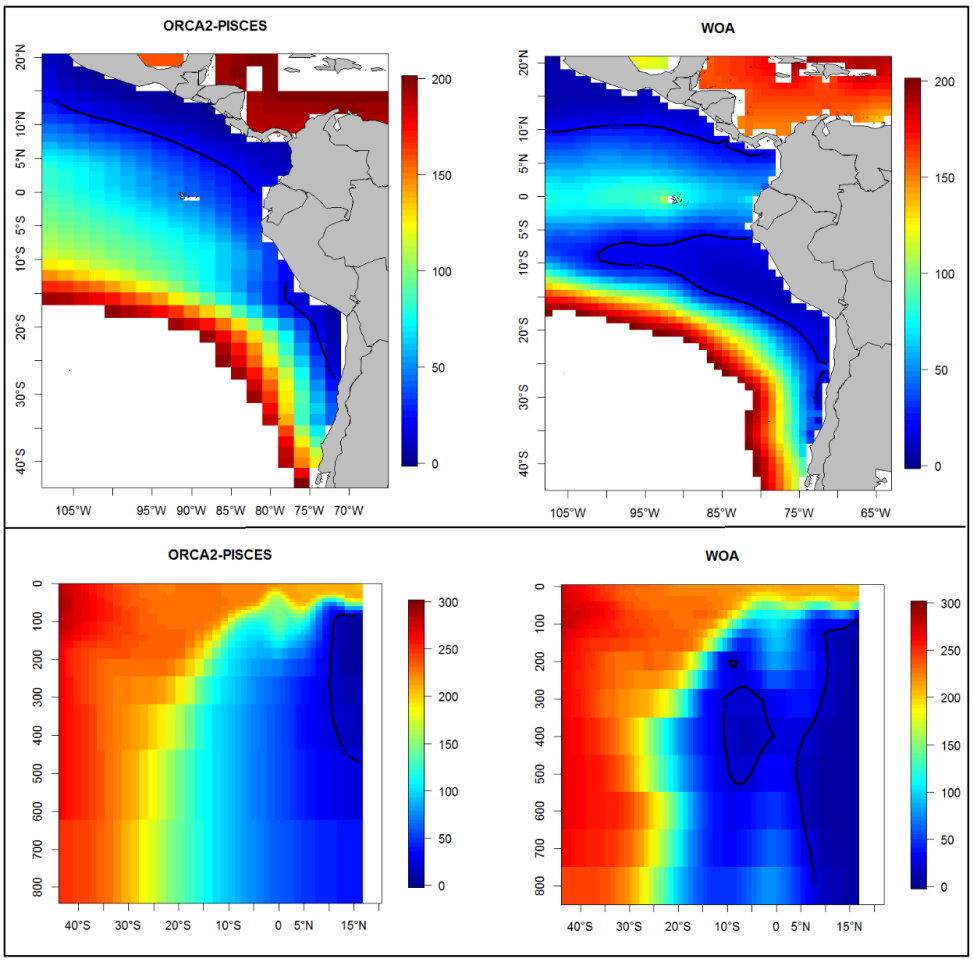

Figure 2. Oxygen concentration (annual mean, in µmol kg^{-1}) averaged between 200 m and 400 m depth (top panel). Meridional section at 100 °W (bottom panel) from ORCA2-PISCES and WOA.

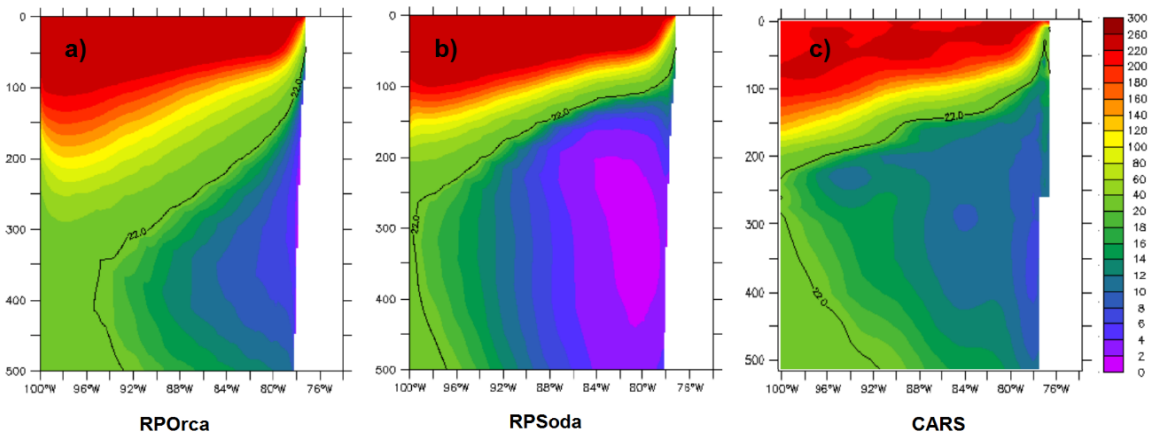

Figure 3. Oxygen concentration (annual mean, in µmol kg-1) at 12°S from RPOrca, RPSoda, and CARS. Isoline of 22 µmol kg-1 represents the limits of the OMZ.

d) Few wind datasets are available for the studied time period. In the present work, we used a statistically downscaled product from NCEP [Goubanova et al., 2010], and a hybrid forcing: a QuikSCAT climatology (0.25°) to which CFSR (0.75°) and ERA-interim (0.33°) surface wind anomalies were added. These wind fields have different horizontal resolutions, and this affects the representation of the wind intensity and drop-off close to the coast. Furthermore, the wind products present contrasted trends, in some cases of opposite sign. ERA-interim coastal winds tend to decrease between 1980 and 2008, whereas CFSR winds increase (Fig. 4). Last, there are few reliable in situ wind measurements to evaluate the wind products used to force the regional model. Besides, the bulk formulation in ROMS [Liu et al., 1979] used to compute surface wind stress may also introduce a bias. Indeed, satellite wind wind stress from QuikSCAT (2000 – 2008) and ERS (1992 – 2000) suggest that the wind stress derived by the bulk formulation is underestimated by ~20 % when compared with scatterometer measurements.

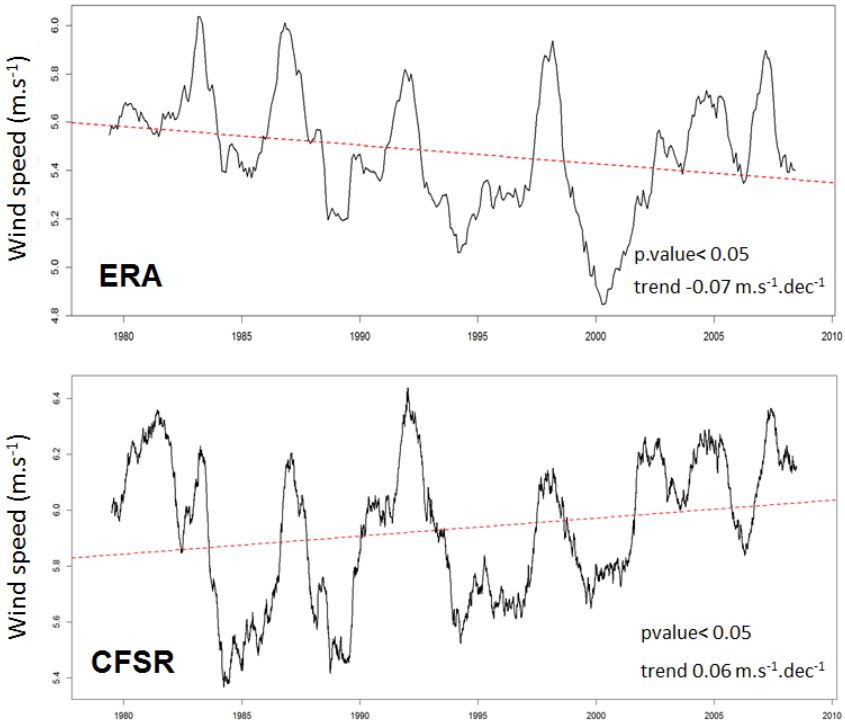

Figure 4. ERA-interim (top) and CFSR (bottom) wind speed over 1958-2008, averaged in a coastal box (from 6°S – 16°S and within the 150 km to the coast).

e) The horizontal resolution of our regional model (1/6, ~20 km) is relatively coarse in comparison to recent studies in the Peru region (e.g. ~ 10 km in Moggollon and Calil et

al., [2017] and ~ 9 km in José et al. [2017]). This resolution enabled to increase the model time step and reduce the number of grid points, allowing to conduct relatively long simulations (several decades) in comparison to these recent studies. However, the impacts of mesoscale and submesoscale processes on productivity and dissolved oxygen (see e.g. Thomsen et al. [2016]) are likely to be underestimated. Increasing the resolution is thus a requirement for future studies.

3. Perspectives

Major scientific questions about the coupling of physics and biogeochemistry in the Peru upwelling system have been adressed in the present thesis. However, important issues remain. Several scientific questions are proposed in this section as perspectives of this work:

a) A large number of IMARPE zooplankton in situ data of zooplankton are available and could be used to evaluate the model zooplankton compartments. However, this data is registered in biovolume, and needs to be converted in carbon biomass to be compared to modeled zooplankton. There are no studies about the evaluation and behavior (in space and time) of the zooplankton from PISCES model in the Peruvian region. This is a crucial topic, as zooplankton groups such as euphausiids represent the linkage between the low and high trophic levels (LTL and HTL). HTL models usually need the spatio-temporal distribution of the zooplankton biomass as a forcing for the modelling of suitable fish habitats. Thus, evaluating PISCES zooplankton will allow to obtain better estimates of fish biomass in the HTL models which represent anchovy, the major Peruvian fishery. As an example, the coupled LTL-HTL (e.g. ROMS-PISCES-OSMOSE) model allows simulating the spatial distribution of zooplankton mortality by predation, which influences the distribution pf zooplankton and phytoplakton [Travers et al., 2009]. On the other hand, zooplankton respiration also impacts the oxygen consumption in subsurface waters as it may survive in anoxic conditions. It is possible that a better representation of the modelled OMZ could be obtained if modelled zooplankton biomass becomes more reliable.
b) Increasing the horizontal resolution in future model configurations is one of our main goals, in order to study the role of eddies and filaments in the biogeochemical coastal processes. Eddies tend to remove nutrient, oxygen and phytoplankton biomass from the coast and transport these characteristics towards the open ocean.

It is crucial to evaluate correctly the role of the mesoscale structures in the budget of these biogeochemical components. In chapter 4, we found that the OMZ lateral boundaries are ventilated by mesoscale eddies. However, it is not clear if this eddy ventilation plays an important role in the interannual movement of the OMZ lateral boundaries. It would be interesting to study simulations based on different horizontal resolutions where the eddies are more or less damped.

c) Recent satellite data (2000-2017) showed a chlorophyll positive trend mainly during spring (Figure 5), which contrasts with our simulation showing a trend mainly in summer-autumn (see Fig.15 in chapter 5) over the period (1979-2008). A blended product of surface Chl using SeaWIFS and MODIS data showed that the surface Chl off Peru presented a positive trend between January 2000 and December 2017. This trend was found during every season but was strongest in spring. A negative trend was evidenced offshore (between 6°S – 11°S) during summer (Fig. 5). Simulating the recent surface chlorophyll trends in the recent decades would be useful to study the processes driving this recent trend. Furthermore, studying the oxygenation/deoxygenation phases in the last years would be interesting. This is possible using QuikSCAT (2000-2008) and ASCAT (2008-present) satellite winds for the atmospheric forcing as well as MERCATOR ORCA12 (1/12°~10 km) global model for physical boundary conditions.

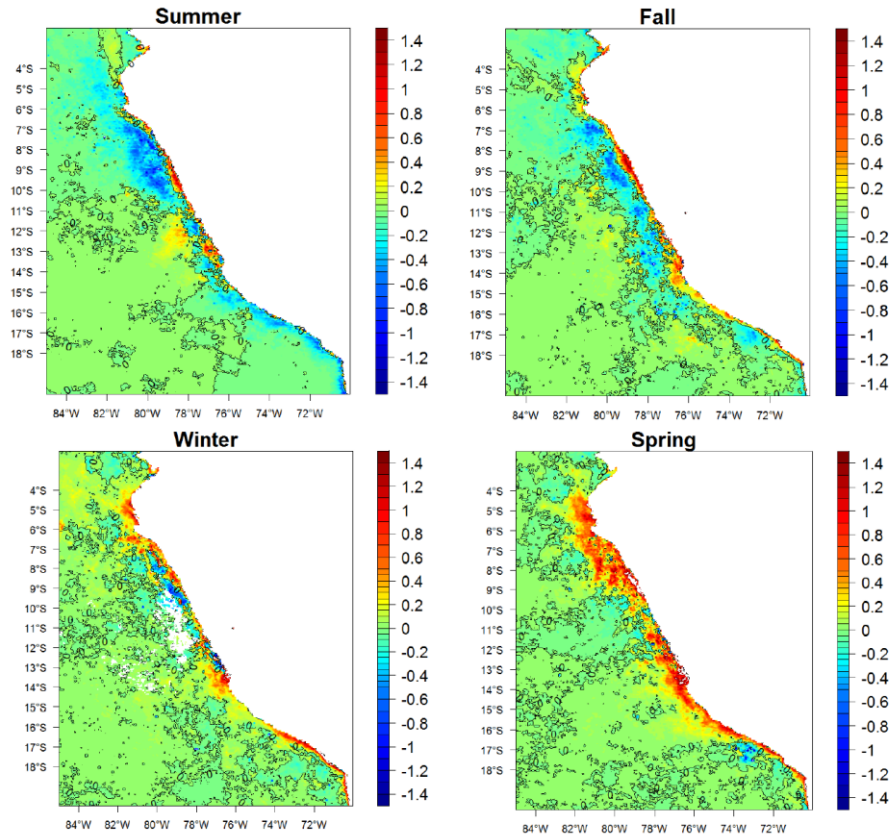

Figure 5. Surface Chl trend (in mg m^{-3} dec^{-1}) by season between 2000 and 2017 from a blended (SeaWIFs-Modis) satellite timeseries.

d) Strong interannual variations can exist even in the absence of ENSO. During summer 2017, an extreme warming of surface waters occurred off the north-central Peruvian coasts (0S-10°S). This event was not related to El Niño as neutral conditions were encountered in the Equatorial Pacific. A local weakening of the coastal winds triggered the event [Garreaud, 2018; Echevin et al., 2018]. This phenomenon was called "the Coastal El Niño". The surface productivity was affected and a notable decrease of the Chl was observed at ~ 8°S, whereas positive anomalies were found in the central region (~14°S) (Fig. 6). The productivity change could be due to the upwelling relaxation in the northern region. The biogeochemical processes associated with this event have not been studied. Using the ROMS-PISCES model, the influence of nutrients availability on the decrease of productivity could be studied. Furthermore, the respective roles of the remote (equatorial waves) forcing (i.e. weak downwelling coastal waves propagated along the coast during the event) and local wind relaxation on the productivity and oxygenation changes

during the event could be studied by performing sensitivity experiments with modified forcing (see e.g. Echevin et al. ,2018) with the PISCES model.

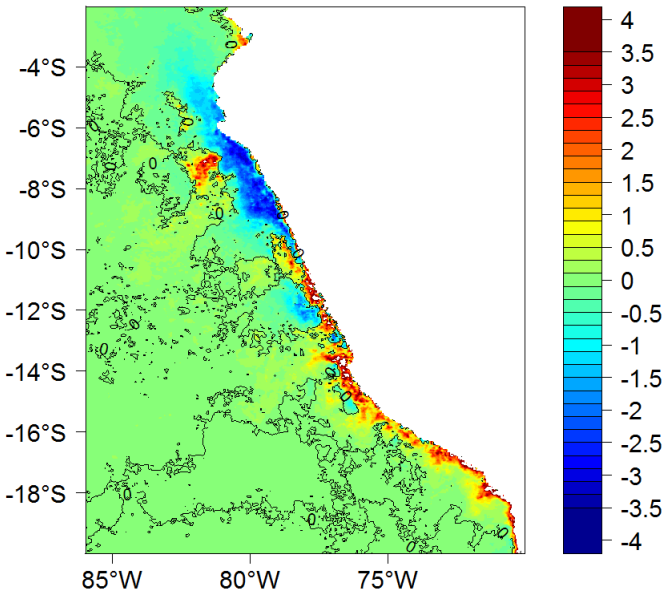

Figure 6. Surface Chl anomalies during summer 2017 from satellite data (SeaWIFS+MODIS). The climatology to compute the anomalies was computed between January 2000 and December 2017.

e) The response of primary productivity to regional climate change is a crucial question. Will the important Peruvian fisheries be limited by lack of phytoplankton biomass in future decades? Future studies should address this topic. Currently, only a few global earth-system models include the marine biogeochemical cycles and simulate changes in productivity. Most of these models forecast a decrease of productivity near the Peruvian coast [e.g. Bopp et al., 2013]. However, the coarse resolution (~100-200 km) of current earth-system models does not allow to simulate coastal upwelling with the necessary accuracy. A dynamical downscaling using the ROMS-PISCES model of different climate change scenarios from different earth-system models is necessary to have robust estimates of the productivity in the future. This work is under way (BID project, Fig. 7) and will have to be pursued in the future using CMIP6 simulations.

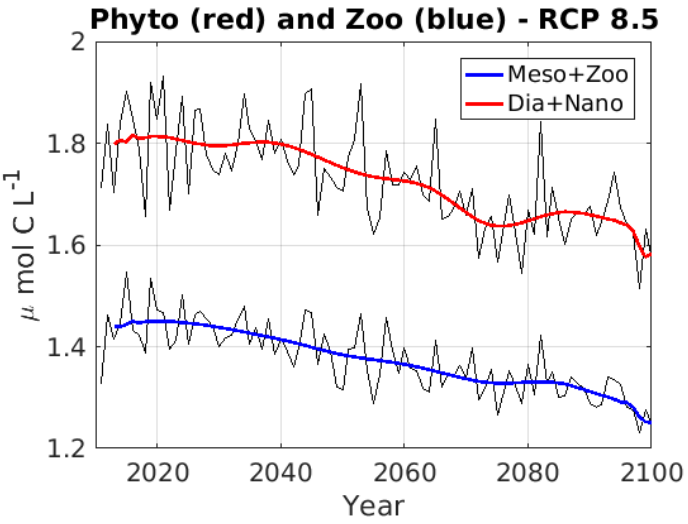

Figure 7. Evolution of Phytoplankton and zooplankton biomass from a ROMS-PISCES (10 km) simulation off Peru. Data is averaged between 0 and 50 m, and in a coastal box (7-13°S, 100 km offshore) during 2010 - 2100 in the pessimistic scenario RCP 8.5 (Gévaudan et al., 2017).

REFERENCES

Albert, A., V. Echevin, M. Lévy, and O. Aumont (2010), Impact of nearshore wind stress curl on coastal circulation and primary productivity in the Peru upwelling system, J. Geophys. Res., 115, C12033, doi:10.1029/2010JC006569.

Alheit, J., and M. Ñiquen (2004), Regime shifts in the Humboldt Current ecosystem, Prog. Oceangr., 60, 201-222, doi:10.1016/j.pocean.2004.02.006.

Arntz, W. E., V. A. Gallardo, D. Gutíerrez, E. Isla, L. A. Levin, J. Mendo, C. Neir, G. T. Rowe, J. Tarazona, and M. Wolff (2006), El Nino and similar perturbation effects on the benthos of the Humboldt, California, and Benguela Current upwelling ecosystems, Adv. Geosci., 6, 243–265.

Aumont, O. and L. Bopp (2006), Globalizing results from ocean in situ iron fertilization studies, Gl. Biogeochem. Cyc., 20, GB2017.

Aumont, O., Ethé C., Tagliabue A., Bopp L. and M. Gehlen (2015), PISCES-v2: an ocean biogeochemical model for carbon and ecosystem studies, Geosci. Model Dev., 8, 2465-2513, doi:10.5194/gmd-8-2465-2015.

Ayón, P., M. I. Criales-Hernandez, R. Schwamborn and H. -J. Hirche (2008a), Zooplankton research off Peru: A review. Prog. Oceanogr., 79, 238-255, doi:10.1016/j.pocean.200810.020.

Ayón, P., G. Swartzman, A. Bertrand, M. Gutiérrez and S. Bertrand (2008b), Zooplankton and forage fish species off Peru: Large-scale bottom-up forcing and local-scale depletion, Prog. Oceanogr., 79, 208-214, doi:10.1016/j.pocean.200810.023.

Babbin, A. R., R. G. Keil, A. H. Devol and B. B. Ward (2014), Organic Matter Stoichiometry, Flux, and Oxygen Control Nitrogen Loss in the Ocean, Science, 344 (6182), 406 – 408, doi:10.1126/science.1248364.

Bakun, A. (1973), Coastal upwelling indices, west coast of North America, 1946-71, U.S. Dept. of Commerce, NOAA Tech. Rep., NMFS SSRF-671, 103pp.

Bakun, A. (1990), Global climate change and intensification of coastal ocean upwelling, Science, 247(4939), 198-201.

Bakun, A. and S. J. Weeks (2008), The marine ecosystem off Peru: What are the secrets of its fishery productivity and what might its future hold?, Prog. Oceanogr., 79, 290–299, doi:10.1016/j.pocean.2008.10.027.

Bakun, A., D. B. Field, A. Redondo-Rodriguez, S. J. Weeks (2010), Greenhouse gas, upwelling-favorable winds, and the future of coastal ocean upwelling ecosystems, Global Change Biol., 16: 1213–1228, doi:10.1111/j.1365-2486.2009.02094.x.

Bakun, A., B. A. Black, S. J. Bograd, M. García-Reyes, A. J. Miller, R. R. Rykaczewski and W. J. Sydeman (2015), Anticipated Effects of Climate Change on Coastal Upwelling Ecosystems, 1(2), 85-93.

Ballón, M., A. Bertrand, A. Lebourges-Dhaussy, M. Gutiérrez, P. Ayón, D. Grados and F. Gerlotto (2011), Is there enough zooplankton to feed forage fish populations off Peru? An acoustic (positive) answer, Prog. Oceanogr., 91(4), 360-381, doi:10.1016/j.pocean.2011.03.001.

Barber, R. T., and F. P. Chavez (1983), Biological consequences of El Niño, Sciences, 222, 1203–1210, doi:10.1126/science.222.4629.1203.

Belmadani, A., V. Echevin, B. Dewitte and F. Colas, (2012), Equatorially forced intraseasonal propagations along the Peru–Chile coast and their relation with the nearshore eddy activity in 1992–2000: a modeling study, J. Geophys. Res., 117, C04025, doi:10.1029/2011JC007848.

Bentamy A., P. Queffeulou, Y. Quilfen and K. Katsaros (1999), Ocean surface wind fields estimated from satellite active and passive microwave instruments, IEEE Trans. Geosci. Remote Sensing, 37, 2469-2486.

Bertrand, A., A. Chaigneau, S. Peraltilla, J. Ledesma, M. Graco, F. Monetti and F. Chavez (2011), Oxygen: A Fundamental Property Regulating Pelagic Ecosystem Structure in the Coastal Southeastern Tropical Pacific, PLOS ONE, 6(12), e29558, doi.org/10.1371/journal.pone.0029558.

Bertrand, A, D. Grados, F. Colas, S. Bertrand, X. Capet, A. Chaigneau, G. Vargas, A. Mousseigne and R. Fablet (2014), Broad impacts of fine-scale dynamics on seascape structure from zooplankton to seabirds, Nat Commun 5:5239. doi:10.1038/ncomms6239.

Bettencourt, J. H., C. López, E. Hernández-García, I. Montes, J. Sudre, B. Dewitte, A. Paulmier and V. Garçon (2015), Boundaries of the Peruvian Oxygen Minimum Zone shaped by coherent mesoscale dynamics, Nat. Geosci., 8, 937–40, doi:10.1038/ngeo2570.

Bianchi, D., J. P. Dunne, J. L. Sarmiento, and E. D. Galbraith (2012), Data-based estimates of suboxia, denitrification, and N2O production in the ocean and their sensitivities to dissolved O2, Global Biogeochem. Cycles, 26, GB2009, doi:10.1029/2011GB004209.

Bopp L., L. Resplandy, J. C. Orr, S. C. Doney, J. P. Dunne, M. Gehlen, P. Halloran, C. Heinze, T. Ilyina, R. Séférian, J. Tjiputra and M. Vichi (2013), Multiple stressors of ocean ecosystems in the 21st century: projections with CMIP5 models, Biogeosciences, 10, 6225-6245.

Bouchón, M., and C., Peña (2008), Impactos de los eventos La Niña en la pesquería peruana, Inf. Inst. Mar Perú. 35 (3): 193-198.

Boyd, P., T. Jickells, C. S. Law, S. Blain, E. A. Boyle, K. O. Buesseler, K. H. Coale, J. J. Cullen8, H. J. W. de Baar, M. Follows, M. Harvey, C. Lancelot, M. Levasseur, N. P. J. Owens, R. Pollard, R. B. Rivkin, J. Sarmiento, V. Schoemann, V. Smetacek, S. Takeda, A. Tsuda, S. Turner, A. J. Watson (2007), Mesoscale Iron Enrichment Experiments 1993-2005: Synthesis and Future Directions, Science, 315, 612-617.

Breitburg, D, L. A. Levin, A. Oschlies, M. Grégoire, F. P. Chavez, D. J. Conley, V. Garçon, D. Gilbert,D. Gutiérrez, K. Isensee, G. S. Jacinto, K. E. Limburg, I. Montes, S. W. A. Naqvi, G. C. Pitcher, N. N. Rabalais, M. R. Roman, K. A. Rose, B. A. Seibel, M. Telszewski, M. Yasuhara

and J. Zhang (2018), Declining oxygen in the global ocean and coastal waters, Science, 359 (6371), eaam7240, doi:10.1126/science.aam7240.

Brink, K. H., D. Halpern, A. Huyer, and R. L. Smith (1983), The physical environment of the Peruvian upwelling system, Prog. Oceanogr., 12, 285–305, doi:10.1016/0079-6611(83)90011-3.

Brochier, T., V. Echevin, J. Tam, A. Chaigneau, K. Goubanova and A. Bertrand (2013), Climate change scenarios experiments predict a future reduction in small pelagic fish recruitment in the Humboldt Current system, Global Change Biol., 19, 1841–1853, doi:10.1111/gcb.12184.

Brochier T., P. A. Auger, L. Pecquerie, E. Machu, X. Capet, M. T. Baye, Ch. Mbaye, Ch. Braham, O. Ettahiri, N. Charouki, O. N. Sène, F. Werner and P. Brehmer (2018), Complex small pelagic fish population patterns arising from individual behavioral responses to their environment, Progress in Oceanography, 164, 12-27, doi:10.1016/j.pocean.2018.03.011.

Brockmann, C., E. Fahrbach, A. Huyer, and R. L. Smith (1980), The poleward undercurrent along the Peru coast: 5 to 15°S, Deep Sea Res. Part A, 27, 847–856.

Bruland, K. W., E. L. Rue, G. J. Smith and G. R. DiTullio (2005), Iron, macronutrients and diatom blooms in the Peru upwelling regime: brown and blue waters of Peru, Mar. Chem., 93, 81–103.

Buitenhuis, E., C. Le Quéré, O. Aumont, G. Beaugrand, A. Bunker, A. Hirst, T. Ikeda, T. O'Brien, S. Piontkovski, and D. Straile (2006), Biogeochemical fluxes through mesozooplankton, Global Biogeochem. Cycles, 20, GB2003, doi:10.1029/2005GB002511.

Cabré, A., I. Marinov, R. Bernardello and D. Bianchi, D. (2015), Oxygen minimum zones in the tropical Pacific across CMIP5 models: mean state differences and climate change trends, Biogeosciences, 12, 5429-5454, doi :10.5194/bg-12-5429-2015.

Calienes, R., O. Guillén and N. Lostaunau (1985) Variabilidad espacio-temporal de clorofila, produccion primaria y nutrientes frente a la costa peruana. Bol. Inst. Mar Perú (10): 6-12.

Calienes, R. (2014), Producción primaria en el ambiente marino en el Pacífico sudeste, Perú, 1960-2000, Bol. Inst. Mar Perú, 29(1-2).

Carr, M. –E. and K. Broad (2000), Satellites, society and the Peruvian fisheries during the 1997-1998 El Niño. In Halpern, D. (Ed.), Satellites, Oceanography and Society, Elsevier, Amsterdam, pp. 171-191.

Carr, M. -E., P. T. Strub, A. C. Thomas and J. L. Blanco (2002), Evolution of 1996–1999 La Niña and El Niño conditions off the western coast of South America: A remote sensing perspective, J. Geophys. Res., 107(C12), 3236, doi:10.1029/2001JC001183.

Carr, M. -E. (2003), Simulation of carbon pathways in the planktonic ecosystem off Peru during the 1997–1998 El Niño and La Niña, J. Geophys. Res., 108(C12), 3380, doi:10.1029/1999JC000064.

Capet, X. J., P. Marchesiello, and J. C. McWilliams (2004), Upwelling response to coastal wind profiles, Geophys. Res. Lett, 31, L13311, doi:10.1029/2004GL02123.

Capet, X., J. C. McWilliams, M. J. Molemaker and A. F. Shchepetkin (2008), Mesoscale to submesoscale transition in the California Current System. Part I: Flow structure, eddy flux, and observational tests, J. Phys. Oceanogr., 38(1), 29-43.

Carrit, D. E. and J. H. Carpenter (1966), Recommendation procedure for Winkler analyses of sea water for dissolved oxygen, J. Mar. Res., 24, 313-318.

Carton, J. A., and B. Giese (2008), A Reanalysis of Ocean Climate Using Simple Ocean Data Assimilation (SODA), Mon. Weather Rev., 136, 2999-3017.

Casey, K. S., T. B. Brandon, P. Cornillon, and R. Evans (2010), The Past, Present and Future of the AVHRR Pathfinder SST Program, in Oceanography from Space: Revisited, edited by V. Barale, J. F. R. Gower and L. Alberotanza, Springer, doi: 10.1007/978-90-481-8681-5_16.

Cavan, E. L., M. Trimmer, F. Shelley and R. Sanders (2017), Remineralization of particulate organic carbon in an ocean oxygen minimum zone, Nature Communications, 8, 14847, doi: 10.1038/ncomms14847.

Chaigneau, A., G. Arnaud Gizolme and C. Grados (2008), Mesoscale eddies off Peru in altimeter records: Identification algorithms and eddy spatio-temporal patterns, Prog. Oceanogr., 79, 106-119, doi:10.1016/j.pocean.2008.10.013.

Chaigneau, A., N. Dominguez, G. Eldin, L. Vasquez, R. Flores, C. Grados, and V. Echevin (2013), Near-coastal circulation in the Northern Humboldt Current System from shipboard ADCP data, J. Geophys. Res. Oceans, 118, 5251–5266, doi: 10.1002/jgrc.20328.

Chamorro, A., V. Echevin, F. Colas, V. Oerder, J. Tam and C. Quispe-Ccalluari, C. (2018), Mechanisms of the intensification of the upwelling-favorable winds during El Niño 1997–1998 in the Peruvian upwelling system, Climate Dynamics, 1-17.

Chavez, F. A., R. T. Barber and H. S. Soldi (1984), Propagated temperature changes during onset and recovery of the 1982/83 El Niño, Nature, 309, 47-49.

Chavez, F., A. Bertrand, R. Guevara-Carrasco, P. Soler and J. Csirke (2008), The northern Humboldt Current System: brief history, present status and a view towards the future, Prog. Oceanogr., 79, 95–105, doi:10.1016/j.pocean.2008.10.012.

Chavez, F., and M. Messié (2009), A comparison of Eastern Boundary Upwelling Ecosystems, Prog. Oceanogr., 83, 80-96, doi:10.1016/j.pocean.2009.07.032.

Cheung, W. W. L. (2018), The future of fishes and fisheries in the changing oceans, Journal of Fish Biology, 92, 790–803, doi:10.1111/jfb.13558.

Codispoti, L.A. and J. P. Christensen (1985), Nitrification, denitrification and nitrous oxide cycling in the eastern tropical South Pacific Ocean, Marine Chemestry, 16 (4), 277-300, doi: 10.1016/0304-4203(85)90051-9.

Codispoti, L. A., R. T. Barber, and G. E. Friederich (1989), Do nitrogen transformations in the poleward undercurrent off Peru and Chile have a globally significant influence? In: Neshyba, S. J., N. K. Mooers, R. L. Smith and R. Barber (Eds.), Poleward Flows Along Eastern Ocean Boundaries. Coastal and Estuarine Studies. Springer-Verlag, pp. 281–310.

Conkright, M., R. Locarnini, H. Garcia, T. D. O'Brien, T. P. Boyer, C. Stephens and J Antononov (2002), World Ocean Atlas 2001: objectives, analyses, data statistics and figures [CD-ROM], NOAA Atlas NESDIS 42, Silver Spring Md.

Colas, F., X. Capet, J. C. McWilliams and A. Shchepetkin (2008), 1997–98 El Niño off Peru: a numerical study, Prog. Oceanogr., 79, 138–155.

Colas, F., J. C. McWilliams, X. Capet and J. Kurian (2012), Heat balance and eddies in the Peru-Chile current system, Clim. Dyn., 39, 509-529, doi:10.1007/s00382-011-1170-6.

Colas, F., X. Capet, J. C. McWilliams and Z. Li (2013), Mesoscale Eddy Buoyancy Flux and Eddy-Induced Circulation in Eastern Boundary Currents, J. Phys. Oceanogr., 43, 1073-1095, doi: 10.1175/JPO-D-11-0241.

Czeschel, R., L. Stramma, F. U. Schwarzkopf, B. S. Giese, A. Funk, and J. Karstensen (2011), Middepth circulation of the eastern tropical South Pacific and its link to the oxygen minimum zone, J. Geophys. Res., 116, C01015, doi:10.1029/2010JC006565.

Czeschel, R., L. Stramma, R. A. Weller and T. Fischer (2015), Circulation, eddies, oxygen, and nutrient changes in the Eastern Tropical South Pacific Ocean, Ocean Sci., 11, 455 – 470, doi:10.5194/os-11-455-2015.

Da Silva, A. M., C. C. Young and S. Levitus (1994), Atlas of surface marina data 1994, Technical report, Natl. Oceanogr. And Atmos. Admin, Silver Spring Md.

Dale A. W., M. Graco, K. Wallmann (2017), Strong and Dynamic Benthic-Pelagic Coupling and Feedbacks in a Coastal Upwelling System (Peruvian Shelf), Front. Mar. Sci., 4, 29, doi:10.3389/fmars.2017.00029

Dalsgaard, T., B. Thamdrup, L. Farías and N. P. Revsbech (2012), Anammox and denitrification in the oxygen minimum zone of the eastern South Pacific, Limnol. Oceanogr., 57(5), 1331–1346, doi:10.4319/lo.2012.57.5.1331.

Dee, D. P., Uppala, S. M., Simmons, A. J., Berrisford, P., Poli, P., Kobayashi, S., Andrae, U., Balmaseda, M. A., Balsamo, G., Bauer, P., Bechtold, P., Beljaars, A. C. M., van de Berg, L., Bidlot, J., Bormann, N., Delsol, C., Dragani, R., Fuentes, M., Geer, A. J., Haimberger, L., Healy, S. B., Hersbach, H., Hólm, E. V., Isaksen, L., Kållberg, P., Köhler, M., Matricardi, M., McNally, A. P., Monge-Sanz, B. M., Morcrette, J.-J., Park, B.-K., Peubey, C., de Rosnay, P., Tavolato, C., Thépaut, J.-N. and Vitart, F. (2011), The ERA-Interim reanalysis: configuration and performance of the data assimilation system. Q.J.R. Meteorol. Soc., 137: 553–597.

del Giorgio, P. A., and C. M., Duarte (2002), Total respiration and the organic carbon balance of the open ocean, Nature, 420, 379–384.

Demarcq, H. (2009) Trends in Primary Production, Sea Surface Temperature and Wind in Upwelling Systems (1998- 2007). Progress in Oceanography, 83, 376-385. doi :10.1016/j.pocean.2009.07.022

Devol, A. H., A. G. Uhlenhopp, S. W. A. Naqvi, J. A. Brandes, D. A. Jayakumar, H. Naik, S. Gaurin, L. A. Codispoti and T. Yoshinari (2006), Denitrification rates and excess nitrogen gas concentrations in the Arabian Sea oxygen deficient zone, Deep-Sea Res., 53, 1533 – 1547, doi:10.1016/j.dsr.2006.07.005.

Dewitte, B., J. Vazquez-Cuervo, K. Goubanova, S. Illig, K. Takahashi, G. Cambon, S. Purca, D. Correa, D. Gutierrez, A. Sifeddine and L. Ortlieb (2012), Change in El Niño flavours over 1958–2008: Implications for the long-term trend of the upwelling off Peru, Deep-Sea Res. II, 77–80, 143–156, doi:10.1016/j.dsr2.2012.04.011.

Diaz, R. J. and R. Rosenberg (2008), Spreading Dead Zones and Consequences for Marine Ecosystems, Science, 321, 926-29, doi: 10.1126/science.1156401.

Dugdale R. C., J. J. Goering, R.T. Barber, R. L. Smith and T. T. Packard (1977), Denitrification and hydrogen sulfide in the Peru upwelling region during 1976, Deep Sea Research, 24, 6, 601-608, doi:10.1016/0146-6291(77)90530-6.

Duteil, O., A. Oschlies, and C. W. Böning (2018), Pacific Decadal Oscillation and recent oxygen decline in the eastern tropical Pacific Ocean, Biogeosciences Discuss., in review, doi :10.5194/bg-2018-16.

Echevin, V., O. Aumont, J. Ledesma and G. Flores (2008), The seasonal cycle of surface chlorophyll in the Peruvian upwelling system: A model study, Prog. Oceanogr., 79, 167-76.

Echevin, V., F. Colas, A. Chaigneau and P. Penven (2011), Sensitivity of the Northern Humboldt Current System nearshore modeled circulation to initial and boundary conditions, J. Geophys. Res., 116, C07002, doi:10.1029/2010JC006684.

Echevin, V., A. Albert, M. Lévy, O. Aumont, M. Graco and G. Garric, (2014), Remotely-forced intraseasonal variability of the Northern Humboldt Current System surface chlorophyll using a coupled physical-ecosystem model, Cont. Shelf Res., 73, 14-30, doi:10.1016/j.csr.2013.11.015.

Echevin V., F. Colas, D. Espinoza-Morriberon, T. Anculle, L. Vasquez and D. Gutierrez (2018), Forcings and evolution of the 2017 coastal El Niño off Northern Peru and Ecuador, Frontiers in Marine Science, accepted, doi:10.3389/fmars.2018.00367.

ENFEN (2017), Technical Report ENFEN, year 3, number 03, March 2017, 65p, accessed in: https://www.dhn.mil.pe/Archivos/oceanografia/enfen/informe-tecnico/03-2017.pdf

Enfield, D. B. (1981), Thermally driven wind variability in the planetary boundary layer above Lima, Peru, J. Geophys. Res., 86(C3), 2005–2016, doi:10.1029/JC086iCO3p02005.

Espinoza, P. and A. Bertrand (2008), Revisiting Peruvian anchovy (Engraulis ringens) trophodynamics provides a new vision of the Humboldt Current system. Prog. Oceanogr., 79, 215-227.

Espinoza-Morriberón, D. (2012), Impacto de la circulación ecuatorial en la Zona Mínima de Oxígeno presente en el Norte del Ecosistema de la Corriente de Humboldt, Master Tesis, Universidad Peruana Cayetano Heredia, 136pp.

Espinoza-Morriberon D., V. Echevin, C. Y. Romero, J. Ledesma, R. Oliveros-Ramos and J. Tam (2016), Biogeochemical validation of an interannual simulation of the ROMS-PISCES coupled model in the Southeast Pacific, Revista peruana de biología, 23(2), 159–168. doi:10.15381/rpb.v23i2.12427

Espinoza-Morriberón, D., V. Echevin, F. Colas, J. Tam, J. Ledesma, L. Vásquez, and M. Graco (2017), Impacts of El Niño events on the Peruvian upwelling system productivity, J. Geophys. Res. Oceans, 122, 5423–5444, doi:10.1002/2016JC012439.

Espinoza-Morriberón D., E. Echevin, F. Colas, J. Tam, D. Gutierrez, M. Graco, J. Ledesma, C. Quispe-Ccalluari (2018), Oxygen variability during ENSO in the Tropical South Eastern Pacific, Frontier in Marine Science, in revision.

Falvey M. and R. D. Garreaud (2009), Regional cooling in a warming world: Recent temperature trends in the southeast Pacific and along the west coast of south tropical South America (1979-2006). Journal of Geophysical Research, 114: D04102. doi:10.1029/2008JD010519.

Fiedler, P. C. and L. D. Talley (2006), Hydrography of the eastern tropical Pacific: a review, Progress in Oceanography, 69 (2–4), 143 – 180.

Flores R., M. Espino, G. Luque and J. Quispe (2013), Patrones de variabilidad ambiental en el mar peruano, Rev. peru. biol., 20(1), 21-28.

Freon, P., M. Barange and J. Aristegui (2009), Eastern boundary upwelling ecosystems: integrative and comparative approaches preface, Prog. Oceanogr., 83 (1–4), 1-15, doi:10.1016/j.pocean.2009.08.001

Fuenzalida, R., W. Schneider, J. Garcés-Vargas, L. Bravo and C. Lange (2009), Vertical and horizontal extension of the oxygen minimum zone in the eastern South Pacific Ocean, Deep-Sea Res. II, 56 (16), 992-1003, doi: 10.1016/j.dsr2.2008.11.001.

Garcia, H. E., R. A. Locarnini, T. P. Boyer, J. I. Antonov, O.K. Baranova, M. M. Zweng, J. R. Reagan and D. R. Johnson (2014), World Ocean Atlas 2013, Volume 3: Dissolved Oxygen, Apparent Oxygen Utilization, and Oxygen Saturation, S. Levitus Ed., A. Mishonov Technical Ed., NOAA Atlas NESDIS 75, 27 pp.

Garreaud, R. D. (2018), A plausible atmospheric trigger for the 2017 coastal El Niño, Int. J. Climatol., doi:10.1002/joc.5426.

Gévaudan, M., F. Colas, V. Echevin, D. Grados, J. Tam, D. Gutiérrez. Cambios en la biogeoquímica y productividad del ecosistema marino peruano bajo escenarios de Cambio Climático. Interantional congress on climate change and its impacts, Huaraz, 29 November-1 December, 2017. Poster session.

Goubanova, K., V. Echevin, B. Dewitte, F. Codron, K. Takahashi, P. Terray and M. Vrac (2010), Statistical downscaling of sea-surface wind over the Peru-Chile upwelling region: diagnosing the impact of climate change from the IPSL-CM4 model, Clim. Dyn., 36, 1365, doi:10.1007/s00382-010-0824-0.

Graco, M., J. Ledesma, G. Flores and M. Girón (2007), Nutrientes, oxígeno y procesos biogeoquímicos en el sistema de surgencias de la corriente de Humboldt frente a Perú. Rev. Per. Biol., 14(1), 117-28.

Graco, M., S. Purca, B. Dewitte, O. Morón, J. Ledesma, G. Flores, C. Castro and D. Gutiérrez (2017) The OMZ and nutrients features as a signature of interannual and low frequency variability off the peruvian upwelling system, Biogeosci. Discuss., in review. doi:10.5194/bg-2015-567.

Graco, M., T. Anculle, O. Morón, J. Ledesma, G. Flores, A. Chaigneau, F. Monetti and D. Gutiérrez (in press), Variabilidad espacial y temporal del oxígeno disuelto y de la ZMO en el sistema de afloramiento frente a Perú. III Libro de la Anchoveta. Instituto del Mar del Perú.

Grados, C., A. Chaigneau, V. Echevin and N. Dominguez (2018), Upper ocean hydrology of the Northern Humboldt Current System at seasonal, interannual and interdecadal scales, Progress in Oceanography, 165, 123-144, doi:10.1016/j.pocean.2018.05.005.

Gruber, N., H. Frenzel, S. C. Doney, P. Marchesiello, J. C. McWilliams, J. R. Moisan, J. J. Oram, G.-K. Plattner, and K. D. Stolzenbach (2006), Eddy-resolving simulation of plankton ecosystem dynamics in the California Current System, Deep Sea Res. I, 53(9), 1483–1516.

Gruber, N., Z. Lachkar, H. Frenzel, P. Marchesiello, M. Munnich, J. McWilliams, T. Nagai and G. Plattner (2011) Eddy-induced reduction of biological production in eastern boundary upwelling systems, Nat. Geosci., 4, 787–792.

Gutiérrez, D., E. Enríquez, S. Purca, L. Quipúzcoa, R. Marquina, G. Flores and M. Graco (2008), Oxygenation episodes on the continental shelf of central Peru: Remote forcing and benthic ecosystem response, Progress in Oceanography, 79 (2), 177-189, doi:10.1016/j.pocean.2008.10.025.

Gutiérrez, D., I. Bouloubassi, A. Sifeddine, S. Purca, K. Goubanova, M. Graco, D. Field, L. Méjanelle, F. Velazco, A. Lorre, R. Salvatteci, D. Quispe, G. Vargas, B. Dewitte and L. Ortlieb (2011a), Coastal cooling and increased productivity in the main upwelling zone off Peru since the mid-twentieth century, Geophys. Res. Lett., 38, L07603, doi:10.1029/2010GL046324.

Gutierréz D., A. Bertrand, C. Wosnitza-Mendo, B. Dewitte, S. Purca, C. Peña, A. Chaigneau, J. Tam, M. Graco, V. Echevin, C. Grados, P. Freón and R. Guevara-Carrasco (2011b), Sensitivity of the Peruvian upwelling system to climate change and ecological implications, Revista Peruana Geo-atmosférica (3), 1-24.

Gutiérrez, D., M. Akester, and L. Naranjo (2016), Productivity and Sustainable Management of the Humboldt Current Large Marine Ecosystem under climate change, Environmental Development, 17, 126-144, doi:10.1016/j.envdev.2015.11.004.

Gutiérrez D., M. Graco, R. Salvatteci, J. Cardich, D. Espinoza-Morriberón, A. Sifeddine and V. Echevin (in prep), The Tropical South Eastern Pacific Oxygen Minimum Zone: past variability, recent trends and ecosystem effects over the continental margin, Progress in Oceanography.

Gutknecht, E., I. Dadou, B. Le Vu, G. Cambon, J. Sudre, V. Garçon, E. Machu, T. Rixen, A. Kock, A. Flohr, A. Paulmier and G. Lavik (2013), Coupled physical/biogeochemical modeling including O2-dependent processes in the Eastern Boundary Upwelling Systems: application in the Benguela, Biogeosciences, 10, 3559–3591, doi:10.5194/bg-10-3559 2013.

Halpern, D. (2002), Offshore Ekman transport and Ekman pumping off Peru during the 1997–1998 El Niño, Geophys. Res. Lett., 29(5), 1075, doi:10.1029/2001GL014097.

Hernandez, O., P. Lehodey, I. Senina, V. Echevin, P. Ayón, A. Bertrand and P. Gaspar (2014), Understanding mechanisms that control fish spawning and larval recruitment: Parameter optimization of an Eulerian model (SEAPODYM-SP) with Peruvian anchovy and sardine eggs and larvae data, Prog. Oceanogr., 123, 105-122.

Hernández-León, S., and T., Ikeda (2005), A global assessment of mesozooplankton respiration in the ocean, Journal of Plankton Research, Volume 27 (2), 153–158, doi:10.1093/plankt/fbh166.

Holm-Hansen O., C. J. Lorenzen, R. W. Holmes and J. D. H. Strickland (1965), Fluorometric determination of chlorophyll, J. Cons. Perm. Int. Explor. Mer., 30, 3-15.

Huang, B., V. F. Banzon, E. Freeman, J. Lawrimore, W. Liu, T. C. Peterson, T. M. Smith, P. W. Thorne, S. D. Woodruff, and H. -M. Zhang (2015), Extended Reconstructed Sea Surface Temperature version 4 (ERSST.v4): Part I. Upgrades and intercomparisons, J. Clim., 28, 911–930, doi:10.1175/JCLI-D-14-00006.1.

Hutchins, D. A., C. E. Hare, R. S. Weaver, Y. Zhang, G. F. Firme, G. R. DiTullio, M. B. Alm, S. F. Riseman, J. M. Maucher, M. E. Geesey, C. G. Trick, G. J. Smith, E. L. Rue, J. Conn and K. W. Bruland (2002), Phytoplankton iron limitation in the Humboldt Current and Peru Upwelling, Limnol. Oceanogr., 47, 997-1011, doi: 10.4319/lo.2002.47.4.0997.

Huyer, A., R. L. Smith and T. Paluszkiewicz (1987), Coastal upwelling off Peru during normal and El Niño times, J. Geophys. Res., 92, 14,297–14,307, doi:10.1029/JC092iC13p14297.

Huyer, A., M. Knoll, T. Paluszkiewic and R. L. Smith (1991), The Peru Undercurrent: A study of variability, Deep Sea Res. Part A, 38, S247–S271.

Ishida, A., H. Mitsudera, Y. Kashino, and T. Kadokura (2005), Equatorial Pacific subsurface countercurrents in a high-resolution global ocean circulation model, J. Geophys. Res., 110, C07014, doi:10.1029/2003JC002210.

Irwin, A. J., Z. B. Finkel, O. M. E.Schofield and P. G. Falkowsky (2006), Scaling-up from nutrient physiology to the size-structure of phytoplankton communities, J. Plankton Res., 28(5), 459 – 471. doi:10.1093/plankt/fbi148.

Ito, T., and C. Deutsch (2013), Variability of the oxygen minimum zone in the tropical North Pacific during the late twentieth century, Global Biogeochem. Cycles, 27, 1119–1128, doi:10.1002/2013GB004567.

Jacox, M. G., S. J. Bograd, E. L. Hazen, and J. Fiechter (2015), Sensitivity of the California Current nutrient supply to wind, heat, and remote ocean forcing, Geophys. Res. Lett., 42, doi:10.1002/2015GL065147.

Johnson, G. C., and D. W. Moore (1997), The Pacific subsurface countercurrents and an inertial model, J. Phys. Oceanogr., 27, 2448–2459.

Kahru, M., B. G. Mitchell, A. Diaz and M. Miura (2004), MODIS Detects a Devastating Algal Bloom in Paracas Bay, Peru. Eos, Trans. Amer. Geophys., 85(45), 465–472, doi:10.1029/2004EO450002.

Kalvelage, T., G. Lavik, M. M. Jensen, N. P. Revsbech, C. Löscher, H. Schunck, D. K. Desai, H. Hauss, R. Kiko, M. Holtappels, J. LaRoche, R. A. Schmitz, M. I. Graco and M. M. M. Kuypers (2015), Aerobic Microbial Respiration In Oceanic Oxygen Minimum Zones, PLoS ONE, 10(7), e0133526, doi:10.1371/journal.pone.0133526.

Kampf, J. and P. Chapman (2016), Upwelling Systems of the World: A Scientific Journey to the Most Productive Marine Ecosystems, Springer International Publishing, 433pp.

Karstensen, J., L. Stramma and M. Visbeck (2008), Oxygen minimum zones in the eastern tropical Atlantic and Pacific Oceans. Prog Oceanogr, 77, 331–50.

Kessler, W. S., and M. J. McPhaden (1995), Oceanic equatorial waves and the 1991-1993 El Niño, J. Clim., 8, 1757–1774.

Kessler, W. S. (2006), The circulation of the eastern tropical Pacific: A review, Prog. Oceanogr., 69, 181–217.

Kock, A., D. L. Arévalo-Martínez, C. R. Löscher and H. W. Bange (2016), Extreme N2O accumulation in the coastal oxygen minimum zone off Peru, Biogeosciences, 13, 827–840, doi:10.5194/bg-13-827-2016.

Lachkar, Z., and N. Gruber (2012), A comparative study of biological production in eastern boundary upwelling systems using an artificial neural network, Biogeosciences, 9, 293–308, doi:10.5194/bg-9-293-2012.

Lam, P., G. Lavik, M. M. Jensen, J. Van de Vossenberg, M. Schmid, D. Woebken, D. Gutiérrez, R. Amann, M. S. M. Jetten and M. M. M. Kuypers (2009), Revising the nitrogen cycle in the Peruvian oxygen minimum zone, PNAS, 106 (12) 4752-4757, doi:10.1073/pnas.0812444106.

Lathuilière, C., V. Echevin, M. Lévy, and G. Madec (2010), On the role of the mesoscale circulation on an idealized coastal upwelling ecosystem. J. Geophys. Res., 115, C09018, doi:10.1029/2009JC005827.

Ledesma, J., J. Tam, M. Graco, V. León, G. Flores and O. Morón (2011), Caracterización de la Zona de Mínimo de Oxígeno (ZMO) frente a la costa peruana entre 3°N y 14°S, 1999 – 2009, Bol Inst Mar Perú, 26(1-2), 49-57.

Lefort, S., O. Aumont O., L. Bopp, T. Arsouze, M. Gehlen and O. Maury (2015), Spatial and body-size dependent response of marine pelagic communities to projected global climate change. Global Change Biol., 21(1), 154-164.

Lee, T., and M. J. McPhaden (2010), Increasing intensity of El Niño in the central-equatorial Pacific, Geophys. Res. Lett., 37, L14603, doi: 10.1029/2010GL044007.

Lee, K.-W., S.-W. Yeh, J.-S. Kug, and J.-Y. Park (2014), Ocean chlorophyll response to two types of El Niño events in an ocean-biogeochemical coupled model, J. Geophys. Res. Oceans, 119, 933–952, doi:10.1002/2013JC009050

Levin, L. A. (2003), Oxygen minimum zone benthos: Adaptation and community response to hypoxia, Oceanography and Marine Biology, 41, 41:1-45.

Liu, W. T., Katsaros, K. B., and Businger, J. A. (1979). Bulk parameterization of air-sea exchanges of heat and water vapor including the molecular constraints at the interface. Journal of the Atmospheric Sciences, 36(9), 1722-1735.

Llanillo, P. J., J. Karstensen, J. L. Pelegrí and L. Stramma (2013), Physical and biogeochemical forcing of oxygen and nitrate changes during El Niño/El Viejo and La Niña/La Vieja upper-ocean phases in the tropical eastern South Pacific along 86°W, Biogeosciences, 10, 6339–6355, doi:10.5194/bg-10-6339-2013.

Llanillo, P. J., J. L. Pelegrí, L. D. Talley, J. Peña-Izquierdo and R. R. Cordero (2018), Oxygen pathways and budget for the eastern South Pacific Oxygen Minimum Zone, Journal of Geophysical Research Oceans, 123. doi:10.1002/2017JC013509.

López-Urrutia, Á. E. S. Martin, R. P. Harris, and X. Irigoien (2006), Scaling the metabolic balance of the oceans, Proc. Natl. Acad. Sci. U.S.A., 103, 8739–8744.

Lukas, R. (1986), The termination of the Equatorial Undercurrent in the eastern Pacific, Prog. Oceanogr., 16, 63–90, doi:10.1016/0079-6611(86)90007-8.

Luyten, J. R., J. Pedlosky and H. Stommel (1983), The ventilated thermocline, J. Phys. Oceanogr. 13, 292–309.

Marchesiello, P., and P. Estrade (2010), Upwelling limitation by onshore geostrophic flow, J. Mar. Res., 68, 37-62, doi:10.1357/002224010793079004.

McPhaden M. J. (1999), Genesis and evolution of the 1997-98 El Niño, Science, 283 (5404), 950-954.

McWilliams, J. C. (2016), Submesoscale currents in the ocean, Proc. R. Soc. London, Ser. A, 472, 20160117, doi:10.1098/rspa.2016.0117.

Mendo, J., L. Pizarro, and S. Castillo (1987), Monthly upwelling and turbulence indices of the Peruvian coast at Callao and Trujillo during the period 1953-1983, in The Peruvian *anchoveta and its* upwelling *ecosystem*: *three decades of change*, edited by D. Pauly and I. Tsukayama, ICLARM, Studies and Reviews 15,351 p

Messié, M. and F. P. Chavez (2015), Seasonal regulation of primary production in eastern boundary upwelling systems, Prog. Oceanogr., 134, 1-18, doi:10.1016/j.pocean.2014.10.011.

Mogollón, R. and P. H. R. Calil (2017), On the effects of ENSO on ocean biogeochemistry in the Northern Humboldt Current System (NHCS): A modeling study, Journal of Marine Systems, 172, 137-159, doi:10.1016/j.jmarsys.2017.03.011.

Mogollón, R. and P. H. R. Calil (2018), Counterintuitive effects of global warming-induced wind patterns on primary production in the Northern Humboldt Current System, Glob Change Biol., 2018, 0,1–12, doi:10.1111/gcb.14171

Montes, I., F. Colas, X. Capet and W. Schneider (2010), On the pathways of the equatorial subsurface currents in the eastern equatorial Pacific and their contributions to the Peru-Chile Undercurrent, J. Geophys. Res. Oceans, 115, C09003, doi:10.1029/2009JC005710.

Montes, I., S. Wolfgang, F. Colas, B. Blanke and V. Echevin (2011), Subsurface connections in the eastern tropical Pacific during La Niña 1999–2001 and El Niño 2002–2003, J. Geophys. Res., 116, C12022, doi:10.1029/2011JC007624.

Montes, I., B. Dewitte, E. Gutknecht, A. Paulmier, I. Dadou, A. Oschlies and V. Garçon (2014), High-resolution modeling of the Eastern Tropical Pacific oxygen minimum zone: Sensitivity to the tropical oceanic circulation, J. Geophys. Res. Oceans, 119(8), 5515-5532, doi:10.1002/2014JC009858.

Morón, O. (2000), Características del ambiente marino frente a la costa peruana, Bol. Inst. Mar Perú, 19(1-2):179-204.

Narayan, N., A. Paul, S. Mulitza and M. Schultz (2010), Trends in coastal upwelling intensity during the late 20th century, Ocean Science, 6, 815–823.

Ochoa, N., M. H. Taylor, S. Purca and E. Ramos (2010), Intra- and interannual variability of nearshore phytoplankton biovolume and community changes in the northern Humboldt Current system, Journal of Plankton Research, 32(6), 843-855.

Ñiquen, M., and M. Bouchón (2004), Impact of El Niño event on pelagic fisheries in Peruvian waters, Deep Sea Res. Part II, 51, 563-574, doi:10.1016/j.dsr2.2004.03.001.

Oerder, V., F. Colas, V. Echevin, F. Codron, J. Tam, and A. Belmadani (2015), Peru-Chile upwelling dynamics under climate change, J. Geophys. Res. Oceans, 120, 1152–1172, doi:10.1002/2014JC010299.

O´Reilly, J.E., S. Maritorena, B. G. Mitchell, D. A. Siegel, K. L. Carder, S. A. Garver, M. Kharu and C. McClain (1998), Ocean color chlorophyll algorithms for SeaWIFS, J. Geophys. Res., 103, C11, 24,937-24,953, doi:10.1029/98JC02160.

Packard, T. T., P. C. Garfield and L. A. Codispoti (1983), Oxygen consumption and denitrification below the peruvian upwelling, in E. Suess and J. Thiede (eds.), Coastal Upwelling, Plenum Press. NY., p. 147-173.

Paulmier, A., D. Ruiz-Pino, V. Garçon and L. Farías (2006), Maintaining of the Eastern South Pacific Oxygen Minimum Zone (OMZ) off Chile, Geophys. Res. Lett., 33, L20601, doi:10.1029/2006GL026801.

Paulmier, A. and D. Ruiz-Pino (2009), Oxygen minimum zones (OMZs) in the modern ocean, Prog Oceanogr, 80 (3-4),113-28, doi:10.1016/j.pocean.2008.08.001.

Pauly, D. and V. Christensen (1995), Primary production required to sustain global fisheries, Nature, 374, 255–257.

Pennington, J. T., K. L. Mahoney, V. S. Kuwahara, D. D. Kolver, R. Calienes and F. P. Chavez (2006), Primary production in the eastern tropical Pacific: a review, Prog. Oceanogr., 69, 285-317, doi:10.1016/j.pocean.2006.03.012.

Penven, P., V. Echevin, J. Pasapera, F. Colas, and J. Tam (2005), Average circulation, seasonal cycle, and mesoscale dynamics of the Peru Current System: A modeling approach, J. Geophys. Res., 110, C10021, doi:10.1029/2005JC002945.

Penven, P., L. Debreu, P. Marchesiello, and J. C. McWilliams (2006), Evaluation and application of the ROMS 1-way embedding procedure to the central California upwelling system. Ocean Modell., 12, 157–187.

Penven, P., P. Marchesiello, L. Debreu and J. Lefèvre (2008), Software tools for pre- and post-processing of oceanic regional simulations, Environ. Modell. Software, 23, 660-662, doi:10.1016/j.envsoft.2007.07.004.

Philander, S. G. H. (1980), The equatorial undercurrent revisited, Annu. Rev. Earth Planet Sci., 8, 191–204.

Picaut, J., M. Ioualalen, C. Menkes, T. Delcroix and M. J. McPhaden (1996), Mechanisms of the zonal displacements of the Pacific warm pool: Implications for ENSO, Science, 274, 1486–1489, doi:10.1126/science.274.5292.1486.

Picaut J., E. Hackert, A. J. Busalacchi, R. Murtugudde and G. S. E. Lagerloef (2002), Mechanisms of the 1997–1998 El Niño–La Niña, as inferred from space-based observations, J. Geophys. Res. Oceans, 107 (C5), 5-1, 5-18, doi: 10.1029/2001JC000850.

Pietri, A., V. Echevin, P. Testor, A. Chaigneau, L. Mortier, C. Grados, and A. Albert (2014), Impact of a coastal-trapped wave on the near-coastal circulation of the Peru upwelling system from glider data, J. Geophys. Res. Oceans, 119, 2109–2120, doi:10.1002/2013JC009270.

Qiu B. and S. Chen (2006), Decadal Variability in the Large-Scale Sea Surface Height Field of the South Pacific Ocean: Observations and Causes, Journal of Physical Oceanography 36(9):1751-1762, doi:10.1175/JPO2943.1

Renault, L., C. Deutsch, J.C. McWilliams, H. Frenzel, J.-H. Liang and F. Colas (2016), Partial decoupling of primary productivity from upwelling in the California Current system, Nature, 46, 273-289.

Resplandy, L., M. Levy, L. Bopp, V. Echevin, S. Pous, V. V. S. S. Sarma and D. Kumar (2012), Controlling factors of the oxygen balance in the Arabian Sea's OMZ, Biogeosciences, 9, 5095–5109, doi:10.5194/bg-9-5095-2012.

Reynolds, G. L. (2007), The impact of facilities on recruitment and retention of students. New Directions for Institutional Research, 2007: 63-80. doi:10.1002/ir.223

Ridgway, K. R., J. R. Dunn and J. L. Wilkin (2002), Ocean interpolation by four-dimensional least squares-Application to the waters around Australia, J. Atmos. Oceanic Technol., 19(9), 1357-1375.

Risien, C. M., and D. B. Chelton (2008), A Global Climatology of Surface Wind and Wind Stress Fields from Eight Years of QuikSCAT Scatterometer Data, J. Phys. Oceanogr., 38, 2379-2413.

Saha, S., et al. (2010), NCEP Climate Forecast System Reanalysis (CFSR) Selected Hourly Time-Series Products, January 1979 to December 2010, https://doi.org/10.5065/D6513W89, Research Data Archive at the National Center for Atmospheric Research, Computational and Information Systems Laboratory, Boulder, Colo. Accessed [20 April 2017].

Sánchez, S. (2000), Variación estacional e interanual de la biomasa fitoplanctónica y concentraciones de clorofila frente a la costa peruana durante 1976-2000. Bol. Inst. Mar Perú, 19(1-2), 29-43.

Segschneider, J., and J. Bendtsen (2013), Temperature-dependent remineralization in a warming ocean increases surface pCO2 through changes in marine ecosystem composition, Global Biogeochem. Cycles, 27, 1214–1225.

Shchepetkin, A. F., and J. C. McWilliams (1998), Quasi-monotone advection schemes based on explicit locally adaptive dissipation, Mon. Weather Rev., 126, 1541–1580.

Shchepetkin, A. F. and J. C. McWilliams (2005), The regional oceanic modeling system: a split-explicit, free-surface, topography-following-coordinate ocean model, Ocean Modell., 9, 347–404.

Shchepetkin A.F. and J. C. McWilliams J.C. (2009), Computational kernel algorithms for fine-scale, multiprocess, longtime oceanic simulations, In: P.G. Ciarlet, Editor(s), Handbook of numerical analysis, Elsevier, 2009, Vol. 14, 121-183.

Schmidtko, S., L. Stramma and M. Visbeck (2017), Decline in global oceanic oxygen content during the past five decades, Nature, 542, 335 – 339, doi:10.1038/nature21399.

Silva, N., and S. Neshyba (1979), On the southernmost extension of the Peru-Chile Undercurrent, Deep Sea Res. Part A, 26, 1387–1393, doi:10.1016/0198-0149(79)90006-2.

Smith, W. H. F., and D. T. Sandwell (1997), Global sea floor topography from satellite altimetry and ship depth soundings, Science, 277, 1957–1962.

Smith, P., C. Fang, J. J. C. Dawson and J. J. B. Moncrieff (2008), Impact of global warming on soil organic carbon, Adv. Agron, 97, 1-43.

Song, Y. and D. B. Haidvogel (1994), A semi-implicit ocean circulation model using a generalized topography-following coordinate system, J. Comp. Phys., 115(1), 228-244.

Stramma, L., G. C. Johnson, J. Sprintall and V., Mohrholz (2008), Expanding Oxygen-Minimum Zones in the Tropical Oceans, Science, 320, 655-58, doi:10.1126/science.1153847.

Stramma, L., G. C. Johnson, E. Firing, and S. Schmidtko (2010), Eastern Pacific oxygen minimum zones: Supply paths and multidecadal changes, J. Geophys. Res., 115, C09011, doi:10.1029/2009JC005976.

Stramma, L., H. W. Bange, R. Czeschel, A. Lorenzo, and M. Frank (2013), On the role of mesoscale eddies for the biological productivity and biogeochemistry in the eastern tropical Pacific Ocean off Peru, Biogeosciences, 10, 7293–7306, doi:10.5194/bg-10-7293-2013.

Stramma, L., T. Fischer, D. S. Grundle, G. Krahmann, H. W. Bange, and C. A. Marandino (2016), Observed El Niño conditions in the eastern tropical Pacific in October 2015, Ocean Sciences, 12, 861–873, doi:10.5194/os-12-861-2016.

Strickland, J. D. H. and T. R. Parsons (1972), A Practical Hand Book of Seawater Analysis, Fisheries Research Board of Canada Bulletin 157, 2nd Edition, 310 p.

Strub, P. T., J. M. Mesias, V. Montecino, J. Rutllant, and S. Salinas (1998), Coastal ocean circulation off western South America, in The Sea, vol. 11, edited by A. R. Robinson and K. H. Brink, pp. 273–314, John Wiley, Hoboken, N. J.

Sunda, W. G., and S. A. Huntsman (1997), Interrelated influence of iron, light and cell size on marine phytoplankton growth, Nature, 390, 389–392.

Sverdrup H. (1953), On conditions for the vernal blooming of phytoplankton, Journal du Conseil/Conseil Permanent International pour l'Exploration de la Mer, 18, 287–295.

Sydeman, W. J., M. García-Reyes, D. S. Schoeman, R. R. Rykaczewski, S. A. Thompson, B. A. Black and S. J. Bograd (2014), Climate change and wind intensification in coastal upwelling ecosystems, Science, 345(6192), 77-80.

Takahashi, K., A. Montecinos, K. Goubanova and B. Dewitte (2011), ENSO regimes: Reinterpreting the canonical and Modoki El Niño, Geophys. Res. Lett., 38, L10704, doi:10.1029/2011GL047364.

Takahashi, K., and A. G. Martínez (2017), The very strong coastal El Niño in 1925 in the far-eastern Pacific, Climate Dynamics, 1-27, doi:10.1007/s00382-017-3702-1.

Tam, J., M. H. Taylor, V. Blaskovic, P. Espinoza, R. M. Ballón, E. Díaz, C. Wosnitza-Mendo, J. Argüelles, S. Purca, P. Ayón, L. Quipuzcoa, D. Gutiérrez, E. Goya, N. Ochoa, M. Wolff

(2008), Trophic modeling of the Northern Humboldt Current Ecosystem, Part I: Comparing trophic linkages under La Niña and El Niño conditions, Prog. Oceanogr., 79, 352–365, doi:10.1016/j.pocean.2008.10.007.

Tarazona, J. and W. Arntz (2001), The Peruvian Coastal Upwelling System, Coastal Marine Ecosystems of Latin America, 144, 229-244, doi:10.1007/978-3-662-04482-7_17.

Thomas, A. C., M. E. Carr and P. T. Strub (2001), Chlorophyll variability in eastern boundary currents, Geophys. Res. Lett., 28(18), 3421–3424, doi:10.1029/2001GL013368.

Thomas, A. C., P. Brickley and R. Weatherbee (2009), Interannual variability in chlorophyll concentrations in the Humboldt and California Current Systems, Prog. Oceanogr., 83, 386-392, doi:10.1016/j.pocean.2009.07.020.

Thomsen, S., T. Kanzow, F. Colas, V. Echevin, G. Krahmann, and A. Engel (2016), Do submesoscale frontal processes ventilate the oxygen minimum zone off Peru?, Geophys. Res. Lett., 43, 8133–8142, doi:10.1002/2016GL070548.

Tovar, H., and D. Cabrera (1985), Las aves guaneras y el fenómeno "El Niño", in El fenómeno "El Niño" y su impacto en la fauna marina, edited by W. F. Arntz, A. Landa and J. Tarazona, Bol. Inst. Mar Perú, extraordinary volume, 181-186.

Travers, M., Y. J. Shin, S. Jennings, E. Machu, J. A. Huggett, J. G. Field and P. Cury (2009), Two-way coupling versus one-way forcing of plankton and fish models to predict ecosystem changes in the Benguela, Ecol. Modell., 220(21), 3089-3099, doi:10.1016/j.ecolmodel.2009.08.016.

Tsuchiya, M. (1975), Subsurface countercurrents in the eastern equatorial Pacific, J. Mar. Res., 33, 145–175.

Tsuchiya, M., R. Lukas, R. A. Fine, E. Firing and E. Lindstrom (1989), Source waters of the Pacific Equatorial Undercurrent, Prog. Oceanogr., 23, 101–147.

Tsuchiya, M., and L. D. Talley (1998), A Pacific hydrographic section at 88°W: Water-property distribution, J. Geophys. Res., 103, 12,899–12,918.

Ulloa, O., R. Escribano, S. Hormazabal, R. A. Quiñones, R. R. González, and M. Ramos (2001), Evolution and biological effects of the 1997–98 El Niño in the upwelling ecosystem off northern Chile, Geophys. Res. Lett., 28(8), 1591–1594, doi:10.1029/2000GL011548.

Ulloa, O. and S. Pantoja (2009), The oxygen minimum zone of the eastern South Pacific, Deep-Sea Res. II, 56 (16), 987-91, doi: 10.1016/j.dsr2.2008.12.004.

Uppala, S. M., P.W. KÅllberg, A.J. Simmons, U. Andrae, V.D.C. Bechtold, M. Fiorino, J.K. Gibson, J. Haseler, A. Hernandez, G.A. Kelly, X. Li, K. Onogi, S. Saarinen, N. Sokka, R.P. Allan, E. Andersson, K. Arpe, M.A. Balmaseda, A.C.M. Beljaars, L.V.D. Berg, J. Bidlot, N. Bormann, S. Caires, F. Chevallier, A. Dethof, M. Dragosavac, M. Fisher, M. Fuentes, S. Hagemann, E. Hólm, B.J. Hoskins, L. Isaksen, P.A.E.M. Janssen, R. Jenne, A.P. Mcnally, J.-F. Mahfouf, J.-J. Morcrette, N.A. Rayner, R.W. Saunders, P. Simon, A. Sterl, K.E. Trenberth,

A. Untch, D. Vasiljevic, P. Viterbo and J. Woollen (2005), The ERA-40 re-analysis, Q. J. R. Meteorolog. Soc., 131: 2961–3012. doi:10.1256/qj.04.176.

Vallivattathillam, P., I. Suresh, M. Lengaigne, C. Ethé, J. Vialard, M. Levy, S. Neetu, O. Aumont, L. Resplandy, H. Naik and W. Naqvi (2017), Positive Indian Ocean Dipole events prevent anoxia off the west coast of India, Biogeosciences, 14, 1541-1559, doi:10.5194/bg-14-1541-2017.

Varela, R., I. Álvarez, F. Santos, M. deCastro and M. Gómez-Gesteira (2015), Has upwelling strengthened along worldwide coasts over 1982-2010?, Scientific Reports, 5, 10016.

Vergara, O., B. Dewitte, I. Montes, V. Garçon, M. Ramos, A. Paulmier and O. Pizarro (2016), Seasonal variability of the oxygen minimum zone off Peru in a high-resolution regional coupled model, Biogeosciences, 13, 4389–4410, doi:10.5194/bg-13-4389-2016.

Walczyńska A. And L. Sobczyk (2017), The underestimated role of temperature–oxygen relationship in large-scale studies on size-to-temperature response. Ecol Evol. 2017;7:7434–7441. https://doi.org/10.1002/ece3.3263

Wilson, C. and R. G. Williams (2006), When are eddy tracer fluxes directed down gradient? Journal of Physical Oceanography, 36 (2), 189-201.

Wood, R., C. R. Mechoso, C. S. Bretherton, R. A. Weller, B. Huebert, F. Straneo, B. A. Albrecht, H. Coe, G. Allen, G. Vaughan, P. Daum, C. Fairall, D. Chand, L. Gallardo-Klenner, R. Garreaud, C. Grados, D. S. Covert, T. S. Bates, R. Krejci, L. M. Russell, S. De Szoeke, A. Brewer, S. E. Yuter, S. R. Springston, A. Chaigneau, T. Toniazzo, P. Minnis, R. Palikonda, S. J. Abel, W. O. J. Brown, S. Williams, J. Fochesatto, J. Brioude and K. N. Bower (2011), The VAMOS Ocean-Cloud-Atmosphere-Land Study Regional Experiment (VOCALS-REx): goals, platforms, and field operations, Atmos. Chem. Phys., 11(2), 627-654, doi:10.5194/acp-11-627-2011.

Wyrtki, K (1967), Circulation and water masses in the eastern equatorial Pacific Ocean, Int. J. Oceanol. Limnol., 1, 117–147.

Xu, X., J. Segschneider, B. Schneider, W. Park, and M. Latif (2015), Oxygen minimum zone variations in the tropical Pacific during the Holocene, Geophys. Res. Lett., 42, 8530–8537, doi:10.1002/2015GL064680.

Yang, S., Gruber, N., Long, M. C., & Vogt, M. (2017). ENSO driven variability of denitrification and suboxia in the Eastern Tropical Pacific Ocean. Global Biogeochemical Cycles, 31, 1470–1487. https://doi.org/10.1002/2016GB005596.

Yeh, S.-W., J.-S. Kug, B. Dewitte, M.-H. Kwon, B. Kirtman, and F.-F. Jin (2009), El Niño in a changing climate, Nature, 461, 511–514, doi:10.1038/nature08316.

Yonss. J. S., H. Dietze, and A. Oschlies (2017), Linking diverse nutrient patterns to different water masses within anticyclonic eddies in the upwelling system off Peru, Biogeosciences, 14, 1349-1364, https://doi.org/10.5194/bg-14-1349-2017.

Yoshioka, Y. and Y. Saijo (1984), Photoinhibition and recovery of NH+4-oxidizing bacteria and NO2-oxidizing bacteria, Journal of General and Applied Microbiology, 30, 151-66.

Zuta, S., and O. G. Guillén (1970), Oceanografía de las aguas costeras del Perú, Bol. Inst. Mar Perú, 2: 157-324.